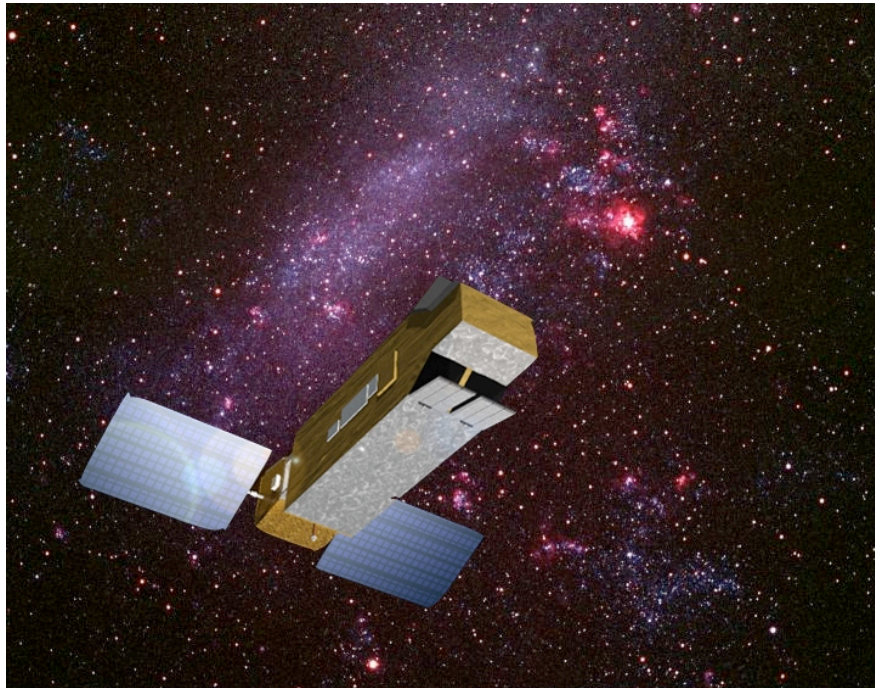


FUSE Archival Instrument Handbook



June 16, 2009 Edition

The FUSE Archival Instrument Handbook was produced by the FUSE project at JHU after the end of FUSE operations, and is meant to convey relevant information about the science instrument and its performance over the 8+ year lifetime of the mission.

Edited by Mary Elizabeth Kaiser & Jeffrey Kruk

Significant contributions from Thomas Ake, William Blair, Pierre Chayer, Mary Elizabeth Kaiser, Jeffrey Kruk, and David Sahnou.

FUSE ARCHIVAL INSTRUMENT HANDBOOK	1
1 INTRODUCTION.....	13
2 INSTRUMENT DESIGN.....	16
2.1 SCIENTIFIC MOTIVATION	16
2.2 INSTRUMENT OVERVIEW	16
2.3 OPTICAL DESIGN	18
2.4 FOCAL PLANE ASSEMBLIES.....	22
2.5 SPECTROGRAPH	27
2.5.1 <i>Optical Design</i>	27
2.5.2 <i>Wavelength Coverage and Dispersion</i>	29
2.5.3 <i>Spectral Image Characteristics</i>	30
2.6 DETECTOR DESIGN AND OPERATION.....	32
2.6.1 <i>Hardware and Software Description</i>	32
2.6.2 <i>Stim Lamp Assembly</i>	34
2.7 FINE ERROR SENSOR CAMERAS.....	35
2.7.1 <i>Camera Assembly</i>	35
2.7.1.1 <i>Optics</i>	35
2.7.1.2 <i>FES CCD Detector</i>	37
2.7.2 <i>FES Images</i>	38
2.8 INSTRUMENT DATA SYSTEM (IDS).....	40
3 THE FUSE SPACECRAFT	42
3.1 COMMAND AND DATA HANDLING SYSTEM	42
3.2 ATTITUDE CONTROL SYSTEM	42
4 IN-FLIGHT INSTRUMENT PERFORMANCE	45
4.1 TELESCOPE FOCUS.....	45
4.1.1 <i>Post-launch Focus Assessment</i>	45
4.1.2 <i>Tails of the Telescope PSF</i>	46
4.2 TELESCOPE ALIGNMENT PERFORMANCE.....	48
4.2.1 <i>Initial Alignment</i>	48
4.2.2 <i>Target Peakups</i>	49
4.2.3 <i>Mirror Motion Anomaly</i>	50
4.2.3.1 <i>On-orbit Mirror Motion Mitigation Strategy</i>	51
4.3 SPECTROGRAPH PERFORMANCE	51
4.3.1 <i>Spectrograph Resolving Power</i>	51
4.3.2 <i>Scattered Light</i>	55
4.3.3 <i>Effective Area</i>	55
4.3.4 <i>"The Worms"</i>	58
4.3.5 <i>Spectral Motion</i>	67
4.4 DETECTOR ON-ORBIT PERFORMANCE	70
4.4.1 <i>High Voltage Operations</i>	70
4.4.2 <i>Gain Sag and HV Adjustments</i>	72
4.4.2.1 <i>Gain Sag and Detector "Walk" Effects</i>	72
4.4.2.2 <i>High Voltage Adjustments</i>	76
4.4.3 <i>Detector Background</i>	77
4.4.3.1 <i>Internal Background</i>	77
4.4.3.2 <i>South Atlantic Anomaly</i>	78
4.4.3.3 <i>Event Bursts</i>	79
4.4.3.4 <i>High Background Periods</i>	82
4.4.4 <i>Geometric Distortion</i>	83
4.4.4.1 <i>Thermal Distortion and Stability</i>	84
4.4.5 <i>Flat Field / MCP Effects</i>	86

4.4.5.1	Chicken Wire.....	87
4.4.5.2	Moiré Pattern.....	88
4.4.5.3	Brush Marks.....	89
4.4.5.4	Dead Zones.....	89
4.4.6	<i>Pulse Height Effects</i>	91
4.4.6.1	Y1 = Y2 Feature.....	91
4.4.6.2	Counts at Left and Right Edges of Segments.....	92
4.4.6.3	Loss of High Gain Events at Top and Bottom of Detectors.....	92
4.4.6.4	The Fold.....	93
4.4.7	<i>Count Rate Dependent Effects</i>	94
4.4.7.1	Y Blooming.....	95
4.4.7.2	Phantom Spectra.....	95
4.4.7.3	Resolution vs. count rate.....	95
4.4.7.4	Dead Time.....	95
4.4.8	<i>SAA Shutdowns</i>	96
4.4.8.1	SAA Incursions at full voltage.....	97
4.5	FES PERFORMANCE.....	97
4.5.1	<i>FES Photometry</i>	98
4.5.2	<i>Stray Light</i>	100
4.5.3	<i>FES A Failure</i>	102
5	BRIGHT TARGET OBSERVING STRATEGIES & RESTRICTIONS.....	103
5.1	FLUX LIMITATIONS.....	103
5.2	BRIGHT TARGET OBSERVING STRATEGIES.....	103
5.2.1	<i>Bright Target Observing Strategies Implemented</i>	104
5.2.1.1	SiC Only Observations.....	104
5.2.1.2	HIRS LiF Only.....	104
5.2.1.3	Single Detector Segment.....	105
5.2.2	<i>Bright Target Strategies Evaluated - But Not Implemented</i>	105
5.2.2.1	Defocus technique.....	105
5.2.2.2	Lowered HV method.....	106
5.2.2.3	Scattered Light Technique.....	106
6	FUSE INSTRUMENT TECHNICAL APPENDIX.....	107
6.1	TELESCOPE MIRRORS.....	107
6.1.1	<i>Telescope Mirror Design</i>	107
6.1.2	<i>Optical Bench Structure</i>	109
6.1.3	<i>Thermal Control</i>	110
6.1.4	<i>Pre-launch Performance Specification & Evaluation</i>	110
6.1.5	<i>Mirror Positioning System Design</i>	111
6.2	FPA MOTION CONTROL.....	114
6.2.1	<i>FPA X Axis</i>	114
6.2.2	<i>FPA Z Axis</i>	114
6.3	DETECTOR DESIGN AND PRE-LAUNCH CHARACTERIZATION.....	115
6.3.1	<i>Hardware and Software Description</i>	115
6.3.1.1	Vacuum Assembly.....	117
6.3.1.2	Electronics Assembly.....	121
6.3.1.2.1	Digitizers.....	123
6.3.1.2.1.1	Stim Pulses and Thermal Stability.....	123
6.3.1.2.2	Data Processing Unit.....	126
6.3.1.2.2.1	Overview.....	126
6.3.1.2.2.2	Calculation of Y Position.....	126
6.3.1.2.2.3	Masks and counters.....	127
6.3.1.2.2.4	Pulse Height Histograms.....	129
6.3.1.2.2.5	Current Protection.....	130
6.3.1.2.2.6	Detector Diagnostic Codes.....	130
6.3.1.2.2.7	DPU Code Versions.....	131
6.3.1.3	Stim Lamp Assembly.....	132
6.3.2	<i>Normal Detector Operations</i>	133

6.3.2.1	High Voltage Ramp-up	133
6.3.2.2	High Voltage Management: Occultation Manager	133
6.3.3	<i>SIA tables</i>	134
6.3.4	<i>Single Event Upsets</i>	136
6.3.5	<i>High Voltage Transients (Crackles)</i>	138
6.4	FINE ERROR SENSOR CAMERAS	142
6.4.1	<i>FES CCD Detector</i>	142
6.4.2	<i>Performance and Anomalies</i>	142
6.4.2.1	FES-A Failure	142
6.4.2.2	FES-B Focusing	143
6.5	IDS: INSTRUMENT DATA SYSTEM	143
6.5.1	<i>IDS-ACS Interface</i>	143
6.5.2	<i>Observation Sequencing and Fine Guiding</i>	144
6.5.3	<i>IDS Thermal Control</i>	145
6.5.3.1	Thermal Design	145
6.5.3.2	Thermal Performance	145
6.6	INSTRUMENT ON-ORBIT PERFORMANCE	146
6.6.1	<i>Telescope Focus</i>	146
6.6.1.1	Post-launch Focus Assessment Details	146
6.7	TELESCOPE ALIGNMENT PERFORMANCE	149
6.7.1	<i>Initial Alignment</i>	149
6.7.2	<i>Mirror Motion Anomaly</i>	150
6.7.3	<i>On-orbit Mirror Motion Mitigation Strategy</i>	150
6.7.3.1	Mirror Alignment: Baseline Maintenance	150
6.7.3.2	Mirror Alignment: Predictive Modeling	151
6.7.3.3	Channel Alignment Operations	151
6.7.3.4	Orbital Motion	152
6.7.3.5	Impact and Evolution of Image Motion Corrections	153
6.7.3.6	Target Peak-up Strategy for MDRS and HIRS Observations	154
6.7.4	<i>Channel Alignment: Observations and Analysis</i>	154
6.7.5	<i>Mirror Motion Accuracy</i>	159
6.7.5.1	Mirror Motion Tracking and Actuator Performance	159
6.7.6	<i>Spectral Motion Anomaly: Thermal & Mechanical Analysis</i>	163
6.8	OPTICAL DESIGN SPECIFICATIONS	168
6.9	DEAD TIME	179
7	ATTITUDE CONTROL SYSTEM TECHNICAL APPENDIX	186
7.1	IN-FLIGHT ACS PERFORMANCE SUMMARY	186
7.2	INERTIAL REFERENCE UNIT FAILURES	187
7.3	REACTION WHEEL FAILURES	188
7.3.1	<i>Pitch & Yaw Reaction Wheel Failures: ~December 2001</i>	189
7.3.2	<i>Roll Reaction Wheel Failure: December 2004</i>	190
7.3.3	<i>Skew Reaction Wheel Failure: May 2007 & Observatory Decommissioning</i>	191
7.4	GYROLESS ATTITUDE DETERMINATION	191
7.4.1	<i>Basic Considerations</i>	191
7.4.2	<i>Flight Software Modifications</i>	192
8	SATELLITE TO TARGET COORDINATE TRANSFORMATION	195
8.1	BASIC DEFINITIONS	195
8.2	CONVERSION OF RAW FES PIXEL COORDINATES TO CELESTIAL COORDINATES	198
9	AIRGLOW APPENDIX	200
9.1	UPWARD-LOOKING AIRGLOW	200
9.2	DOWNWARD-LOOKING AIRGLOW	200
10	FUSE DEVELOPMENT AND OPERATIONS TEAMS	202
10.1	TEAM LIST	202

11	ACRONYM LIST	210
12	REFERENCES AND FURTHER READING	214
12.1	PRE-LAUNCH INSTRUMENT DESIGN AND TESTING	214
12.1.1	<i>Optics</i>	214
12.1.2	<i>Detectors</i>	215
12.1.3	<i>Instrument Data System</i>	215
12.2	IN-FLIGHT INSTRUMENT PERFORMANCE.....	216
12.3	TARGET ACQUISITION AND GUIDING, ATTITUDE CONTROL SYSTEM.....	216
12.4	MISSION OPERATIONS AND OBSERVATION SCHEDULING	217
12.5	OTHER.....	217

TABLE OF FIGURES

FIGURE 2-1 : TOP: THE INTEGRATED FUSE SATELLITE. BOTTOM: OPTICAL LAYOUT OF FUSE INSTRUMENT SHOWING 4 CHANNEL DESIGN BUT ONLY TWO DETECTORS.	20
FIGURE 2-2 : EXPLODED VIEW OF THE FUSE INSTRUMENT STRUCTURE. THIS FIGURE ILLUSTRATES THE RELATIONSHIP BETWEEN THE PHOTOGRAPH OF THE ASSEMBLED, FLIGHT-READY, FUSE INSTRUMENT IN THE PREVIOUS FIGURE AND THE SCHEMATIC OF THE OPTICAL LAYOUT OF THE TELESCOPE AND SPECTROGRAPH.	21
FIGURE 2-3: SCHEMATIC OF THE LiF1 AND SiC1 FPAs SHOWN RELATIVE TO THE INSTRUMENT OPTICAL DESIGN AND BEAM SIZE (TOP), WITH A DETAIL OF THE FPAs AND THEIR RELATIONSHIP TO THE ROWLAND CIRCLE AND THE IPCS COORDINATE SYSTEM (BOTTOM). IN THE LiF CHANNEL, LIGHT FROM THE STAR FIELD IN THE VICINITY OF THE TARGET IS REFLECTED INTO AN FES CAMERA.	24
FIGURE 2-4: THE LOCATIONS OF THE FUSE APERTURES PROJECTED ON THE SKY FOR A SLIT POSITION ANGLE OF 0° WITH NORTH IN THE -Y DIRECTION. POSITIVE APERTURE POSITION ANGLES CORRESPOND TO A COUNTER-CLOCKWISE ROTATION OF THE APERTURES ON THE SKY. IN THE FPA COORDINATE SYSTEM THE LWRS, HIRS, AND MDRS APERTURES ARE CENTERED AT Y= -118.07", -10.27", AND +90.18", RESPECTIVELY. THIS DIAGRAM REPRESENTS ONLY A PORTION OF THE FPA; THE FULL ACTIVE AREA IS ~19ARCMIN × 19 ARCMIN.	26
FIGURE 2-5 PHOTOGRAPH OF THE FUVS IN A CLEAN ROOM AT UNIVERSITY OF COLORADO BOULDER JUST PRIOR TO SHIPMENT TO JOHNS HOPKINS UNIVERSITY, WITH THE MAJOR OPTICAL COMPONENTS IDENTIFIED.	28
FIGURE 2-6: WAVELENGTH COVERAGE, DISPERSION DIRECTIONS, AND IMAGE LOCATIONS FOR THE FUSE DETECTORS. IN THIS FIGURE, THE COORDINATE SYSTEM AS USED FOR THE DETECTORS IS SHOWN, WHERE X IS THE DISPERSION DIRECTION.	29
FIGURE 2-7 THE ASTIGMATIC HEIGHT OF THE FUSE SPECTRA ARE SHOWN IN THESE FIGURES. THE UNITS OF BOTH AXES FOR BOTH THE TOP AND BOTTOM FIGURES ARE DETECTOR ELEMENTS, OR PIXELS.	30
FIGURE 2-8: MOLECULAR HYDROGEN EMISSION SPECTRUM RECORDED BY DETECTOR 1B. THIS FIGURE SHOWS THE FULL EXTENT OF THE SEGMENT IN THE Y DIRECTION (1024 PIXELS) BUT ONLY A VERY SMALL EXTENT IN X (1000 PIXELS OR ABOUT 6 Å). THIS IMAGE WAS CONSTRUCTED BY ADDING TOGETHER 6 DIFFERENT IMAGES, EACH MADE WITH THE LAMP SOURCE ILLUMINATING AN INDIVIDUAL APERTURE. FROM THE TOP TO THE BOTTOM OF THE IMAGE, THE SPECTRA ARE LiF (MDRS APERTURE), LiF (HIRS APERTURE), LiF (LWRS APERTURE), SiC (MDRS APERTURE), SiC (HIRS APERTURE), AND SiC (LWRS APERTURE). THE PINHOLES WERE NOT ILLUMINATED. THE LiF SPECTRA ARE CENTERED AT ~1160 Å WHILE THE SiC SPECTRA ARE CENTERED AT ~930 Å.	32
FIGURE 2-9: DRAWING SHOWING THE LIGHT PATH INSIDE THE FES.	37
FIGURE 2-10 DIAGRAM OF AN FES-A IMAGE WITH ITS DIFFERENT COORDINATE FRAMES. THE RAW FES CCD COORDINATES ARE (X _{FES} , Y _{FES}) WITH ITS ORIGIN AT THE LOWER LEFT CORNER OF THE IMAGE. THE FES IPCS COORDINATES AS PROJECTED ONTO THE SKY ARE (X _{IPCS} , Y _{IPCS}) WITH ITS ORIGIN LOCATED BELOW THE HIRS APERTURE. THE EXACT LOCATION AND SIZE OF THE THREE APERTURES ARE NOT TO SCALE.	39
FIGURE 3-1: ACS COORDINATE FRAMES. RED: ORIGINAL, GREEN: REVISED FOR MAGNETIC CONTROL SYSTEM.	43
FIGURE 4-1 THE LOG OF THE COUNT RATE, NORMALIZED TO UNITY, IS SHOWN PLOTTED AS A FUNCTION OF THE X-POSITION OF A POINT-SOURCE IMAGE RELATIVE TO THE CENTER OF THE HIRS APERTURE IN EACH CHANNEL. THIS IS EQUIVALENT TO THE CONVOLUTION OF THE TELESCOPE PSF WITH THE HIRS APERTURE.	46
FIGURE 4-2 SAME AS FIGURE 4-1 ABOVE, BUT FOR THE MDRS APERTURE.	47
FIGURE 4-3 SAME AS FIGURE 4-1 ABOVE, BUT FOR THE LWRS APERTURE.	48
FIGURE 4-4 PEAKUP SCANS OVER 5 SUCCESSIVE ORBITS FOR OBSERVATION P203:04:01. THE COUNT RATES AS A FUNCTION OF SCAN STEP ARE SHOWN IN DIFFERENT COLORS; THE FIRST SCAN OF THE OBSERVATION IS PLOTTED IN BLACK AND SHOWS THE LARGEST CHANNEL ALIGNMENT ERRORS. FPA ADJUSTMENTS REQUIRED IN SUBSEQUENT ORBITS WERE MUCH SMALLER.	50
FIGURE 4-5 SPECTRAL RESOLUTION MEASURED FROM ISM ABSORPTION LINES ALONG THE LINE OF SIGHT TO K1-16.	53

FIGURE 4-6 SPECTRAL RESOLUTION MEASURED FROM ISM ABSORPTION LINES ALONG THE LINE OF SIGHT TO RX J2117+3412.	54
FIGURE 4-7 THE IN-FLIGHT DERIVED EFFECTIVE AREA AS A FUNCTION OF WAVELENGTH FOR EACH DETECTOR SEGMENT. EACH CURVE FOR A GIVEN DETECTOR SEGMENT REPRESENTS A SNAPSHOT OF THE EFFECTIVE AREA AS A FUNCTION OF TIME AND WAVELENGTH. THE FAMILY OF CURVES FOR EACH SEGMENT REPRESENTS THE DEGRADATION OF THE EFFECTIVE AREA OVER THE EIGHT YEAR ON-ORBIT LIFETIME OF THE MISSION.	57
FIGURE 4-8 SPECTRAL IMAGES OF A STELLAR SPECTRUM OBTAINED IN THE LiF1 CHANNEL FOR EACH APERTURE ARE PLOTTED FOR DETECTOR SEGMENT 1A. THE GREY SCALE IS INVERTED, SO THAT REGIONS OF HIGH COUNT RATE APPEAR DARK. THE NARROW VERTICAL LINES ARE ABSORPTION FEATURES ARISING FROM INTERSTELLAR GAS, PRIMARILY H ₂ . THE BROAD.....	60
FIGURE 4-9 AS IN FIGURE 4-8 ABOVE, BUT FOR LiF1B. NOTE THE STRONG WORM FEATURE IN THE LWRS SPECTRAL IMAGE.	61
FIGURE 4-10 AS IN FIGURE 4-8 ABOVE, BUT FOR LiF2A. IN ADDITION TO THE WORM FEATURES PRESENT IN EACH SPECTRAL IMAGE, FAINT SINGLE-PIXEL-WIDE HORIZONTAL MOIRE PATTERNS ARE EVIDENT, WHICH ARE AN ARTIFACT OF THE DISTORTION CORRECTIONS.	62
FIGURE 4-11 AS IN FIGURE 4-8 ABOVE, BUT FOR LiF2B.	63
FIGURE 4-12 AS IN FIGURE 4-8 ABOVE, BUT FOR SiC1A.	64
FIGURE 4-13 AS IN FIGURE 4-8 ABOVE, BUT FOR SiC1B.	65
FIGURE 4-14 AS IN FIGURE 4-8, BUT FOR SiC2A. WORMS ARE WEAK OR NOT PRESENT.	66
FIGURE 4-15 AS IN FIGURE 4-8, BUT FOR SiC2B. WORMS ARE WEAK OR NOT PRESENT. THE VERY THIN WHITE JAGGED LINE RUNNING ACROSS THE MDRS SPECTRAL IMAGE IS AN ARTIFACT FROM THE DISTORTION CORRECTION; SOME RESIDUAL VERTICAL DISTORTION IS PRESENT IN THE HIRS AND MDRS SPECTRAL IMAGES BEYOND PIXEL 12000.....	67
FIGURE 4-16 FOR A SINGLE OBSERVATION (S505702) THE POSITION OF THE LiF1A LYMAN-B AIRGLOW LINE ON THE DETECTOR IS SHOWN AS A FUNCTION OF TIME. EACH POINT REPRESENTS THE AVERAGE POSITION ON THE DETECTOR OF ~500 CONSECUTIVE AIRGLOW PHOTONS.	69
FIGURE 4-17 THE SAME DATA AS IN FIGURE 4-16 IS SHOWN BOTH BEFORE (TOP PANEL) AND AFTER (BOTTOM PANEL) THE CALFUSE GRATING MOTION CORRECTION IS APPLIED.	70
FIGURE 4-18 A BINNED PORTION OF DETECTOR SEGMENT 1B ILLUMINATED IN FLIGHT BY THE STIM LAMP, USING JUST PHOTONS WITH PULSE HEIGHTS OF (A) 2, (B) 4, (C) 8, AND (D) 16. THE X RANGE COVERS 1200 PIXELS, WHILE Y INCLUDES THE FULL HEIGHT OF THE DETECTOR. THE SHADOWS OF THE TWO SETS OF GRID WIRES ARE CLEARLY SEEN IN THE VERTICAL DIRECTION, BUT BECAUSE OF THE BINNING IN Y, THE HORIZONTAL WIRES ARE DIFFICULT TO SEE. IT IS OBVIOUS FROM COMPARING THESE FIGURES THAT THERE IS AN APPARENT SHIFT IN THE POSITION OF THE GRID WIRES AS A FUNCTION OF PULSE HEIGHT. THE DARK HORIZONTAL BANDS SHOW REGIONS WHERE A LARGE AMOUNT OF EXPOSURE HAS CAUSED GAIN VARIATIONS.	73
FIGURE 4-19 A SMALL PORTION OF A LiF SPECTRUM ON SEGMENT 1A, SHOWING THE SAME DATA BOTH WITH AND WITHOUT THE CALFUSE WALK CORRECTION APPLIED; THE TWO SPECTRA ARE OFFSET IN THE Y AXIS BY AN ARBITRARY AMOUNT SO THAT THE DIFFERENCES CAN BE SEEN MORE EASILY. THE WALK-CORRECTED SPECTRUM HAS A DIFFERENT WAVELENGTH SCALE AND SHOWS HIGHER RESOLVING POWER.	75
FIGURE 4-20 GAIN SAG ON DETECTOR SEGMENT 1A. THE MEAN PULSE HEIGHT IS SHOWN AS A FUNCTION OF X PIXEL AT TWO Y LOCATIONS ON THE DETECTOR: AT THE LiF LWRS SPECTRUM LOCATION (SOLID LINE) AND IN A BACKGROUND REGION (DOTTED LINE) IN SEPTEMBER 2000 (EXPOSURE M9980101001 - RED) AND IN SEPTEMBER 2007 (M9986701001 - GREEN). THE GAIN OF THE BACKGROUND REGION INCREASED SUBSTANTIALLY DURING THE MISSION DUE TO THE INCREASES IN HIGH VOLTAGE, AND REMAINED FAIRLY FLAT AS A FUNCTION OF X PIXEL. THE LiF1 LWRS REGION, HOWEVER, SHOWS A SIGNIFICANT GAIN VARIATION AS A FUNCTION OF X. THE GAIN SAG AT LYMAN-B (x ≈ 7000) IS ESPECIALLY OBVIOUS.	76
FIGURE 4-21 AN EXAMPLE OF THE COUNT RATE AS A FUNCTION OF TIME DURING AN EVENT BURST SHOWING A HIGH-FREQUENCY COMPONENT IS 10 SECONDS. THE SIZE, SPATIAL DISTRIBUTION, AND TEMPORAL PROFILE OF THE BURSTS VARIED SIGNIFICANTLY DURING THE MISSION.	80
FIGURE 4-22 A PORTION OF ONE DETECTOR SHOWING AN EXAMPLE OF A SCALLOPED BURST	81

FIGURE 4-23 AN EXAMPLE OF A VERY LARGE CHECKERBOARD BURST ON SEGMENT 1A, SHOWN IN FARF COORDINATES. NOTE THAT THE CHECKERBOARD PATTERN IS DISTORTED, WHILE THE SPECTRUM REMAINS UNDISTORTED.....	81
FIGURE 4-24 SEGMENT 2A WITH A HIGH DETECTOR BACKGROUND.....	82
FIGURE 4-25 SEGMENT 2B WITH A HIGH DETECTOR BACKGROUND.....	83
FIGURE 4-26 TEMPERATURES MEASURED BY TWO OF THE DETECTOR THERMISTORS DURING A TWO DAY PERIOD BEGINNING ON 29 AUGUST 2002 (MJD 52515), ALONG WITH THE HIGH VOLTAGE ON DETECTOR SEGMENT 1A AT THE SAME TIME. THESE DATA ARE TAKEN FROM THE ENGINEERING SNAPSHOTS, AND THEREFORE ARE ONLY COLLECTED DURING SCIENCE EXPOSURES. THE ORBITAL VARIATION OF THE $\sim 1^\circ$ C OF THE TEMPERATURES IS SEEN, SUPERIMPOSED ON LONGER-TERM VARIATIONS, SUCH AS THAT DUE TO THE HIGH VOLTAGE DROPPING TO ZERO AT ~ 1.2 DAYS.....	84
FIGURE 4-27 THE X SHIFT (SHIFT OF THE MEAN POSITION OF THE TWO STIMS) AND STRETCH (CHANGE IN SEPARATION BETWEEN THE TWO STIM PULSES) ON SEGMENT 1A, MEASURED FROM THE STIM PULSES FOR THE SAME TIME PERIOD SHOWN IN FIGURE 4-26. LARGE CHANGES IN BOTH SHIFT AND STRETCH ARE SEEN WHEN THE HIGH VOLTAGE SHUTS DOWN.....	86
FIGURE 4-28 A SMALL SECTION OF A FLAT FIELD TAKEN BEFORE LAUNCH. THIS REGION COVERS 950 X 150 PIXELS OF A SINGLE SEGMENT. THE HEXAGONAL MULTIFIBER BUNDLES ARE VISIBLE, AS ARE SOME BRUSH MARKS AND DEAD SPOTS ON THE LEFT SIDE OF THE IMAGE. THIS IMAGE CONTAINS ~ 100 COUNTS PER PIXEL.....	87
FIGURE 4-29 THIS SMALL SECTION OF A SEGMENT 2B GROUND FLAT SHOWS THE MOST PROMINENT MOIRÉ PATTERN, VISIBLE AS THE NEARLY VERTICAL RIPPLES RUNNING ACROSS THE IMAGE. THE RIPPLES HAVE A PEAK-TO-PEAK AMPLITUDE OF $\pm 15\%$ AND A PERIOD OF ~ 9 PIXELS IN X (~ 54 MICRONS OR ~ 1.5 RESOLUTION ELEMENTS).....	88
FIGURE 4-30 AN ISOLATED TYPE I DEAD ZONE ON SEGMENT 1A IS SHOWN. THIS DEAD SPOT IS NOT COMPLETELY BLACK AT THE CENTER, BUT THE SENSITIVITY IS DOWN BY A FACTOR OF ~ 4 FROM THE SURROUNDING REGION.....	90
FIGURE 4-31 AN ISOLATED TYPE II DEAD ZONE ON SEGMENT 1A IS SHOWN. NOTE THE BRIGHT OUTER RIM. THE SPOT IS LOCATED AT $(X, Y) = (10515, 530)$, AND IT HAS A DIAMETER OF 40 PIXELS IN X AND 25 IN Y (~ 250 MICRONS). THE $Y_1=Y_2$ FEATURE IS ALSO PROMINENT.....	91
FIGURE 4-32 Y PROJECTION OF THE NORMALIZED COUNTS IN A SEGMENT 2B STIM LAMP IMAGE FOR PULSE HEIGHTS 24 TO 31. AT A PULSE HEIGHT OF 24 OR BELOW, ALL Y PIXELS IN THE ACTIVE REGION HAVE COUNTS. FOR PULSE HEIGHTS ABOVE 24, HOWEVER, COUNTS ARE DISCARDED SYMMETRICALLY ABOUT PIXEL 512. NOTE THAT THE SHAPE OF EACH PROJECTION IS DETERMINED BY THE GAIN OF THE SEGMENT AS A FUNCTION OF POSITION.....	93
FIGURE 4-33 RAW DATA FROM THE FAR RIGHT EDGE OF SEGMENT 1A IN A STIM LAMP EXPOSURE. COUNTS THAT SHOULD HAVE BEEN LOST BEYOND THE ACTIVE AREA TO THE RIGHT ARE INSTEAD FOLDED BACK INTO THE ACTIVE REGION.....	94
FIGURE 4-34 FES-A 1×1 IMAGE (A1080201001FESAFRAW.FIT) OF THE FIELD OF VIEW IN THE DIRECTION OF THE GLOBULAR CLUSTER NGC 6723.....	98
FIGURE 4-35 FES INTENSITIES (TOP) AND POSITIONAL ERRORS (BOTTOM) COMPARED WITH HST GSC VALUES.....	100
FIGURE 4-36 A RAW IMAGE FROM FES-A WITH A HIGH LEVEL OF SCATTERED LIGHT IS SHOWN. THE DARK BORDER SEEN ON ALL SIDES IS THE APERTURE MASK. THE SPECTROGRAPH APERTURES ARE VISIBLE: MDRS, HIRS, AND LWRS IN ORDER FROM LEFT TO RIGHT. LIGHT SCATTERED BY THE EDGES OF THE HIRS APERTURE CAUSE IT TO APPEAR BRIGHT IN THIS IMAGE. THE DIMPLED REGION SURROUNDING THE APERTURES IS AN ARTIFACT OF THE MANUFACTURE OF THE FPA MIRRORS. THE FEATURE CENTERED AT $X=97, Y=344$, THAT APPEARS SOMEWHAT OBLONG IS A GLINT CAUSED BY A DEFECT IN THE FPA SURFACE. IT EXTENDS ROUGHLY ± 5 PIXELS ALONG EITHER AXIS, AND MAY MOVE ± 5 PIXELS IN THE VERTICAL DIRECTION, DEPENDING ON THE FPA POSITION. THERE ARE A FEW OTHER DEFECTS ON THE LiF1 FPA, BUT THEY ARE SMALL AND ARE RARELY SEEN.....	101
FIGURE 4-37 A RAW FES-B IMAGE WITH A HIGH LEVEL OF SCATTERED LIGHT IS SHOWN. THE DARK BORDER SEEN ON THREE SIDES IS THE APERTURE MASK. THE SPECTROGRAPH APERTURES ARE VISIBLE: LWRS, HIRS,MDRS IN ORDER FROM LEFT TO RIGHT. LIGHT SCATTERED BY EDGES OF HIRS MAKE IT APPEAR BRIGHT IN THIS IMAGE. THE DIMPLED REGION SURROUNDING THE APERTURES IS AN ARTIFACT OF THE MANUFACTURE OF THE FPA MIRRORS. A LONG SCRATCH IN THE FPA IS VISIBLE ON THE LEFT SIDE OF THE IMAGE.....	102

FIGURE 6-1 LEFT: FUSE MIRROR RESTING FACE-UP ON FLEXURES PRIOR TO INTEGRATION INTO THE MIRROR ASSEMBLY. RIGHT: BACKSIDE OF THE FUSE PRIMARY MIRROR ILLUSTRATING THE AGGRESSIVE LIGHTWEIGHTING OF THE ZERODUR MIRROR SUBSTRATE.	108
FIGURE 6-2: FACE-ON VIEW OF MIRROR ACTUATOR ASSEMBLY SHOWING THE THREE ACTUATORS AND COMPOSITE STRUCTURE.	109
FIGURE 6-3 LEFT: DUMMY ALUMINUM MIRROR WITH ACTUATOR ASSEMBLY (REF OHL). RIGHT: FULL FLIGHT MIRROR ASSEMBLY, INCLUDING PIE-PAN THERMAL ENCLOSURE AND APERTURE STOP.	112
FIGURE 6-4 THE ACTUATOR LOCATIONS RELATIVE TO THE MIRRORS AND THE IPCS COORDINATE FRAME.	113
FIGURE 6-5 EXPANDED VIEW OF THE DETECTOR STACK MOUNTING IN THE FUSE DETECTOR. THE QE GRID IS HELD BY THE FRAME AT THE TOP, AND THE CURVED MCPs ARE MOUNTED TO A CYLINDRICAL SURFACE TO MATCH THE ROWLAND CIRCLE.	119
FIGURE 6-6 A FUSE DETECTOR VACUUM ASSEMBLY MOUNTED TO THE DETECTOR MOUNTING BRACKET IN THE SPECTROGRAPH CAVITY. THE DOOR ASSEMBLY IS AT THE TOP, WITH THE LIGHT BAFFLE PROTRUDING. TWO ION PUMPS ARE VISIBLE AT THE FRONT RIGHT, AND THE HIGH VOLTAGE FILTER MODULE, CHARGE AMPLIFIERS, AND TIMING AMPLIFIERS ARE VISIBLE BEHIND THEM. THE LADDER-LIKE STRUCTURES AT THE TOP ON EITHER SIDE OF THE DETECTOR ARE SPECTROGRAPH BAFFLES.	120
FIGURE 6-7 ELECTRONICS ASSEMBLY AND STIM LAMP ASSEMBLY OF THE SPARE DETECTOR.	121
FIGURE 6-8 BLOCK DIAGRAM OF THE ENCODING ELECTRONICS FOR THE FUSE DETECTORS.	122
FIGURE 6-9 FUNCTIONAL BLOCK DIAGRAM OF THE DETECTOR ELECTRONICS ASSEMBLY (HARDWARE AND SOFTWARE).	123
FIGURE 6-10 DETECTOR X SHIFT, AS MEASURED BY THE CHANGE IN POSITION OF THE STIM PULSES, FOR ALL FOUR SEGMENTS DURING THE MISSION. LONG TERM TRENDS APPEAR TO DOMINATE SHORT TERM TEMPERATURE EFFECTS, PARTICULARLY ON SEGMENTS 1B AND 2B.	125
FIGURE 6-11 POSITIONS OF SEUS DURING THE MISSION. THE DASHED LINE SHOWS THE SAA REGION USED BY MISSION PLANNING AFTER 17 SEPTEMBER 2003. NO EVENTS OCCUR BELOW -25° DUE TO THE ORBIT OF THE SATELLITE.	138
FIGURE 6-12 HVIA, HVIB, AND AUXI DURING A CRACKLE.	140
FIGURE 6-13 NUMBER OF CRACKLES AND MINI-CRACKLES VS. TIME.	141
FIGURE 6-14: ORBITAL DEPENDENCY OF IMAGE MOTION FOR SELECTED TARGETS.	153
FIGURE 6-15: XY ALIGNMENT SCANS AS DEPICTED USING THE ALIGNMENT TOOL GRAPHICAL ANALYSIS. THESE DATA ARE DISCUSSED IN SECTION 6.7.4.	155
FIGURE 6-16: EXAMPLE OF CHANNEL ALIGNMENT TOOL (CHAT) RESULTS.	156
FIGURE 6-17: (REVISED) ONE WHEEL MODE ALIGNMENT SCAN PATTERN.	157
FIGURE 6-18: ONE WHEEL MODE ALIGNMENT SCAN PATTERN RESULTS.	157
FIGURE 6-19: ADDITIONAL CHAT SAMPLE RESULTS.	158
FIGURE 6-20: TIME SERIES OF INDIVIDUAL MIRROR MOTIONS EXECUTED TO MAINTAIN CO-ALIGNMENT OF THE LIF CHANNELS.	160
FIGURE 6-21: TIME SERIES OF INDIVIDUAL MIRROR MOTIONS EXECUTED TO MAINTAIN CO-ALIGNMENT OF THE SIC CHANNELS.	161
FIGURE 6-22: THE RANGE OF MOTION FOR EACH OF THE LIF1 (TOP) AND LIF2 (BOTTOM) MIRRORS ILLUSTRATING THAT ALTHOUGH TO CO-ALIGNMENT POSITION FOR EACH ACTUATOR EXHIBITS A SECULAR DRIFT WITH TIME, THIS CHANGE IS SMALL AND WELL WITHIN THE RANGE OF TRAVEL FOR EACH OF THE ACTUATORS.	162
FIGURE 6-23: THE RANGE OF MOTION FOR EACH OF THE SIC1 AND SIC2 MIRROR ACTUATORS.	163
FIGURE 6-24: LIF2B DATA OVER AN ORBITAL PERIOD ILLUSTRATING THAT THE SPECTRAL MOTION OBSERVED WITH THE GMA SHROUD AT 19 C (TOP) IS SHIFTED/OFFSET BY ~ 5 -6 PIXELS FROM THE DATA ACQUIRED WITH THE GMA SHROUD AT THE NOMINAL 23 C (BOTTOM).	167
FIGURE 6-25 OPTICAL ELEMENT LAYOUT FOR LIF1, SIC1 CHANNELS.	169
FIGURE 6-26 OPTICAL ELEMENT LAYOUT FOR LIF2, SIC2 CHANNELS.	170
FIGURE 6-27 OPTICAL ELEMENT LAYOUT, TOP VIEW.	171
FIGURE 6-28 LINE DRAWING OF AN FPA MECHANISM, SHOWING THE TWO-AXIS STAGE AND APERTURE PLATE.	172
FIGURE 6-29 DETAILS OF OPTICS LAYOUT AT DETECTOR SURFACES.	173
FIGURE 6-30 POSITIONS OF OPTICAL ELEMENTS.	174
FIGURE 6-31 SIDE VIEWS OF INSTRUMENT, SHOWING THE STRUCTURE, OPTICS, BAFFLES, ELECTRONICS, AND RADIATORS. LEFT: Y-Z VIEW, RIGHT: X-Z VIEW.	175

FIGURE 6-32 SECTION VIEWS OF A PRIMARY MIRROR. TOP: "PIE-PAN" ENCLOSURE, INTERMEDIATE PLATE AND BENCH ARE SHOWN, WITH POSITIONS OF THE ACTUATORS. BOTTOM: MIRROR DIMENSIONS AND VERTEX POSITION ARE SHOWN.	177
FIGURE 6-33 CLOSE-UP VIEW OF LIGHT PATHS AT THE FPA-FES INTERFACE.	178
FIGURE 6-34 A SECTION VIEW OF A GRATING MOUNT ASSEMBLY AND GRATING ARE SHOWN.	179
FIGURE 6-35 FUNCTIONAL BLOCK DIAGRAM SHOWING THE FLOW OF EVENTS THROUGH THE DETECTOR ELECTRONICS (1 OF 2). COUNTS INCIDENT ON THE DETECTOR CAN BE LOST (1) AT THE DIGITIZER; (2) DUE TO COUNTS FALLING OUTSIDE THE ACTIVE IMAGE MASK; AND (3) IN THE ROUND ROBIN, WHICH COMBINES THE DATA FROM TWO SEGMENTS ON ONE DETECTOR.....	180
FIGURE 6-36 FUNCTIONAL BLOCK DIAGRAM SHOWING THE FLOW OF EVENTS THROUGH THE DETECTOR ELECTRONICS (2 OF 2). COUNTS CAN BE LOST (4) IN THE IDS IF THE COUNT RATE IS ABOVE 32,000 CPS (HIST ONLY); (5) DUE TO SCREENING BY THE SIA TABLE (HIST ONLY); (6) IN THE IDS IF THE COUNT RATE IS ABOVE 8,000 CPS (TTAG); (7) IF THE FIFO FILLS (TTAG); OR (8) BETWEEN THE SPACECRAFT AND THE GROUND SYSTEM.	181
FIGURE 6-37 APPARENT COUNT RATE AS A FUNCTION OF TIME FOR EXPOSURE Q11401001, WHICH WAS OBTAINED IN TTAG MODE, DESPITE HAVING A COUNT RATE OF MORE THAN 100,000 COUNTS PER SECOND. FOR THE FIRST ~520 SECONDS THE COUNT RATES ON ALL FOUR SEGMENTS.....	183
FIGURE 6-38 DETECTOR LIVE-TIME CALIBRATION USED BY CALFUSE.	184
FIGURE 6-39 UPDATED LIVE-TIME CALIBRATION CURVES.	185
FIGURE 8-1 THIS TYPICAL FUSE GUIDE STAR PLOT SHOWS THE USABLE GUIDE STARS AND APERTURE POSITIONS. THE PIXEL COORDINATE SCALE IS FOR FES-A. THE ORIENTATION OF NORTH AND EAST IS SHOWN IN THE LOWER LEFT CORNER.	196

TABLE OF TABLES

TABLE 2.2-1: FUSE INSTRUMENT SPECIFICATIONS; CHANNEL 1.....	17
TABLE 2.2-2: FUSE INSTRUMENT SPECIFICATIONS – CHANNEL 2.....	17
TABLE 2.4-1: APERTURES.....	24
TABLE 2.4-2 FPA LOCATIONS AND POINTING OFFSETS FOR A TYPICAL FP-SPLIT PATTERN.....	26
TABLE 2.5-1: SPECTROGRAPH AND GRATING PROPERTIES.....	27
TABLE 2.5-2: WAVELENGTH RANGES FOR DETECTOR SEGMENTS.....	29
TABLE 2.6-1 DETECTOR SPECIFICATIONS.....	34
TABLE 2.7-1 FES CAMERA CHARACTERISTICS.....	37
TABLE 2.7-2 FES CCD CHARACTERISTICS.....	38
TABLE 2.7-3 CENTER POSITIONS OF THE THREE APERTURES AND THE REFERENCE POINT IN FES-A AND FES-B 1 × 1-BINNED IMAGES.....	39
TABLE 4.3-1 SUMMARY OF WORMS IDENTIFIED IN THE FUSE DATA.....	59
TABLE 4.4-1 DEFAULT HIGH VOLTAGE VALUES USED DURING THE MISSION.....	77
TABLE 4.4-2 ASC THRESHOLDS USED DURING NORMAL OPERATIONS.....	96
TABLE 6.1-1: FUSE MIRROR PROPERTIES.....	107
TABLE 6.2-1 HISTORY OF FPA Z-AXIS MOTIONS. THE FIRST THREE COLUMNS GIVE THE OBSERVATION ID, DATE, AND START TIME FOR THE OBSERVATION IMMEDIATELY FOLLOWING A CHANGE IN FPA Z POSITION.....	115
TABLE 6.3-1 DETECTOR SPECIFICATIONS.....	116
TABLE 6.3-2 DETECTOR 1 THERMISTORS.....	117
TABLE 6.3-3 SUMMARY OF DETECTOR MASK CHANGES DURING THE MISSION.....	128
TABLE 6.3-4 DETECTOR MASKS AND COUNTERS.....	129
TABLE 6.3-5 SELECTED DPU DIAGNOSTIC CODES.....	130
TABLE 6.3-6 DPU CODE VERSIONS AND CRACKLE-DETECTION THRESHOLDS USED DURING THE MISSION. DIFFERENT VALUES WERE USED DURING STIM LAMP EXPOSURES.....	132
TABLE 6.3-7 SiC HIRS SIA TABLES USED DURING THE MISSION.....	135
TABLE 6.3-8 SiC MDRS SIA TABLES USED DURING THE MISSION.....	135
TABLE 6.3-9 SiC LWRS SIA TABLES USED DURING THE MISSION.....	135
TABLE 6.3-10 LiF HIRS SIA TABLES USED DURING THE MISSION.....	135
TABLE 6.3-11 LiF MDRS SIA TABLES USED DURING THE MISSION.....	136
TABLE 6.3-12 LiF LWRS SIA TABLES USED DURING THE MISSION.....	136
TABLE 6.3-13 SEUS BY DETECTOR AND MEMORY CORE.....	137
TABLE 6.3-14 NUMBER OF MINI-CRACKLES AND CRACKLES DURING THE MISSION. THE VALUES IN PARENTHESES ARE THE DIAGNOSTIC VALUE (IN HEX) ISSUED BY THE DETECTOR.....	141
TABLE 6.6-1 INITIAL IN-FLIGHT TELESCOPE FOCUS ADJUSTMENTS MADE NOVEMBER 23, 1999. ADJUSTMENTS IN THE FOCUS (Z) DIRECTION ARE LIMITED TO 10 MICRON INCREMENTS OF THE FPAS. SMALL RESIDUAL ERRORS ACCOUNT FOR THE SLIGHT DEPARTURES FROM INTEGRAL 10 MICRON CHANGES IN THE ADJUSTMENT VALUES ABOVE. THE TRUE UNCERTAINTY IN THE MAGNITUDE OF THE COMPUTED FOCUS ADJUSTMENT WAS AT LEAST 30 MICRONS.....	147
TABLE 6.6-2 SPECTROGRAPH FOCUS ADJUSTMENTS EXECUTED ON DECEMBER 12 TH , 1999 AS A RESULT OF THE I817 POST-LAUNCH PROGRAMS.....	148
TABLE 6.6-3 SPECTROGRAPH FOCUS ADJUSTMENTS EXECUTED AS A RESULT OF THE I817 AND I819 POST- LAUNCH PROGRAMS. THE SPECTROGRAPH FOCUS ADJUSTMENTS IMPLEMENTED MARCH 16 TH , 2000, WERE USED FOR NOMINAL OPERATIONS FOR THE REMAINDER OF THE FUSE MISSION.....	149
TABLE 6.9-1 DETECTOR DEADTIME PARAMETER VALUES USED BY CALFUSE.....	182
TABLE 6.9-2 UPDATED DETECTOR DEADTIME PARAMETERS.....	182
TABLE 7.2-1: IRU (GYRO) CHRONOLOGY OF EVENTS.....	188
TABLE 7.3-1: FUSE REACTION WHEEL EVENTS.....	189
TABLE 8.2-1 OPTICAL DISTORTION COEFFICIENTS FOR FES-A.....	199
TABLE 8.2-2 OPTICAL DISTORTION COEFFICIENTS FOR FES-B.....	199
TABLE 8.2-3 REFERENCE POINT POSITIONS IN CORRECTED PIXEL COORDINATES.....	199
TABLE 9.2-1 AIRGLOW EMISSION LINES SEEN DURING ORBITAL DAY WHEN LOOKING UP.....	201

TABLE 9.2-2 STRONGEST AIRGLOW EMISSION LINES SEEN LOOKING DOWN DURING ORBITAL DAY.201
TABLE 10.1-1 FUSE DEVELOPMENT AND OPERATIONS PERSONNEL.209

1 Introduction

This handbook provides a description of the Far Ultraviolet Spectroscopic Explorer (FUSE) science instrument, focusing on its design and performance from the perspective of an archival scientist interested in the impact of the instrument on the data quality. This approach is targeted primarily to the archival data miner, but much of the technical information may be of interest to future instrument builders as well. To address these audiences, we have organized this presentation with the main body of the document containing the information of most direct relevance to data users, and the technical details contained in the extensive Appendices attached. For an in-depth description of the FUSE data products and the CalFUSE data reduction pipeline, the reader is referred to the companion volume: *The FUSE Archival Data Handbook (2009)*.

FUSE was a NASA-funded far ultraviolet (FUV) space telescope that was operated for NASA by The Johns Hopkins University Department of Physics and Astronomy in Baltimore, MD. The satellite was launched on a Delta-II rocket from Cape Canaveral on June 24, 1999, at 11:44 a.m. EDT into a circular 760 km (475 mile) orbit inclined 25 degrees to the equator, with an orbital period of 100 minutes.

The FUSE scientific instrument was designed to provide high resolution spectra ($\lambda/\Delta\lambda \geq 20,000$) across the 905 - 1187 Å FUV spectral bandpass. The parabolic telescope mirror and Rowland circle spectrograph design maximized instrument efficiency by employing only two reflections prior to photon detection.

FUSE operated until it was decommissioned on October 18, 2007, after the loss of the fourth and final reaction wheel assembly in mid-2007 caused the termination of nominal science operations.

This handbook was written with two goals in mind: to provide an overview of the instrument and a characterization of instrument effects that affect the data quality and, secondly, to provide a more detailed description of the instrument design as well as some results from the integration, ground test, in-orbit performance of the instrument. On-orbit performance anomalies and the operational procedures for mitigating their effect on the data quality are also discussed.

Below we provide an outline of each chapter's contents with an indication of the primary target audience for each. The designations are either "General" (of interest to all) or if appropriate, broken out for a casual user, advanced user, or as an instrument designer/builder, to facilitate locating relevant information at the desired level of detail.

Chapter 1: (Audience: General) contains this introduction.

Chapter 2: (Audience: General) provides an overview of the FUSE instrument. Basic aspects of the instrument design and functional characteristics are presented for each of the instrument subsystems: telescope, spectrograph, focal plane arrays, guide system camera, and the detector.

Chapter 3: (Audience: General) presents an overview of the FUSE spacecraft. A brief overview of the Command and Data Handling system and the Attitude Control System (ACS) performance is presented. Post-launch spacecraft anomalies, such as the loss of reaction wheels and its effect on operations, are discussed in Section 7 of the technical appendix.

Chapter 4: (Audience: General) discusses the post-launch instrument performance. The mirror motion alignment anomaly (section 4.1, etc.), spectral motion (section 4.3) and detector performance (sections 4.4, etc.) are described here, with additional details presented in the technical appendix (Section 6).

Chapter 5: (Audience: Advanced archive user) presents a description of various overbright target observing strategies, only some of which were used operationally. Since some of these test data are available in the archive, this chapter is included for completeness.

Chapter 6 (Appendix A): (Audience: Instrument designer/builder, advanced user) – presents many details of the instrument design, detector characterization and operation, FES performance, telescope and spectrograph focus, and channel alignment behavior and operational mitigation.

Chapter 7 (Appendix B): (Audience: Instrument designer/builder, advanced user) – presents information on the Attitude Control System on-orbit performance, including the gyro and reaction wheel failures, and the flight software and target acquisition strategies employed to operate despite these limitations.

Chapter 8 (Appendix C): (Audience: Instrument designer/builder, advanced user) Coordinate Transformations.

Chapter 9 (Appendix D): (Audience: Instrument designer/builder, advanced user) Airglow appendix.

Chapter 10 (Appendix E): (Audience: All) Members of the development and operations teams.

Chapter 11: (Audience: All) Acronym List

Chapter 12: (Audience: All) References. This section provides a extensive list of references to papers describing the instrument subsystems, and the modifications to the instrument and ACS software made during the mission. There are also references to a subset of science papers that provide useful information on instrument performance.

This instrument handbook is one of two primary archival support documents describing the FUSE instrument and its data products. For information specific to the pipeline processing and analysis of FUSE data, readers are referred to this handbook's companion volume: *The FUSE Archival Data Handbook (2009)*.

2 Instrument Design

2.1 □ Scientific Motivation

FUSE was conceived by the astronomical community to build upon the scientific legacy of the Copernicus mission (Rogerson et al. 1973) by capitalizing upon the rich spectral diagnostics present in the FUV bandpass. *FUSE* provided unique access to several essential markers for astrophysics: the resonance doublet of O VI $\lambda\lambda$ 1032, 1038, the only unambiguous tracer of gas in the crucial $10^5 < T < 10^6$ K regime, and the ground state electronic transitions of H₂, which are many orders of magnitude stronger than the infrared transitions. For the study of molecular material, abundant in galaxies and dominant in star forming regions, access to H₂ is as fundamental as access to the Lyman and Balmer series lines for atomic hydrogen. FUSE also provided unique access to Deuterium transitions shortward of Lyman alpha, which are essential for measuring column densities for lines of sight beyond the Local Bubble. Many other spectral diagnostics for the properties of interstellar and intergalactic gas, stellar photospheres, and other astronomical objects are present in the spectral range covered by FUSE. Effective access to these diagnostics required a sensitive instrument with high spectral resolution. Every aspect of the FUSE design was driven by these considerations.

2.2 □ Instrument Overview

FUSE was designed to provide high resolution spectra ($\lambda/\Delta\lambda \geq 20,000$) with large effective area (20 -70 cm²) across the 905 - 1187 Å FUV spectral bandpass.

The FUSE satellite consisted of two primary sections: the spacecraft bus and the scientific instrument. Integrated, these components stood 18 feet (5.4 m) tall and weighed just under 3000 lbs. (1360 Kg). The payload is shown at Kennedy Space Center in June 1999 in Figure 2-1 (left). A schematic of the light path for the science instrument is shown in Figure 2-1 (right).

The challenge of designing a high-throughput FUV instrument and maintaining it throughout the lifetime of the mission was met by adopting a design that minimized the number of optical elements, employed a large-format, low-background detector, and retained throughput through vigilant maintenance of a tight contamination control plan and operational strategy to avoid degradation of the mirror coatings.

The resulting FUSE science instrument consisted of four separate telescopes and spectrographs. Each of the four FUSE telescopes was comprised of a co-aligned, normal incidence, off-axis parabolic primary mirror that illuminated a separate Rowland circle spectrograph channel equipped with a holographically-ruled diffraction grating that

illuminated one of the two FUV microchannel plate (MCP) detectors. The essential features of this design are illustrated schematically in Figure 2-1. Each of the two delay line MCP detectors recorded spectra from a pair of optical channels. At the entrance to each spectrograph was a Focal Plane Assembly (FPA) that could be moved in both the tangential and radial directions with respect to the Rowland circle. Adjustable Mirror Positioning Assemblies (MPAs) along with the FPAs permitted co-alignment and focus of the four channels. Attitude determination for target acquisition and fine pointing guidance data was provided by one of the Fine Error Sensor (FES) CCD (slit jaw) cameras operating in the visible on two of the four channels. The prime advantages of this design of four independent UV optical paths was that it permitted the optical coatings to be tailored to maximize instrument effective area across the FUSE bandpass, and that a high effective area could be combined with good aberration control in a package that would fit into the fairing of a practical launch vehicle. Some basic properties of the FUSE instrument are summarized in Table 2.2-1 and Table 2.2-2. Only ranges of effective area and spectral resolution are shown for each channel/segment; see Figure 4-7 for plots of the effective area as a function of wavelength and Figure 4-5, Figure 4-6 for the spectral resolution as a function of wavelength.

Active thermal control and science instrument operations were performed by the Instrument Data System (IDS) computer. Instrument power was obtained from the spacecraft and was managed by the Instrument Power Switching and Distribution Unit (IPSDU) for instrument subsystems.

Table 2.2-1: FUSE Instrument Specifications; Channel 1

Channel	SiC1	LiF1	SiC1	LiF1
Detector Segment	A	A	B	B
Wavelength Range [Å]	1090.9 – 1003.7	987.1 – 1082.3	992.7 – 905.0	1094.0 – 1187.7
Spectral Resolution	12000-23000	10000-21000	10000-20000	11000-21000
Plate Scale [arcsec/mm]	84.4	84.4	84.4	84.4
Inverse dispersion [Å/mm]	1.03	1.12	1.03	1.12
Effective Area [cm ²]	5.5-9.0	3.5-28	6.0-8.5	12-28
At launch				
Effective Area [cm ²]	2.5-5.0	3.0-24	2.5-5.0	8.0-21
End-of-Mission				

Table 2.2-2: FUSE Instrument Specifications – Channel 2

Channel	SiC2	LiF2	SiC2	LiF2
Detector Segment	A	A	B	B
Wavelength Range [Å]	916.6 - 1005.5	1181.9 - 1086.7	1016.4 – 1103.8	1075.0 – 979.2
Spectral Resolution	11000-19000	14000-23000	12000-20000	9000-19000
Plate Scale [arcsec/mm]	84.4	84.4	84.4	84.4
Inverse dispersion [Å/mm]	1.03	1.12	1.03	1.12
Effective Area [cm ²]	10-12	19-30	3.5-6.5	2.0-17.5
At launch				
Effective Area [cm ²]	5.0-6.0	14-21	2.0-3.5	2.0-16
End-of-Mission				

2.3 □ Optical Design

The FUV instrument (see Figure 2-1) consisted of four separate optical paths, or channels. Each channel was illuminated by its own normal-incidence, off-axis parabolic primary mirror with a Focal Plane Assembly (FPA), containing a set of three spectrograph apertures/slits, located at the focus of its telescope mirror. The four telescope primary mirrors were identical off-axis paraboloids, each with a rectangular 352 mm x 387 mm clear aperture, a 2245-mm focal length, and approximately 5.5° off-axis angle (Kennedy et al. 1996). At the focal plane, ~90% of the light in the point spread function (PSF) was within a circle of diameter 1.5 arcseconds. Each spectrograph was a Rowland circle design whose holographically-ruled diffraction grating illuminated a section of a FUV delay line detector. Figure 2-1 (right) illustrates the detector multiplexing layout whereby two channels (one SiC and one LiF) illuminate different areas on a single detector. The channels had to be co-aligned so that light from a single target properly illuminated all four channels, thereby maximizing the throughput of the instrument. This co-alignment was accomplished with actuators on the mirror assemblies and the FPAs.



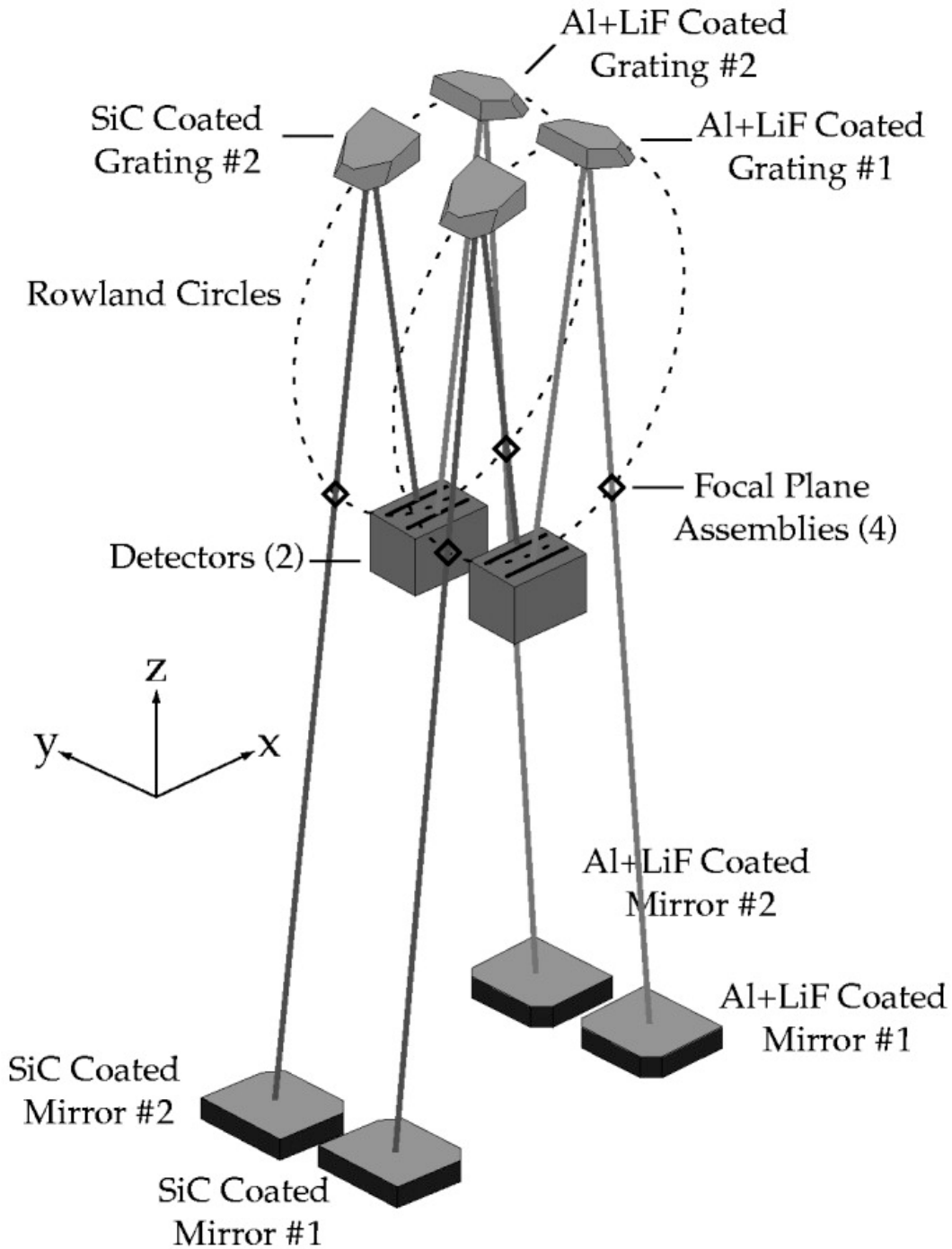


Figure 2-1 : Top: The integrated FUSE satellite. Bottom: Optical layout of FUSE instrument showing 4 channel design but only two detectors.

The multi-channel aspect of the FUSE design was a key element in maximizing instrument throughput. It permitted the use of different optical coatings on different channels. Two mirrors and two gratings were optimized for reflectivity in the 905-1100 Å bandpass using an ion beam sputtered silicon carbide (SiC) coating over an evaporated

aluminum layer. The aluminum layer lowered the emissivity of the surface permitting better thermal control. The reflectivity of the remaining two mirrors and gratings was maximized from 1025-1187 Å using lithium fluoride (LiF) over aluminum. SiC has nearly constant reflectivity (~30%) across the FUSE bandpass. The reflectivity of LiF/Al is low shortward of ~1025 Å, then rises sharply to ~70% near 1200 Å (*The FUSE Data Handbook 2009*). The LiF/Al coatings provided approximately twice the reflectivity of SiC at wavelengths > 1050 Å, but very little throughput below ~1020 Å. Throughout this document the four channels will be referred to as either "the SiC channels" or the "LiF channels" according to their coatings and hence their performance characteristics.

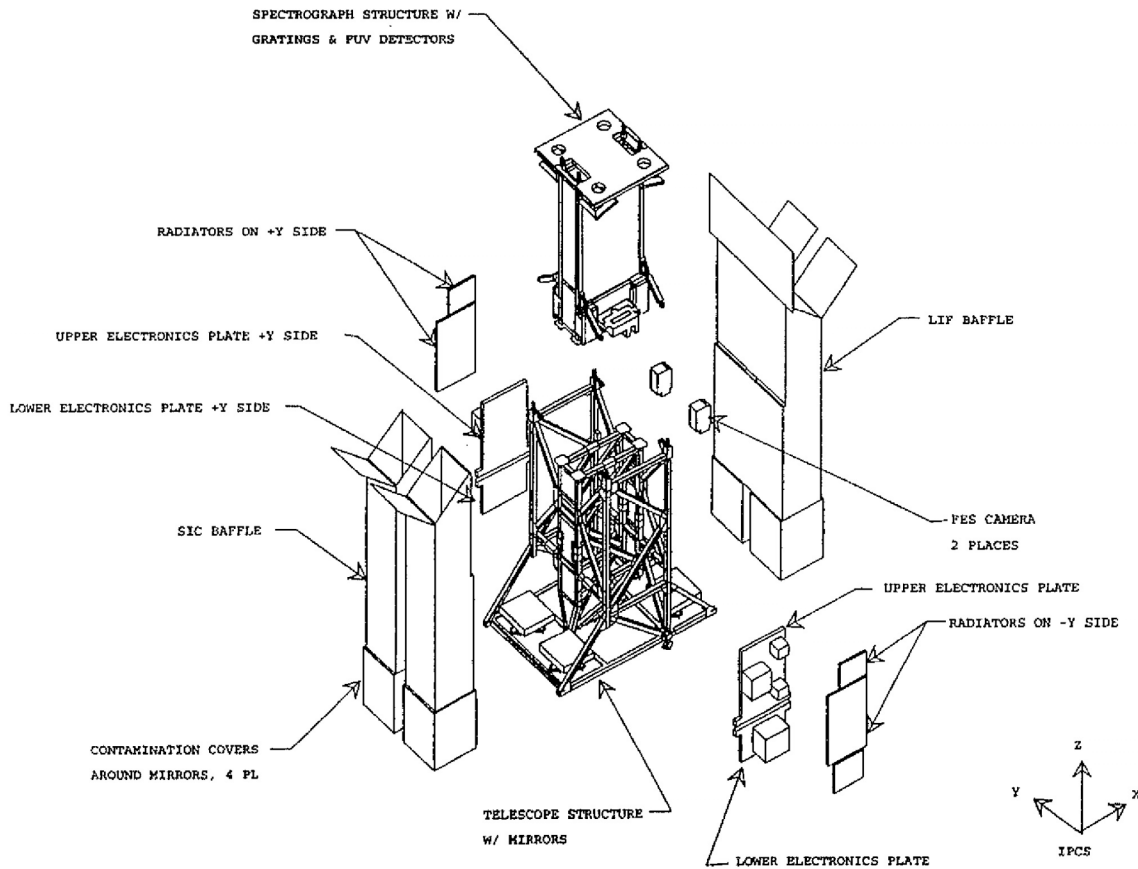


Figure 2-2 : Exploded view of the FUSE instrument structure. This figure illustrates the relationship between the photograph of the assembled, flight-ready, FUSE instrument in the previous figure and the schematic of the optical layout of the telescope and spectrograph.

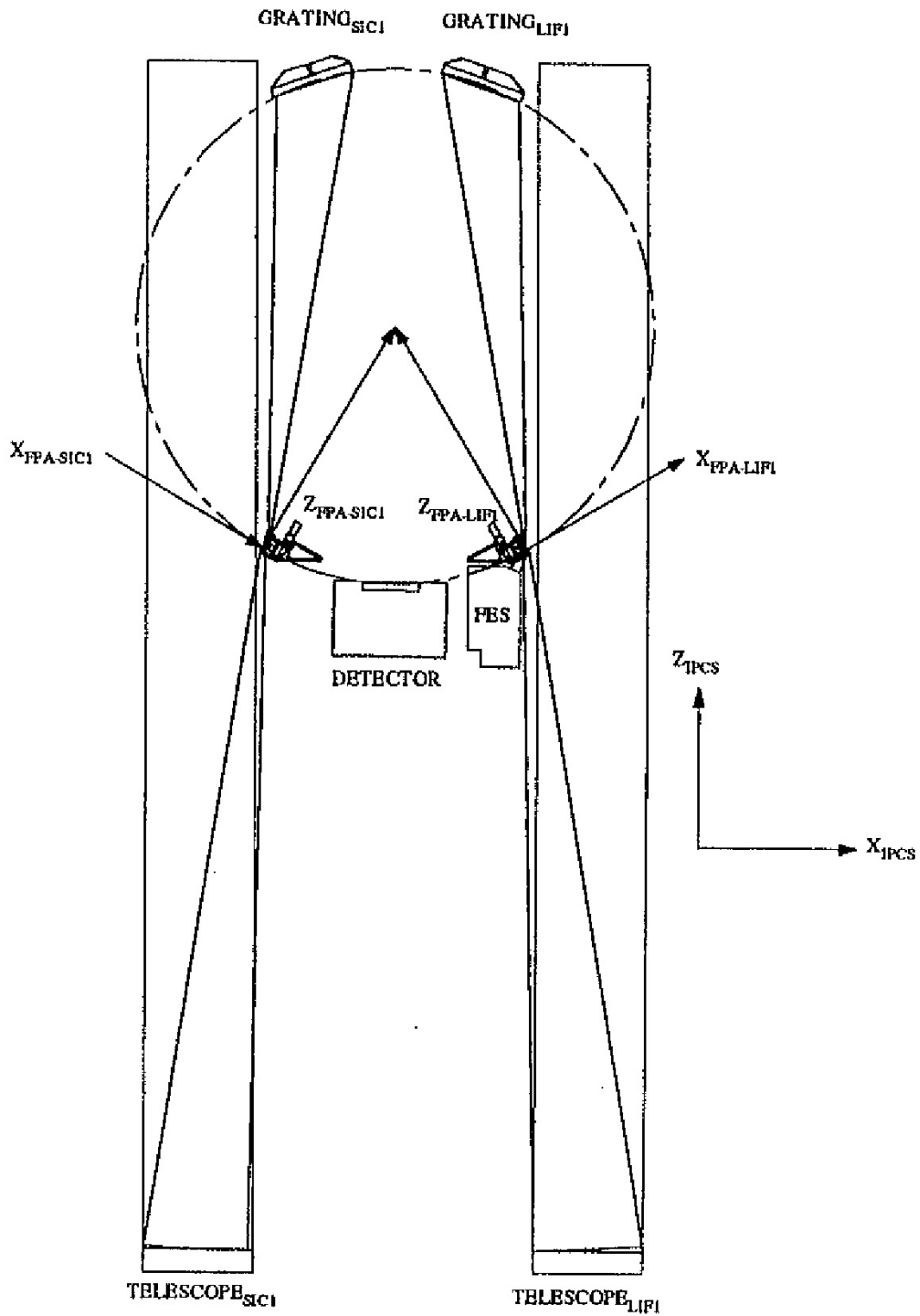
These four channels comprised two nearly identical "sides" of the instrument, where each side consisted of one LiF and one SiC channel. Each side of the instrument produced two spectra, one from each channel, that fell onto a single detector. Each channel had a band pass of about 200 Å, requiring spectra from two channels to span the ~290 Å wavelength range of the instrument. All four channels covered the ~1015-1075 Å region.

The orientation of the instrument in the instrument prime coordinate system (IPCS: X, Y, Z) is shown in Figure 2-1. The +X side of the instrument always pointed away from the sun throughout an orbit, while the -X side always pointed toward the sun. This orientation minimized the amount of sunlight that could make its way down the baffles surrounding the LiF channels, which were located on the +X (i.e. shaded) side of the instrument. Minimizing stray light in the LiF channels was crucial to the operation of the Fine Error Sensor (FES) guidance cameras, which operated at visible wavelengths on the LiF channels. To ensure that the radiator of the operational FES was kept in the shade, the satellite orientation was biased by several degrees in roll around the Z axis. These design and operational strategies succeeded in keeping Solar stray light to acceptable levels; however, when observing at low Earth-limb angles, stray light from the bright Earth could drown out all but the brightest guide stars. FES star field images acquired at orbit noon (Figure 4-36 and Figure 4-37) illustrate the impact scattered light in the FES guidance camera could have when attempting to acquire and track guide stars.

2.4 □ Focal Plane Assemblies

At the focus of each telescope mirror was a Focal Plane Assembly (FPA) that acted as the optical entrance aperture for each spectrograph channel (Figure 2-3). The front surface of each FPA was a diamond milled, flat mirror with vapor deposited aluminum to provide a highly reflective surface in the visible. This optical flat mirror was mounted on a precision two-axis flight-adjustable stage. Light from the off-axis parabolic telescope entered the spectrograph through the four laser drilled FPA apertures (1.25" × 20", 4" × 20", 30" × 30", and a 0.5" pinhole, Table 2.4-1) that had been cut into the flat. For ease of reference, the three primary apertures were dubbed HIRS, MDRS, and LWRS; the pinhole aperture was never located on orbit, and never used operationally. Although these apertures were offset in the direction perpendicular to dispersion, the apertures were not shuttered: all light (including the night sky and serendipitous targets) incident at an aperture was passed through the aperture to the grating, which then dispersed the light onto the detector. Since these apertures were offset in the spatial direction, light passed by each of the apertures was imaged onto a different section of the detector. The geometric arrangement of these apertures is shown in Figure 2-4. The aperture plates were not mounted perpendicular to the telescope focal plane, but were rotated 10.8 degrees about the Y axis; the reflected beams in the LiF channels were directed into the corresponding FES cameras, and against the sides of the telescope baffles in the SiC channels.

For the LiF channels, light that did not pass through an entrance aperture was reflected by the mirrored surface into the FES visible light CCD camera system. Images of stars in the field of view (FOV) around the apertures were then used for acquisition and guiding by the FES, which provided feedback to the spacecraft attitude control system for stabilizing the pointing (Section 2.7). Only the LiF channels were equipped with FES systems, because the Al/LiF coatings on the telescopes were far more reflective in the visible than the SiC coatings and because a prime and backup system were considered to be sufficient.



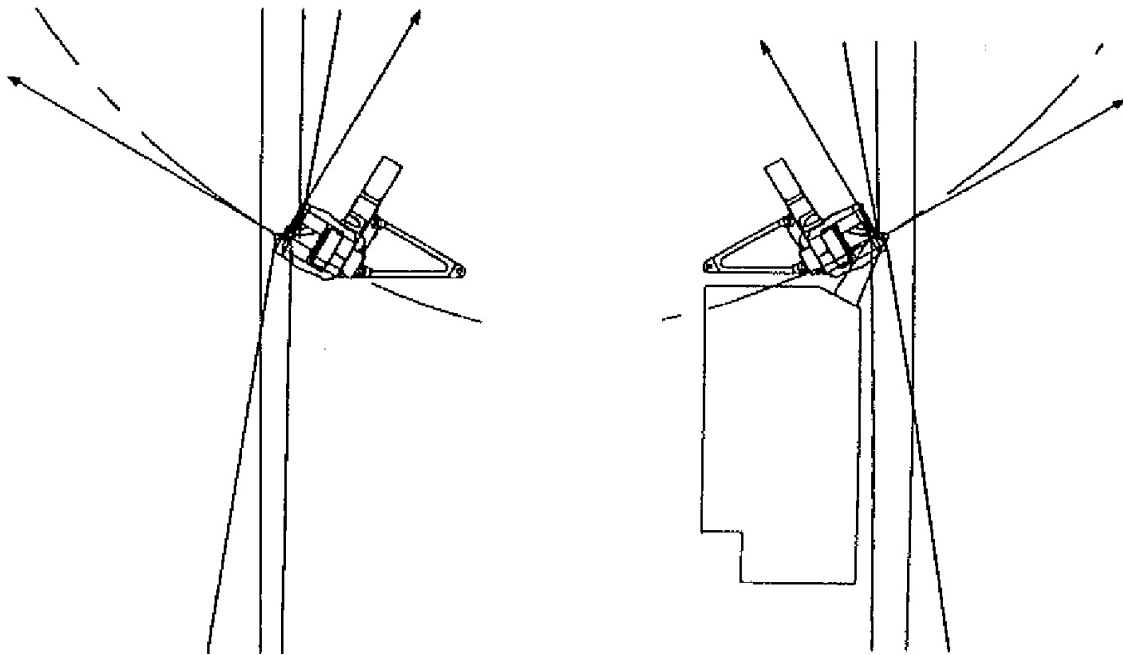


Figure 2-3: Schematic of the LiF1 and SiC1 FPAs shown relative to the instrument optical design and beam size (top), with a detail of the FPAs and their relationship to the Rowland Circle and the IPCS coordinate system (bottom). In the LiF channel, light from the star field in the vicinity of the target is reflected into an FES camera.

Table 2.4-1: Apertures

Aperture	Keyword	Dimension (arcsec)	Y FPA position (arcsec)	Comments
High resolution	HIRS	1.25 × 20	-10.27	
Medium resolution	MDRS	4.0 × 20	+90.18	
Low resolution	LWRS	30 × 30	-118.07	Default Aperture
Pinhole	PINH	~0.5 (diameter)		Not Used

This set of apertures was designed to permit the following functionality.

- The high resolution aperture (HIRS: 1.25 × 20 arcsec) passes ~70 % of the light from a centered point source (throughput as high as 90% has been measured, but 70% is more typical). The HIRS aperture was designed to maintain the highest resolution at the expense of photometric accuracy. This was the expectation even for perfectly stable optics. Because of the difficulties encountered with maintaining channel alignment on-orbit, this aperture was used sparingly during the mission.

- The medium resolution aperture (MDRS: 4×20 arcsec) provided maximum throughput (~98%) while minimizing airglow contamination. With stable mirror alignment, this aperture provided a spectral resolution that was only slightly reduced from the actual resolution achieved when using the HIRS aperture for a point source target. However, on-orbit thermal drifts of the channels with respect to the LiF guide channel resulted in limited use of this aperture due to the effort required to maintain alignment. Significant loss of the SiC channel data typically resulted with use of this aperture under nominal operations. The impact of on-orbit thermal drifts is discussed further in Section 4.2.
- The low resolution aperture (LWRS: 30×30 arcsec) was a large square aperture intended for observations of faint extended objects. It produced a filled-aperture resolution of about ~100 km/s. However, as a result of the on-orbit motion of the instrument channels with respect to one another, use of the LWRS was most likely to result in obtaining data in all channels. Consequently, the LWRS aperture became the preferred aperture for point source observations. The thermal motions had the potential to degrade the resolution, but this was limited by the short duration of HIST exposures and was corrected by CalFUSE for TTAG exposures; see Sections 2.8, 4.2.3, and 4.3.1 for details. For nominal operations, this was the default aperture.
- The pinhole aperture (PINH: approximately 0.5 arcsec in diameter) was not used on orbit.

Each of the four FPAs included precision actuators that permitted independent motion of the FPAs in two axes: tangential to the Rowland circle and along the radius. The FPAs could not be moved in the Y direction. FPA motion along the radius of the Rowland circle enabled focusing of the apertures with respect to the spectrograph grating and detector (Section 6.2). This was performed infrequently over the course of the mission. The motion tangential to the spectrograph Rowland circle was parallel to the dispersion direction and perpendicular to the apertures. Adjustments of the FPAs along this axis were used to compensate for small X-axis mirror motion misalignments (Section 4.2.3.1) and were often performed as part of the set up for an observation. They also permitted "focal plane split" (FP-split) observations to enable high signal-to-noise measurements of bright targets. FP-splits were performed by taking spectra at different FPA settings so that detector fixed-pattern noise could be smoothed out when the data were co-added. Different position patterns were used depending on the observation. Table 2.4-2 shows the FPA locations at the nominal telescope alignment and the adjustments in position and corresponding telescope offset to place the target in the aperture for a typical FP-split observation. The FPAs had a 400um commandable range in X, at 12.63 um/arcsec.

FP-split step	LiF1 FPA	Other FPAs	Slew Offset
Nominal position	117 μm	175 μm	0.0''
1	65 μm	123 μm	-4.1''
2	142 μm	200 μm	+2.0''
3	185 μm	243 μm	+5.4''
4	277 μm	335 μm	+12.7''

Table 2.4-2 FPA locations and pointing offsets for a typical FP-split pattern.

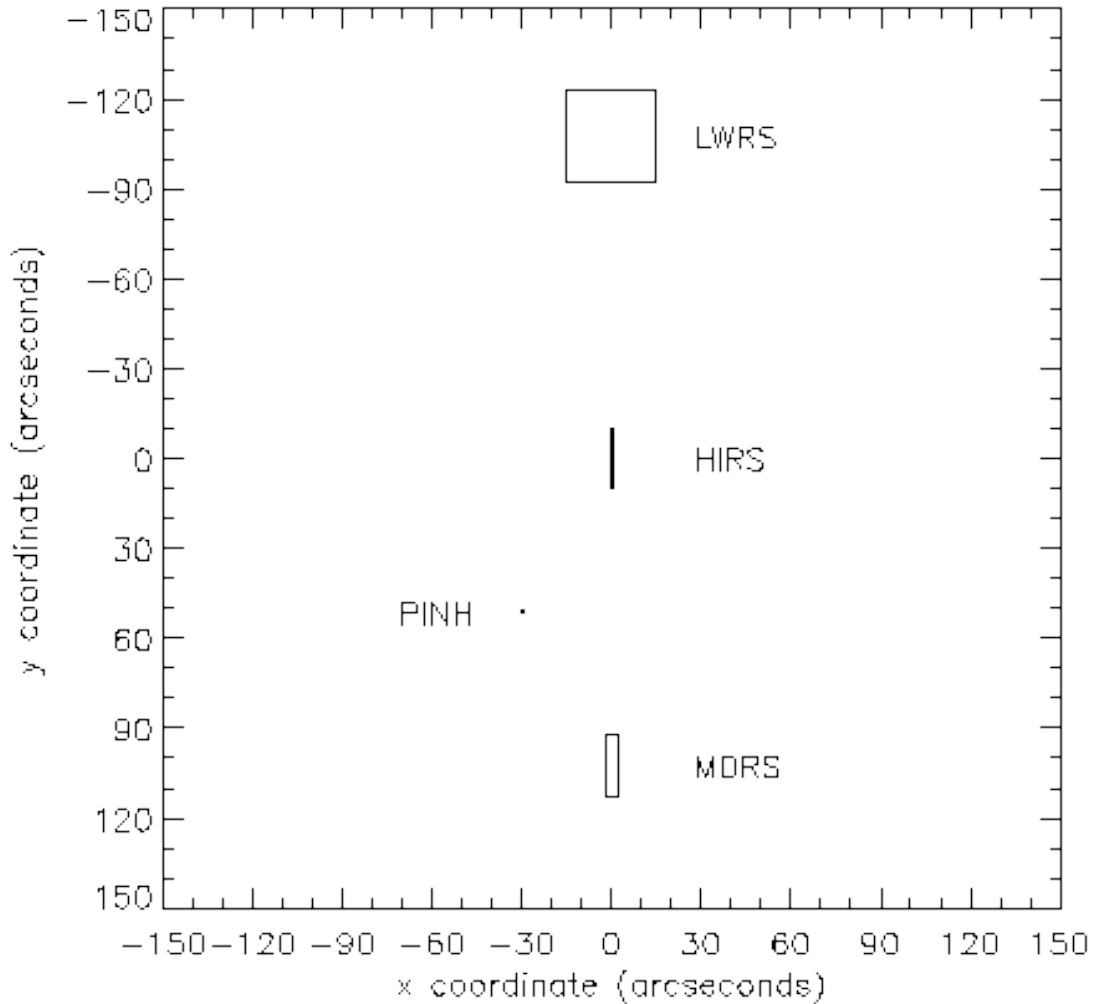


Figure 2-4: The locations of the FUSE apertures projected on the sky for a slit position angle of 0° with North in the -Y direction. Positive aperture position angles correspond to a counter-clockwise rotation of the apertures on the sky. In the FPA coordinate system the LWRS, HIRS, and MDRS apertures are centered at $Y = -118.07''$, $-10.27''$, and $+90.18''$, respectively. This diagram represents only a portion of the FPA; the full active area is $\sim 19 \text{ arcmin} \times 19 \text{ arcmin}$.

2.5 □ Spectrograph

2.5.1 Optical Design

The Far Ultraviolet Spectrograph, FUVS, had four spectrograph channels: one for each of the four telescope channels (Figure 2-1). Each spectrograph channel was conceptually similar to a Rowland circle spectrograph, except that aberration corrected, holographically-ruled, gratings were used to control the astigmatism typically encountered in a Rowland system. Light from the diverging f/5.3 telescope beam passed through an FPA aperture at the telescope focal plane and entered into the spectrograph cavity. The beam was then incident on one of the four diffraction gratings, which focused the spectra onto one of two, double delay line MCP detectors. The gratings were paired so that a single detector had spectra from both a SiC and a LiF grating spatially offset from each other. Because of the multiple apertures, there were typically three spectra from each channel projected onto a single detector.

The grating substrates were fused silica with 270mm x 265mm rectangular apertures. The concave grating surfaces were holographically-ruled aberration-corrected spheres with a radius of curvature of 1652mm. The holographic recording parameters were optimized to reduce the astigmatism from approximately 60 mm (using standard parallel groove gratings) to less than 1 mm while maintaining resolution. This dramatically increased the sensitivity of the instrument. The characteristic groove densities were 5767 grooves/mm for the SiC-coated gratings and 5350 grooves/mm for the Al/LiF-coated gratings (Wilkinson et. al. 1998, and references therein). This resulted in a reciprocal linear dispersion of 1.03 Å/mm for the SiC channel and 1.12 Å /mm dispersion for the LiF channel. Coupled with the detector pixel size, this resulted in a scale of 6.2 mÅ/pixel for the SiC channel and ~6.7 mÅ/pixel for the LiF channel, in the dispersion direction. Selected design parameters for the spectrograph and diffraction gratings are listed in Table 2.5-1.

The diffracted light then focused onto the double delay line, MCP detectors. Each detector had an active area of 190 mm × 10 mm that was divided into two 85 mm × 10 mm MCP stacks, referred to as the A segment and the B segment. The MCPs were curved to 826 mm and a potassium bromide (KBr) photocathode was applied to the top MCP plates to enhance the detection quantum efficiency in the FUV. The average resolution of the FUSE detectors is 25 μm in the spectral direction and 50-60 μm in the spatial dimension. The FUSE detectors are described further in sections 2.6 and 4.4.

Table 2.5-1: Spectrograph and Grating Properties

Property	SiC	LiF
Rowland Circle diameter	1652	1652
Ruling density at grating ctr.	5767 mm ⁻¹	5350 mm ⁻¹
Grating angle (α)	24.0°	25.0°
Grating angle (β)	9.31660° at 986 Å	9.76612° at 1107 Å
Grating dimensions	260 mm (dispersion) × 275 mm (spatial)	
Grating type	First generation, type II holographic	

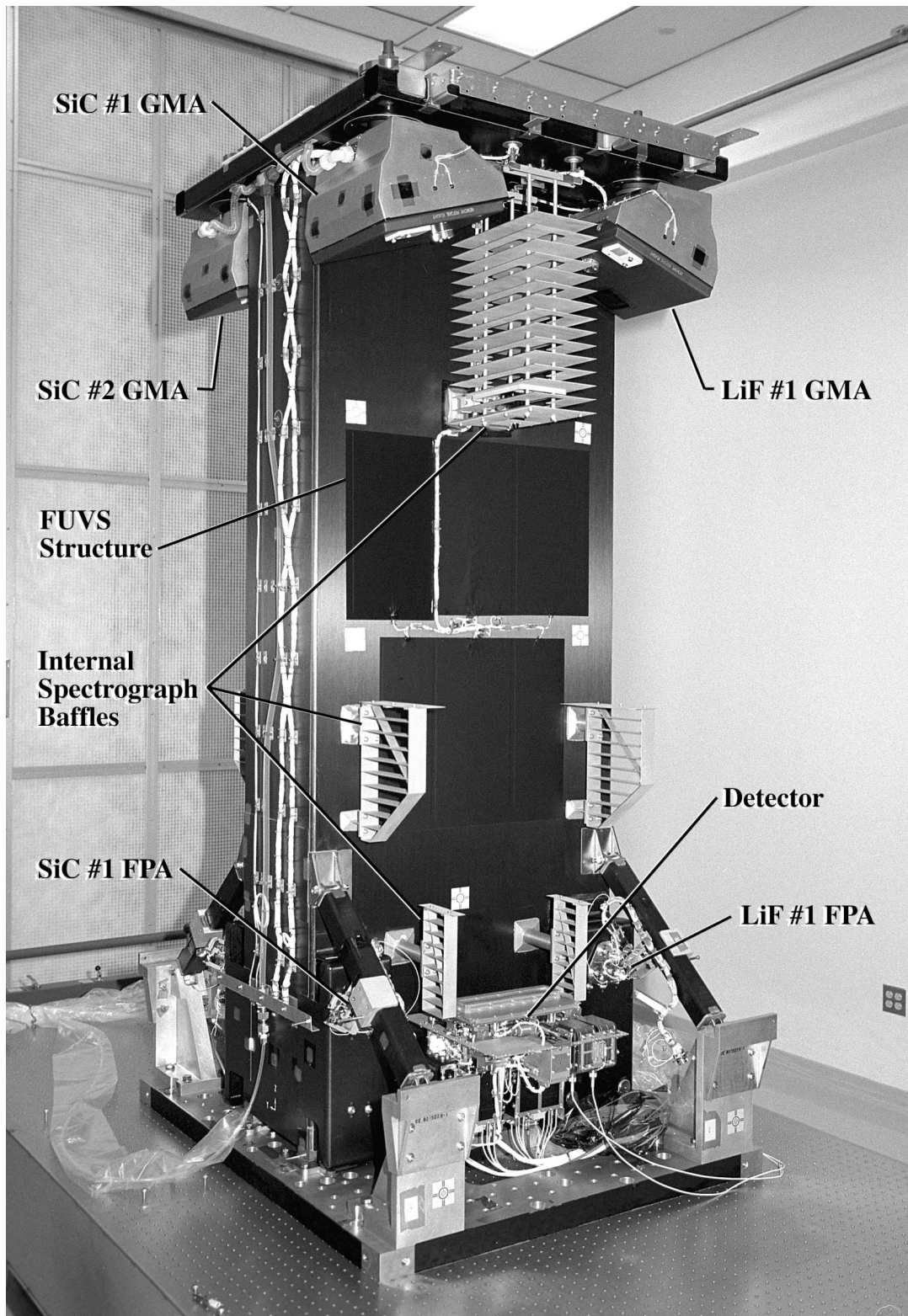


Figure 2-5 Photograph of the FUVS in a clean room at University of Colorado Boulder just prior to shipment to Johns Hopkins University, with the major optical components identified.

2.5.2 Wavelength Coverage and Dispersion

The FUSE spectral range extended from about 905 Å to 1187 Å. Each detector had one SiC spectrum and one LiF spectrum imaged onto it, and therefore covered the entire wavelength range. The two channels were offset on the detector perpendicular to the dispersion direction to prevent the spectra from overlapping. The dispersion for the SiC and LiF spectra were in opposite directions from each other (Figure 2-6). Each detector was divided into two functionally independent segments (A and B) separated by a small gap. To ensure that the gaps did not fall at the same wavelength region in both detectors, they were offset slightly with respect to each other. Table 2.5-2 lists the wavelength coverage of each of the eight detector segment/channel combinations. Nearly the entire wavelength range is covered by more than one channel, and the important 1015–1075 Å range is covered by all four, providing the highest effective area and the greatest redundancy.

Table 2.5-2: Wavelength Ranges for Detector Segments

Channel	Segment A	Segment B
SiC1	1090.9 – 1003.7 Å	992.7 – 905.0 Å
LiF1	987.1 – 1082.3 Å	1094.0 – 1187.7 Å
SiC2	916.6 – 1005.5 Å	1016.4 – 1103.8 Å
LiF2	1181.9 – 1086.7 Å	1075.0 – 979.2 Å

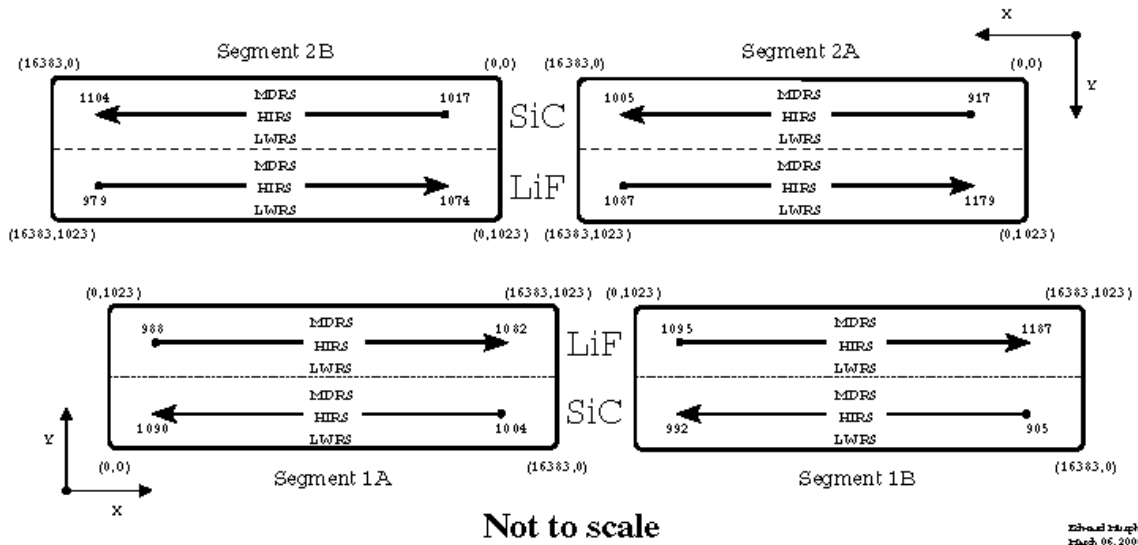


Figure 2-6: Wavelength coverage, dispersion directions, and image locations for the FUSE detectors. In this figure, the coordinate system as used for the detectors is shown, where X is the dispersion direction.

2.5.3 Spectral Image Characteristics

The FUSE spectrographs were based on the highly efficient Rowland circle design. The holographically-ruled gratings partially corrected the inherent aberrations in this design, but the remaining astigmatism restricted spatial imaging capabilities. The image of a point source had a vertical extent of 150 to 1100 μm (~ 14 to 100 arcsec) on the detector, depending on wavelength. In comparison: the height of the HIRS and MDRS apertures were 20 arcsec, or 220 μm projected on the detector, smaller than the astigmatic height of a point source image at most wavelengths. The astigmatism of the FUSE optical system was corrected near the O VI line for LiF spectra, and near 920 \AA and 1090 \AA for the SiC spectra (**Figure 2-7**). Differences in alignment, fabrication, etc. for the two sides, resulted in slightly different locations for the minimum height. The approximate wavelengths at which the astigmatic correction points occurred were: 916 \AA (SiC1B), 926 \AA (SiC2A), 1026 \AA (LiF1A), and 1036 \AA (LiF2B).

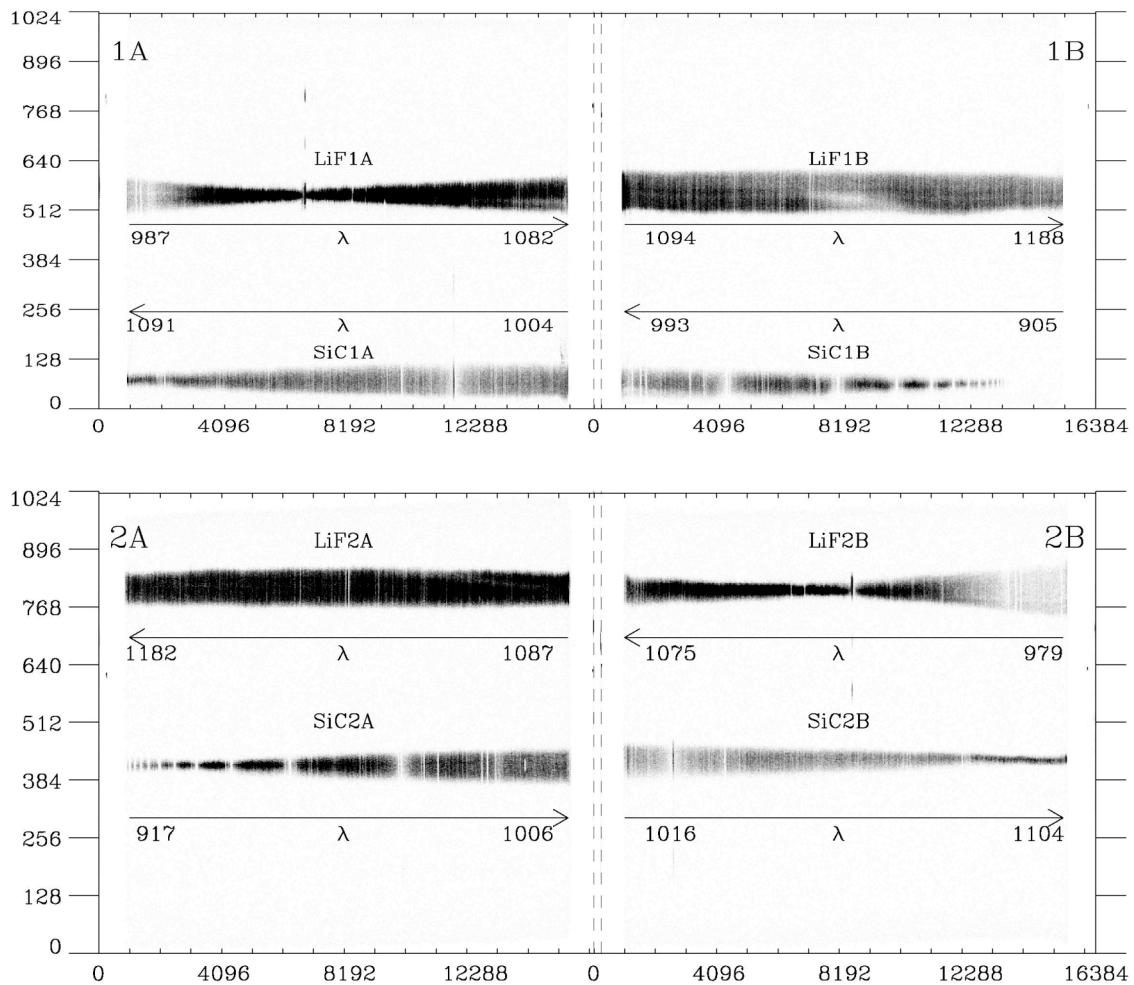


Figure 2-7 The astigmatic height of the FUSE spectra are shown in these figures. The units of both axes for both the top and bottom figures are detector elements, or pixels.

A small portion of an H₂ spectrum recorded by flight detector segment 1B during Spectrograph I&T at the University of Colorado is shown in **Figure 2-8**. A number of interesting characteristics of the spectral design and the test configuration are illustrated in this Figure. First, note that the spectral resolution degrades with the width of the aperture. This is due to the fact that the aperture was fully illuminated during the test. Emission from large extended sources (e.g. supernova remnants, planetary nebulae, galaxies, etc.) exhibited this dependence of spectral resolution on aperture width. Under conditions of nominal pointing accuracy and jitter, a point source spectrum would have roughly the same spectral resolution in all apertures. Second, notice the astigmatic height and curvature of the spectra in the LiF channel (the upper 3 spectra). This is a natural consequence of the optical design. The narrow aperture is on-axis, and the spectrum through this slit is symmetric about the dispersion axis. Note that the other two LiF spectra are asymmetric since they are off-axis. The spectrum through the MDRS aperture (the top spectrum) is tilted slightly to the left while the spectrum through the LWRS (the 3rd spectrum down from the top of the image) is tilted to the right. The SiC spectra all have much smaller astigmatic heights because the spectra are nearer to a holographic correction point at these wavelengths. Comparison of the widths of the LiF and SiC spectral lines clearly illustrates the fact that the spectral resolution is lower at a spatial focus point.

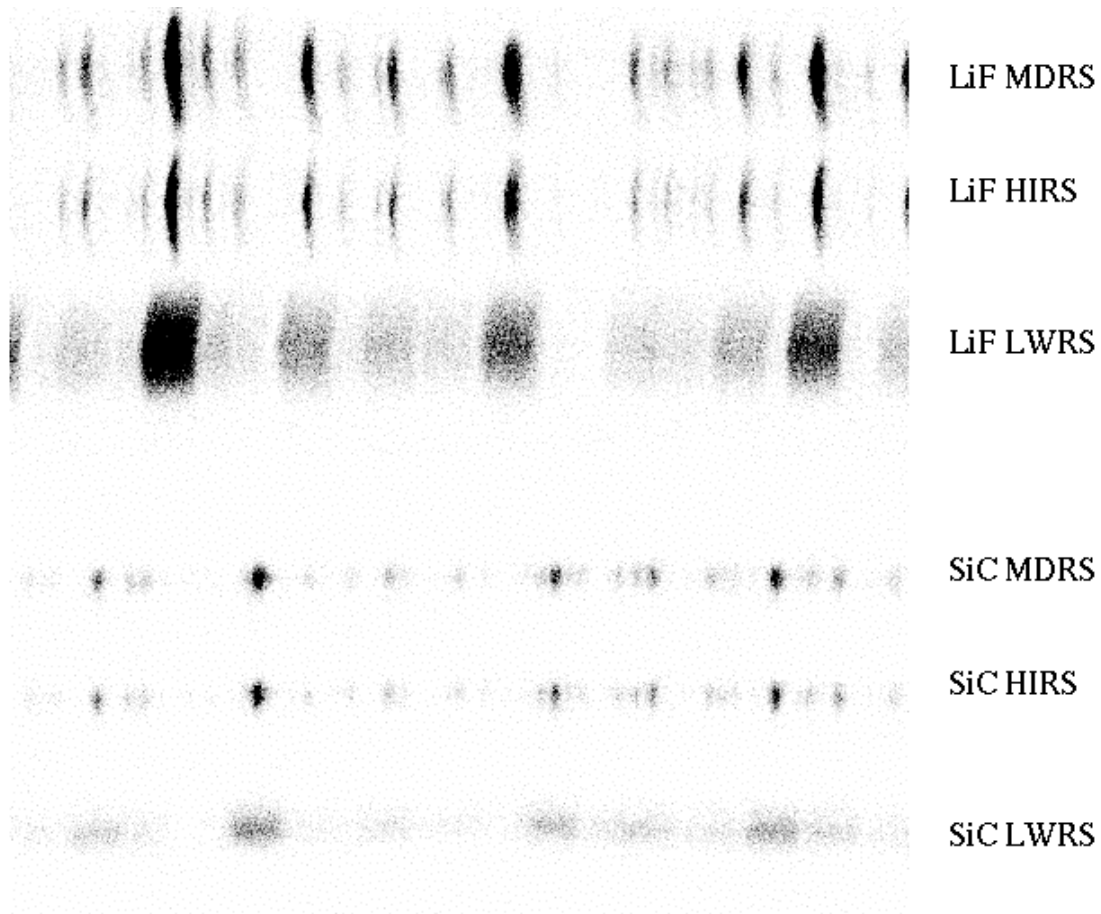


Figure 2-8: Molecular hydrogen emission spectrum recorded by detector 1B. This figure shows the full extent of the segment in the Y direction (1024 pixels) but only a very small extent in X (1000 pixels or about 6 Å). This image was constructed by adding together 6 different images, each made with the lamp source illuminating an individual aperture. From the top to the bottom of the image, the spectra are LiF (MDRS aperture), LiF (HIRS aperture), LiF (LWRS aperture), SiC (MDRS aperture), SiC (HIRS aperture), and SiC (LWRS aperture). The pinholes were not illuminated. The LiF spectra are centered at ~ 1160 Å while the SiC spectra are centered at ~ 930 Å.

2.6 □ Detector Design and Operation

2.6.1 Hardware and Software Description

The FUSE instrument included two Double Delay Line (DDL) detectors which collected incoming photons and measured their positions. Three FUV detectors were built at the Space Sciences Laboratory at the University of California, Berkeley. Unit FL01 remained on the ground as a spare and was later used for ground testing, while units FL02 and FL03 were used in the instrument as Detector 1 (side 1 of the instrument, collecting photon events as part of the SiC1 and LiF1 channels) and Detector 2 (SiC2 and LiF2),

respectively. The three detectors had identical physical characteristics, and were designed to be as similar as possible. Differences between them are due primarily to differences in the microchannel plates (MCPs) and the adjustments of the electronics to account for those variations. The differences in wavelength coverage between side 1 and side 2 of the instrument were determined by the mounting locations on the Rowland circle.

Each detector consisted of two segments. Mechanically, each detector was a single unit; electrically each segment was unique with most of its own electronics. Keeping the segments separated permitted each to be individually optimized. In addition, it ensured that a problem with one segment did not prevent its companion from being operated normally. Thus, if desired one detector segment could be operated normally while the high voltage on the adjacent segment was turned off.

Light coming from one of the FUSE gratings to the detector first passed through a 95% transmission, +15 volt ion repeller grid, then through a 95% transmission 'QE Grid' designed to improve the quantum efficiency of the system, before reaching the KBr-coated MCPs. The photons striking the photocathode were converted to electrons via the photoelectric effect, multiplied as they passed through the stack of three (Z-stack) MCPs, then proximity-focused onto the DDL anode. The DDL electronics determined the location of each charge cloud by measuring the time it took for the charge to propagate along the anode (for the X, or dispersion direction) or by charge division (for Y, or cross-dispersion). Thus, the reported positions of detected photons do not represent physical pixels, as would be the case for a CCD detector, but rather are digitized representations of analog measurements. The measurement process and implications for the data are described in subsequent sections. The top-level detector specifications are summarized in **Table 2.6-1**.

Table 2.6-1 Detector Specifications

Specification	Description
MCP pore size (pore diameter / center-to-center spacing)	10 μm / 12.5 μm (top & bottom plates) 12.5 μm / 15 μm (middle plates)
MCP pore bias angle	13°
MCP Configuration	Z-stack
MCP size	95 mm x 20 mm, 80:1 L/D
MCP resistance	< 30 M Ω
Anode Type	Double Delay Line
Photocathode	KBr
Ion Repeller Grid	95% transmission, 1247 x 1247 μm spacing, flat
QE enhancement Grid	95% transmission, 1042 x 1009 μm spacing, curved to match MCPs
QE in FUSE bandpass	14 – 30%
Active Area	85 x 10 mm x 2 segments ~7 mm gap between segments
Curvature of front surface of MCPs	826 mm radius
Number of Pixels	16,384 x 1024 per segment
Pixel size	6 μm x 10–17 μm , depending on segment
Detector resolution	~20 μm x ~80 μm
Lifetime Specification	> 10 ⁷ events per 10 ³ μm^2

Each detector subsystem was divided into three interconnected, modular assemblies. These were the Vacuum Assembly, Electronics Assembly, and Stim Lamp Assembly. The Vacuum Assembly was mounted in the spectrograph cavity and contained the detector imaging elements (grids, MCPs, anode, etc.) in a stainless steel vacuum housing, along with a high voltage filter module, charge amplifiers, timing amplifiers, a motorized door and mechanism, and ion pumps to maintain a high vacuum inside the vacuum box before launch. The Electronics Assembly, mounted to the instrument electronics baseplate in the electronics cavity, included the low- and high-voltage power supplies, Time-to-Digital-Converters (TDCs), Charge-to-Digital-Converter (CDCs), and a Data Processing Unit (DPU), along with an interface to the instrument computer – the Instrument Data System (IDS). The Stim Lamp Assembly consisted of a mercury vapor lamp that was mounted to the spectrograph structure inside the spectrograph cavity and was powered and controlled via the detector electronics. Details on each of these assemblies are given in the sections below.

Each detector subsystem included thirteen thermistors to monitor the temperature of the detector hardware. Although the temperatures of the anode and some parts of the electronics were known to affect the data, the thermistor information was only used as a general diagnostic, and detector stim pulses, described below, were used to account for temperature effects in the data.

2.6.2 Stim Lamp Assembly

The detector Stim Lamp Assemblies (one for each detector) allowed direct, quasi-uniform illumination of each detector, with count rates of ~2,000 to ~12,000 counts per

second, depending on the segment. These stim lamps were designed to provide general diagnostics of detector health. They were not designed to provide a true flat field of the detectors.

Each stim lamp assembly included the mercury vapor stimulation (or “stim”) lamp, a mounting bracket, and a pinhole aperture to coarsely control the amount and direction of light reaching the detectors. They were mounted to a structural bracket in the spectrograph cavity, approximately 1.25 meters from the detectors. Before launch, the lamps were used to provide detector aliveness tests while the instrument was at atmospheric pressure by illuminating the MCPs through the sapphire windows in the vacuum doors. On orbit, they were used regularly throughout the mission as a means of monitoring detector performance, especially gain sag (Section 4.4.2).

The stim lamps were powered through the detector auxiliary power supply, which also powered the ion pumps.

2.7 □ Fine Error Sensor Cameras

The fine pointing of the FUSE satellite was achieved by using the FES, a visible light imaging camera. The primary functions of the FES were to (1) image the focal plane in order to acquire a target, and (2) provide the fine pointing guidance data to be used by the spacecraft attitude control system to maintain accurate pointing during science observations. Two FES cameras were included onboard FUSE. One FES was used at any given time with the second as a backup.

Each FES directly viewed the focal plane of one of the FUSE primary mirrors. The prime FES unit (FES-A) was mounted just below the FPA (Focal Plane Assembly) in the LiF1 optical channel, so that the mirrored surface of the FPA slit-plate redirects the light into the FES where it is reimaged onto a CCD detector. A schematic view of the LiF1 light path is shown in Figure 2-3 and Figure 6-33. The redundant FES (FES-B) was similarly mounted in the LiF2 channel. A complete visible-light subsystem consisted of an FES, an FPA, a primary mirror, and the baffle tube assembly that protected the optics from stray light. Each FES was composed of three subassemblies: the camera assembly, containing the optics, CCD detector, and preamps; the controller assembly, containing all the remaining electronics and external electrical interfaces, and a radiator and heat strap used to cool the CCD.

2.7.1 Camera Assembly

2.7.1.1 Optics

The optical system consisted of two off-axis aspherical mirrors, a filter wheel, and a doublet lens. Figure 2-9 shows a schematic illustration of the light path inside the FES. The FES imaged a field of view of $21' \times 21'$ onto the surface of a CCD detector, which was reduced to a usable area of $19.3' \times 18.3'$ by an aperture mask located at the surface of

each FPA mirror. The point spread function (PSF) of the system had a typical full-width at half maximum (FWHM) of about 2 pixels ($\sim 5''$) everywhere in the field of view, consistent with the original design and pre-flight measurements, and ideal for centroiding with sub-pixel accuracy. The system throughput was also consistent with pre-flight estimates: a typical $V = 13.5$ mag star produced a signal of 9350 e-/sec. Table 2.7-1 summarizes the characteristics of the FES.

Distortions across the FOV were small, at most 1.5% in the far corners of the FOV. The distortions for FES-A were measured during in-orbit checkout and polynomial corrections were uplinked to the IDS. A more extensive set of calibration observations was performed for both cameras in late 2001, which significantly improved the residuals in the corners of the field.

Imperfections in the optical surfaces and obstructions in the light path (such as mis-aligned baffles) would scatter and diffract light from sources in the FOV. This limited the ability of the system to detect and track faint guide stars when very bright objects were present in the FOV. Initial tests showed that the IDS could identify star fields and track on guide stars at the nominal faint limit when stars as bright as $V = 1.5$ mag were present in the FOV. Using special procedures (such as performing initial acquisitions at offset fields) we were able to acquire and track when much brighter objects were present, without having to use the attenuating filter in the FES. This performance was much better than was expected prior to launch.

No internal focus adjustment mechanisms were included in the FES, due to the cost and schedule constraints, the limited volume available for the camera assembly, and because a limited range of focus adjustment (100 microns) was expected to be required. Instead, the choice was made that the optical design had to produce a PSF that was insensitive to the expected changes in focus, and that the FES would have to be carefully aligned and focused at the time it was installed on the telescope.

A three-position filter wheel was located between the FES secondary mirror and the doublet lens. The filters incorporated in the filter wheel were a clear filter, a neutral filter for use with very bright objects, and a broadband filter (red in one FES, blue in the other). Once it was determined, early in the mission, that the neutral density filter was not needed for acquisitions of bright objects, the FUSE operations team decided to keep the filter wheel in the clear filter position, and not to turn it. Given the critical role of the FES for fine pointing the observatory, the FUSE operation team recognized that a malfunction of the wheel could jeopardize the pointing of the observatory. Consequently, the neutral and broadband filters were never used during the mission.

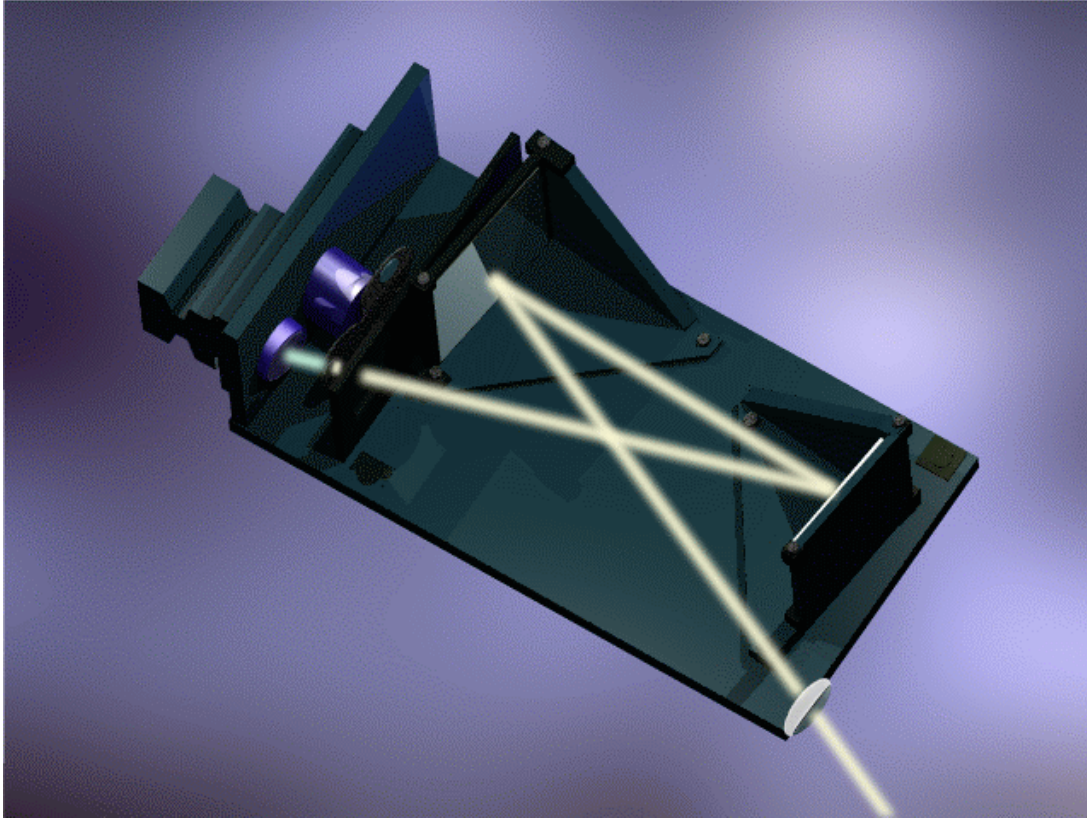


Figure 2-9: Drawing showing the light path inside the FES.

Table 2.7-1 FES Camera Characteristics

FES Properties	Value
FOV	19.3' × 18.3'
Photometric bandpass	4000 – 9000 Å
Plate Scale	2.55" / pixel
Noise Equivalent Angle (typical)	≤ 0.15"
Sensitivity (typical)	9350 e ⁻ / sec @ V = 13.5
PSF	5" FWHM
Exposure time	0.048 – 300 sec
Subimage	3 – 25 pixels square
Centroid rate	6 10×10 subimages @ 1Hz T _{exp} = 0.4 s
	4 16×16 subimages @ 1Hz T _{exp} = 0.4 s
	6 16×16 subimages @ 0.5Hz T _{exp} = 1.2 s

2.7.1.2 FES CCD Detector

The CCD detector was 1024 × 1024 pixel thinned backside-illuminated CCD mounted on a 2-stage thermo-electric cooler (TEC) and sealed in a kovar package with a fused silica window. The CCD quantum efficiency, full-well depth, charge-transfer efficiency, dark current, and readout noise were all in accord with pre-flight measurements. The CCD was

cooled using an external radiator in combination with the TEC. Basic characteristics of the CCD are given in **Table 2.7-2**.

Table 2.7-2 FES CCD Characteristics

CCD Properties	Value
Pixel Size	24 μ m
Read Noise	7 e^-
QE	55% @ 400nm, 65% @ 700nm, 37% @ 900nm
Gain	5 e^- / ADU
Full Well	280,000 e^-
Digitization rate	50 Kpixels/sec
Parallel Clock rate	5,000 lines/sec
Dark current (MPP)	4.1 e^- /pixel/sec at -30C (preflight)
Dark current (MPP)	33 e^- /pixel/sec at -32C (1 yr post-launch)

2.7.2 FES Images

The FES provided two types of data: images of the field of view, and centroided positions of up to six selected stars. This information was transferred to the FUSE Instrument Data System (IDS) which used this information to 1) identify the field of view of the planned science observation and move the target in the desired spectrograph aperture, and 2) to acquire and track on guide stars during the observation in order to stabilize the line of sight. The target recognition and fine guidance of the FUSE attitude control is described further in Section 6.5.2 and by Ake et al. (2000).

The locations of the FPA apertures in the FES image and the relative orientation of IPCS coordinates and raw FES-A pixel coordinates are depicted in **Figure 2-10**. FES-B is similar, except that the X-axis in FES-B is inverted: a corresponding image for FES-B would have CCD column 0 on the right and column 511 on the left. Table 2.7-3 gives the aperture and Reference Point positions in FES pixel coordinates. The Reference Point is not a physical feature on the FPAs, but is an arbitrary position offset from the apertures used in the target acquisition process; see Section 8 for additional information on coordinate conversion.

FES images taken during the identification process or at the end of an observation for the purpose of pointing verification are archived at MAST as part of the science program observation (see Section 5.1 of the [FUSE Data Handbook \(2009\)](#) for additional information). Conversion from the FES image coordinates to the world coordinate system is discussed in Section 8.

2.8 □ Instrument Data System (IDS)

The IDS was the primary computer of the FUSE science instrument. It was a fully redundant, programmable processor that provided command and data handling functions for all other subsystems in the instrument. The main functions performed by the IDS include:

- 1) processing, management, and storage of science data from the FUV detectors
- 2) commanding the FES, computing fine pointing measurements from stellar positions and images generated by the FES, and transmitting the results to the spacecraft ACS;
- 3) managing instrument thermal control;
- 4) synchronizing time with the spacecraft;
- 5) running a script engine, that provides absolute time and relative time commanding, and rule-based autonomy capabilities for both scripted operations and health and safety monitoring.

Only the first of these items is described here; the other items are discussed in Sections 3 and 6.5

The IDS detector manager was a task designed to read science data from the detectors and then process and store the data as quickly as possible. The manager operated in either of two modes: address stream (also called time-tag or TTAG) or spectral imaging (also called histogram or HIST). These modes were selected for a specific exposure by the Mission Planning system, typically based on the expected brightness of the target.

In address stream mode, raw detector data were saved in a software FIFO in bulk memory. The IDS inserted time markers into the data stream as the data were ingested. The default rate for inserting markers was 1 Hz, but the rate could be set as high as 125 Hz. These markers were accurate to 8 ms. The maximum rate at which the IDS could ingest data in this mode was 8000 events/sec. The FIFO was readout continuously as the exposure was taken. The maximum readout rate was roughly 3500 events/sec, lower than the maximum ingest rate. Thus, once the FIFO filled the effective data acquisition limit in TAG mode was 3500 events/sec. The issues affecting the overall system deadtime are discussed in Section 6.9.

Observing in time-tag mode allowed the data to be taken at full detector sampling (6 μm in X and 9-16 μm in Y), along with photon event pulse height values. This permitted CalFUSE to perform sophisticated filtering and corrections when extracting the resultant spectra. Spectral shifts on the detector, either by grating or image motion (Sections 4.3.5, 4.2.3) or pointing instability (Sections 6.5.2 and 7), were removed by modeling or using additional engineering telemetry. Doppler smearing and shifts in areas of high gain sag (Section 4.4.2.1) were also corrected. Periods of detector related problems, such as anomalous HV levels and event bursts (Section 4.4.3.3) were edited out. Finally, in time-

tag mode data from the entire active area of the segments were downlinked, providing spectra through all apertures for extended sources.

Histogram mode was used when the expected count rate of the target exceeded 2500 counts per second. This mode allowed brighter targets to be observed, but with certain disadvantages. The data were binned by 8 pixels in Y and most of the temporal corrections available for time-tagged exposures could not be made. Doppler smearing was minimized by keeping the exposures short ($\sim < 7$ minutes). In this mode, the IDS accumulated an image of part of the detector in bulk memory by computing an array location from the detector raw coordinates and incrementing the number of counts in that location. Only limited portions of the detector could be stored in the IDS in this mode, as a result of memory size limitations. The regions to be stored were defined by the Spectral Image Allocation (SIA) Tables, which are described in Section 6.3.3. The maximum event rate that could be ingested by the IDS in this mode was 32,000 events/sec.

At the end of the exposure, the image was read out. The IDS appended an 8 character observation ID and 3 character exposure number assigned by the Mission Planning system to the downlinked packets. While the exposures were in progress, periodic engineering snapshots of instrument telemetry were taken to assist in the processing of the science data on the ground. At a minimum, a snapshot was obtained at the beginning and end of the exposure, and usually every 5 minutes during a longer integration.

A description of other IDS functions is presented in Section 6.5 and a more detailed description of the IDS is given by Heggstad & Moore (1999) and Artis et al. (2000). Further information about CalFUSE processing of time-tag and histogram exposures can be found in Section 4 of the [FUSE Data Handbook 2009](#) and Dixon et al. (2007).

3 The FUSE Spacecraft

The FUSE satellite consisted of the science instrument and the spacecraft bus. The spacecraft consists of five housekeeping subsystems as follows:

- Command and Data Handling (C&DH) System
- Attitude Control System (ACS) Subsystem
- Power Subsystem
- Radio Frequency (RF) Communications Subsystem
- Thermal Subsystem

Each of the S/C subsystems were fully redundant. With the exception of the ACS, the spacecraft performed flawlessly throughout the mission. Most of the spacecraft functions are transparent to the user of archived science data; only those aspects of the spacecraft affecting the data are described in this document. This section provides an overview of the spacecraft C&DH and ACS subsystems.

3.1 Command and Data Handling System

The FUSE Command and Data Handling (C&DH) system was based on the Small Explorer Data System (SEDS) design developed by OSC and GSFC for the XTE and TRMM missions. The SDS design implemented CCSDS packet telemetry and command standards that were consistent with the Advanced Orbiting Systems recommendations. The solid state recorder provided 240Mbytes of storage for telemetry, of which approximately 100Mbytes was available for science data. The storage available was a significant factor in observation scheduling, and in particular it drove the brightness limit for time-tag observations and the choice of binning, duration, and frequency of histogram exposures.

The C&DH system also provided accurate UTC time to the Instrument. The on-board clock was measured to drift from near zero to a few milliseconds per day. The clock was monitored daily, and was adjusted from the ground whenever the cumulative drift reached 70ms.

3.2 □ Attitude Control System

At launch, the FUSE ACS was a zero momentum system that provided inertially-fixed pointing. Coarse attitude determination was performed using Inertial Reference Unit (IRU) gyro data for spacecraft angular rate measurements and Tri-Axial Magnetometer (TAM) data for attitude measurements; fine pointing employed Fine Error Sensor (FES) measurements that were processed by the Instrument Data System (IDS) and provided to the ACS via Fine Pointing Data (FPD) packets. All of the attitude and rate measurements were processed by the on-board Kalman Filter. Coarse Sun Sensor (CSS) data was used in safe modes. CSS data was accurate to roughly $4^\circ 1\sigma$, TAM derived filter attitude to better than $2^\circ 1\sigma$, and FPD derived attitude to better than $0.5 \text{ arcsec } 1\sigma$ pitch/yaw. Attitude control was provided by reaction wheels, and momentum unloading was

performed with magnetic torquer bars. Prior to reaction wheel and gyro failures, the pointing stability varied from 0.3 to 0.7 arcsec, RMS, depending on the axis and environmental conditions.

The ACS subsystem was fully-redundant, with two 3-axis Ring Laser Gyro IRUs, two TAMs, two CSS assemblies, three dual wound Magnetic Torquer Bars (MTBs) each controlled by two sets of MTB electronics (MTBE), and four Reaction Wheel Assemblies (RWAs).

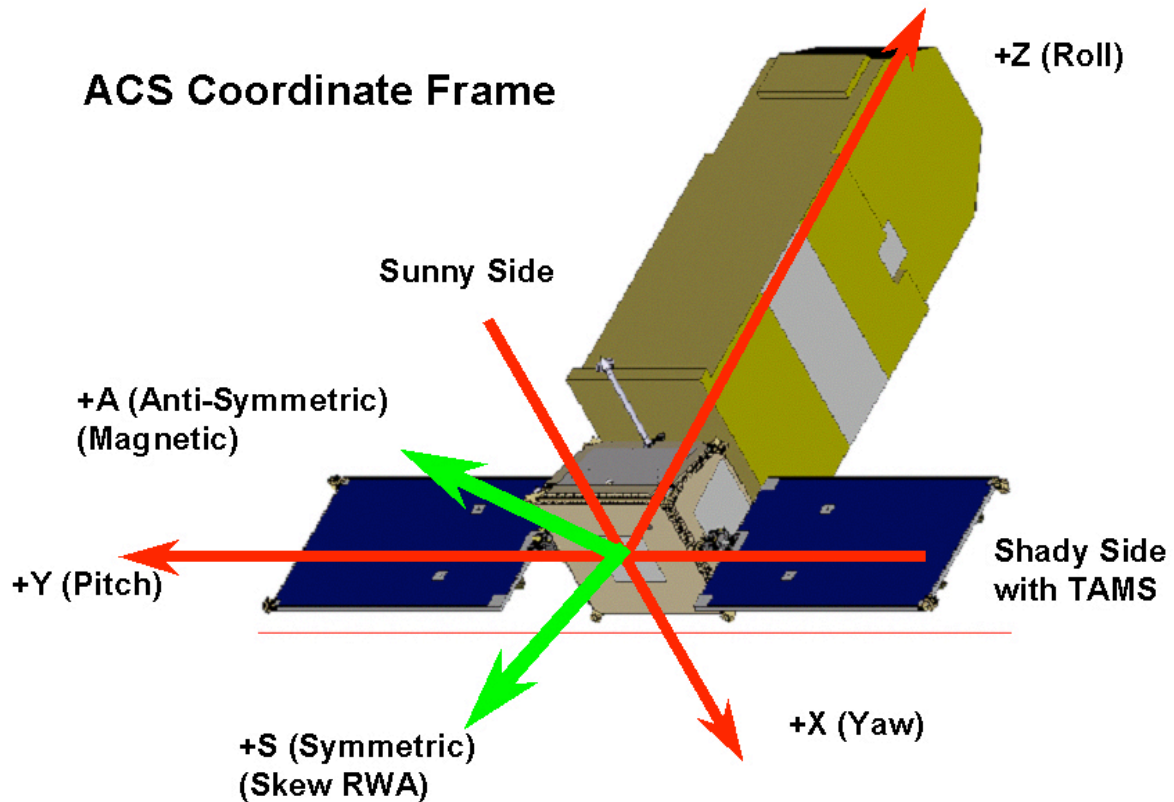


Figure 3-1: ACS coordinate frames. Red: original, Green: revised for magnetic control system.

The basic operations concept for the ACS was to hold the satellite inertially fixed at the last commanded attitude, and to re-orient the satellite when a new attitude was commanded. Ordinarily, new attitudes would be commanded from observation scripts executing in the IDS. Slews could also be commanded from the ground, but this option was not used for science operations. The solar arrays were moved by the ACS during slews so as to be pointed at the Sun when the new attitude was reached.

The nominal configuration of the reaction wheels was to operate the skew wheel at a fixed speed, and to bias the other wheels in the opposite direction so as to maintain the total angular momentum stored in the reaction wheels near zero. This bias kept the wheel speeds away from zero, as bearing life and pointing performance were both expected to

be adversely affected at very low wheel speeds. The magnetic torquer bars were operated continuously to remove excess momentum from the wheels.

Target acquisitions were scheduled after every slew and after every occultation of the target by the Earth. All observation sequencing and target acquisition logic was handled by scripts executing in the IDS. Processing of FES image data to locate stars and attitude determination from the positions of stars were performed by the IDS guidance task software. This division of functions between the ACS, IDS, and FES provided the performance necessary to meet the mission requirements and resulted in simple interfaces that facilitated rapid development and integration of the subsystems prior to launch.

The target acquisition process is described in Section 6.5, and further information on the ACS is provided in Sections 6.5.2 and 7.

4 In-Flight Instrument Performance

4.1 □ Telescope Focus

4.1.1 Post-launch Focus Assessment

The FUSE instrument was focused pre-flight with the provision for in-flight focus adjustments for the mirrors and FPAs. On-orbit focus adjustments were expected due to (1) the unavailability of a full-aperture laboratory FUV source with a light beam collimated to one arcsecond accuracy and (2) the anticipated focus changes associated with gravity release and changes in the positions of the optical elements resulting from moisture desorption from the optical bench structure.

The on-orbit instrument focus procedure was a two-step process. First, the telescope was focused by adjusting the mirror to FPA distance for each channel. Then each spectrograph was focused by adjusting the distance from the telescope mirror to the spectrograph grating for each of the four instrument channels. The FPAs were then re-adjusted to maintain the previously determined telescope focus. There was no separate focus for the FES cameras.

The telescope focus was determined through a series of knife-edge tests performed by scanning a target across the edge of the FPA slit at a series of different FPA Z-positions. The FPA Z positions were adjusted November 24th, 1999, based on these tests. Details of the motions are given in Section 6.6.1 and **Table 6.6-1**.

Two programs were executed to determine the spectrograph focus. The first of these programs, I817, was executed during the December 7 – December 9, 1999 time interval. Multiple stellar spectra of HD208440 were acquired through the LWRS aperture for each of 5 mirror positions, which were stepped in 150 micron increments along the optical axis. These data were analyzed to determine the mirror position that yielded the sharpest spectral absorption features. The resulting adjustments to the mirror and FPA Z positions were implemented on December 12th 1999. These adjustments are discussed further in Section 6.6.1.1 and presented in **Table 6.6-2**.

The signal-to-noise of the I817 data was relatively low for the SiC channels, hence a second spectrograph focus test was executed two months later as part of program I819. The quality of the resulting data was significantly better in all four channels, leading to a final focus adjustment on March 16th, 2000. The adjustments are tabulated in **Table 6.6-3**.

4.1.2 Tails of the Telescope PSF

The tails of the telescope PSF after the final focus were evaluated by a retrospective analysis of the peakup and alignment scan data. The peakup procedure produced count-rate measurements for a small range of offsets from the PSF peak, and the alignment scans produced measurements of count rates for a larger range of offsets, but typically with fewer samples at any given offset. The peakup procedure and sample data are described in Section 4.2.2, and the channel alignment procedure and sample data are provided in Section 6.7.4. The results of this analysis are show plotted in Figure 4-1, Figure 4-2, and Figure 4-3, for the HIRS, MDRS, and LWRS apertures, respectively.

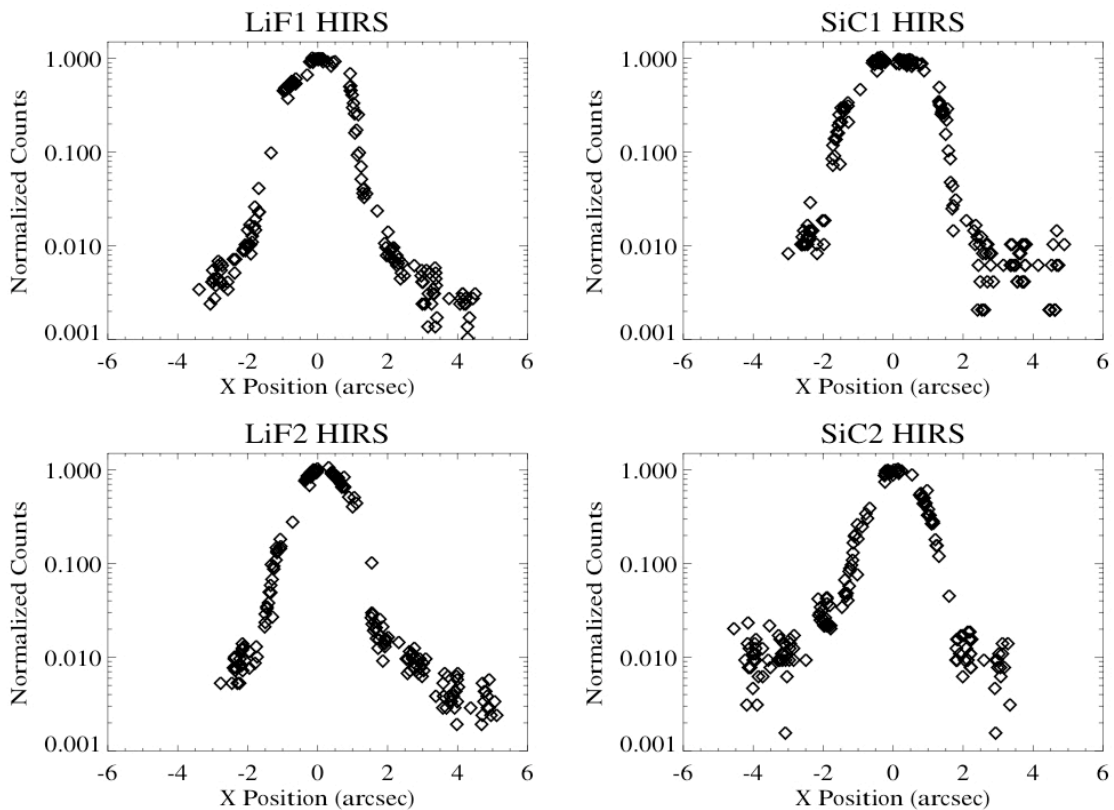


Figure 4-1 The log of the count rate, normalized to unity, is shown plotted as a function of the X-position of a point-source image relative to the center of the HIRS aperture in each channel. This is equivalent to the convolution of the telescope PSF with the HIRS aperture .

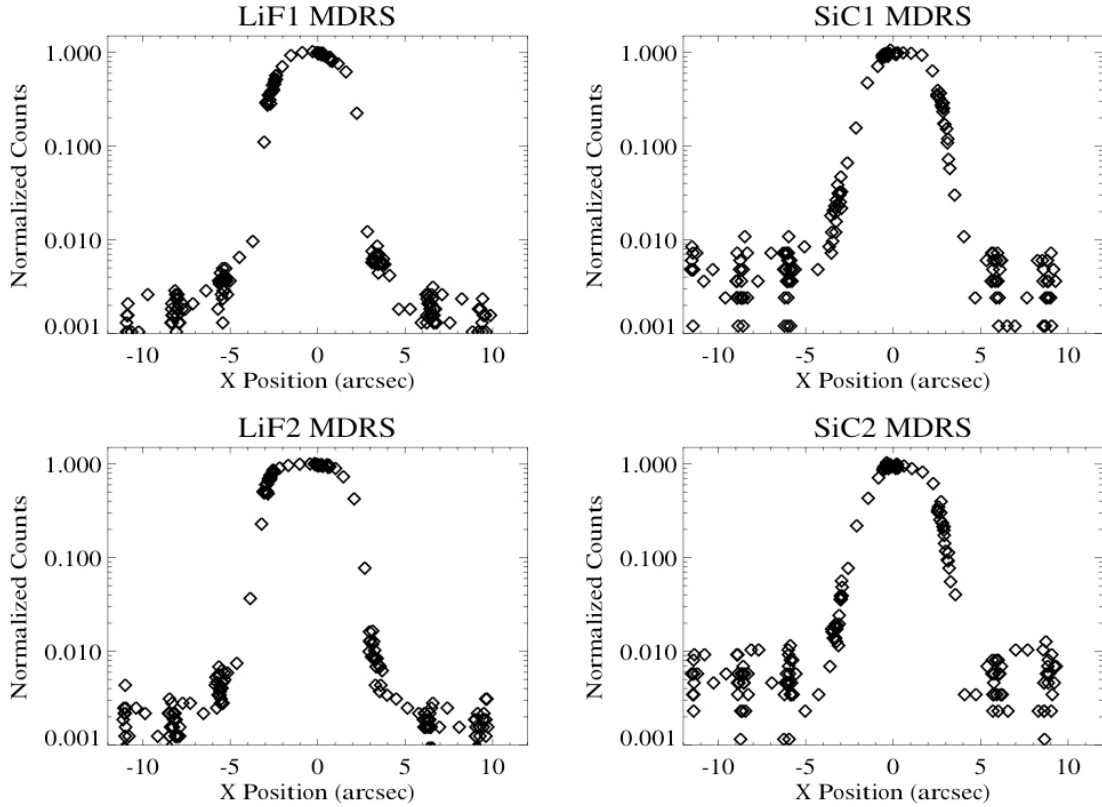


Figure 4-2 Same as Figure 4-1 above, but for the MDRS aperture.

Following the focus adjustments made in early 2000, the throughput of the MDRS aperture was measured to be 98%, and that of the HIRS aperture was 90%. The effective throughput of the narrow apertures was quite sensitive to drifts of the channel alignment on orbital timescales, and thus varied from one exposure to another in the SiC channels and in whichever LiF channel was not in use for guiding. Throughput in the HIRS aperture was also sensitive to the accuracy of both the peakup calculation and the slew executed as the final step of the peakup procedure; mis-centering of a few tenths of an arcsecond were possible and would have a noticeable impact on the throughput. When FES-B was made the guide camera in July 2005, the LiF2 FPA was moved by 400 microns along its Z-axis (see Sections 6.2.2 and 6.4.2). This had no adverse effect on the spectral resolution of point sources, but the throughput in the LiF2 channel was reduced to ~70% for MDRS and ~15% for HIRS.

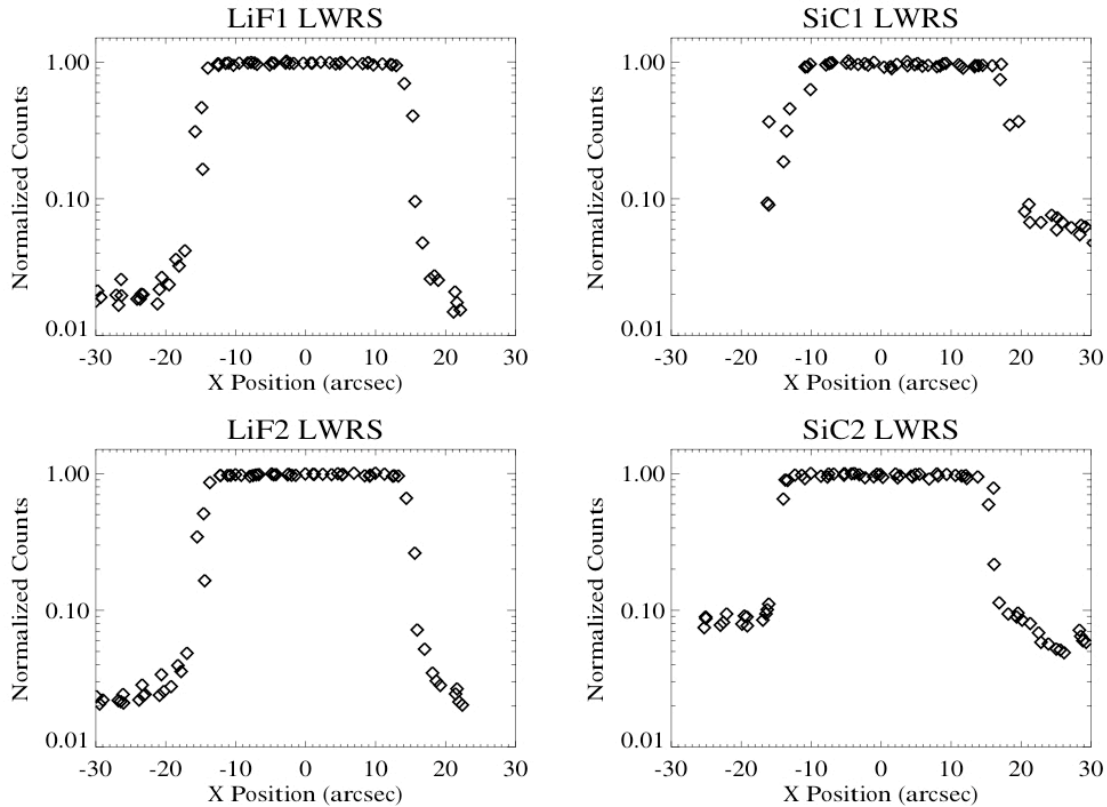


Figure 4-3 Same as Figure 4-1 above, but for the LWRs aperture.

4.2 □ Telescope Alignment Performance

During the IOC period shortly after launch, it was realized that the telescope mirrors underwent periodic motions that shifted the target's image at the telescope focal plane and thus its spectrum in both X and Y on the detector. A source in either of the SiC channels could move as much as 6 arcseconds in a 2 ks time interval. This motion had two effects on the data: first, flux was lost if the source drifted (partially or completely) out of the aperture; second, the was spectrum shifted on the detector, degrading spectral resolution for observations using the LWRs (30 arcsecond) aperture.

4.2.1 Initial Alignment

The procedure for the initial post-launch channel alignment was to perform a spiral search pattern of motions on LiF2, SiC1, and SiC2 while guiding on the target using FES-A with LiF1 and the LWRs aperture. The FUV count rate was monitored while using the mirror actuators to locate the target position in the three non-guide channels. This method required use of a moderately bright FUV point source in a fairly isolated star field to provide sufficient counts and prevent confusion from nearby field stars. Overall, this method worked well and was used to initially align channels to a 15-arcsec precision.

Finer co-alignment was then performed by stepping the roughly co-aligned images across the edge of the LWRS slits. The data were analyzed to determine the mirror rotations required to remove the measured alignment errors at that attitude for each of the three non-guiding channels relative to the LiF1 channel. This method allowed for co-alignment to approximately 2 arcsec.

As further alignments and observations were attempted, it was found that all of the channels were moving with respect to each other, with misalignments as great as 40 arcsec. It was quickly realized that the coalignment was being lost following large changes in spacecraft attitude that changed the thermal environment of the instrument. As a result, grouping observations by Solar beta angle and boresight-to-orbit-pole angle became a constraint on mission planning, and channel coalignment procedures were needed roughly weekly instead of the expected few times per year.

4.2.2 Target Peakups

Small misalignments of the channels could be removed by performing peakups in either the MDRS or HIRS aperture. This involved performing small maneuvers of the spacecraft in the X direction and measuring the FUV counts as the target crossed the narrow axis of the slit. Before ACS components began to fail, the pointing of the spacecraft was dithered in a step and dwell pattern, with nine steps separated by 3 arcsec (MDRS) or 1 arcsec (HIRS), and dwells lasting 10 seconds long at each step. Later in the mission, when adapting to operations with a single reaction wheel, the step and dwell sequence was replaced by a continuous scan. Photons occurring in the LiF and SiC counter masks for each detector (Sec.) were accumulated. At the end of the scan, a flux-weighted positional centroid was computed for each channel and a test was performed to verify a peak occurred in the data: the maximum count had to be at least $5 \times \sqrt{\text{mean}}$. The spacecraft was moved back to the position where the guiding channel (LiF1 or LiF2) had maximum counts and the other three FPAs were moved into alignment. If no peak was found in the guiding channel, the spacecraft was moved to the target acquisition position. For the other channels, an absence of a peak meant the FPA was not moved. Figure 4-4 shows an example of the counts obtained during a peakup scan.

The peakup software and FPAs were designed to eliminate channel misalignments on the order of 5-10 arcsec in the X direction. Similar misalignment in Y was accommodated by making the slits 20 arcsec long. The larger errors found on-orbit impeded peakup alignments in two ways. First, if the initial position of a target in a channel was further than the width of the slit beyond the range of the scan, the target would likely not be found. Secondly, if multiple peakups were scheduled during an observation or a spurious peak were found, a motion could be computed to move an FPA past its limit. The IDS software at launch would reject all FPA motions if any one were out of bounds, effectively allowing one bad channel to cancel the peakup results. After the software was changed to allow all valid FPA motions to occur, better alignment was achieved. Other peakup problems that occurred less often were false peaks being found due to event bursts on the detector (Section 4.4.3.3) and peaks contaminated by other objects near to the target.

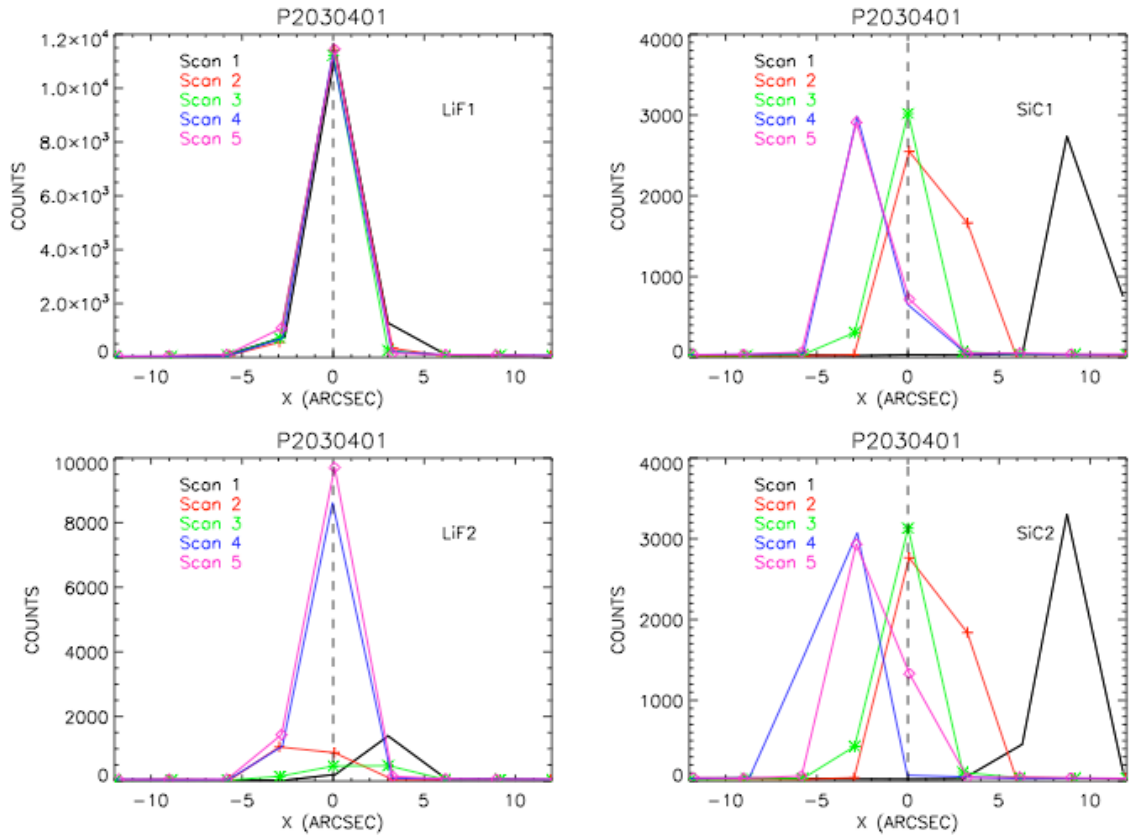


Figure 4-4 Peakup scans over 5 successive orbits for observation P203:04:01. The count rates as a function of scan step are shown in different colors; the first scan of the observation is plotted in black and shows the largest channel alignment errors. FPA adjustments required in subsequent orbits were much smaller.

4.2.3 Mirror Motion Anomaly

The FUSE “Image Motion” was defined as the variation of the alignment of the SiC1, LiF2, and SiC2 channels with respect to the reference LiF1 channel used for guiding. Although these motions were generally quantified as being associated with the non-guiding channels, they were caused by the motions of LiF1 in combination with the other channels. (Any LiF1 motion was corrected by the ACS using FES Fine Pointing Data, so it appeared to remain steady.) After the switch to FES-B in July 2005, LiF2 replaced LiF1 as the reference channel. The observed image motion was attributed to the thermal changes induced in the instrument by changes in boresight beta angle and orbital pole angle. The boresight beta angle is the supplement of the angle between the satellite-sun line and the instrument line of sight, and the orbital pole angle is the angle between the orbit pole and the instrument line of sight.

To mitigate loss of data due to channel misalignment while retaining observing efficiency, the LWRS aperture became the primary observing aperture for most

programs. For MDRS and HIRS observations, two peakups per orbit were executed when necessary to maintain channel alignment during an observation and obtain full spectral coverage while using these apertures.

4.2.3.1 On-orbit Mirror Motion Mitigation Strategy

A two-part strategy was developed to maintain alignment of the four mirror channels. This strategy included both a predictive component based on empirical modeling of changes in mirror position as a function of boresight attitude and a periodic hard re-baselining of the alignment.

Sections 6.7 through 6.7.5.1 discuss further the procedures necessary to maintain channel alignment, its impact on observatory efficiency, mirror motions over an orbital observing period, the analysis tools required to maintain alignment, and mirror motion trending.

CalFUSE corrects the non-guide channels for the mirror motion on orbital timescales using an empirically derived correction. A more detailed discussion is presented in the the CalFUSE pipeline paper (Dixon et al. 2007).

4.3 □ Spectrograph Performance

4.3.1 Spectrograph Resolving Power

The resolving power of FUSE depends largely upon the residual aberrations in the spectrographs, primarily astigmatism, and on the imaging properties of the double-delay line MCP detectors. The detector imaging resolution is best at the center of each segment and degrades somewhat towards either end. In addition, fixed-pattern noise introduced by the MCPs can cause localized degradation of the resolution (see Sections 4.4.2, 4.4.5, 4.4.6, 4.4.7 for details). These effects cause the resolution to vary as a function of wavelength, and with spectrograph aperture. Variations in detector gain over the mission (Section 4.4.2) cause some of the detector contributions to the LSF to vary as well. Finally, the combined effects of target motion and uncertainties in the corrections for grating motion can cause the point source resolving power of *FUSE* data to vary between observations and from exposure to exposure within a given observation.. CalFUSE applies corrections for these effects to each photon in the event list for TTAG data. However, histogram data cannot be corrected on photon event timescales and the 1×8 binning factor of histograms gives rise to a ~5-10% reduction in resolving power compared to time-tagged data. As a result, TTAG data will almost always exhibit a higher resolving power than HIST data obtained with the same aperture. The exception is long exposures of targets that are too faint to correct properly for image motion. Careful analysis of time-tagged exposures with good S/N may yield spectra with somewhat higher resolving power than the nominal value of $R=20,000$.

The LSF has been characterized by modeling ISM absorption along the line of sight for two representative targets: K1-16 and RX J2117+3412. The former was observed in TTAG mode for all three apertures, and the latter was observed in HIST mode through

LWRS and MDRS. The data were processed with CalFUSE v.3.2.3. Spectra from each exposure were coaligned on narrow absorption features and combined. All usable exposures obtained during the FUSE mission were included. The column density and b-value were determined from profile fitting for OI, NI, FeII, and each H₂ J-level observed; the b-value was also determined for HI. (Profile fits were performed using the program OWENS, developed by Martin Lemoine and the French FUSE Team.) Fits were performed independently for each channel and for the combined data set to check internal consistency, and a curve of growth analysis was performed for the H₂ J=1 lines in the K1-16 spectra and for the H₂ J=3 lines in the RX J2117+3412 spectra. The width of a Gaussian instrumental LSF was fit as a free parameter for each absorption line.

The results are shown in Figure 4-5 for K1-16, and in Figure 4-6 for RX J2117+3412. The LSF measurements exhibit greater scatter for K1-16 than for RX J2117+3412, because the signal to noise is lower for the K1-16 data sets, and because the IS absorption lines are generally weaker for the K1-16 line of sight. The K1-16 TTAG data do tend to show somewhat better spectral resolution than the RX J2117+3412 HIST data, but the differences are not dramatic. The K1-16 data do show a systematic trend of better resolution in HIRS than in MDRS, and in MDRS compared to LWRS. The results for the SiC channels clearly show better resolution at the midpoint of each detector segment, as expected, but the behavior in the LiF channels appears to be dominated by other effects. The LWRS LiF 2B data in particular show a dramatic decrease in resolution near the midpoint of the detector segment. The results shown here are generally consistent with the LWRS TTAG LSF measurements of Williger et al. (2005); the exception is LiF2B, for which they obtained 25 km/s at the midpoint of the segment, rising to 35 km/s at either end.

A detailed characterization of the LSF obtained from analyses of lines of sight towards white dwarfs within the Local Bubble was presented by Kruk et al. (2002) and Wood et al. (2002). They found that a two-component Gaussian LSF was needed to fit the HI Lyman series lines. A two-component LSF was not pursued in the present analysis, partly for simplicity in presenting the results, and in part because the more complex ISM and photospheric absorption spectra made it difficult to isolate the effects of two LSF components. The width of the narrow components obtained by Kruk et al (2002) and Wood et al. (2002) were similar and correspond to ~20 km/s, consistent with the single-Gaussian results presented here.

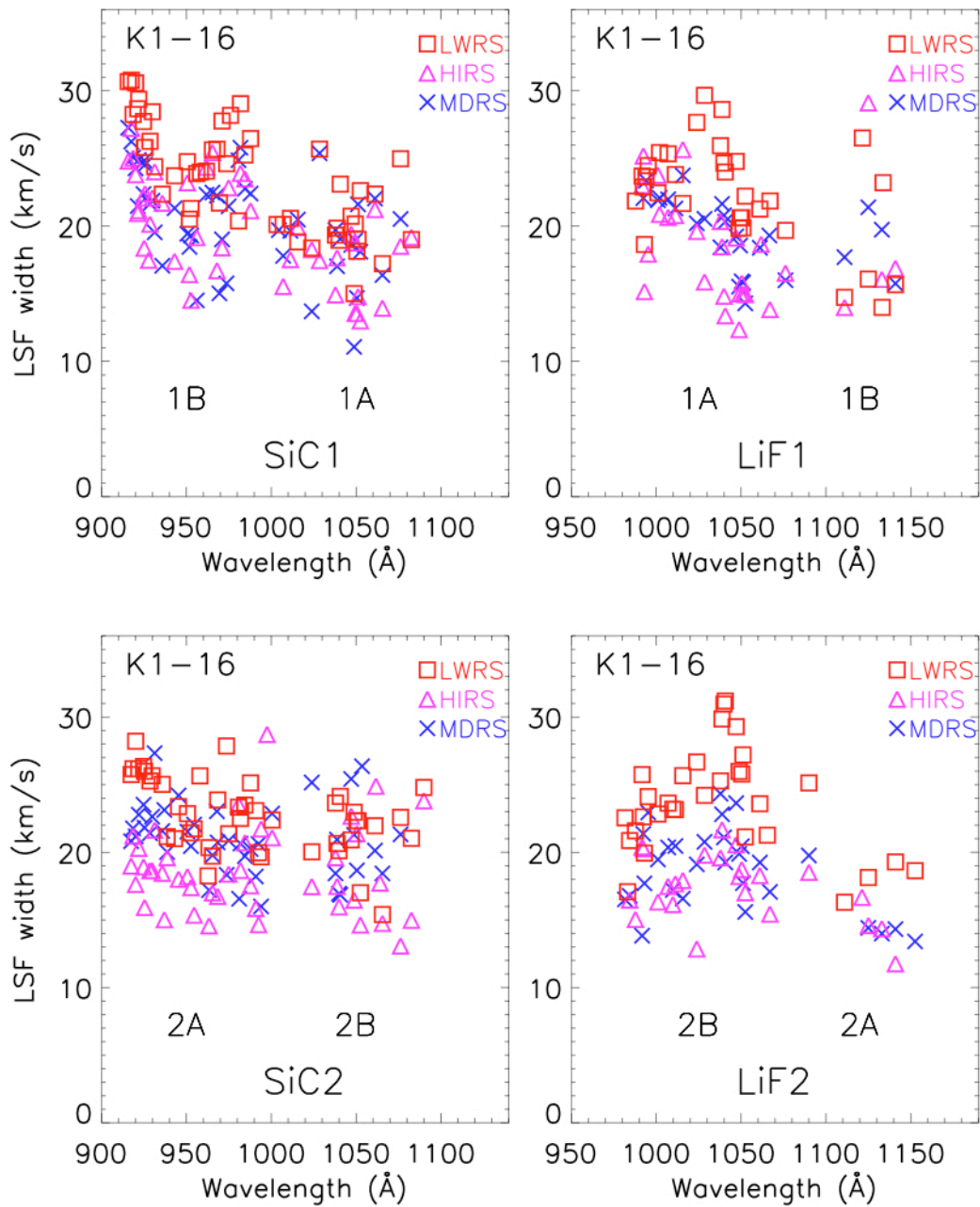


Figure 4-5 Spectral resolution measured from ISM absorption lines along the line of sight to K1-16.

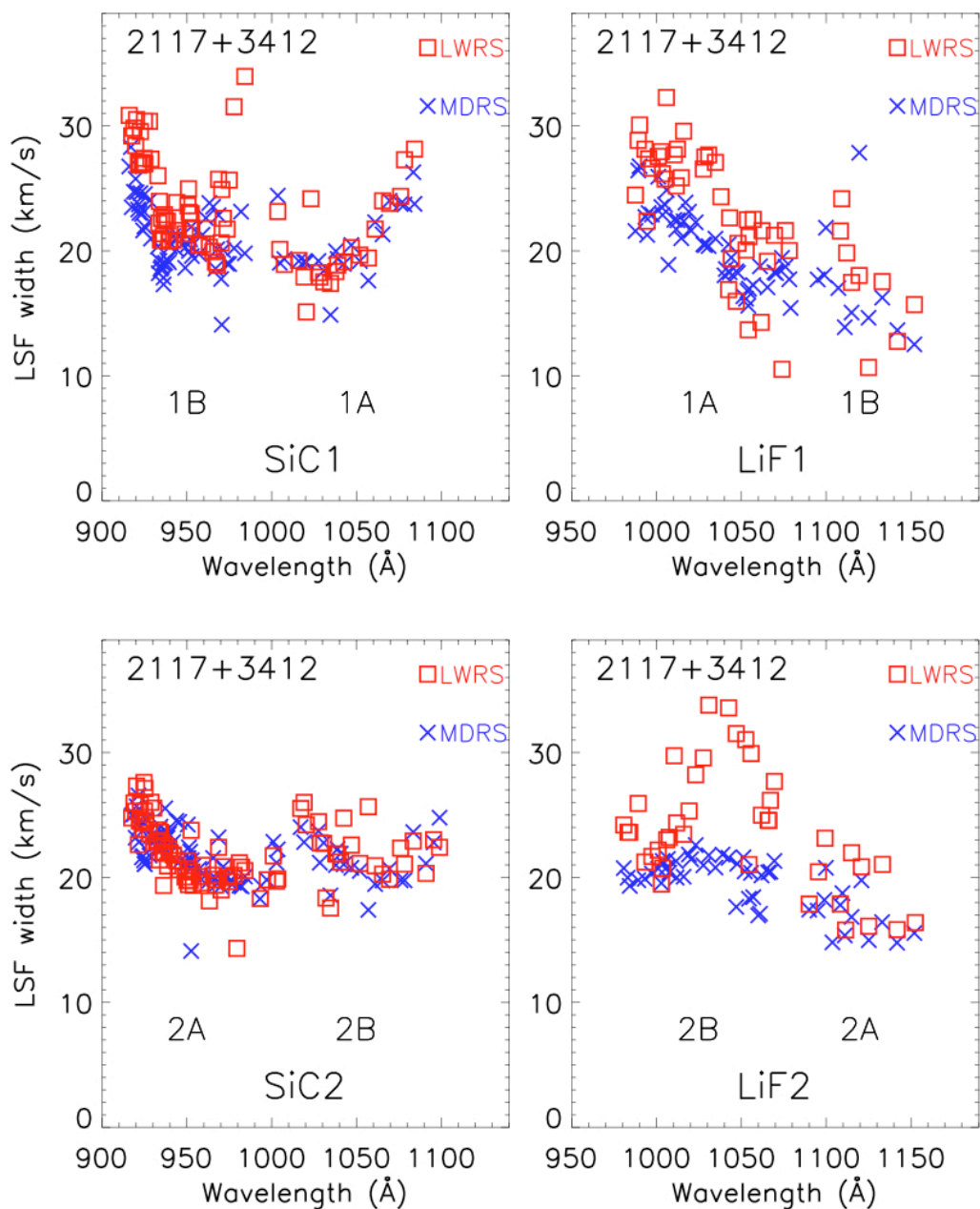


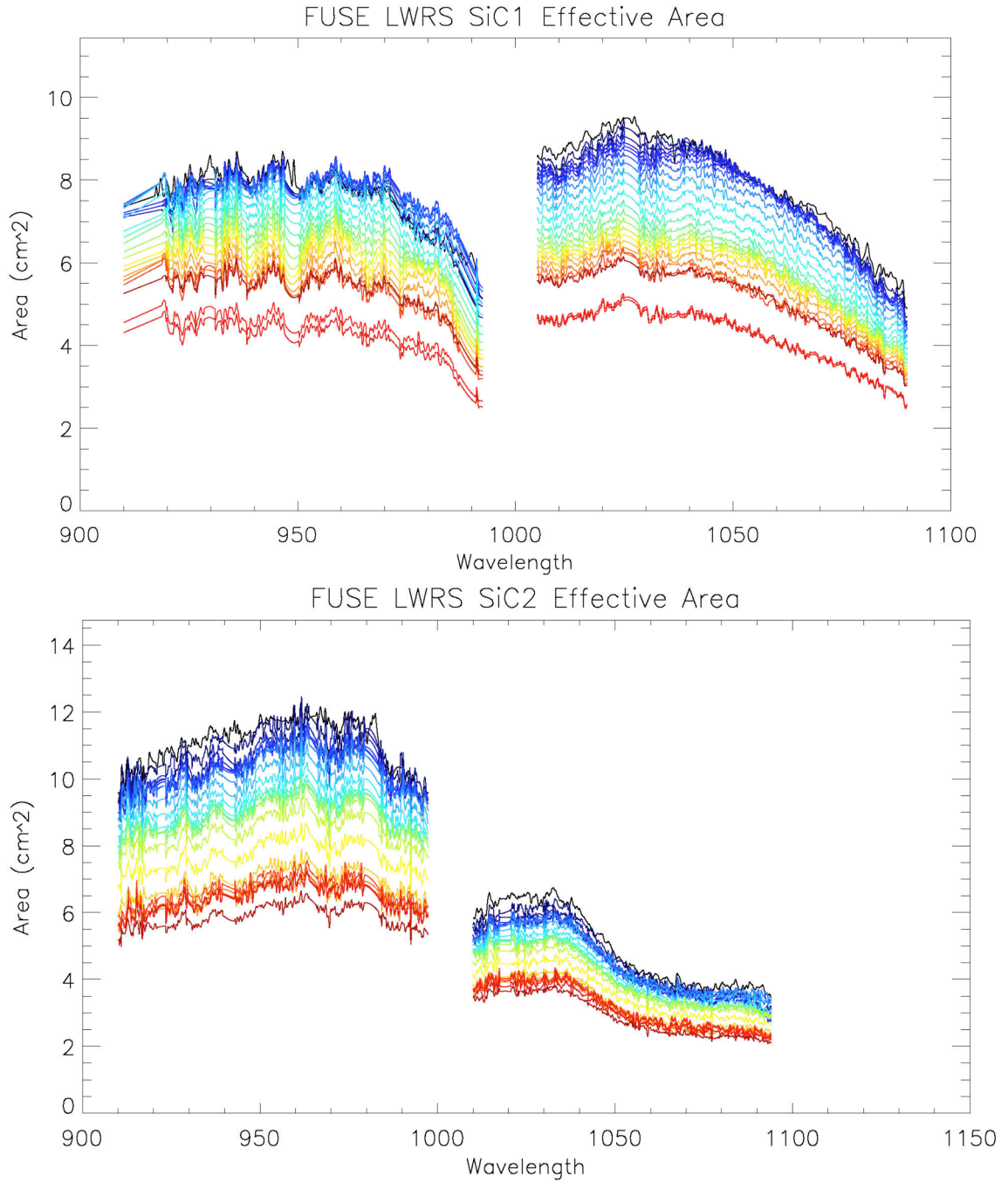
Figure 4-6 Spectral resolution measured from ISM absorption lines along the line of sight to RX J2117+3412.

4.3.2 Scattered Light

There are two sources of scattered light that can add to the background and thus compromise the instrument sensitivity: in-band scatter from the grating itself and stray light scattered from surfaces such as the internal spectrograph baffles or other illuminated surfaces within the spectrograph cavity. The in-band, grating scatter was measured at the component level to be $1 \times 10^{-5} / \text{\AA}$. This is a typical scattering number for holographically-ruled gratings. In-flight measurements give a consistent result: the integrated scattered light present in heavily-saturated absorption line profiles was typically less than 1% of the continuum flux. This contribution to the background scales with the intensity of the source. Stray light differs in that it scales roughly with the overall airglow line intensity. It is expected to be caused by geocoronal Lyman α emission entering the spectrograph cavity through either the FPA apertures or the vent. The distribution of the stray light is not uniform, but shows considerable structure across the detector. *The FUSE Data Handbook (2009) Section 7.2* provides quantitative results of the on-orbit scattered light measurements.

4.3.3 Effective Area

The combination of SiC and LiF coatings on the primary mirrors and gratings was designed to maximize the effective area across the whole FUV band. Because the reflectivity of LiF drops rapidly below approximately 1020 \AA , the effective area changed significantly with wavelength. In addition, the gaps between the detector segments created narrow bands (typically 10 \AA wide) where the total effective area dropped by as much as a factor of 2. Plots of the effective areas as a function of wavelength and time for the individual detector segments are shown in Figure 4-7. The definition of the flux calibration and the evolution of the sensitivity over time is discussed in further detail in *Section 7.5 of The FUSE Data Handbook (2009)*.



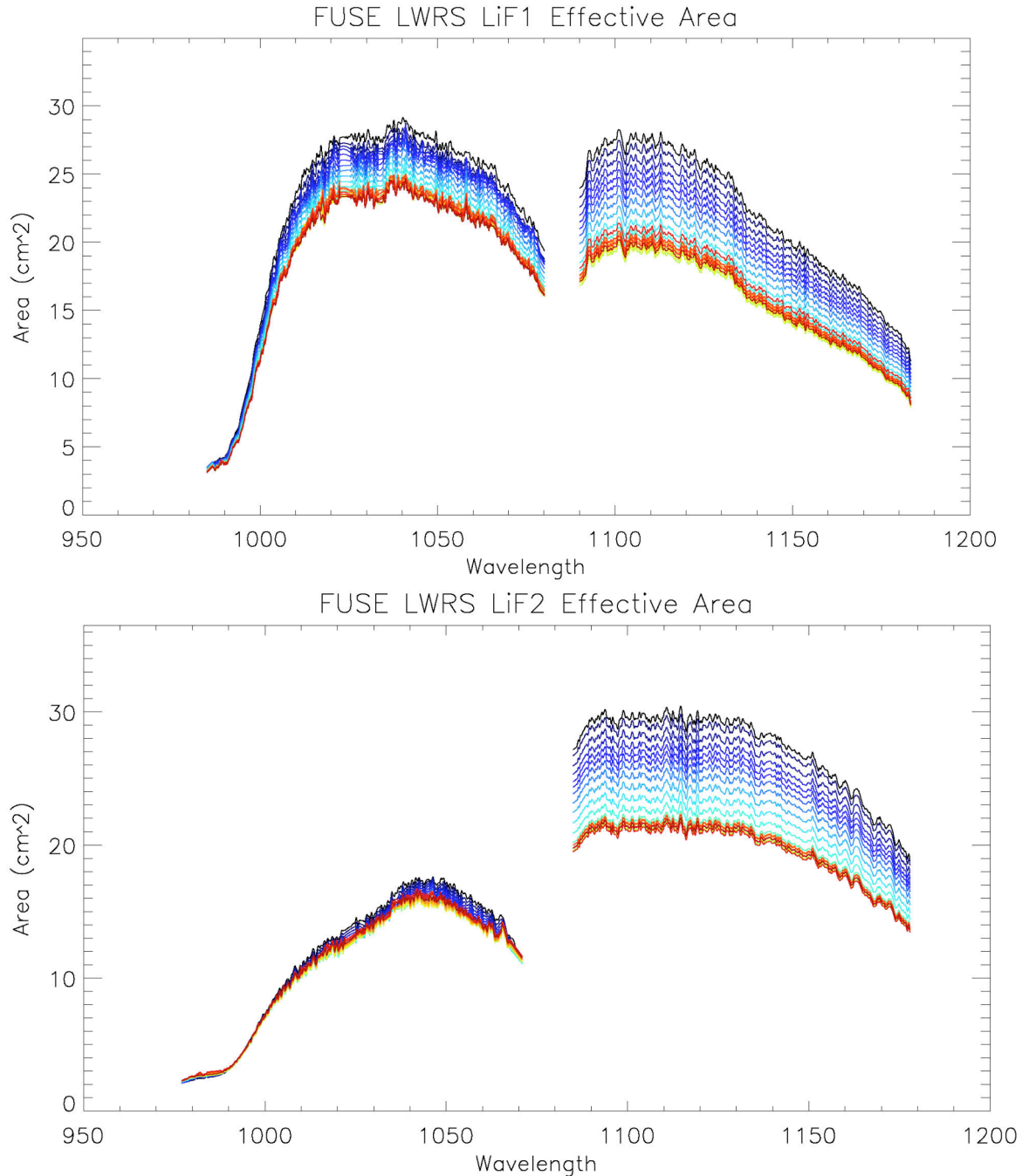


Figure 4-7 The in-flight derived effective area as a function of wavelength for each detector segment. Each curve for a given detector segment represents a snapshot of the effective area as a function of time and wavelength. The family of curves for each segment represents the degradation of the effective area over the eight year on-orbit lifetime of the mission.

4.3.4 “The Worms”

The spectra of point-source targets often show a depression in the flux that spanned as much as 50 Å of the spectrum (Figure ref). In two-dimensional detector images, these depressions appear as narrow stripes roughly parallel to the dispersion axis. Investigations early in the mission showed that they were highly variable as a function of time, even within a single orbit. These stripes, known as “worms” because of the way they moved during an orbit, can attenuate portions of the LWRS LiF1B spectra by as much as 50%.

Worms were due to an unfortunate interaction between the focus of the spectrograph and the detector’s quantum efficiency grid. The optical design of the spectrograph resulted in astigmatic images with separate sagittal and tangential focal surfaces. The detector was placed at a location to obtain good spectral resolution, close to the sagittal focus. At some wavelengths, the tangential focus fell close to the location of the QE grid, which was about 6 mm in front of the detector surface, and was curved to match the MCP curvature. The grid had 25.3 μm wires spaced ~1 mm apart, to give an open area of 95%. Since the vertical extent of the spot was much less than the spacing between grid wires near the tangential focus, the effect of the grid wires could be significantly magnified; close to 50% of the light could be blocked by a single horizontal grid wire if it fell in the right place.

The complex relationship between the position and alignment of the grid wires, the exact locations of the optical elements, the illumination of the telescope, the pointing stability, the wavelength of the light, and the optical design meant that only detailed models can predict exactly what effects the grid wires were expected to produce on the spectra. Raytrace predictions made during the mission were qualitatively similar to what was observed.

In flight, the effects of the grid wire shadows were found to be extremely sensitive to the exact position of the spectrum on the detector. Therefore, as the spectra moved slightly on the detector due to grating motion, the shape and location of a worm could change dramatically. Small displacements of the source image along the vertical axis of the spectrograph slits could cause similar variations in the effects of a worm. Because every object had minor coordinate errors, they would be placed at different positions along the slits and thus might be affected differently. Multiple observations of a given star might also have varying worm effects, either resulting from use of different guide stars or from differing thermal environments at different seasons. The nature of these variations depends in part on the orientation of the grid wires. When the wires are oriented parallel to the dispersion plane, the degree of obstruction is sensitive to the position of the spectrum primarily at wavelengths in the vicinity of the astigmatic correction points. For these portions of the detectors, the effects of the worms are fairly stable and the flux calibration is reliable. In some places, however, the grid wires are oriented at a modest angle with respect to the dispersion plane. In these cases, vertical motion of the spectral image causes the region being obscured to shift in wavelength space. The flux calibration is not reliable in these cases, but

fortunately the regions affected in this manner are limited. The worm in LWRS LiF1B was by far the strongest and most variable; for this channel, the flux calibration was defined so as to represent the sensitivity in the absence of the worm, so that it would always appear as absorption. The calibration for the other channels was not adjusted in this manner, but rather was defined from the mean of numerous observations of standard stars. The case that may have the greatest effect on users is the worm in LWRS SiC1B, which cuts diagonally across the spectrum at wavelengths longward of about 975 Å. At times when the worm is shifted towards the midplane of the spectrum, the reported flux will be too low, but at times when the worm is shifted further away from the midplane, the reported flux will be too high. The flux calibration issues are discussed in more detail in Section 7.5 of the [FUSE Data Handbook](#). (The spectra of GD 659 in this section of the Data Handbook illustrate the case where the SiC1B LWRS worm has shifted off of the spectrum, causing a spuriously-high flux to be reported for the last few angstroms of the spectrum.)

While the worm was most prominently seen in LWRS LiF1B spectra (with flux loss on the order of 50% at some wavelengths), it was present at a lower level in most FUSE channels and apertures. Although no systematic investigation of all worms could be made, a large number of calibration exposures were examined in order to understand the effects of the worm on the data. Table 4.3-1 summarizes the results of this investigation.

Table 4.3-1 Summary of worms identified in the FUSE data.

Spectrum	LWRS	MDRS	HIRS
LiF1A	> 1050 Å - horizontal	< 1000 Å – horizontal (weak)	< 1000 Å, >1050 Å – horizontal (weak)
SiC1A	1050 - 1080 Å - horizontal	<1080 Å – horizontal (moderate)	< 1065 Å - horizontal
LiF1B	~1155 Å – diagonal (strong)	Full - horizontal (2 weak stripes)	>1165 Å - diagonal (plus 2 weak horizontal worms)
SiC1B	>975 Å- diagonal (moderate)	> 960 Å – diagonal (moderate)	> 970 Å - diagonal
LiF2A	<1115 Å - diagonal	1100-1130 Å - Diagonal (moderate)	1100-1130 Å - diagonal (moderate)
SiC2A	-	-	-
LiF2B	-	< 990 Å - horizontal (weak)	<1010 Å, > 1050 Å - horizontal (weak)
SiC2B	-	-	< 1035 Å - horizontal (weak)

Since the position and strength of the worm in a given segment varied so strongly as a function of position of the target in the aperture, there is no simple, automated way to correct for it. As a result, worm effects remain uncorrected in the calibrated FUSE

data, and thus observers should examine their data carefully in order to assess the effects of the worm.

It should be noted that for a uniformly filled slit the horizontal grid wires blocked a much smaller fraction of the light, so the effect is much smaller. Thus no worms were seen in the airglow lines.

The following figures provide examples of the worms in each combination of channel, aperture, and detector segment. The images have been corrected for detector distortions and variations in detector Y-scale.

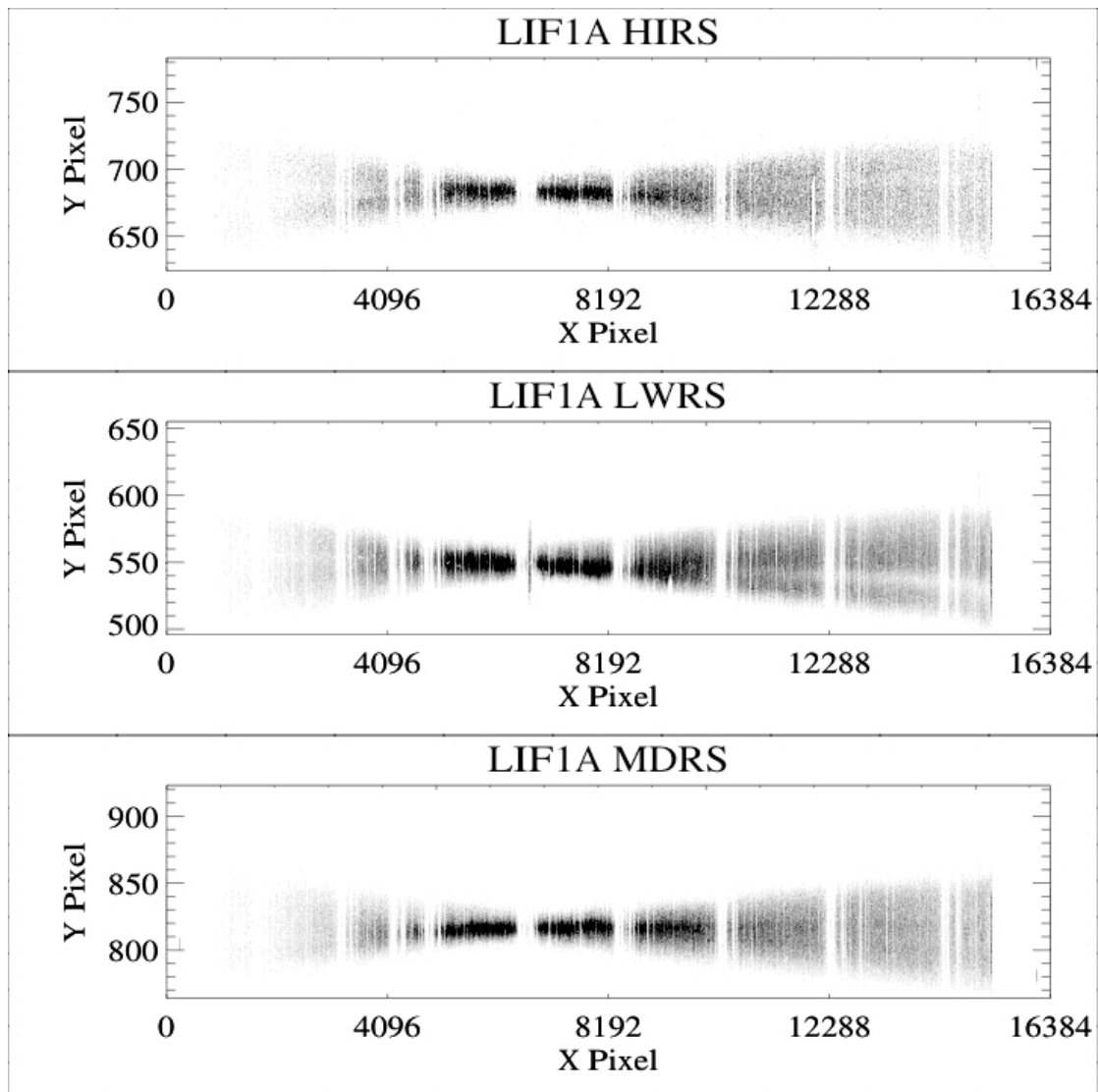


Figure 4-8 Spectral images of a stellar spectrum obtained in the LiF1 channel for each aperture are plotted for detector segment 1A. The grey scale is inverted, so that regions of high count rate appear dark. The narrow vertical lines are absorption features arising from interstellar gas, primarily H_2 . The broad

horizontal stripes are shadows cast by the detector QE grid wires, aka the “worms”.

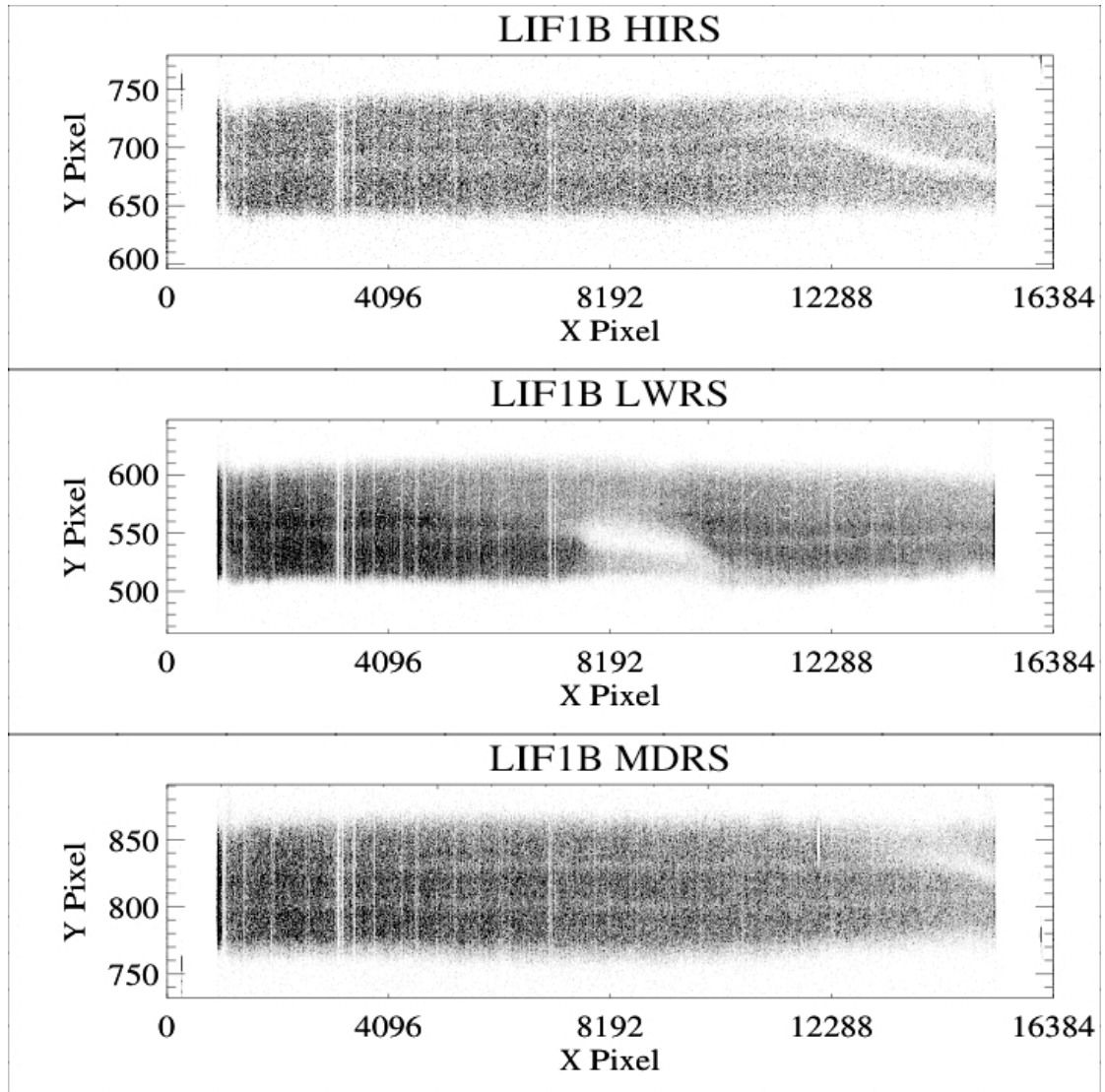


Figure 4-9 As in Figure 4-8 above, but for LiF1B. Note the strong worm feature in the LWRS spectral image.

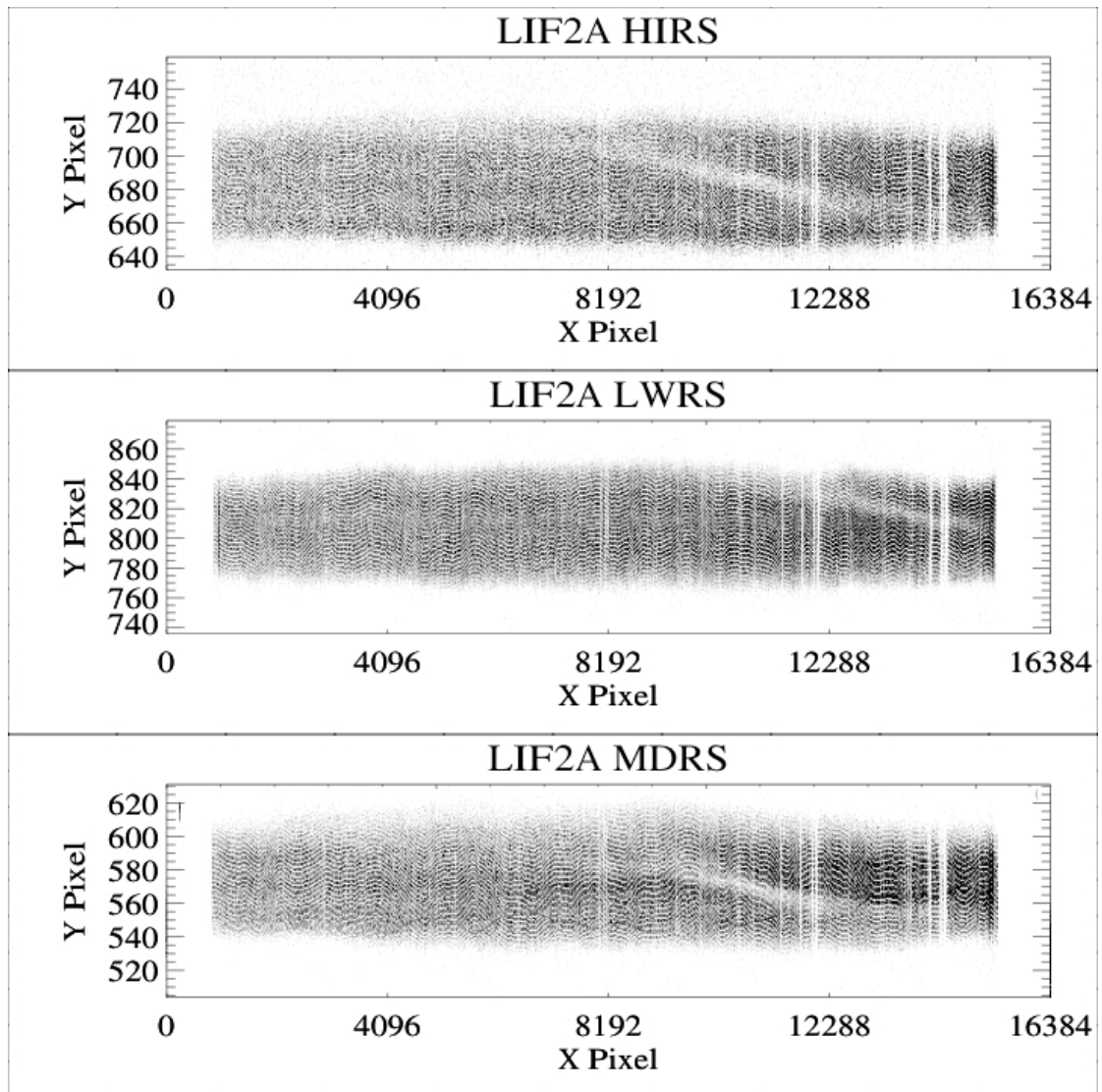


Figure 4-10 As in Figure 4-8 above, but for LiF2A. In addition to the worm features present in each spectral image, faint single-pixel-wide horizontal moiré patterns are evident, which are an artifact of the distortion corrections.

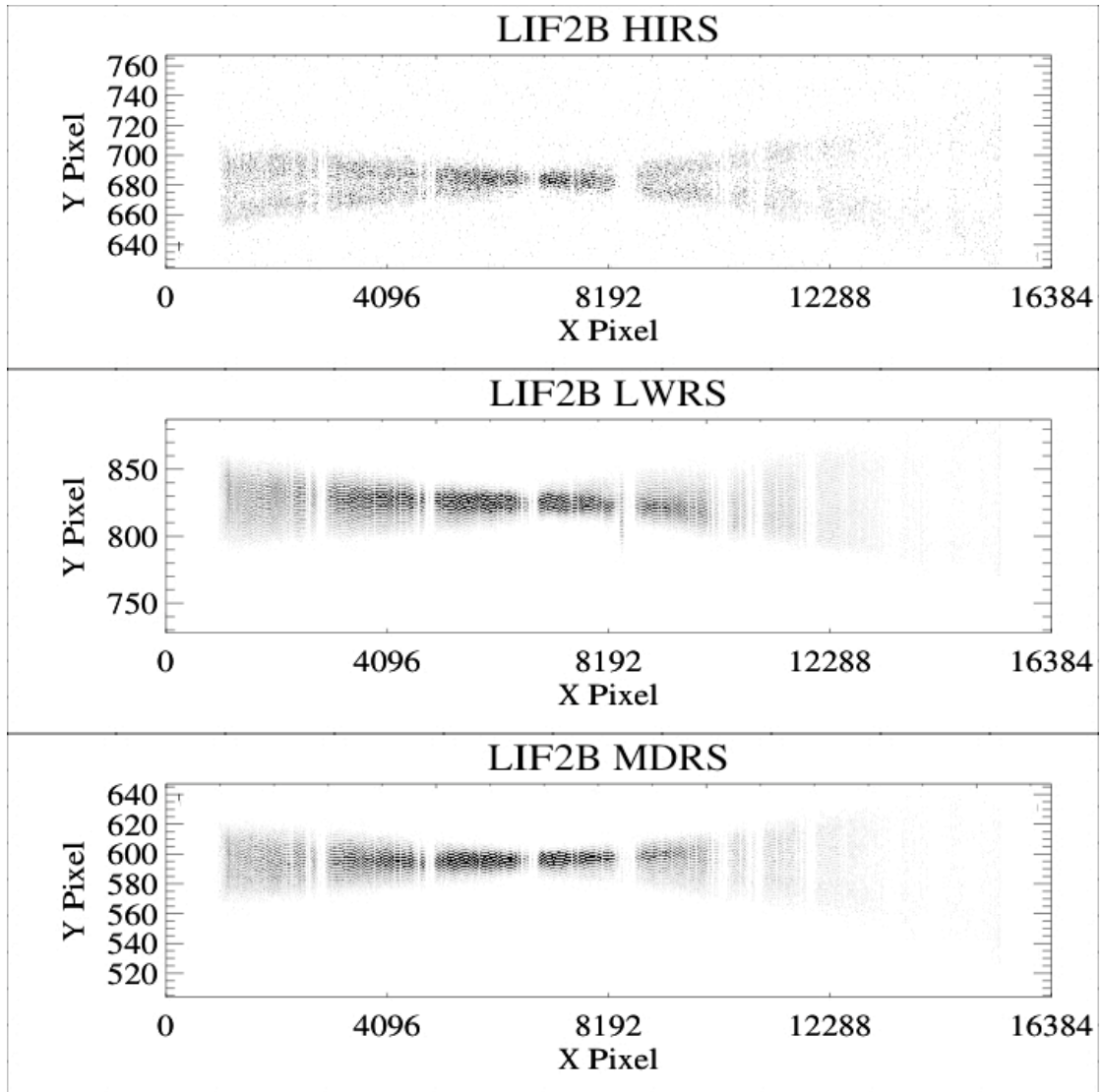


Figure 4-11 As in Figure 4-8 above, but for LiF2B.

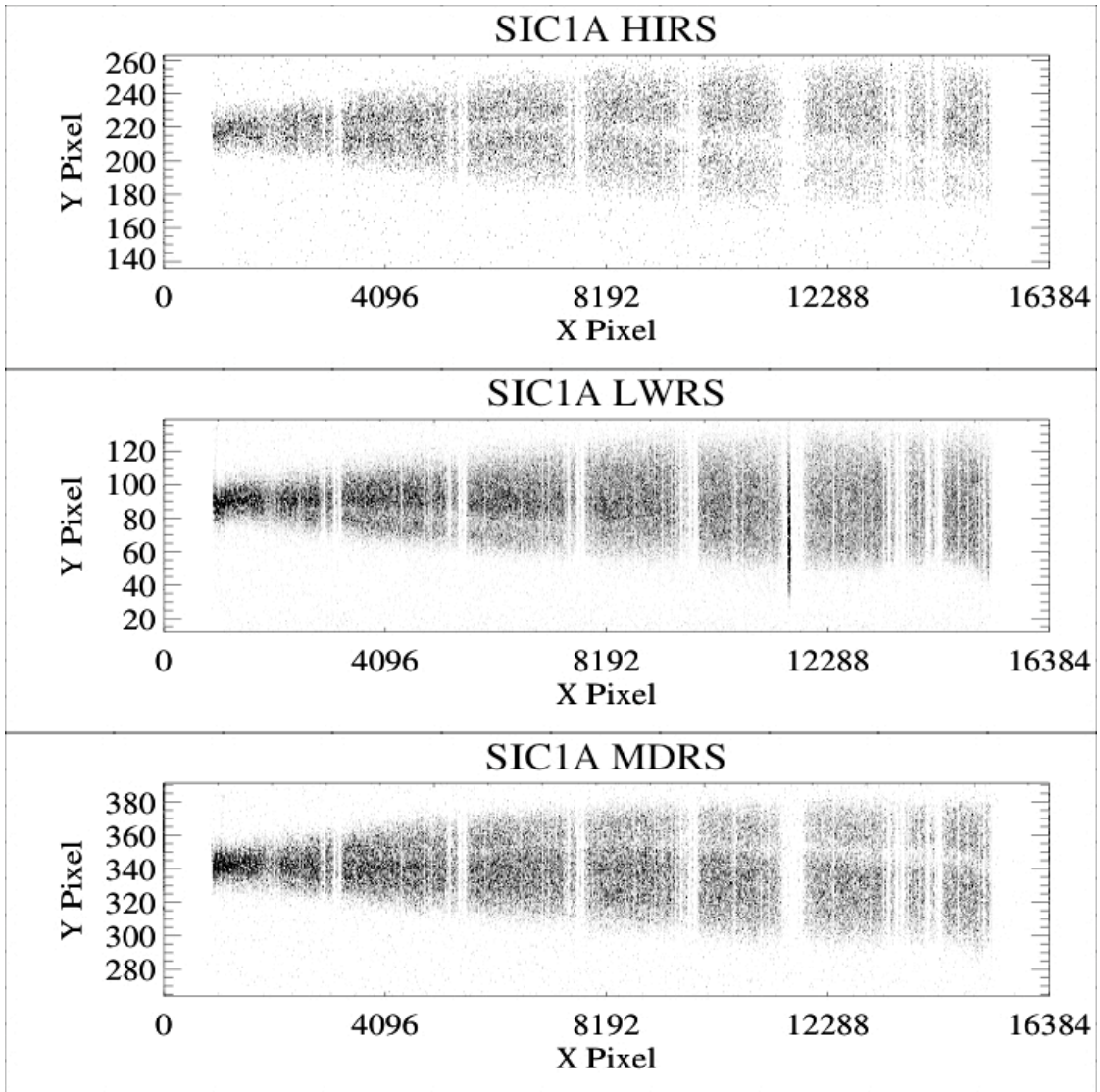


Figure 4-12 As in Figure 4-8 above, but for SiC1A.

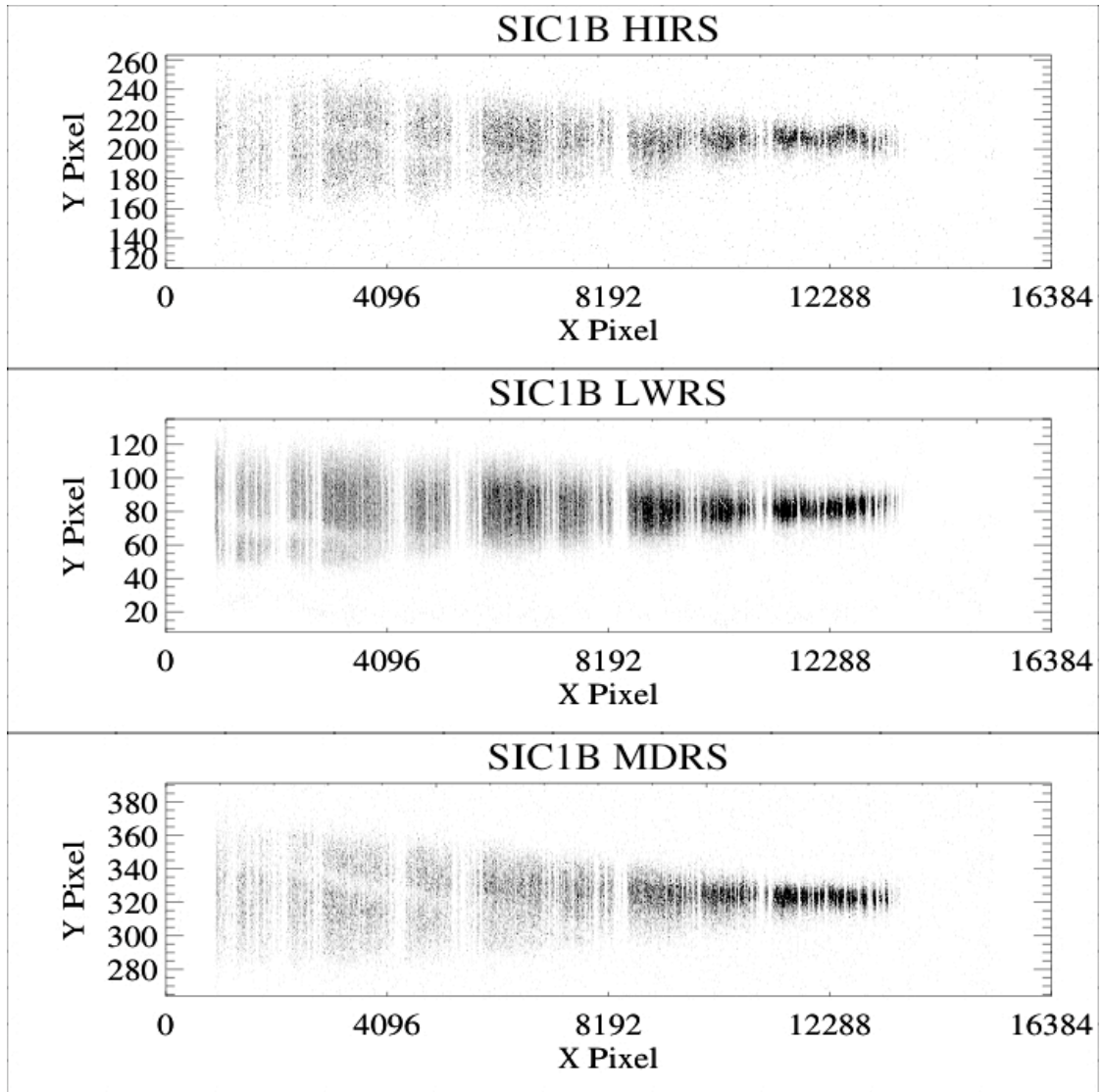


Figure 4-13 As in Figure 4-8 above, but for SiC1B.

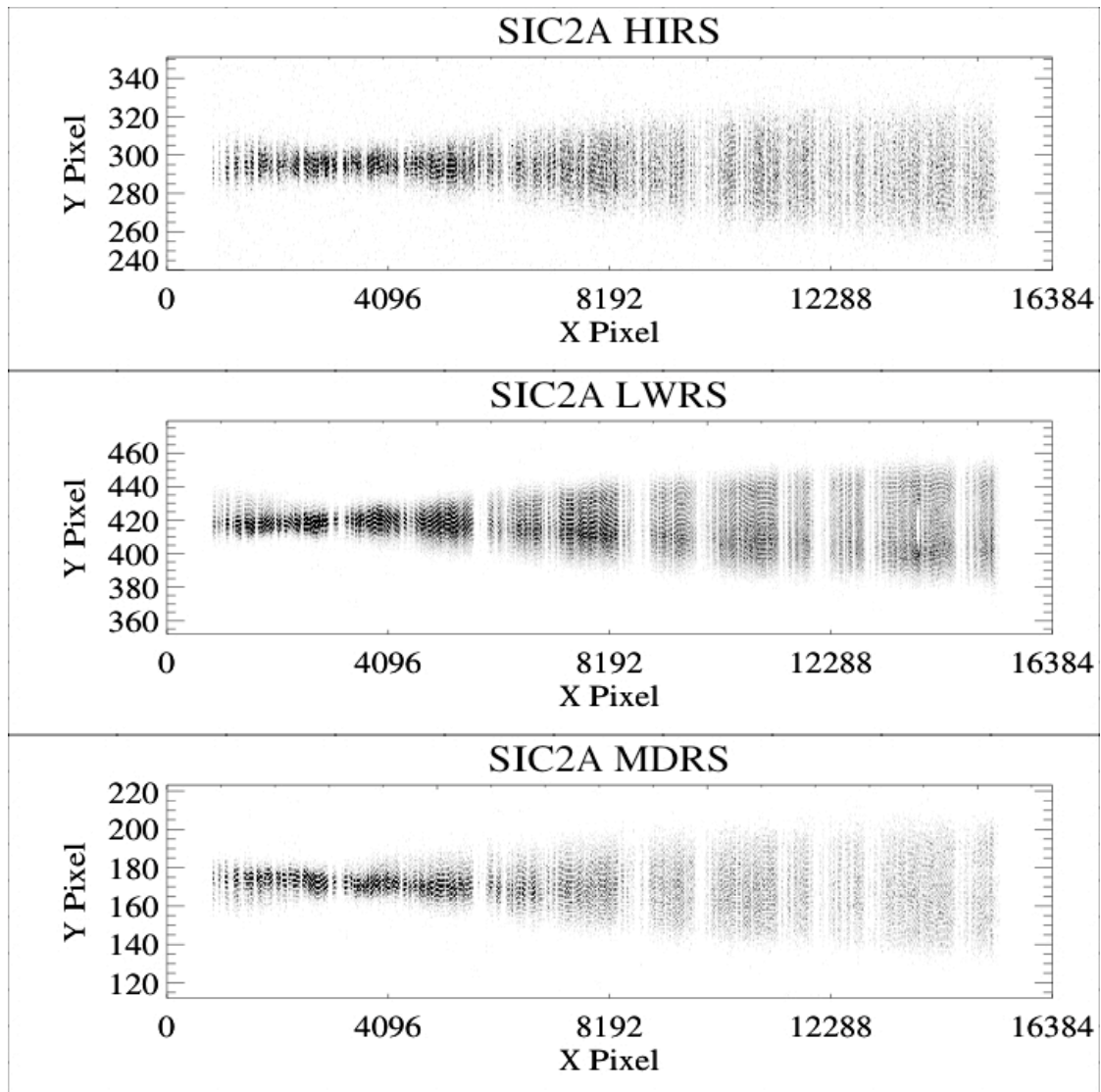


Figure 4-14 As in Figure 4-8, but for SiC2A. Worms are weak or not present.

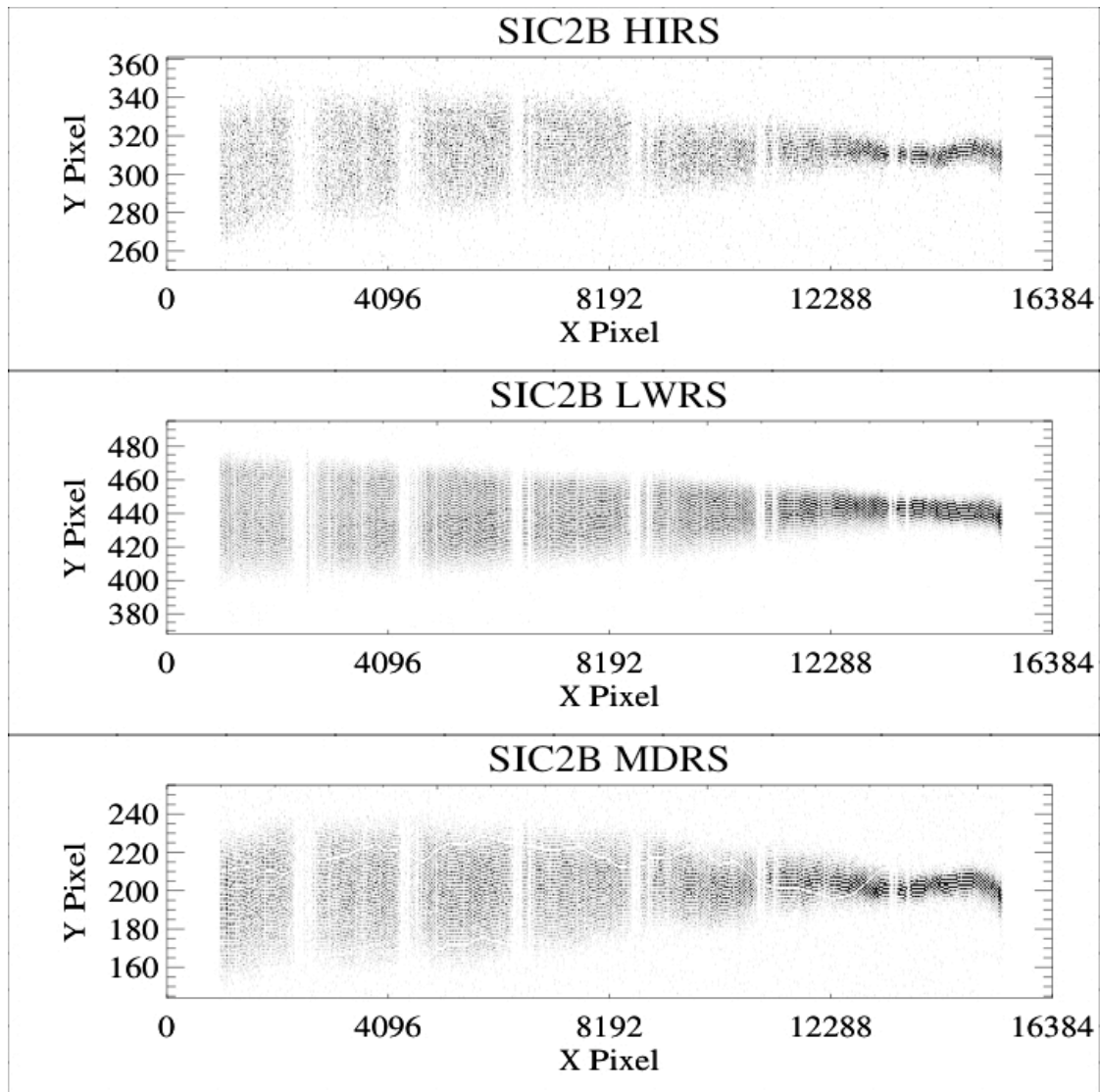


Figure 4-15 As in Figure 4-8, but for SiC2B. Worms are weak or not present. The very thin white jagged line running across the MDRS spectral image is an artifact from the distortion correction; some residual vertical distortion is present in the HIRS and MDRS spectral images beyond pixel 12000.

4.3.5 Spectral Motion

When the first exposures were taken during IOC, it was discovered that the Lyman- β airglow lines were moving on the detector in both the dispersion and cross-dispersion directions as a function of time. Since the airglow emission fills the apertures, these motions are distinct from those due to the motions of the mirrors. Instead, they are due to small rotations of the gratings. The exact cause of these rotations was unclear, but they were apparently due to changing thermal conditions at the top of the instrument where the gratings were mounted.

A detailed examination of the motion of the airglow lines as a function of various orbital parameters showed that both the amplitude and direction of the motion were periodic. The motion was also found to be a strong function of orbital phase and was repeatable for a given beta angle, pole angle, and position angle. These motions shifted both the target and airglow spectra by as much as 15 pixels (peak-to-peak) in both the X and Y axes on the detectors. Figure 4-16 shows an example of the variation for a single observation.

An empirical model of the motion was derived by examining the shifts in many exposures. Early in the mission, the limited data available led to a simplified model that was a function of beta angle and declination, and consisted of a sum of sinusoids with periods of one orbit for each beta and declination range. As more observations were made at different pointings, this model was refined, and the final model was based on all the data collected from the beginning of the mission through early September 2006. Periodic motions on orbital, diurnal, and precessional (~60 day) timescales were identified in this data, although the final calibration file (grat005.fit) uses only constant and orbital terms due to limitations in sky coverage in the data. The motions and offsets were modeled as a function of beta angle, pole angle, and position angle.

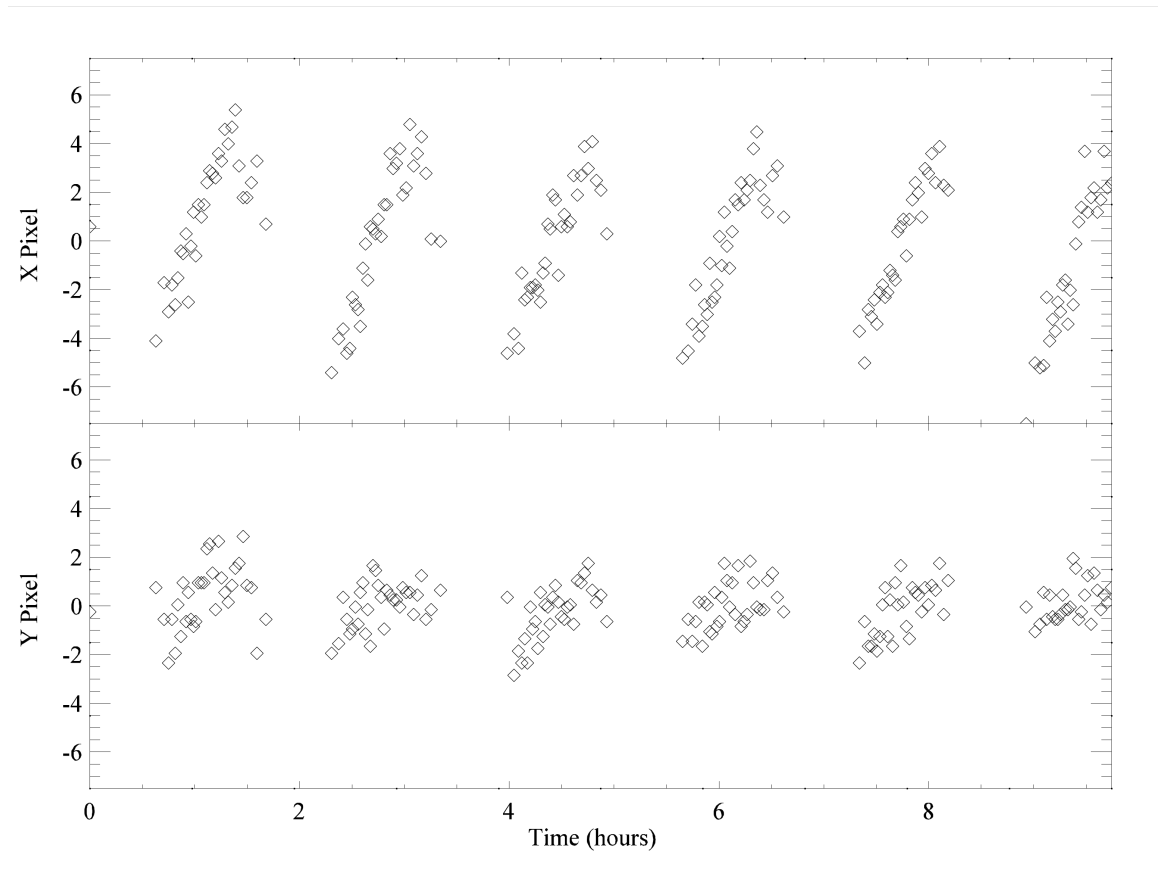


Figure 4-16 For a single observation (S505702) the position of the LiF1A Lyman- β airglow line on the detector is shown as a function of time. Each point represents the average position on the detector of ~ 500 consecutive airglow photons.

As shown in Figure 4-17, the grating motion correction can make a significant improvement in the measured resolving power. In the example shown, each point represents the average position of approximately 500 consecutive Lyman- β photons in the LiF1A spectrum. Without a correction, a peak-to-peak variation of more than 11 pixels is seen. By applying the grating motion correction, this variation is reduced by more than a factor of two.

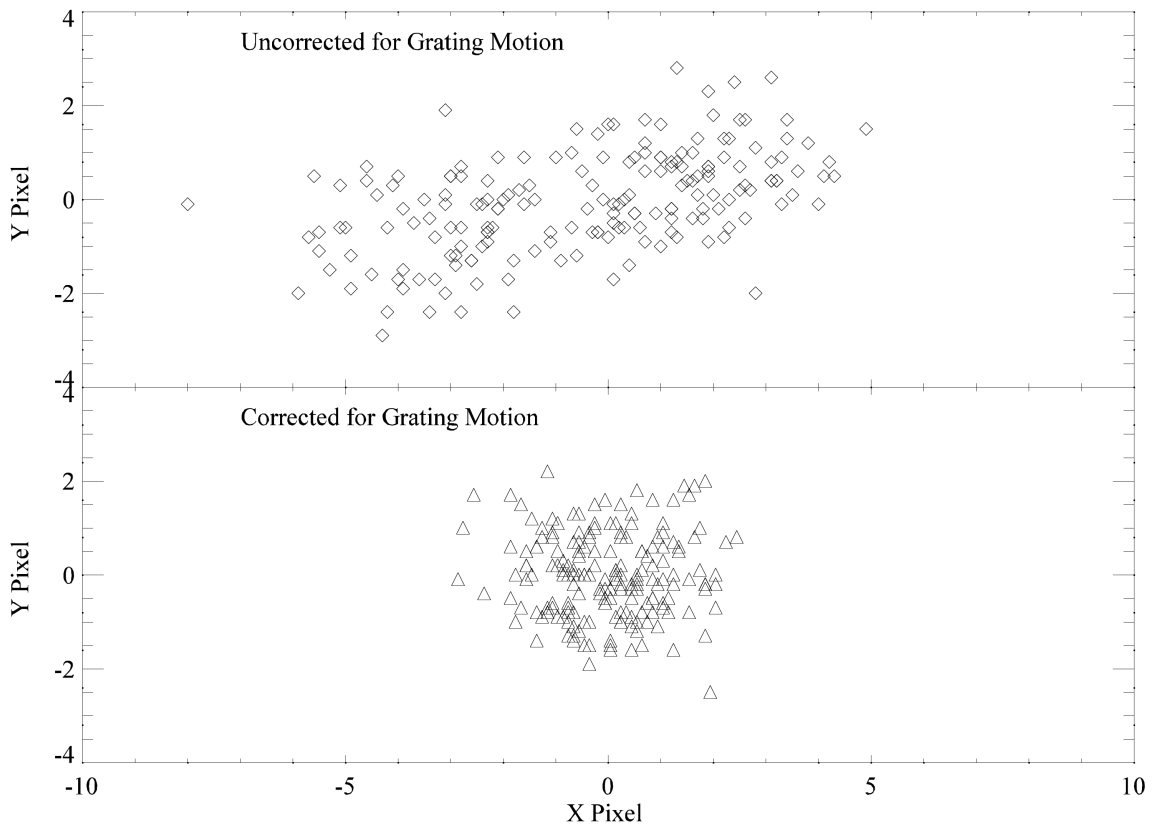


Figure 4-17 The same data as in Figure 4-16 is shown both before (top panel) and after (bottom panel) the CalFUSE grating motion correction is applied.

4.4 Detector On-orbit Performance

4.4.1 High Voltage Operations

The high voltage on each of the four segments was independently controlled. At any given time, there were four important high voltage levels on the MCPs for each segment:

1. HV OFF – When the HV power supply was switched off, no high voltage was present.
2. HV ON – Once the HV power supply was switched on, the high voltage immediately increased to -2500 volts (digital value 0).
3. SAA – Before launch, the SAA level was chosen for each segment so that the gain of the MCPs was low enough that the dark rate was close to zero. When passing through the South Atlantic Anomaly, or SAA (a region of enhanced particle density), the voltage was lowered to this level to minimize charge depletion in the MCPs. Despite this low gain, count rates of up to ~13,500 counts per second were observed in orbit (on segment 2B – the other segments

were substantially less) when passing through the SAA. The SAA high voltage levels were not changed during the mission: segment 2B was set at 60 digital units and the other three segments were set to 70. Early in the mission, the SAA level was used only when the satellite passed through the SAA. Later the SAA level was used whenever science exposures or peak-ups were not being performed (section 6.3.2.2).

4. FULL – This was the normal operating voltage, which was modified throughout the mission in order to optimize performance. The values that were used are shown in Table 4.4-1. The general trend was to increase the voltage with time in order to compensate for gain sag and minimize detector walk (see section 4.4.2.1). However, as the voltage was raised, the number of crackles sometimes increased (section 6.3.5). As a result, the segment 2A FULL voltage value was kept at a lower than optimal level starting in 2002.

During normal operations the high voltage cycled between SAA and FULL. A single command would bring the high voltage from SAA to FULL in a few seconds. These transitions were scheduled to occur autonomously before science exposures began. Similarly, normal FULL to SAA transitions occurred outside of exposures.

Ramping up the high voltage all the way from HV ON to FULL, however, was done manually from the ground, since autonomous ramp ups were never implemented. Such ramp-ups were necessary, for example, whenever a single-event upset (SEU) (Section 6.3.4) caused a detector reboot, or whenever a high-voltage transient, or “crackle”, caused an autonomous shut down of the high voltage (Section 6.3.5). Ramping up the high voltage from the ground was a multi-step process that could take a large fraction of a day; it was typically done using one of two methods. Both included a relatively quick (typically 1 to 3 orbit) ramp to SAA level. The standard ‘slow’ ramp procedure then increased the voltage in six steps up to FULL, usually over 6 orbits. Alternatively, the ‘fast’ ramp up instead involved a wait of about six hours at SAA level followed by a single command to increase the voltage to FULL. Early in the mission, the slow ramp-up was used exclusively. Eventually, the fast procedure was used in order to speed up the process, but the slow one was still used if a fast ramp up resulted in a crackle shutdown.

Because ramp-ups were done asynchronously with the observing schedule, a significant number of observations were taken with one or more segments at HV levels other than those described above. The minimum and maximum high voltage levels during an exposure are recorded in the $DETnHVmL$ and $DETnHVmH$ header keywords in the data files ($n=1,2$; $m=A,B$), and the HV_FLAG notes if the voltage is not at its nominal level. CalFUSE uses these values to determine whether or not the voltages were within the appropriate ranges and if the data should be excluded. High voltage as a function of time during each exposure is also available in the $hskpf.fit$ and Intermediate Data Files (IDFs). By default, CalFUSE excludes data taken when the high voltage is too low.

4.4.2 Gain Sag and HV Adjustments

4.4.2.1 Gain Sag and Detector “Walk” Effects

Among the most serious detector effects impacting the science data was that of gain sag. As a MCP is exposed to incident radiation, its ability to replenish the electrons in the MCP glass is diminished. This effect, though nonlinear and dependent on many variables, worsens with increased exposure. The result is that the secondary emission coefficient drops as a function of time, so that an incident photon will no longer produce as many electrons at the back end of the MCP stack as it once would have. This decrease in charge is known as gain sag.

A small amount of gain sag may produce no noticeable effects on the data; the first effect is simply a shift in the pulse height distribution to lower values. A significant drop in gain could cause the events with the lowest pulse height to be lost below the threshold of the sensing electronics. But before that occurs, there may be other effects. The DDL detectors on FUSE were affected by detector walk, which is a dependence of the calculated X position of the photon on the pulse height of each event. Since the calculation of the incident position relies on a timing measurement between two pulses, the shapes and sizes of the pulses can affect this determination in an important way.

One solution to the problem of gain sag is to increase the high voltage across the MCPs, which boosts the secondary emission coefficient. If the gain sag is not uniform across the detector, however, raising the voltage may not completely solve the problem, since some less-sagged regions may end up with a gain that is too high for proper processing (Section 4.4.6.3).

In addition, higher voltage levels may cause other problems. In the case of FUSE, the incidence of crackles sometimes increased as the high voltage was raised. In particular, the voltage on segment 2A could not be raised above 149 digital units without the number of crackle shutdowns increasing dramatically (section 4.4.1).

Since the FUSE instrument had no shutter, light from the sky fell on the detectors whenever the baffle doors were open. Thus, whenever the high voltage was above SAA level and a science target was placed in the aperture before an exposure began, or was left in the aperture after an exposure ended, charge was extracted from the MCPs even though the data were not being recorded. Similarly, nearly continuous exposure to geocoronal airglow lines from the earth resulted in a large amount of exposure at the locations a few bright emission lines, such as Lyman- β , N I, and O I (Section 9.2)

During detector fabrication, measurements were made of the reported locations of an array of regularly spaced pinholes as the voltage (and thus the detector gain and pulse height) was varied. These tests were then considered when decisions about the final operating voltages and electronics adjustments were made. However, no detailed map of walk as a function of position was made before launch.

After final assembly of the detector these tests could not be repeated, but the plasma and QE grids, which cast strong shadows on the detectors when illuminated by the stim lamps, proved useful for measuring the effects of walk (Section 6.3.1.3). Figure 4-18 shows a small portion of the sum of more than 80 stim lamp exposures at several different pulse height values. It is obvious that the shadows of the grid wires shift in the X direction as a function of pulse height. The amount of the shift varies with both pulse height and X position on the detector.

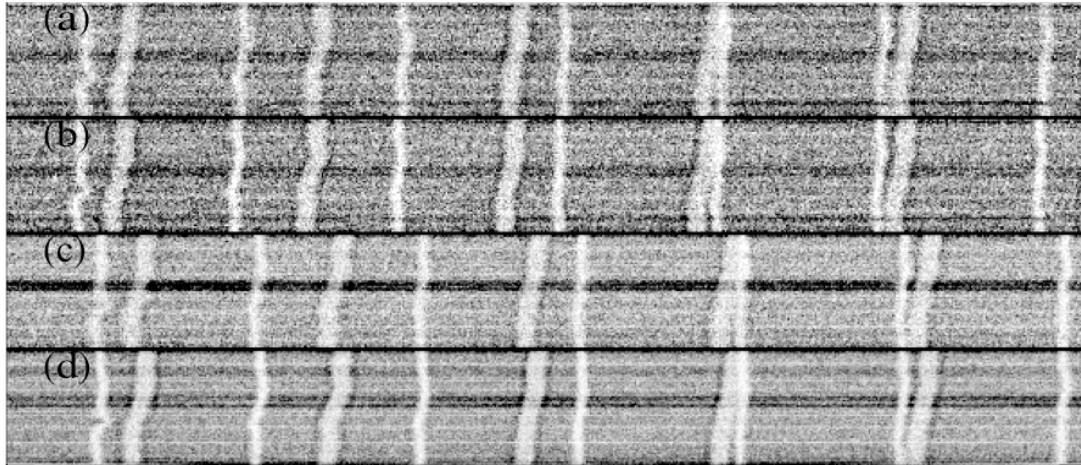


Figure 4-18 A binned portion of detector segment 1B illuminated in flight by the stim lamp, using just photons with pulse heights of (a) 2, (b) 4, (c) 8, and (d) 16. The x range covers 1200 pixels, while y includes the full height of the detector. The shadows of the two sets of grid wires are clearly seen in the vertical direction, but because of the binning in y, the horizontal wires are difficult to see. It is obvious from comparing these figures that there is an apparent shift in the position of the grid wires as a function of pulse height. The dark horizontal bands show regions where a large amount of exposure has caused gain variations.

Multiple techniques were used to minimize the effects of walk on the FUSE data. These included (1) adding an ‘occultation manager’ which lowered the high voltage to SAA level whenever it wasn’t needed (section 6.3.2.2); (2) regularly raising the high voltage, when possible, to increase the overall gain of each segment (section 4.4.2.2); (3) adding a walk correction module to CalFUSE to shift events in x based on their pulse height; and (4) raising the lower level pulse height threshold in CalFUSE to exclude the events which were most seriously affected by walk (TTAG only).

The result of applying the CalFUSE walk correction to a spectrum is shown in Figure 4-19, where the same data is plotted with and without the walk correction. It is clear from the figure that the wavelength scale differs between the two. In addition, it can be seen that the walk-corrected spectrum has a higher resolving power. For TTAG data, the position of each photon can be adjusted based on its pulse height. For HIST data, however, where the pulse height data is not available, shifts are made based on the average pulse height found at each location on the detector based on TTAG

exposures taken at nearby times. Thus the HIST correction was only an average correction and although it helped correct the wavelength scale, it did not do a good job of improving the resolving power. Localized regions of gain-sag caused by airglow emission also resulted in spurious spectral features in HIST data, particularly at the wavelengths of the NI and OI airglow lines falling on LiF2a; see Figure 7.7 in Section 7.3.4 of [The FUSE Data Handbook](#) for an example, and Section 9 of this document for a listing of airglow lines.

The FUSE design did not permit the spectra from a particular aperture to be moved to different locations on the detector, so the same spectral features always fell on the same part of the detector. However, the astigmatic height of the images did spread the damage out in the cross-dispersion direction. In addition, the grating motion (section 4.3.5), moved the spectra in both directions, which lessened the effect. Despite this, however, significant gain variations were seen due to variations in exposure as a function of position on the detector. Figure 4-20 shows an example of the effect on segment 1A. The mean pulse height is shown as a function of X pixel at two Y locations on the detector (where the LiF LWRS spectrum falls and in a background region) near the beginning of the mission (exposure M9980101001) and near the end (M9986701001). The gain of the background region increased substantially during the mission due to the increases in high voltage. The LiF1 LWRS region shows significant gain sag near the end despite the increased voltage. The gain sag at Lyman- β ($x \sim 7000$) is especially obvious, and the gain varies significantly depending on the amount of exposure seen during the mission.

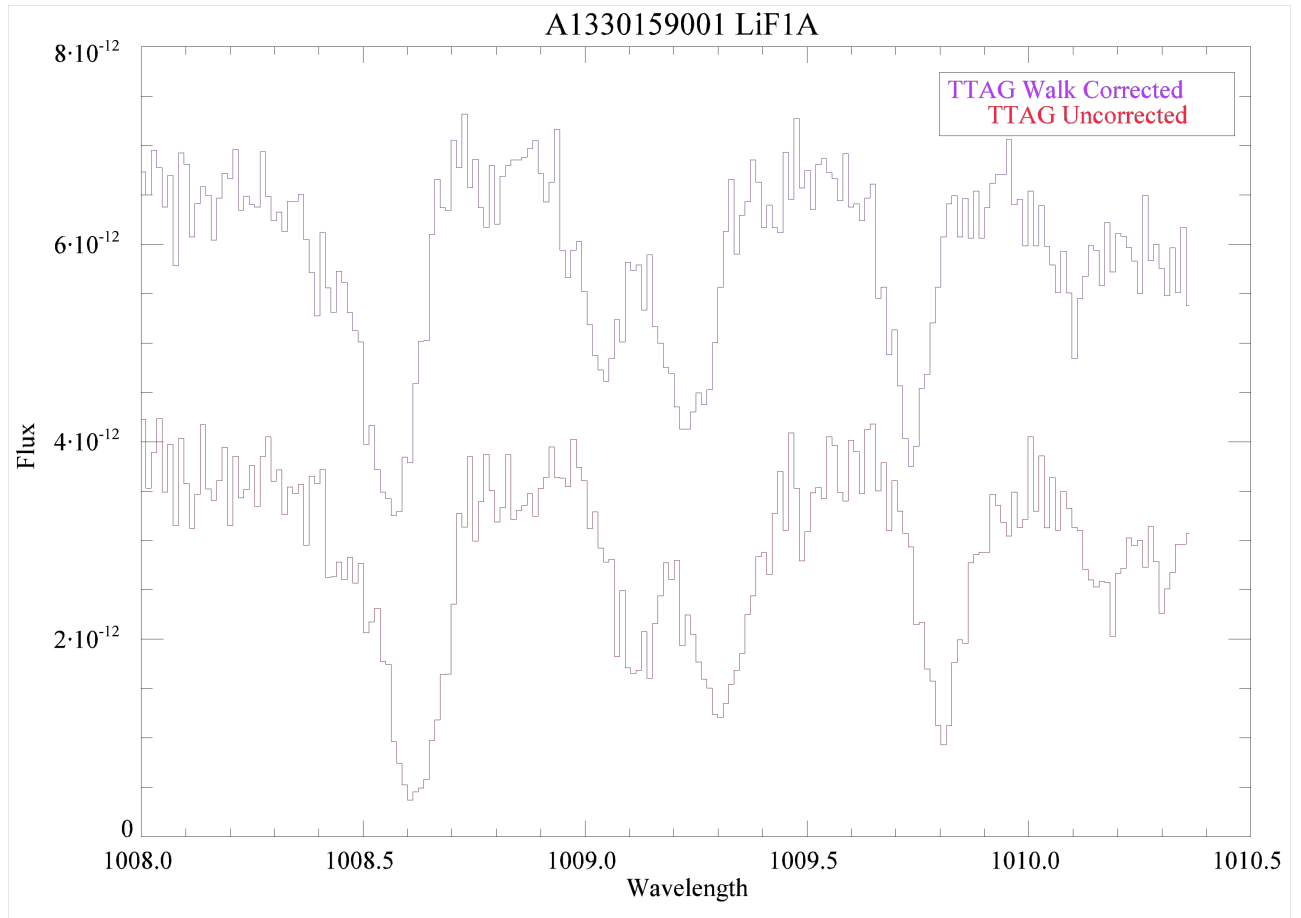


Figure 4-19 A small portion of a LiF spectrum on segment 1A, showing the same data both with and without the CalFUSE walk correction applied; the two spectra are offset in the y axis by an arbitrary amount so that the differences can be seen more easily. The walk-corrected spectrum has a different wavelength scale and shows higher resolving power.

In addition to monitoring of the gain and walk effects using the stim lamp exposures, gain sag as a function of time was tracked by constructing a cumulative exposure map for each detector segment. The number of events at each pulse height value incident on each pixel location was monitored so that trends could be identified early (Sahnou, 2004). These total count map and total gain map files were originally constructed as part of the pipeline flow, but they were later separated to allow more flexibility for reprocessing.

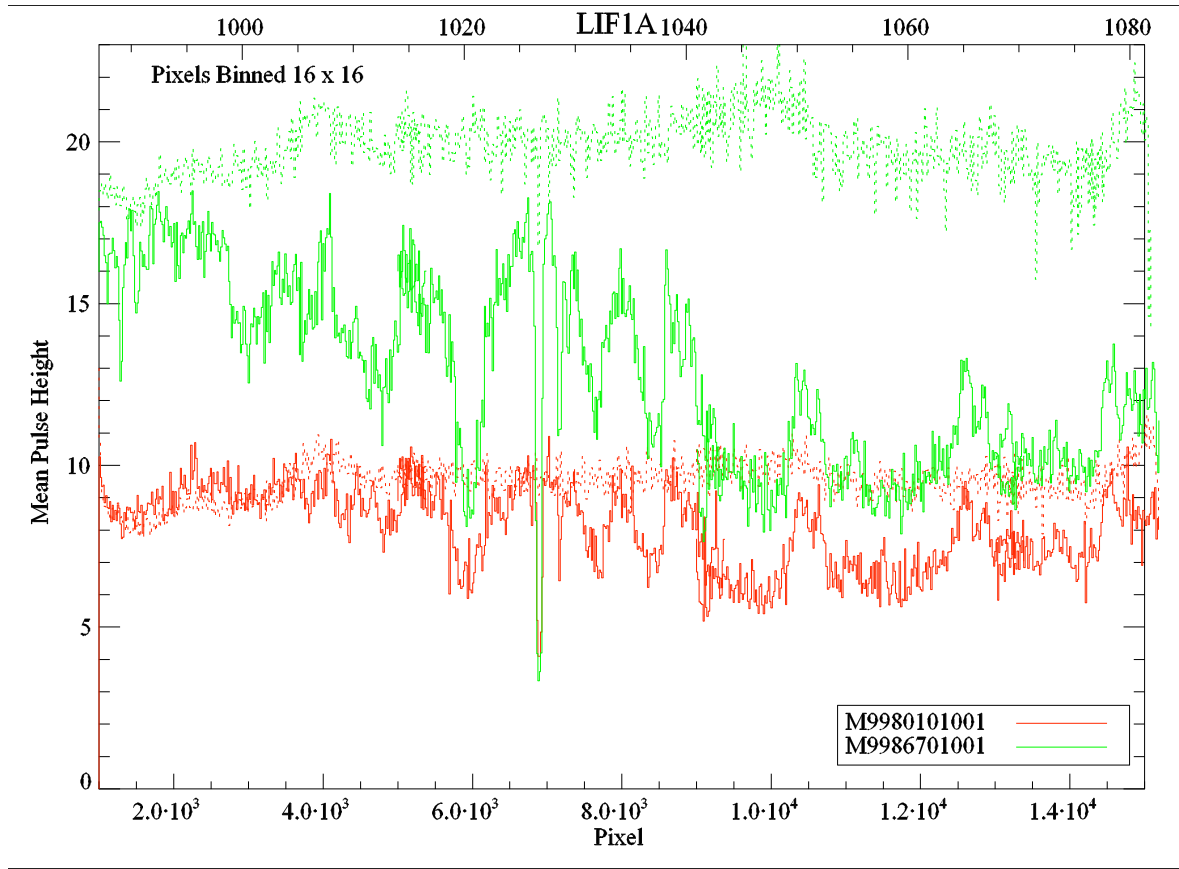


Figure 4-20 Gain sag on detector segment 1A. The mean pulse height is shown as a function of X pixel at two Y locations on the detector: at the LiF LWRS spectrum location (solid line) and in a background region (dotted line) in September 2000 (exposure M9980101001 - red) and in September 2007 (M9986701001 - green). The gain of the background region increased substantially during the mission due to the increases in high voltage, and remained fairly flat as a function of x pixel. The LiF1 LWRS region, however, shows a significant gain variation as a function of x. The gain sag at Lyman- β ($x \sim 7000$) is especially obvious.

4.4.2.2 High Voltage Adjustments

The high voltage was adjusted several times during the mission in order to increase the gain of the MCPs and decrease the effects of detector . The times of these adjustments are listed in Table 4.4-1. Adjustments were required less frequently after the implementation of the occultation manager (Section 6.3.2.2), since the amount of exposure due to airglow lines decreased significantly at that time.

Before each permanent change in voltage, TTAG stim lamp exposures (M998 exposures) were taken at increased voltage levels. The pulse height from those datasets was used to measure the gain as a function of voltage for each aperture on each segment, and thus determine the new voltage levels. The goal with each adjustment was to keep the gain of the detector for the LiF LWRS channels high

enough to avoid serious walk effects – to a pulse height value of 10 or higher. Because of the very high exposure at certain locations (primarily the Lyman- β airglow line), it was not possible to return the entire detector to the desired gain level, however. In addition, raising the voltage to too high a level also had disadvantages. Segment 2A was not able to operate reliably above a value of 149 because the incidence of crackles would increase dramatically when the voltage reached that range. As a result the voltage was below its ideal value for most of the mission, and it suffered from significant walk problems. These problems were most severe at locations illuminated by strong airglow lines present when looking down at the bright Earth; see Figure 7.7 in Section 7.3.4 of [The FUSE Data Handbook](#) for an example, and Section 9 of this document for a listing of airglow lines.

Date and Time	Date	FULL Segment Voltage ¹				Reason for change
		1A	1B	2A	2B	
1999:181	6/30/1999	0	0	0	0	Detectors turned on
1999:225:20:23	8/13/1999	129	129	0	0	Detector 1 HV ramp up
1999:238:16:30	8/26/1999	129	129	129	102	Detector 2 HV ramp up
2001:024:23:12	1/24/2001	141	137	137	108	Compensate for gain sag
2001:212:09:41	7/31/2001	147	143	149	113	Compensate for gain sag
2002:050:08:23	2/19/2002	155	151	161	119	Compensate for gain sag
2002:088:01:06	3/29/2002	155	151	134 – 156	119	2A lowered to minimize crackles
2002:104:17:22	4/14/2002	155	151	149	119	Returned 2A to a lower level
2002:342:21:12	12/8/2002	161	157	161	124	Compensate for gain sag
2002:350:12:00	12/16/2002	161	157	134	124	2A lowered to minimize crackles
2003:034:13:00	2/3/2003	161	157	149	124	Returned 2A to a higher value
2003:228:16:35	8/16/2003	164	160	149	126	Compensate for gain sag
2004:202:17:55	7/20/2004	165	162	149	127	Compensate for gain sag
2007:290:20:56	10/17/2007	0	0	0	0	Turned off HV

Table 4.4-1 Default high voltage values used during the mission.

4.4.3 Detector Background

4.4.3.1 Internal Background

The intrinsic background rate of each detector segment was measured on the ground before launch. This background, due mainly to the beta decay of ^{40}K in the MCP glass, was below the prelaunch specification of $0.5 \text{ counts cm}^{-2} \text{ sec}^{-1}$. After launch, an on-orbit background due to cosmic rays and other high-energy particles added to this rate to give a total rate of $0.5 - 1.0 \text{ counts cm}^{-2} \text{ sec}^{-1}$ using the default pulse height thresholds. Other sources of detector background included scattered light in the spectrograph.

¹ Units for voltage are digital values. The value in volts is approximately $2500 + 16.7 \times (\text{digital value})$.

The detector electronics permitted the adjustment of hardware charge thresholds in order to change the detector's sensitivity to background events. These were adjusted appropriately on the ground before launch and were not changed on orbit except during a few IOC and calibration observations.

For TTAG exposures, pulse height thresholding of the data was applied by CalFUSE. Since the large FUSE detectors had a wide variation in modal gain (which changed as a function of time due to gain sag – see section 4.4.2) and there was no provision for position-dependent pulse height thresholds, default values of the upper and lower thresholds were chosen to accept nearly all photons where an adequate walk correction could be made in order to ensure maximum throughput. No CalFUSE thresholding could be applied to HIST data, so those exposures include events at all pulse heights above the hardware thresholds.

Since there was no shutter on the FUSE spectrograph, there was always light falling on the detectors. As a result, it was not possible to obtain any true dark exposures during the mission. At the end of the mission, however, after the baffle doors were closed for the last time, several weeks of “almost-dark” exposures were made. Since the baffle doors (by design) did not close completely, some light still entered the instrument in this configuration. In addition, since the SiC2 door could no longer be closed at that point, that channel was still open to the sky. Approximately 2.8 million seconds of data were collected; about 35% of that time was at night. The night time dark rate on Detector was $\sim 3.2 \times 10^{-7}$ counts/sec/pixel, or ~ 0.5 counts $\text{cm}^{-2} \text{sec}^{-1}$ with variations of $\sim 20\%$ due to orbital position. Day time rate were less than 10% higher. Structure is visible in the summed data, but even with these long exposure times there was not enough data to create a true dark count map.

The background model used by CalFUSE consists of a spatially-uniform intrinsic dark count, along with separate, spatially-varying day and night components due to scattered light - see Dixon et al. (2007) and [section 7.8 of the FUSE Data Handbook](#). Although different background templates were constructed for different times (and thus different gain regimes), correcting the background is still subject to error since the gain sag changes differently in the spectral and background regions of the detector.

Several other factors that affected the detector background are described in the following sections. No CalFUSE corrections were made for these effects.

4.4.3.2 South Atlantic Anomaly

One of the largest contributors to the detector background was proximity to the South Atlantic Anomaly. An SAA model was chosen before launch based on calculations done at Goddard Space Flight Center, and the detector high voltage was dropped to SAA level and exposures were stopped whenever the satellite was inside this SAA contour. Several SAA mapping tests were run in the summer of 2003 in order to more accurately determine the count rate on the FUSE detectors as a function of latitude

and longitude in the region of the orbit near the SAA, and a permanent change to the model was made on 17 September 2003; the boundaries of this region were shown in Figure 6-11. This model was still only approximate, however, since the size, shape, and position of the SAA varies with time. As a result, a uniform elevated background rate due to proximity to the SAA was a regular occurrence.

For maximum scheduling efficiency, the contour chosen allowed count rates of up to several hundred counts per second across the entire detector, since a uniform count rate at this level has a minimal effect on the data, and CalFUSE processing allowed users to exclude arbitrary time intervals in TTAG exposures where the background was most likely to have had an effect on the signal-to-noise ratio.

4.4.3.3 Event Bursts

Almost immediately after the high voltage was turned on for Detector 1, unexplained intermittent bursts of counts were seen on the detectors. These ‘event bursts’ had count rates of up to 20,000 per second, and could be as short as a few seconds or as long as many minutes. Although they initially were seen only at local noon and had a well-defined spatial distribution across the detector, they were later found to occur throughout orbital morning, and the spatial distributions on the detector were found to vary; they occurred on all four segments, and were seen throughout the entire mission.

The source of the event bursts was never identified. Attempts were made to correlate the time of bursts with satellite orientation, solar activity, pressure in the spectrograph cavity, and other parameters, but no definitive correlations were ever made as to their origin. There were obvious patterns, however:

- (1) They were most likely to occur during orbital morning, and particularly when the instrument was pointed towards the bright earth.
- (2) Multiple segments and detectors were often “bursty” at the same time.
- (3) The time between successive bursts was very often about 6000 seconds, or one orbital period. A series of bursts would often continue throughout an observation, then stop suddenly when the slew to a new target occurred.
- (4) There was often a high-frequency component of the count rate during a burst. In the cases where there enough counts to measure this period accurately, it was found to be about ten seconds. (Figure 4-21).
- (5) When the baffle doors were closed to take detector dark count measurements at the end of the mission (Section 4.4.3), no bursts were observed.

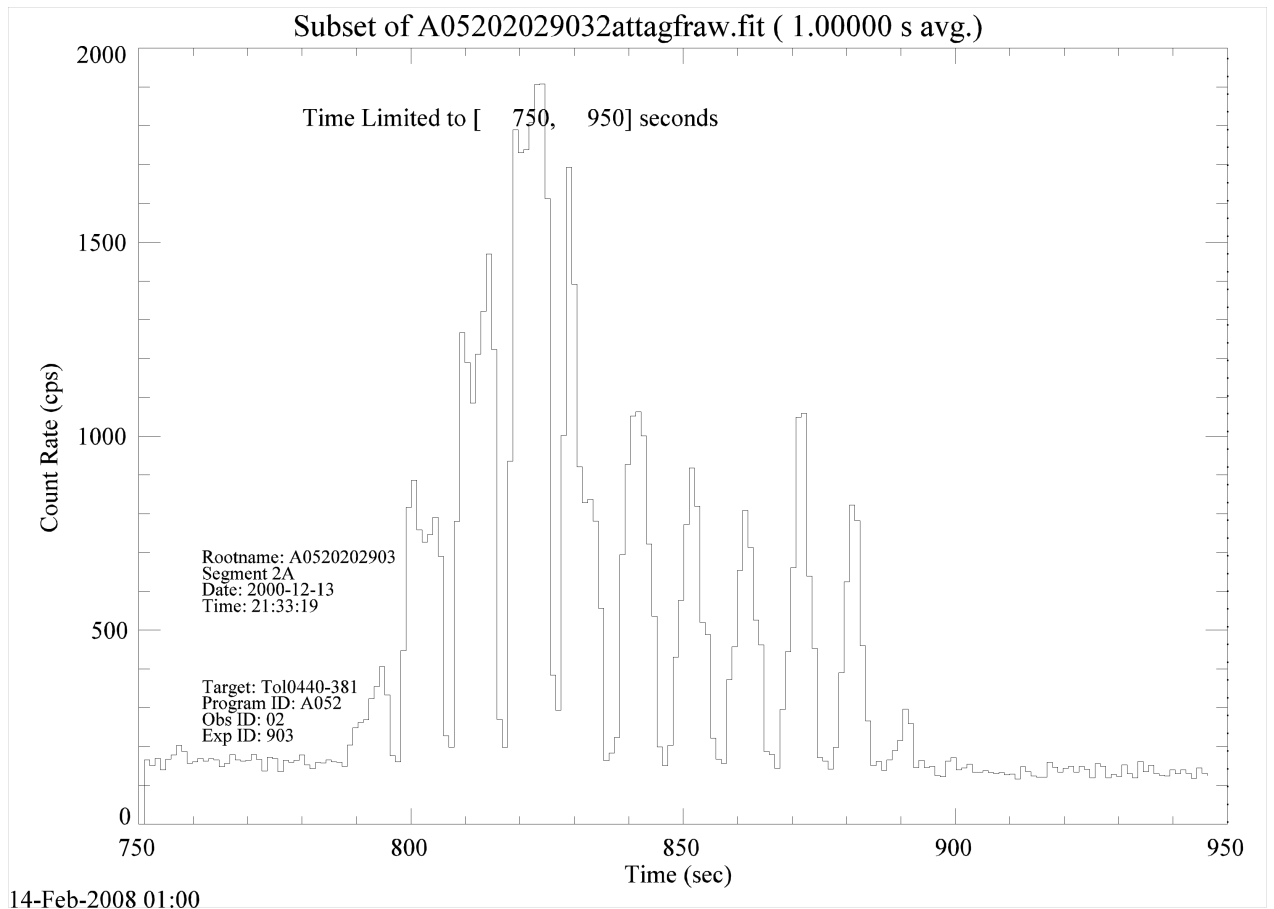


Figure 4-21 An example of the count rate as a function of time during an event burst showing a high-frequency component is 10 seconds. The size, spatial distribution, and temporal profile of the bursts varied significantly during the mission.

Although the bursts were present for the entire mission, their character changed somewhat with time. Initially, they showed a scalloped pattern across the detector (Figure 4-22), suggesting a reflection from the detector baffles or some other regular structure. Later, they were much more likely to show a distorted checkerboard pattern, apparently due to the grid wires shadowing the source of light (Figure 4-23); the distortion near the top of this figure suggests that charged particles are involved. These patterns could only be identified on the brightest bursts; most had too few counts for a pattern to be identified, and could be identified only by the changes in the count rate.

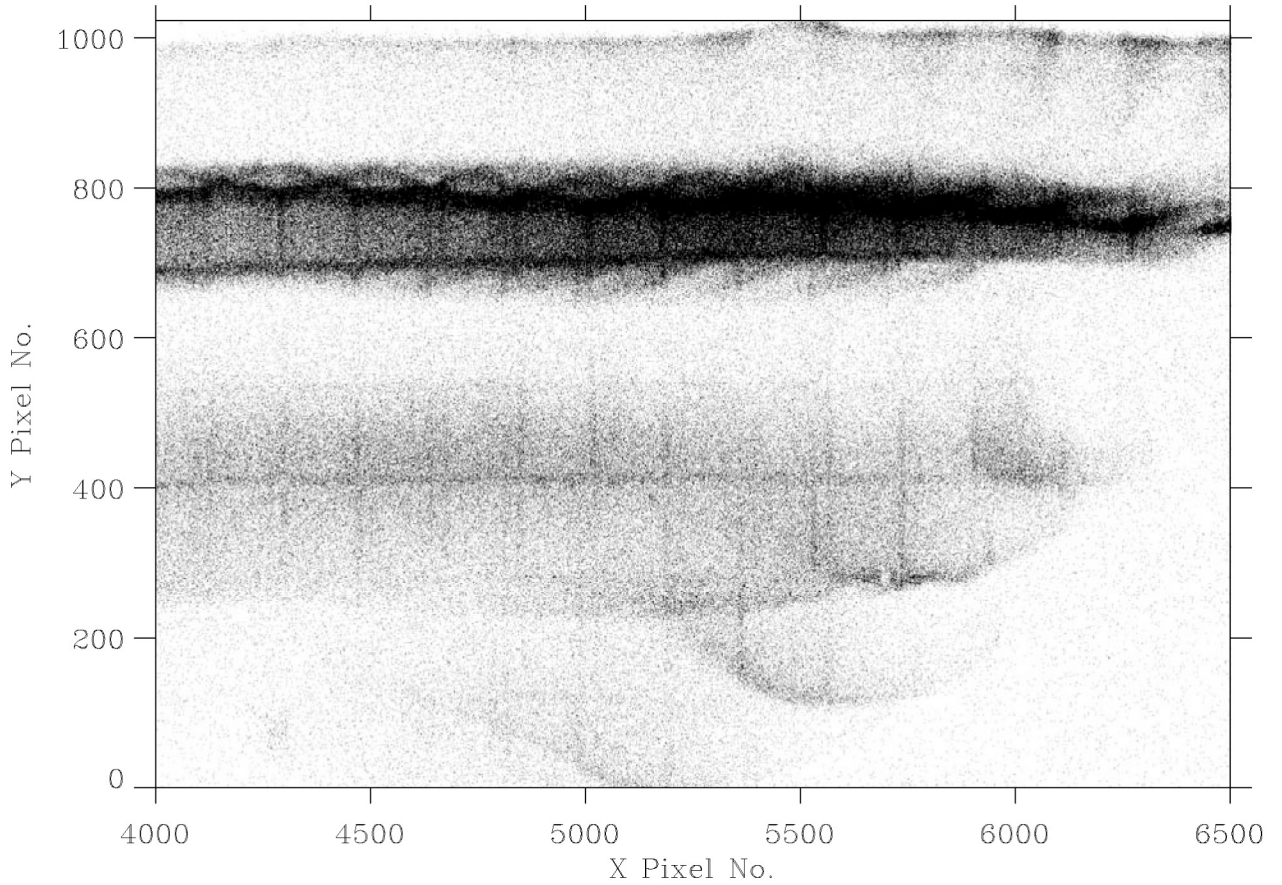


Figure 4-22 A portion of one detector showing an example of a scalloped burst .

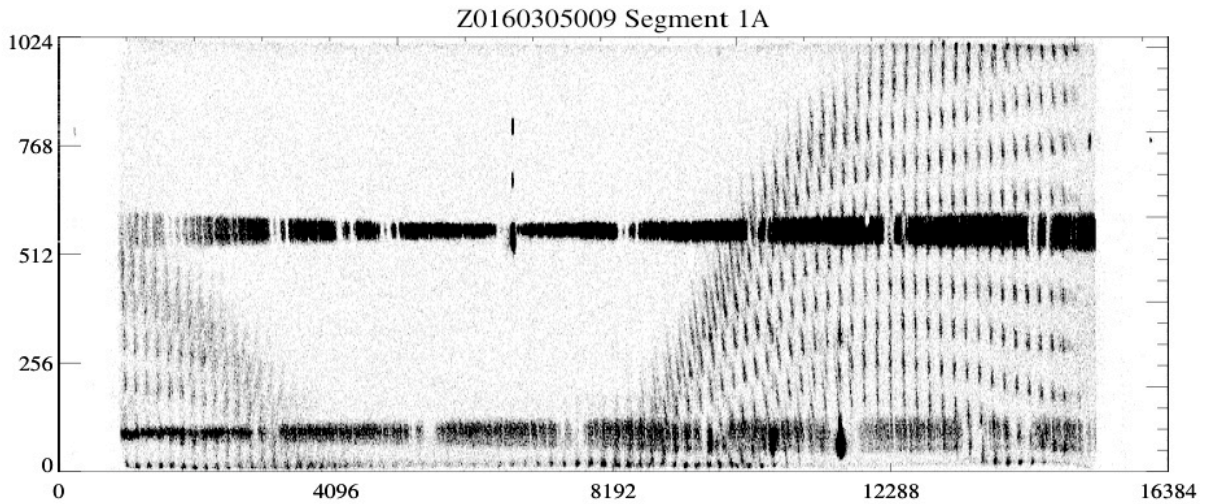


Figure 4-23 An example of a very large checkerboard burst on Segment 1A, shown in FARE coordinates. Note that the checkerboard pattern is distorted, while the spectrum remains undistorted.

Although a large burst could generate a significant number of counts which added to the apparent background, a relatively straightforward filtering module allowed CalFUSE to exclude them in most cases where the contamination was large enough to affect the data. The major impact on operations was due to the largest bursts triggering the detector SAA protection or the IDS FEC protection when the total number of counts in the SAA mask for a given segment exceeded their preset thresholds (see 4.4.8). This would result in an automatic reduction of the detector high voltage, and a concomitant loss of science data until the high voltage was restored.

Although the bursts are described here because of the effects they have on detector operations, analysis suggests that they were not actually caused by the detectors, but rather just detected by them.

4.4.3.4 High Background Periods

Numerous times during the mission periods of high detector background were observed. These often began suddenly and disappeared just as quickly. Figure 4-24 and Figure 4-25 show an example for both segments of detector 2. The source of the counts seems to be between the two segments, and the scalloped pattern is reminiscent of a burst.

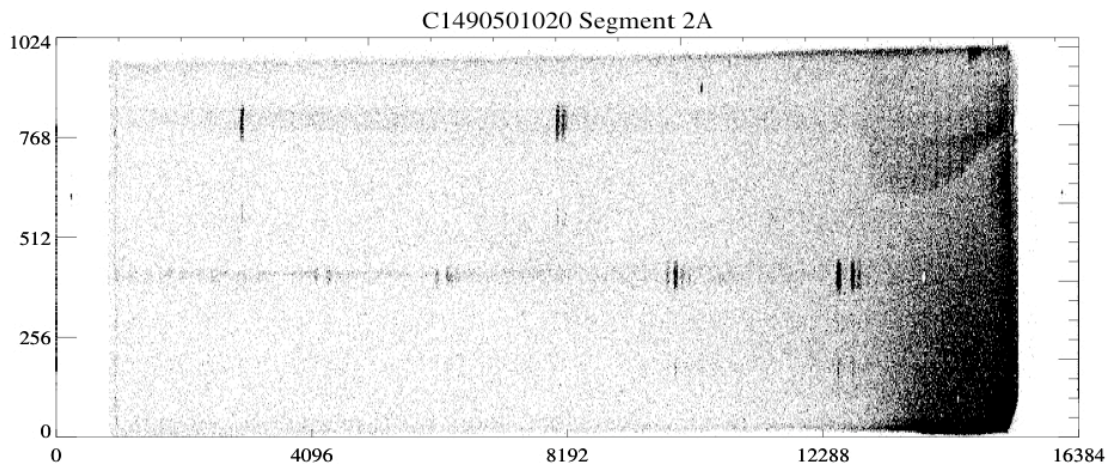


Figure 4-24 Segment 2A with a high detector background.

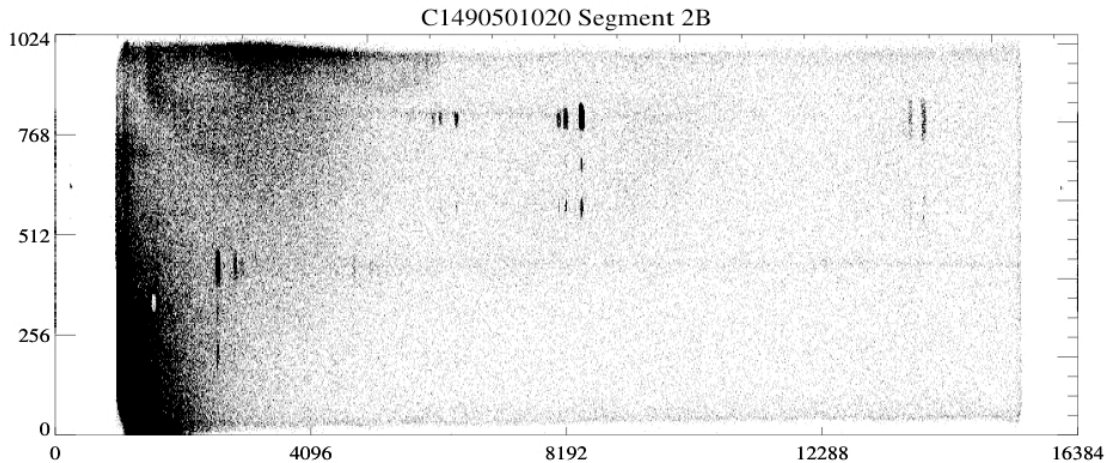


Figure 4-25 Segment 2B with a high detector background.

4.4.4 Geometric Distortion

The analog nature of the FUSE detectors means that geometric and thermal corrections must be applied to the raw data in order to ensure that all data taken is transformed to a common reference frame. In this section we will describe the source of some of these distortions, and how the on-orbit corrections were derived.

There are many sources of distortion, include ringing due to signal reflections at the ends of the delay lines, edge effects due to variations in the electric fields at the ends of the microchannel plates (including in the gap between two adjacent segments), and digital nonlinearity in the Analog-to-Digital Converters.

A correction for geometric distortion in the detector is made by the CalFUSE pipeline. The raw X and Y pixel locations are adjusted to the Flight Alignment Reference Frame (FARF) coordinates (Dixon et al., 2007). FARF coordinates represent the location where a photon actually hit the detector. As part of this correction, the Y pixel scale is adjusted to be the same on all segments. Despite this correction, the spectra do not line up perfectly on multiple segments in the corrected reference frame (Figure 2-7).

During detector construction and testing before launch, detector distortions were measured by placing a grid of 10 μm pinholes, spaced 1 – 2 mm apart on the front surface of the MCPs, and the linearity was determined. On orbit, final distortion corrections were determined by measuring the positions of the grid wires (separated by 1.0 – 1.2 mm) from stim lamp exposures, and by comparing the measured locations of spectral lines to the locations expected from raytrace models of the instrument.

An additional distortion effect discovered after launch was a slow change in the detector Y scale as a function of time. Although the cause of this phenomenon was not understood, it was monitored by tracking the slow change in the Y separation

between the Lyman- β airglow lines while analyzing the spectral motion (Section 4.3.5). A calibration file was constructed with this information and used by CalFUSE.

4.4.4.1 Thermal Distortion and Stability

As described in section 6.3.1.2.1, two stim pulses were inserted into the data stream for each detector segment at the beginning and end of each exposure as a way to monitor changes in the pixel scale due to thermal variations. In addition, thermistors continually measured the temperature at a number of locations on the detector (although not on the anode).

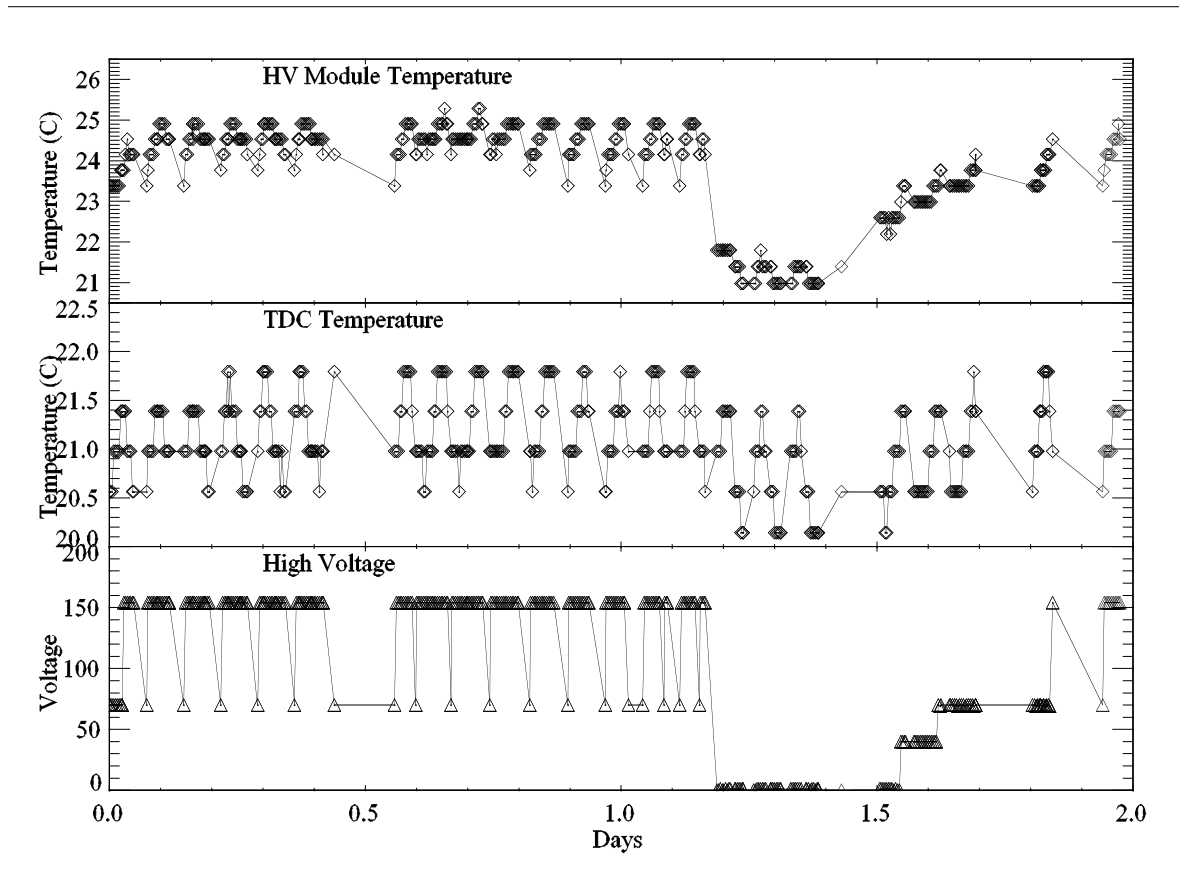


Figure 4-26 Temperatures measured by two of the detector thermistors during a two day period beginning on 29 August 2002 (MJD 52515), along with the high voltage on detector segment 1A at the same time. These data are taken from the engineering snapshots, and therefore are only collected during science exposures. The orbital variation of the $\sim 1^\circ\text{C}$ of the temperatures is seen, superimposed on longer-term variations, such as that due to the high voltage dropping to zero at ~ 1.2 days.

The on-orbit thermal environment of the detectors was quite stable during the mission as long as active control of the temperature of the spectrograph cavity was

maintained. The temperatures of the FUSE spectrographs, in which the detector vacuum assemblies were mounted, were controlled by the instrument thermal control system to better than 0.2 degrees Celsius. The equipment panels on which the detector electronics assemblies were mounted, however, were not as well controlled: they typically experienced peak-to-peak variations of 1-2 C each day. Thirteen thermistors (Table 6.3-2) were mounted on each detector to monitor how the detector temperatures varied. These temperatures typically varied cyclically by $\sim 1^\circ$ C during an orbit due to changes in the heating from the earth, while slews to a new target could result in changes of several degrees due to changes in solar illumination. In addition, changes to the instrument, such as changing the state of the detector high voltage, would result in changes to the detector temperatures (Figure 4-26).

Stim pulse positions were measured – and corrected for in CalFUSE – in both the X and Y directions. Because of the larger pixel sizes in Y, and the fact that the two stims were at a similar Y location, no correction for Y stretch was made, but this had a negligible effect on the data quality. Also, because stim pulses were only inserted at the beginning and end of each exposure, the correction may not be ideal if the temperature is changing rapidly – such as might happen when the high voltage had been recently ramped up to full. The changes in stim pulse position are on the order of five pixels across the entire detector per degree.

Changes to stim pulse positions generally followed the temperature changes as expected, but there were also long-term trends in the stim pulse positions which did not follow the temperature trends. These changes, which are not understood, may have caused shifts of up to several pixels in the data (Sahnou et al. 2000).

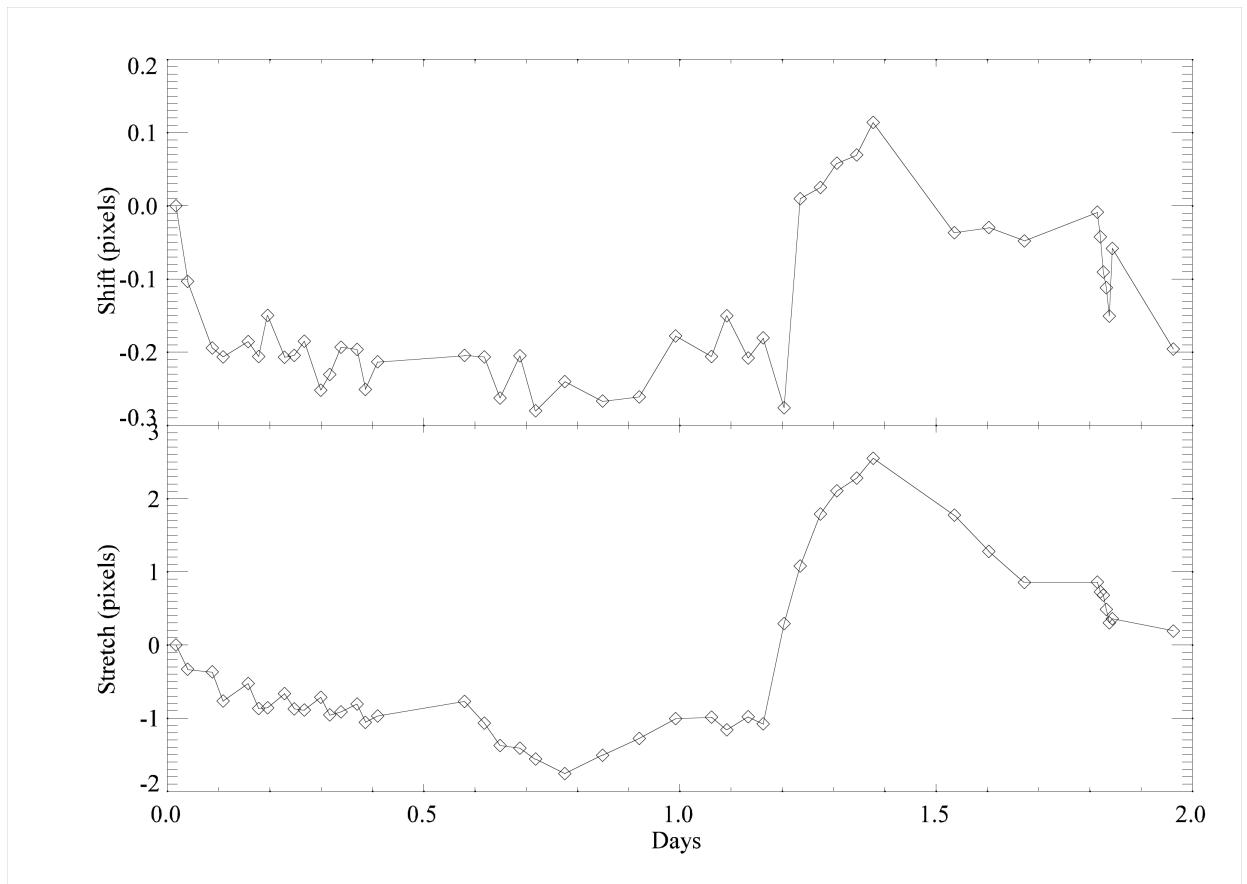


Figure 4-27 The X shift (shift of the mean position of the two stims) and stretch (change in separation between the two stim pulses) on segment 1A, measured from the stim pulses for the same time period shown in Figure 4-26. Large changes in both shift and stretch are seen when the high voltage shuts down.

4.4.5 Flat Field / MCP Effects

The flat field of each detector segment includes a multitude of effects. Some of these are intrinsic to MCPs in general, while others are cosmetic features on these particular MCPs, and still others are due to the detector electronics. Because the FUSE employed detectors employed double delay-line anodes, the measured X and Y coordinates of a photon event did not correspond to a discrete physical pixel on the detector, but were calculated from timing and voltage measurements of the incoming charge cloud. As a result, the detector coordinate system was subject to drifts in the detector electronics caused by temperature changes and other effects. The difficulty of associating individual photon events with a precise location on the detector made the construction of a reliable flat-field image impossible.

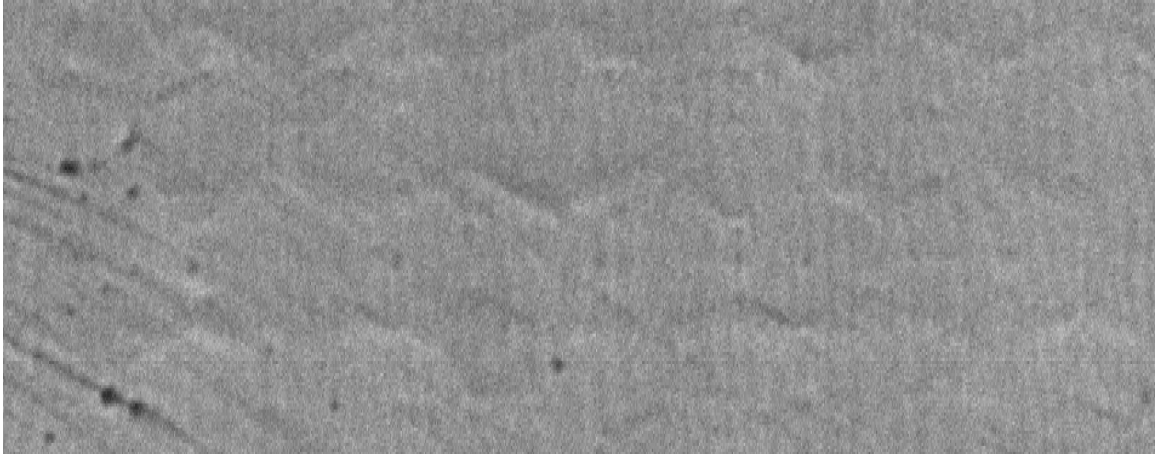


Figure 4-28 A small section of a flat field taken before launch. This region covers 950 x 150 pixels of a single segment. The hexagonal multifiber bundles are visible, as are some brush marks and dead spots on the left side of the image. This image contains ~100 counts per pixel

Because of limitations in count rate due to the detector electronics, and concerns over the lifetime of the MCPs, it was not possible to take deep flat fields with the on-board stimulation lamp on orbit. In addition, the detector grid wires did not allow a uniform illumination.

Before launch, the fixed-pattern uniformity of the detectors was measured by placing a diffuser in front of the detectors and illuminating them with a UV lamp. Flat fields with 40 – 100 counts per pixel were obtained in this way. It had been hoped that the ground flats could be used, after transforming them to the flight reference frame, to flat field the on-orbit data. Due to changing thermal conditions during the ground flat exposures, however, this was not successful. The ground flats did provide a useful catalog of detector features, but they could not be satisfactorily aligned to the flight data. Figure 4-28 shows a 950 x 150 pixel section of one of the ground flats. This area shows a range of features seen, including chicken wire, moiré, brush marks, and dead spots. The following subsections describe some of these features in more detail.

4.4.5.1 Chicken Wire

A hexagonal, "chicken wire", pattern is clearly visible in moderately deep flat fields, as shown in Figure 4-28. These features correspond to the boundaries where individual bundles of fibers were joined in the MCP manufacturing process. Fibers near the edges of the hexagonal bundles are visibly distorted from circles to ellipses upon examination under a microscope.

This compression leads to visible variations in the flat-field characteristics due to geometrical distortion in the mapping of photocathode regions to the pixel space defined by the readout on the anode. Brighter regions in the image are not inherently more sensitive, but rather have more area on the photocathode producing events in those pixels. The measured amplitude variation was as large as ~20%.

4.4.5.2 Moiré Pattern

High-frequency ripples such as those shown in Figure 4-28 and Figure 4-29 dominate the appearance of the flat field on segment 2B, and they are also visible on segments 1A and 1B. These ripples are a Moiré pattern due to beating effects between the pores in the three layers of the MCP stack (Tremisn et. al, 1999). As with the chicken wire, the variations in intensity are not due to variations in local sensitivity, but due to changes in the geometrical mapping of the photocathode to the anode readout. Bright areas in the images have more photocathode area producing events in those pixels than do dark areas.

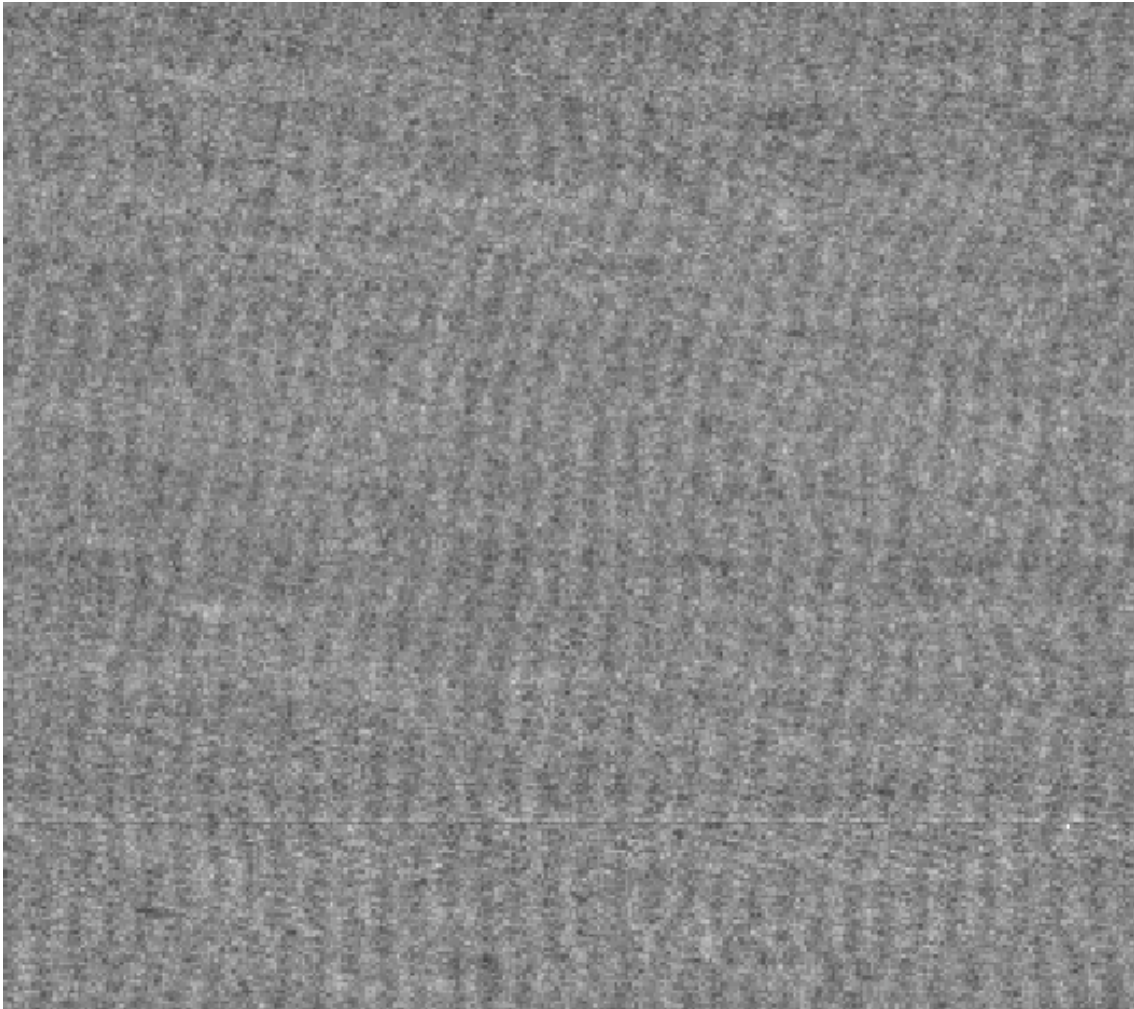


Figure 4-29 This small section of a segment 2B ground flat shows the most prominent Moiré pattern, visible as the nearly vertical ripples running across the image. The ripples have a peak-to-peak amplitude of $\pm 15\%$ and a period of ~ 9 pixels in X (~ 54 microns or ~ 1.5 resolution elements).

4.4.5.3 Brush Marks

Figure 4-28 also shows features due to brush marks that were introduced when contaminants on the detector MCPs, such as dust and filaments projecting from the pores, were manually cleaned with a brush in order to minimize potential hot spots before detector assembly. The brush marks visible in the flat fields originate on the back side of the plate stack. It is believed that the abrasion of the plate surface by the brush bristles causes local variations in the electric field between the back side of the plates and the anode. The result is a geometrical distortion in the mapping of photocathode regions to the electronic pixels encoded by the anode, and brighter regions are simply collecting events from a larger area of the photocathode than are dimmer regions.

4.4.5.4 Dead Zones

Two types of dead zones are visible in the FUSE flat-field images. The first (Type I) are simply dark spots, frequently black at the center. An example is shown in Figure 4-30. These are regions on the detector where the sensitivity is truly lower, or even absent. Most likely they are due to blocked pores in the front face of the MCP stack.

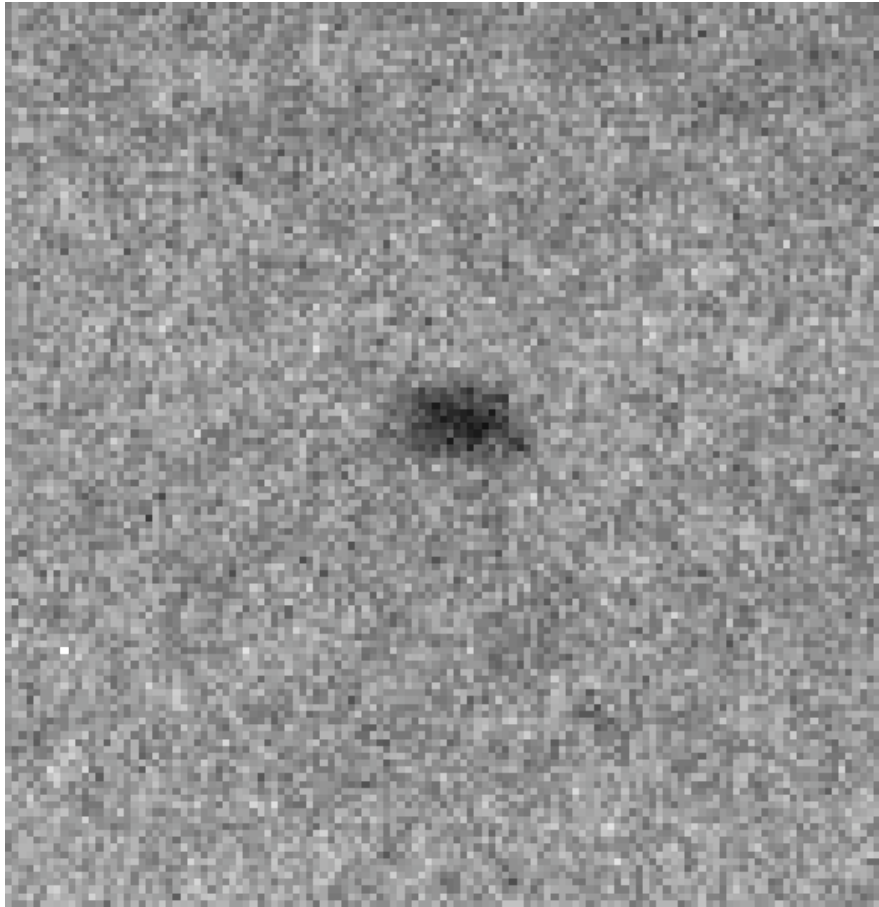


Figure 4-30 An isolated Type I dead zone on segment 1A is shown. This dead spot is not completely black at the center, but the sensitivity is down by a factor of ~ 4 from the surrounding region.

Type II dead regions are also dark spots with low or no detector sensitivity. They have a bright rim around a central hole (see Figure 4-31). Type II dead zones are believed to be due to contaminating particles on the back side of the MCP stack, either dust or whiskers protruding from an MCP pore, or blocked pores in the last plate. Like Type I dead zones, the interiors represent regions of truly reduced or absent sensitivity. The bright rims may arise from two mechanisms. Distortions in the local electric field caused by the contaminating particle or whisker can again lead to geometrical distortions in the mapping of the photocathode onto the anode readout. Another possibility is that a blocked pore only blocks a portion of the charge cloud reaching the back plate. Since the central part of the charge cloud doesn't get to the anode, the centroid is shifted radially outward, causing a bright rim.

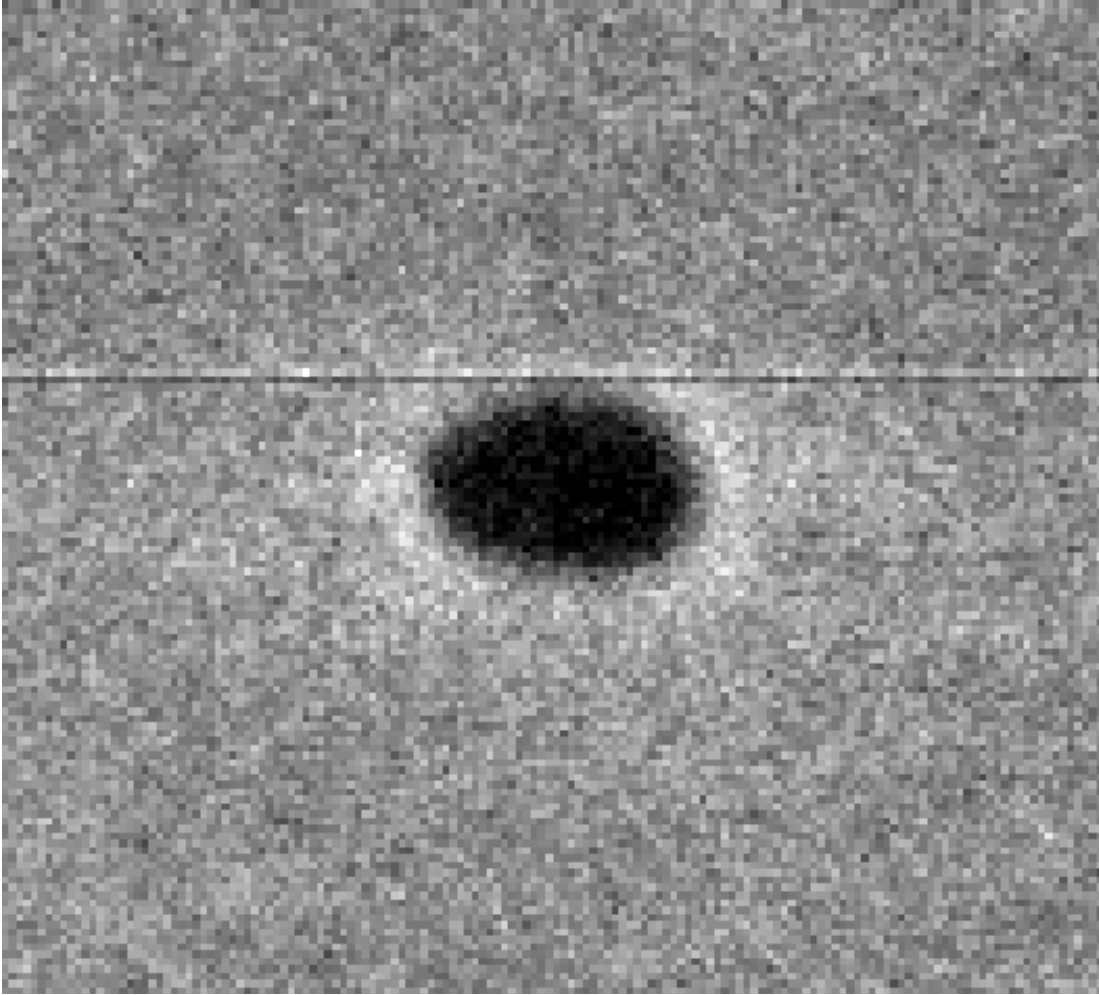


Figure 4-31 An isolated Type II dead zone on segment 1A is shown. Note the bright outer rim. The spot is located at $(X, Y) = (10515, 530)$, and it has a diameter of 40 pixels in X and 25 in Y (~250 microns). The $Y1=Y2$ feature is also prominent.

Type II dead zones have been observed to vary in size and shape with high-voltage cycling. This supports the electrostatic interpretation, but it is not conclusive.

4.4.6 Pulse Height Effects

The pulse height effect known as “walk” is described in Section 4.4.2.1; other effects associated with the pulse heights of individual events are described in this section.

4.4.6.1 $Y1 = Y2$ Feature

The “ $Y1 = Y2$ ” feature is a sharp, two-pixel-width line that runs horizontally across detector images. It is visible just above the dead spot in Figure 4-31. This feature results when a detected event has equal charge collected from both sides of the anode, e.g., charge $Y1$ equals charge $Y2$. Since the Y coordinate is calculated from the ratio $Y1/(Y1 + Y2)$, integer truncation leads to a deficit of events recorded in the row just below the halfway mark and a corresponding excess in the row just above it. This

"halfway mark" is near, but not at Y pixel 512 because of a coordinate shift added digitally in the detector electronics.

4.4.6.2 Counts at Left and Right Edges of Segments

Events appear at both the left and right edges on all detector segments. On the left edge, the events fall in pixel $X=0$, while on the right edge they fall in the last 16 pixels. Most of these events have very low gain, with pulse heights below the lower pulse height thresholds used by CalFUSE. They are misimaged because the pulses are detected above threshold at only one end of the anode. Since these counts fall outside of the active area of the detector, they have no effect on the spectra; however, the lost counts can give inconsistent results between the FEC and DEC counters (Section 6.3.1.2.2.3).

4.4.6.3 Loss of High Gain Events at Top and Bottom of Detectors

Events with large pulse heights were systematically lost at the top and bottom of all detector segments (Figure 4-32). This effect was segment dependent, and thus the default upper pulse height thresholds used for TTAG observations by CalFUSE vary with segment to ensure that counts are not lost.

The loss of counts was due to the method used to determine the Y coordinate of an event: $Y = Y1/(Y1+Y2)$, where $Y1$ and $Y2$ are the measured charges on the upper and lower delay line. If either $Y1$ or $Y2$ exceed a certain threshold, the event is discarded. For a given pulse height ($Y1+Y2$) value, events near the top and bottom are more likely to have $Y1$ or $Y2$ exceed this threshold, and thus those counts are more likely to be discarded.

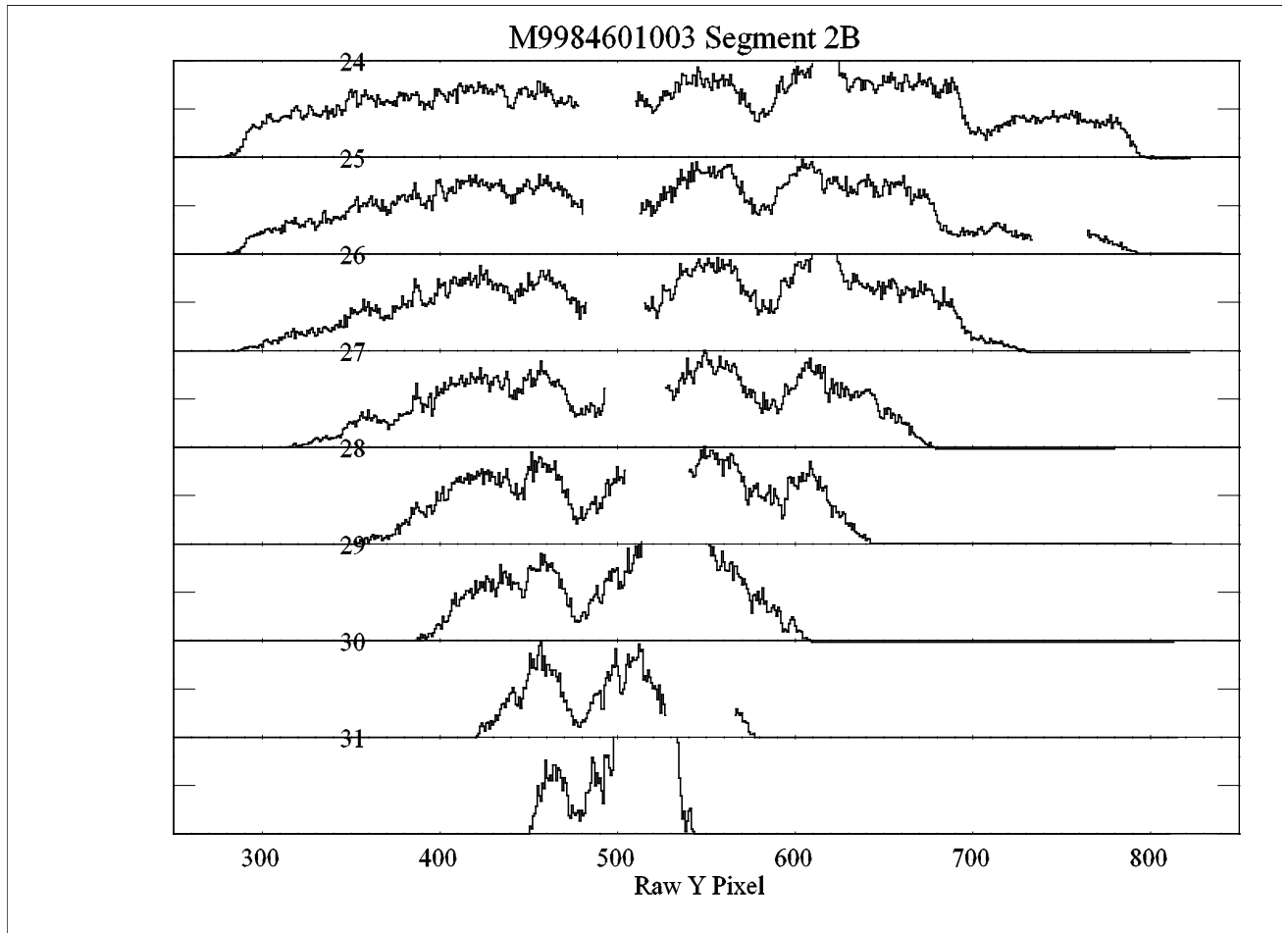


Figure 4-32 Y projection of the normalized counts in a segment 2B stim lamp image for pulse heights 24 to 31. At a pulse height of 24 or below, all Y pixels in the active region have counts. For pulse heights above 24, however, counts are discarded symmetrically about pixel 512. Note that the shape of each projection is determined by the gain of the segment as a function of position.

4.4.6.4 The Fold

Near the high pixel edge of the segment 1A active area, the detector active area sometimes appears to fold over on itself and change direction. Figure 4-33 shows an example of the fold in a stim lamp exposure. The bright region near $X = 60$ is populated by counts that should be lost beyond the right edge of the active area. In addition to being misimaged, the events have low pulse heights.

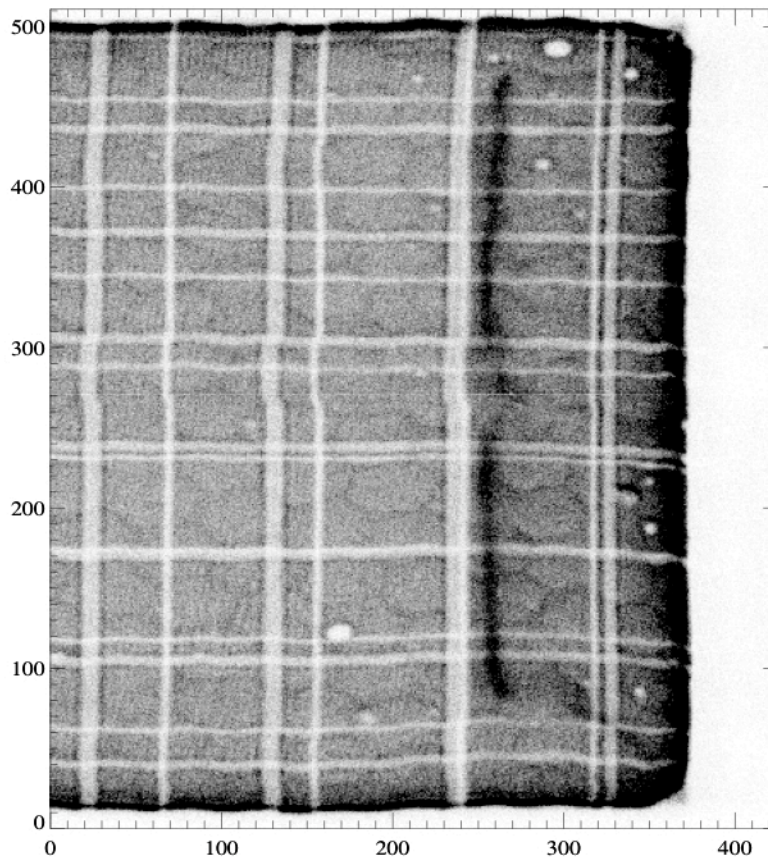


Figure 4-33 Raw data from the far right edge of segment 1A in a stim lamp exposure. Counts that should have been lost beyond the active area to the right are instead folded back into the active region.

It is believed that this effect is due to the MCP output aperture cutting off part of the charge cloud exiting the rear of the MCPs, since the output aperture is smaller than the input aperture. These low-gain events are more easily distorted by the changing electric field near the edges of a segment. A similar effect is responsible for the highly nonlinear X pixel scale seen at the edges of the detectors; in that case, the centroids of the clouds move towards the center. Fold effects may change as a function of the MCP high voltage. No correction is made for this effect in CalFUSE.

4.4.7 Count Rate Dependent Effects

Numerous count rate dependent effects were discovered in the FUSE detectors, and they are discussed in this section. Characterizing some of these effects proved difficult on orbit since TTAG data, which provided the most information, were used only for the lower count rate observations. In addition, stim lamp observations, which were the only ones able to sample the entire detector uniformly, could only be taken at the very highest rates since it was not possible to adjust the lamp flux.

4.4.7.1 Y Blooming

The Y scale of the detectors was found to be a function of count rate; as the count rate increased, the number of Y pixels between two features on the detector increased. CalFUSE applies a correction factor to the raw pixel values so that all data is adjusted to the reference frame where the count rate is zero; these shifts are as much as 20 pixels at the highest count rates. The cause of this effect is not understood.

4.4.7.2 Phantom Spectra

At very high count rates, the detector electronics was sometimes not fast enough to separate individual photon events. The consequence was that two photons reaching the detector at nearly the same time could be reported as a single photon. The resultant event would have the X coordinate of the first photon, along with a combined pulse height and an average Y location. In these cases a faint spectrum appears on the detector between the SiC and LiF spectra. This spectrum may appear to be from a target in the non-prime aperture, but it can be identified as a phantom by the large pulse heights. The total number of counts in the ghost spectrum is usually very low (< 1% of the true spectrum).

4.4.7.3 Resolution vs. count rate

Ground tests on the spare detector showed that the shape of the point spread function varied with count rate, so that the detector resolution degraded as the count rate increased. This effect only became important at count rates above 5,000 total counts per second, so only HIST observations were affected. Since HIST observations were binned by 8 in the cross dispersion (and they were also often affected by detector walk effects), they typically had a slightly lower resolution to begin with, so the effect on the data was minimal.

Using on-orbit data, the width of the stim pulses as a function of total count rate was plotted for each segment. The FWHM of all stims showed a strong correlation with the count rate, although the slope of the correlation varied with both segment and stim pulse. For segment 1A, the FWHM of the right stim increased from ~2.5 to ~4.0 pixels as the count rate increased from 0 to 14,000 counts per second. As the count rate increased, the shape of the stims changed; at low rates, they are approximately Gaussian, while at higher rates a second peak which is offset in both x and y has an increasing fraction of the energy.

4.4.7.4 Dead Time

There were multiple effects which caused photons that were incident upon the front surface of one of the detector MCPs to be lost before they could be properly recorded. We refer to these collectively as “dead time.” Corrections for these effects, which are a function of count rate, are made in the CalFUSE pipeline. Details on dead time effects are given in section 6.9.

4.4.8 SAA Shutdowns

If the count rate in the ASC counter exceeded a particular threshold rate averaged over its defined integration time, the high voltage on that detector segment would drop to SAA level (section 6.3.1.2.2.3). This protection was included in the design primarily to ensure that the voltage would not remain at its full level while passing through the SAA, thus the ASC counter was often called the ‘SAA counter’. However, on orbit most shutdowns triggered this way were caused by bursts, which had not been expected before launch. Other causes of SAA shutdowns during the mission included errors in the placement or set up of the masks.

As more was learned about the properties of the bursts during the first few years, the thresholds were adjusted in an attempt to minimize shutdowns due to bursts while still providing the desired protection during the deepest SAA passages. Table 4.4-2 shows the thresholds and integration times used during the mission for normal observations. These limits were set differently for stim lamp observations.

Table 4.4-2 ASC thresholds used during normal operations.

Approximate Start Date	1A	1B	2A	2B	Detector 1 Integration Time (sec)	Detector 2 Integration Time (sec)
8/11/1999	4096	4096	4096	4096	10	10
8/15/1999	4096	4096	4096	4096	5	10
8/18/1999	8192	4096	4096	4096	10	10
10/4/1999	8192	4096	4096	4096	5	10
10/6/1999	8192	4096	4096	4096	3	10
12/21/1999	32768	32768	32768	32768	30	30
6/5/2001	9000	9000	9000	9000	30	30
9/18/2001	9000	9000	9000	9000	30	18
10/17/2001	9000	9000	10000	18000	30	30
11/19/2001	6900	6900	10000	18000	30	30

After an SAA shutdown, an onboard script prevented the other segment of the triggered detector from returning to full voltage once it was commanded to SAA level; executing a simple onboard script was required to return the voltage to full. Initially, this command was sent from the ground, but the recovery process was later automated so that onboard rules and scripts identified the shutdown, waited a preset time - initially 20 (starting on 5 September 2003), but later 5 minutes (beginning on 27 February 2004), and then returned the segment(s) to full voltage.

A similar voltage shutdown occurred when the FEC threshold was triggered (Section 6.3.1.2.2.3). A similar recovery procedure was used from the ground to recover from these events, which were also normally caused by bursts. These were not automated, however, because no detector diagnostic was issued in that case.

SAA shutdowns were relatively common occurrences. During the mission, 197 occurred, along with 8 FEC shutdowns.

4.4.8.1 SAA Incursions at full voltage

The previous section noted that most ‘SAA shutdowns’ were really due to bursts. However, there were times when the detectors did pass through the SAA with the high voltage at FULL voltage. Since the thresholds had been set relatively high to avoid tripping on bursts, these shutdowns typically did not occur until FUSE passed through the center of the SAA, where the particle flux (and consequently the count rate on the detectors) is the highest. Passing through the SAA at full voltage can cause scrubbing of the detectors; since the scrubbing is uniform, it does not result in differential gain sag, however. The small number of these SAA passages at full voltage during the mission had a negligible effect on the detector lifetime. Most of these incursions were caused for one of two reasons: either the SAA manager rules in the IDS were not running, or an attempt was made to ramp up the high voltage while passing through the SAA.

4.5 □ FES Performance

Following in-orbit checkout, FES A was used almost exclusively for target acquisition and guiding until mid-2005. During this time, FES B was used only during periods when the FES A CCD was being annealed.

Scattering by micro-roughness of the LiF primary mirrors or the internal FES optics was quite low, which enabled tracking of guide stars even when very bright objects such as planets were in the field of view. As a result, there was no operational necessity for use of the filter wheel, and the filter wheels were left in the clear position throughout the mission.

Radiation damage from cosmic rays caused a gradual increase in dark current for a subset of FES pixels. These « warm » pixels are easily seen in Figure 4-34 as small faint spots affecting single pixels. The star images are much larger, as the FES optics were designed to produce spots 2-3 pixels in diameter to ensure good sampling of the PSF for accurate centroiding. This image was obtained on 15 May 2000, after almost 11 months in orbit and one month prior to the first FES annealing cycle. The image was obtained near entry into orbital night : the level of stray light is just slightly elevated, providing just enough contrast to show the borders of the field stop. Many faint warm pixels are visible in the field stop region at the bottom of the image.

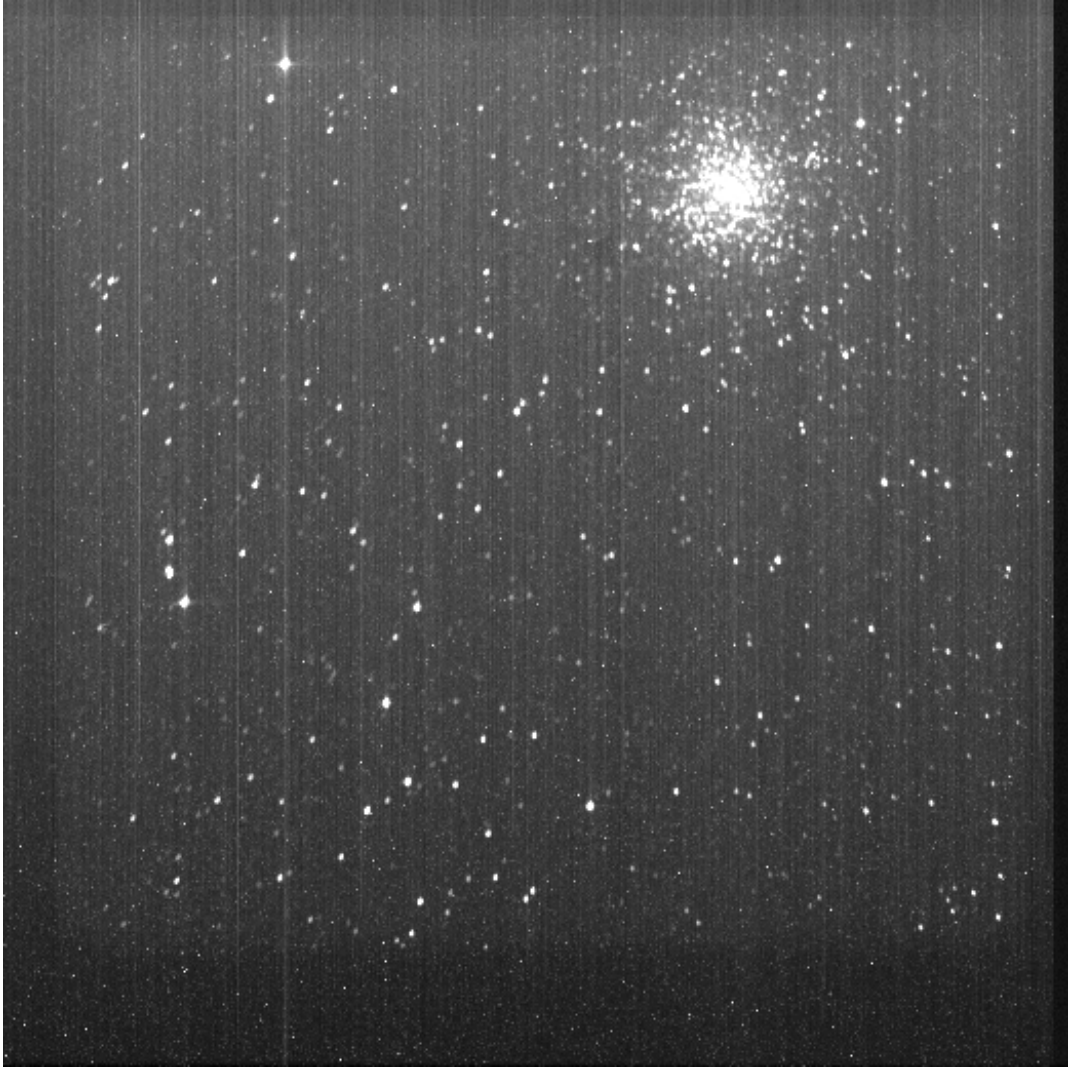
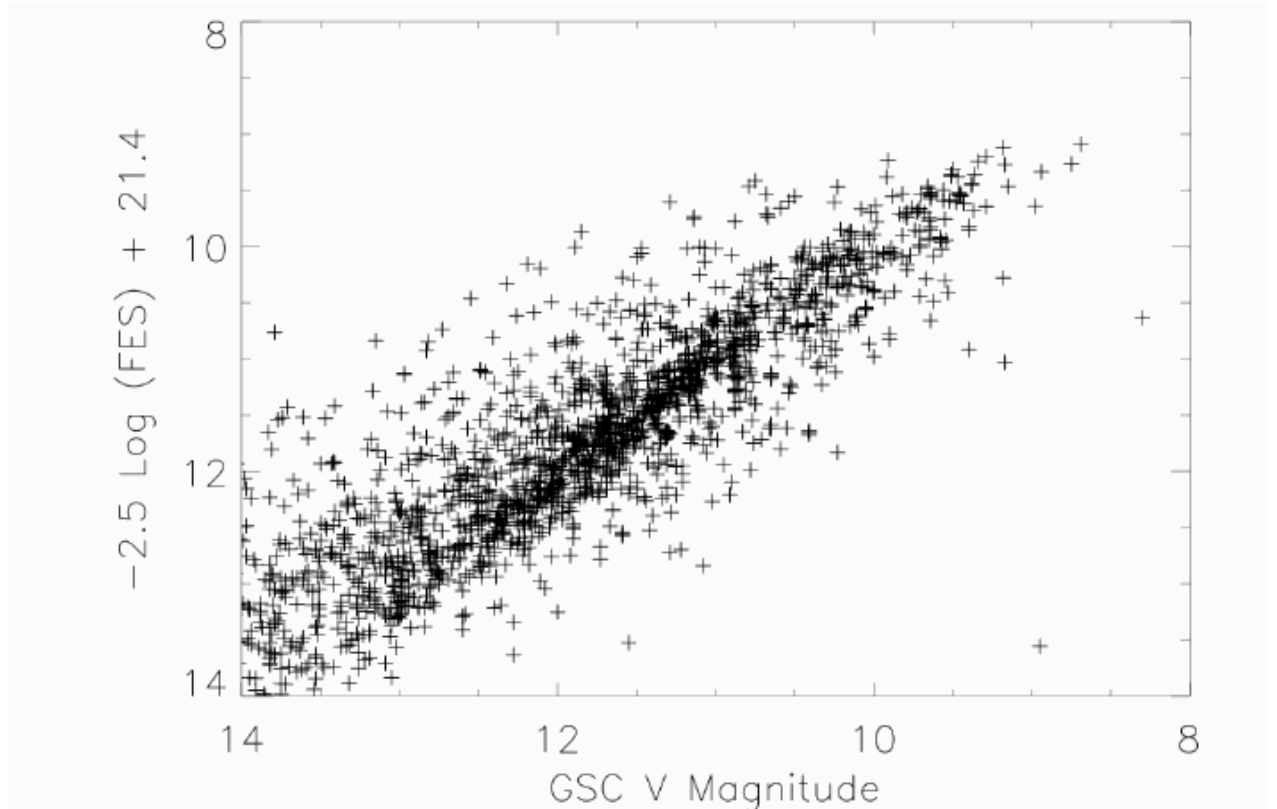


Figure 4-34 FES-A 1×1 image (A1080201001fesafrw.fit) of the field of view in the direction of the globular cluster NGC 6723.

4.5.1 FES Photometry

The photometric calibration of FES intensities measured on 2×2 -binned acquisition images and based on HST Guide Star Catalog (GSC) star magnitudes is shown in the upper panel of Figure 4-35. The large scatter is due to inaccuracies in the GSC (≈ 0.3 mag), the difference in responses of the unfiltered FES and the filters used for the GSC, stellar variability, and to some extent, the location of the stars on the subpixel scale of the FES. The FES intensities were typically larger due to its additional red response. Positional errors are independent of brightness (lower panel of Figure 4-35) a result unexpected based on pre-launch considerations. For the FUSE quaternion estimator, variances used for weighting positional accuracies are scaled from the intensity in a simplification of the algorithm. True variances in the measured position would provide more accurate weighting of stars with poor positions. The

scatter in the lower panel of Figure 4-35 illustrates why object intensity was not an explicit criterion in the star identification method used by FUSE and why up to four guide stars were chosen for tracking, particularly if only faint guide stars were present in the field. It was not uncommon for the FES measurements to be 0.75 mag off from the GSC values, i.e., a factor of 2 in intensity.



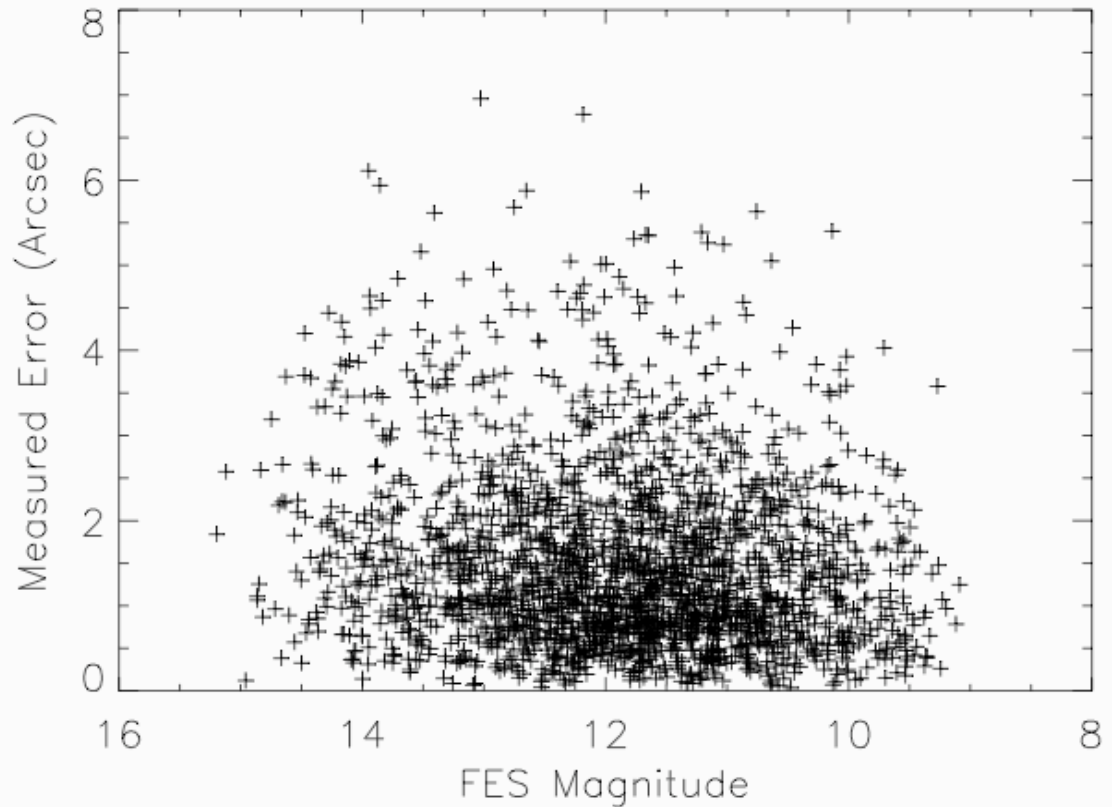


Figure 4-35 FES intensities (top) and positional errors (bottom) compared with HST GSC values.

4.5.2 Stray Light

The FUSE baffles on the LiF channels provided good rejection of stray light from the Sun, and from the sunlit-Earth when the angle between the telescope boresight and the Earth limb was greater than 25 degrees. However, at lower limb angles the stray light entering the FES could be significant, especially near orbit noon.

Examples of FES-A and FES-B images, taken near orbit noon where scattered light from the sun is most pronounced, are shown in Figure 4-36 and Figure 4-37. These figures illustrate the impact of scattered light on the guide star acquisition process.



Figure 4-36 A raw image from FES-A with a high level of scattered light is shown. The dark border seen on all sides is the aperture mask. The spectrograph apertures are visible: MDRS, HIRS, and LWRS in order from left to right. Light scattered by the edges of the HIRS aperture cause it to appear bright in this image. The dimpled region surrounding the apertures is an artifact of the manufacture of the FPA mirrors. The feature centered at $X=97$, $Y=344$, that appears somewhat oblong is a glint caused by a defect in the FPA surface. It extends roughly ± 5 pixels along either axis, and may move ± 5 pixels in the vertical direction, depending on the FPA position. There are a few other defects on the LiF1 FPA, but they are small and are rarely seen.



Figure 4-37 A raw FES-B image with a high level of scattered light is shown. The dark border seen on three sides is the aperture mask. The spectrograph apertures are visible: LWRS, HIRS,MDRS in order from left to right. Light scattered by edges of HIRS make it appear bright in this image. The dimpled region surrounding the apertures is an artifact of the manufacture of the FPA mirrors. A long scratch in the FPA is visible on the left side of the image.

4.5.3 FES A Failure

The first in a series of intermittent spontaneous FES-A reboots occurred on day 105 (April 15) of 2005. When the reboots occurred, FES-A was left in Boot mode, and could not be commanded to application mode without first cycling the power. We operated with this anomaly for several months, *but ultimately decided to switch to FES-B on July 12, 2005*. FES-A was not used for guiding during the rest of the FUSE mission. Further details and a discussion of the FES-B focus performance are presented in Section 6.4.2.

5 Bright Target Observing Strategies & Restrictions

5.1 □ Flux Limitations

The FUV detectors on FUSE were exquisitely sensitive and had a significant dynamic range. However, very bright FUV targets could actually damage the detectors. A bright target observing policy was implemented to protect the detectors whereby an upper limit to the expected target flux of $F(\lambda) = 1 \times 10^{-10}$ ergs cm^{-2} s^{-1} \AA^{-1} anywhere in the FUSE range was imposed. In addition there were hardware and software limits set to protect the detectors. The IDS monitored the total count rate reported for each detector segment, and would reduce the high voltage to SAA level for a segment if the count rate exceeded 45,000 c/s (corresponding to a flux level of approximately 5×10^{-10} ergs s^{-1} cm^{-2} \AA^{-1} across the FUSE bandpass). The detector DPU software monitored the MCP current and would likewise reduce the HV to SAA level if the current exceeded preset thresholds.

As a policy, the project was conservative in observing bright targets in order to conserve sensitivity. Only a finite amount of charge could be extracted from each detector pixel; thus, the critical parameter for preserving detector lifetime sensitivity is the number of extracted counts, not the count rate (flux). Sensitivity suffers at about 10^7 e⁻/pix. Raising the HV could compensate partially, but there were limits to the amount the high voltage can be increased without either incurring detector shutdowns as well as due to limitations of the power supply.

Emission line sources were a particular concern because of their potential to create local regions of reduced sensitivity, or “gain sag” at critical locations. Consequently, an equivalent flux limit “per unit wavelength” for narrow emission lines was also applied in planning to prevent local impacts to the detectors.

5.2 □ Bright Target Observing Strategies

The scientific user community always expressed significant interest in observing targets that were above the bright limit, for a number of reasons. The FUSE project spent considerable resources, especially during late 2002 – 2004, on developing and testing various methods of easing the bright limit. Some of the easier adjustments, for targets up to 5 times the nominal brightness limit, were put into operations, allowing new regions of observational parameter space to be opened. Other techniques, such as utilizing lowered high voltage levels or defocus techniques, were developed and tested but never put into operational usage due to technical difficulties and/or lack of resources. The outline below provides some details of what was done and why. At the FUSE Observers Advisory Committee meeting in November 2004, it was decided to terminate efforts on the more aggressive techniques that would have been required to implement observations of targets more than 5 times the nominal brightness limit.

5.2.1 Bright Target Observing Strategies Implemented

The common thread in all of the attempted techniques was to limit the flux reaching the detectors, such as by observing only in the SiC channels. However, in most of these strategies there was the potential that pointing uncertainty during a target acquisition, or by loss of pointing control when in two-wheel or one-wheel mode, would result in the full flux of the source entering a spectrograph through one of the LWRS apertures in the LiF channels. To safeguard against this possibility, the normal HV management was augmented for bright object observations:

- 1) The HV was left at SAA level until after the target acquisition was complete
- 2) IDS rules would be activated to monitor the pointing error reported by the ACS; these rules would lower the HV to SAA level while the pointing error exceeded 5 arcseconds or if the guide stars were lost and a reacquisition was triggered
- 3) The HV was lowered at the end of every visibility period prior to breaking track on the guide stars.

This enhanced HV management was only possible because the enhanced interface between the IDS and ACS developed for gyroless operations provided the necessary information to the scripts running in the IDS.

No special data reduction is required for any of the implemented bright-object observing techniques.

5.2.1.1 SiC Only Observations

At the time this mode was first implemented, the throughput of the SiC channels was roughly one-fifth that of the pre-launch LiF throughput used to set the bright flux limit. As a result, the flux limit could be set five times higher for sources observed only in the SiC channels. This was accomplished operationally by observing a source only in the MDRS or HIRS aperture and by moving the LiF FPAs to the high end of their range of motion. This technique could not be employed for LWRS observations, as the FPAs could not be moved far enough to ensure that the source would miss the LiF LWRS apertures. The main drawback to this technique was that no data would be obtained longward of 1100Å. This became the primary technique for observing objects brighter than $F(\lambda) = 1 \times 10^{-10} \text{ ergs cm}^{-2} \text{ s}^{-1} \text{ \AA}^{-1}$.

5.2.1.2 HIRS LiF Only

This bright object observing configuration was typically restricted to a single LiF channel - the LiF guide channel, which was LiF1 prior to July 12, 2005 and LiF2 thereafter. The non-guide channel image was typically offset in the y-direction by ~40 arcseconds to ensure that this spectrum was not imaged on the detector. No steps would be taken to avoid the SiC channels, but failure to obtain SiC data would not trigger a re-observation. This mode was planned for only a handful of targets throughout the mission, that happened to be close to the bright limit at LiF channel wavelengths and for which the science programs did not require SiC channel data.

5.2.1.3 Single Detector Segment

In certain borderline circumstances, the flux from a source would be below the bright object limit for one detector segment and above it in another. One example was Sirius-B, which exceeded the bright limit longward of 1100 Å. This star was observed both in SiC-only mode, and subsequently in the LiF1A and LiF2B segments. The high voltage was left at SAA level for segments 1B and 2A in the latter observation. This technique was used in a handful of observations during the mission.

5.2.2 Bright Target Strategies Evaluated - But Not Implemented

Two additional techniques for observations of bright objects were developed and tested. A substantial effort was invested by MP/SciOps staff to safely plan, execute, and assess these tests. The lowered HV technique was not found to be useful and was ultimately discarded. The defocus technique produced usable data of bright objects, but because of the level of effort required on the part of the staff to execute this procedure in a way that maintained the health and safety of the instrument, it was never put into operational use. However, because the test data from these programs resides in the FUSE archive, descriptions are provided here for completeness.

5.2.2.1 Defocus technique

The basic concept of this technique was to defocus one or more telescopes, thus enlarging the size of a stellar image at the focal plane(s). By using the MDRS or HIRS aperture(s) to pick off only a portion of the total light, the flux reaching the detectors would be reduced and targets brighter than the nominal limit could be observed.

It was originally hoped that this technique would enabled observation of targets up to 50 times the brightness limit, but the actual attenuation gained was closer to a factor of 15. The defocus of the primary mirror led to a significant increase in the focal ratio of the beam entering the spectrograph, primarily in the dispersion direction and only slightly in the cross-dispersion direction. This had two impacts on the data: shadows cast by the grid wires that were completely washed out under full illumination became distinct, and the spectral resolution improved. The effects of the grid wire shadows could be removed by FP-splits, which were performed in many of the tests.

Tests were performed that offset the mirrors in both directions and by varying amounts. For safety reasons, only the LiF2 and SiC2 channels were defocussed for these tests, and the high voltage on detector 1 was left at SAA level.

Testing demonstrated this approach to be viable scientifically, but very difficult operationally. The FPA and mirror positions had to be manually determined, scripted, and commanded and the nominal position for the next observation determined. Small

inaccuracies in the relatively large mechanism motions also necessitated additional channel co-alignment procedures, once after the mirrors were defocussed, and again after they were returned to their nominal positions. These operational difficulties and human resource issues made usage impractical. Consequently, this technique was not implemented as a standard procedure.

Test data obtained using this technique are archived under Program IDs S520, S523, and S526.

5.2.2.2 Lowered HV method

The concept behind this technique was to decrease the high voltage on one or more detector segments temporarily, in order to observe overbright targets (35-100x bright limit). Of course, changing the high voltage changes the behavior and calibration of the detectors significantly. It was thought that perhaps one or two “standardized” lower setting might be calibrated for use operationally. Tests and analysis indicated only limited utility of this technique. The behavior of the detectors was very sensitive the HV setting and was not repeatable at the required level. More importantly, reducing the HV to the point where most of the events fell below the detection threshold resulted in very poor imaging performance by the detectors. The resulting spectra were unusable over most of the active area of the detectors. At the conclusion of testing, the lowered HV technique was not considered operationally viable.

Test data obtained using this technique are archived under Program ID S525. In most cases, the star observed at reduced voltage was also observed at normal voltage for comparison purposes. Users should not assume that all observations with Program ID S525 are at reduced voltage: the HV keywords in the FITS headers should be examined to determine the configuration for each observation in this program.

5.2.2.3 Scattered Light Technique

The concept of this technique was to place extremely overbright targets near (but outside) a science aperture and integrate long enough to observe the target via the extended wings of the PSF: the “scattered light”. The resulting flux would fill the spectrograph apertures, so the spectral resolution would be that of an extended source rather than a point source. This technique was tested with observations in the program S521.

This technique, while feasible in principle, was abandoned as a result of several factors: the attenuation factor for the transmitted flux was extremely sensitive to the exact offset of the star from the apertures, this offset varied over an orbit by several arcseconds as a result of the image motion anomaly in all but the guide channel, and the overall pointing itself was potentially variable by many arcseconds as a result of poor controllability with only one or two reaction wheels. The number of stars bright enough for this technique to be applicable was small, and the potential for risk of damage to the detectors was significant, so this technique was not implemented.

6 FUSE Instrument Technical Appendix

6.1 □ Telescope Mirrors

6.1.1 Telescope Mirror Design

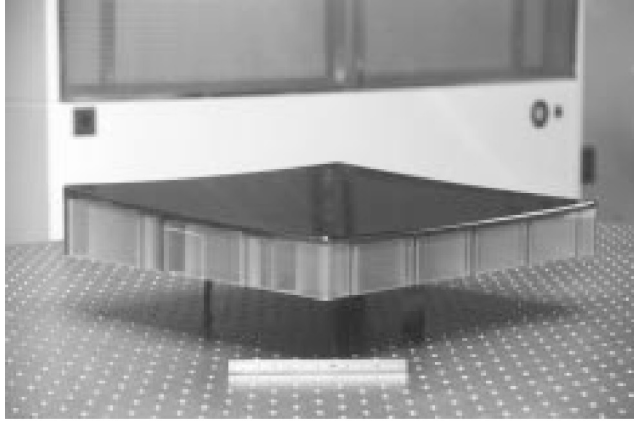
The four telescope primary mirrors were identical off-axis paraboloids, each with a rectangular 352 mm x 387 mm clear aperture, a 2245-mm focal length, and approximately 5.5° off-axis angle (Kennedy et al. 1996).

The primary mirror sections did not contain the vertex of the parent paraboloid. The vertex was about 34.5 mm from the edge of the mirror aperture in X (Figure 6-32). The different grating incidence angles required to optimize the spectrograph channels for the two wavelength bands resulted in slightly different off-axis angles for the SiC and Al+LiF coated mirrors. The off-axis angles were defined by aperture stops placed over the surfaces of the mirrors. Otherwise, the mirrors are identical except for the coatings. The corners of each mirror were masked to match the grating apertures, whose outside corners were removed to satisfy space constraints of the 'Med-Lite' launch vehicle fairing. The resulting geometric area of each mirror was approximately 1330 cm². These apertures were widely separated on the instrument optical bench, resulting in four parallel and separated optical axes. Selected mirror assembly specifications are listed in Table 6.1-1. The point spread function (PSF) at the focal plane places ~90% of the light within a diameter of 1.5 arcsec.

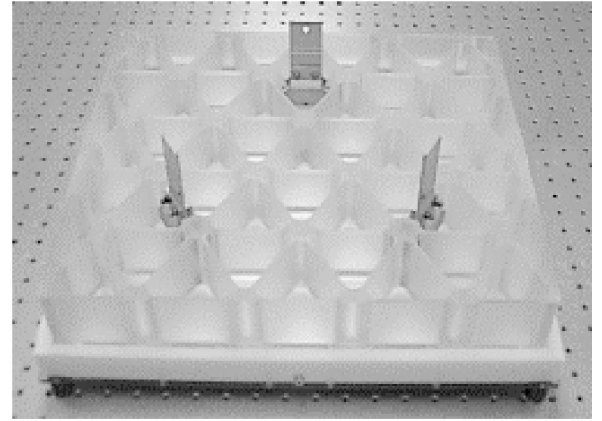
Table 6.1-1: FUSE Mirror Properties

Mirror type	Off axis parabola
Substrate material	Zerodur
Size of clear aperture	387 × 352 mm
Focal length	2245 mm
Off axis angle (to optical center)	5.3668° (SiC mirrors) 5.4678° (LiF mirrors)
Coatings	2 mirrors with SiC 2 mirrors with Al+LiF

The mirrors were fabricated from Zerodur, chosen for its low coefficient of thermal expansion (CTE). The blanks were aggressively weight-relieved: 70% of the substrate material was removed from each, leaving a triangular isogrid rib pattern with a 7.5mm-thick facesheet and a final mass of 7.7 kg (Figure 6-1). This triangular rib structure provided a lightweight but very stiff substrate. SVG Tinsley Laboratories lightweighted the blanks and figured the mirrors into parabolas.



Raymond G. Ohl



Raymond G. Ohl

Figure 6-1 Left: FUSE mirror resting face-up on flexures prior to integration into the mirror assembly. Right: Backside of the FUSE primary mirror illustrating the aggressive lightweighting of the Zerodur mirror substrate.

Each mirror is attached to the front of a honeycomb-sandwich intermediate plate by means of tangential-blade flexures, which minimize mounting-induced stresses and distortions and isolates the mirror from stress induced by adjustments of the actuators (Nikulla, 1997). The flexures are oriented with soft axes radial to the center of the mirror (Figure 6-1 Right), and consist of titanium alloy blades attached to low-CTE Invar fittings. Each Invar fitting is bonded to a mirror rib. Three stepper-motor actuators are attached to the rear of the intermediate plate. This permitted independent tip, tilt, and focus control for on-orbit adjustment of each mirror (Figure 6-2). The tip-tilt mechanism is used to provide rough alignment of the mirrors to the FPA entrance apertures.



Figure 6-2: Face-on view of mirror actuator assembly showing the three actuators and composite structure.

6.1.2 Optical Bench Structure

The instrument optical bench was constructed of hollow rectangular tubes and sheets composed of a graphite/cyanate ester composite material, designed to have a high strength-to-weight ratio, low CTE, and to insure dimensional stability over long integrations (200 kilo-second).

Individual pieces of the optical bench structure were bonded to form subassemblies that were joined by titanium fittings. Optical components were mounted to inserts built into the structure. Other components, such as the mounting plates for the electronics boxes, the baffles, contamination cover, etc., were mounted to the structure by flexures to avoid introducing any loads that might deform the structure and disturb the alignment of the optics. Exceptions to this practice, such as the lower baffle extensions, involved flexible materials that were not expected to apply significant loads. During thermal vacuum testing it was realized that mounting the contamination covers to the spectrographs resulted in undesirable motions of the grating bench. That mounting was modified and the new mounting validated in a second thermal vacuum test prior to launch. The decoupling of secondary hardware from the optical bench was not entirely satisfactory, however. The primary mirrors and gratings were found to move on orbital timescales once on-orbit. These motions,

described in Sections 4.2.3 and 4.3.5, were a significant complication to on-orbit operations.

Mechanical G-release, thermal expansion, and moisture desorption were expected to change the structure's dimensions significantly upon orbital insertion and slowly over the life of the satellite. Any errors in the placement of the mirror assemblies on the instrument optical bench would further misalign the mirrors with respect to the spectrograph (Conard et. al, 1999). Therefore to maintain alignment post-launch and throughout the mission, each mirror was equipped with precision actuators that permitted on-orbit mirror alignment.

6.1.3 Thermal Control

Thermal control is maintained by heaters attached to the intermediate plates, which radiatively couple to the rear of the mirror substrates.

The temperatures of the optical elements were regulated by heaters mounted on their enclosures (“pie pans”), and on the intermediate plate in the case of the mirrors. The instrument thermal control system was always configured to maintain the temperatures of the optics at least two degrees C warmer than their surroundings to minimize the likelihood of contamination.

6.1.4 Pre-launch Performance Specification & Evaluation

Optical testing and modeling of the FUSE primary mirrors were conducted toward a prediction of the on-orbit mirror point spread function (PSF) and its impact on spectrograph slit transmission. The image test was not meant to fully characterize the performance of the telescope mirrors in the FUSE bandpass. Rather, it was designed to insure that there were no severe problems with the flight mirrors and the implications of surface metrology data were understood. The test produced a data set which we used to validate our modeling and extrapolate a prediction into the FUSE bandpass with confidence.

Pre-launch measurements verified that the reflectivities of the optics exceeded their requirements of 32% for the SiC optics and 60% ($\lambda > 1050\text{\AA}$) for the Al/LiF optics. Degradation of total system throughput of up to 20% per year was anticipated, but on-orbit performance was much better. The effective area of FUSE as a function of wavelength and time is presented in Figure 4-7. Total throughput for the Al/LiF channels declined by less than 15% in the mid-wavelength band, and by ~25-30% in the long-wavelength band over the first three years, and was roughly stable thereafter. Performance degradation of the SiC optics differed: throughput declined at a roughly constant rate, falling by ~50% over 8 years. It is not possible to separate degradation of the primary mirrors from that of the gratings.

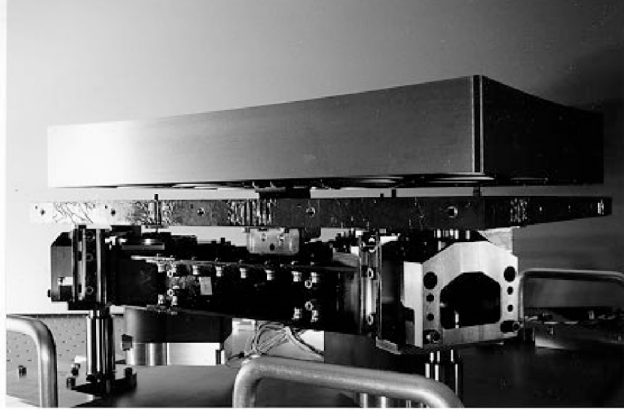
In addition to meeting reflectivity specifications (Oliveira et al. 1999), the fully assembled primary mirrors had an imaging requirement to contain 90% encircled energy (EE) at 100.0 nm in a diameter of 1.5 arcsec. This corresponded to a 16 micron diameter at the focal plane. To meet this requirement, FUSE established fabrication tolerances based on SOHO SUMER mirror heritage (Saha et al. 1996) and a modulation transfer function (MTF) analysis carried out at The Johns Hopkins University (JHU). The surface fabrication specifications were: figure error better than $\lambda/40$ RMS and $\lambda/10$ peak-to-valley (P-V) at $\lambda= 632.8$ nm; midfrequency error less than 20 Å RMS over 10.0-0.1 mm spatial scales; and microroughness less than 10 Å RMS over 100-1 microns. These performance specifications were to ensure adequate transmission through the 1.25 x 20 arcsec, high-resolution spectrograph slit and instrument spectral resolution when using wider slits.

The in-flight mirror PSF performance was consistent with pre-flight measurements and model predictions (Ohl et al. 2000a, Ohl et al. 2000b). The mirror assemblies met the encircled energy requirement of 95% transmission through the 4 arcsecond MDRS aperture, and provided 90% transmission through the 1.25 arcsecond HIRS aperture, far-exceeding the 50% requirement.

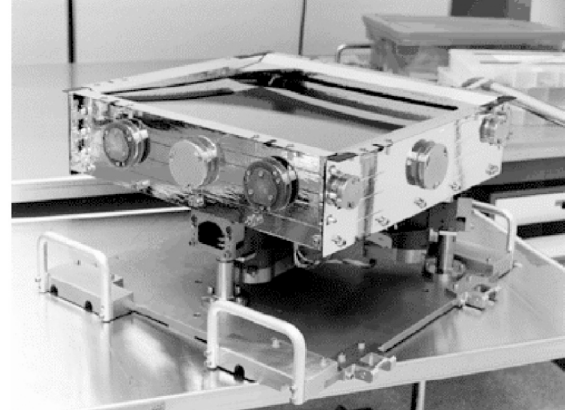
In summary, the primary mirror assemblies were lightweight and adjustable in three degrees of freedom, maximized instrument reflective area in the bandpass, and met a stringent imaging requirement.

6.1.5 Mirror Positioning System Design

The position of each telescope mirror was adjustable through a Mirror Positioning Assembly (MPA). Each MPA (Figure 6-3) consisted of three actuators controlled by one of two Mirror Assembly Electronics (MAE) packages, two thermistors, and one strip heater, with redundant heater elements on the side of the intermediate plate closest to the mirror. The heaters held the assembly to 22 degrees +/- 0.5 degrees C. Each MAE controlled a pair of mirror assemblies with one LiF coated mirror and one SiC coated mirror.



Swales & Associates, Inc.



JHU Applied Physics Laboratory

Figure 6-3 Left: Dummy aluminum mirror with actuator assembly (ref Ohl). Right: Full flight mirror assembly, including pie-pan thermal enclosure and aperture stop.

Three actuators provided focusing and optical alignment for each of the four mirrors (Figure 6-4), enabling a focus resolution of 0.310 microns over a ± 2.1 mm range and a tip/tilt resolution of 0.160 arcsec over a ± 32.34 arcmin range. The “A” actuator controlled the rotation of the telescope mirror about the IPCS y-axis and consequently moved the target in the X-direction on the FPA (and the dispersion direction on the detector). The “B” and “C” actuators controlled the rotation of the telescope mirror about the IPCS X-axis. The combined motion of the “B” and “C” actuators adjusted the position of the target in the y-direction on the FPA. Equal motion of all three actuators moved the mirrors in the z-direction, or focus. Every movement of each actuator had to be tracked on the ground during the mission. Their range of motion is discussed in section 6.7.5.1.

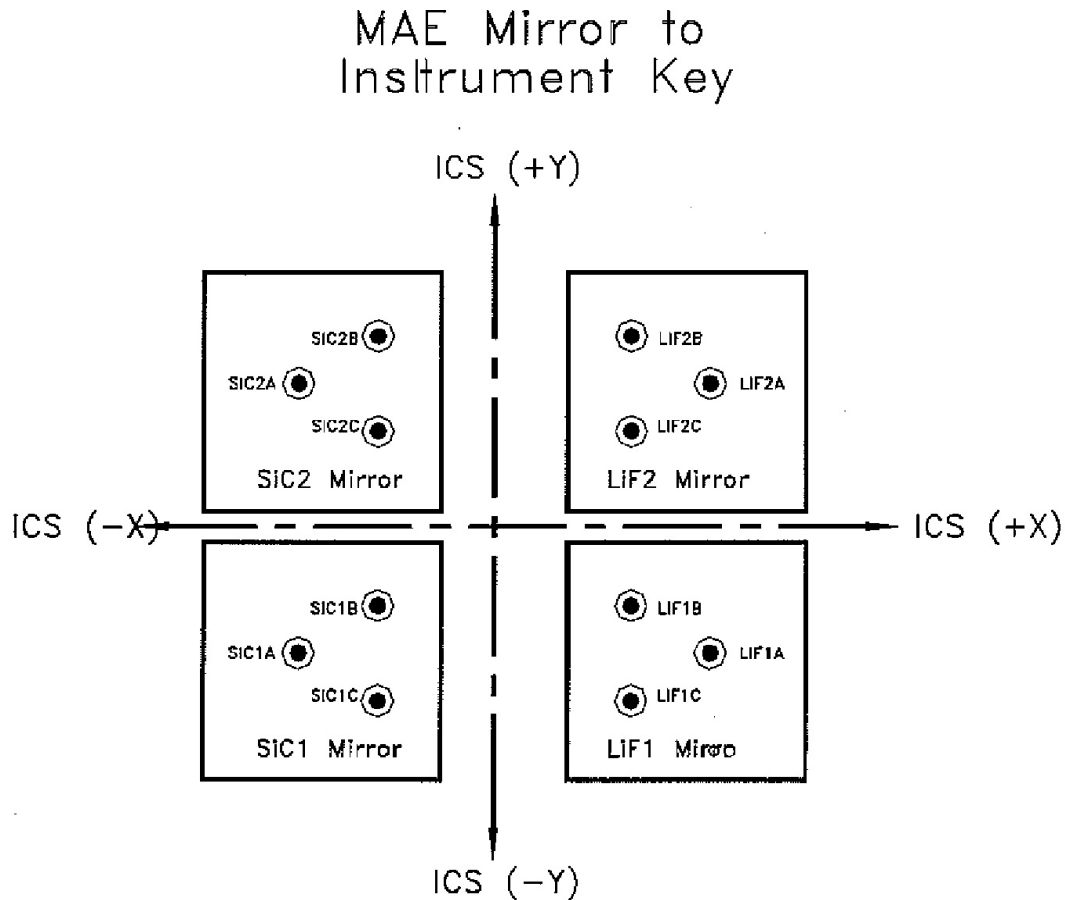


Figure 6-4 The actuator locations relative to the mirrors and the IPCS coordinate frame.

The mirror assembly positioning actuators, each contained a stepper motor and an optical “soft stop” sensor that electrically interfaced with the appropriate MAE. The mirrors were positioned by an open-loop system. The initial on-orbit focus and alignment was determined from ground test. The MAEs had no memory, nor decision-making capability, nor were the absolute positions of the actuators telemetered. The specified stepper motor was commanded to move a certain number of steps in a specified direction, and the MAE attempts to comply with the command. Neither the MAE or the IDS was informed if a hard stop was encountered. The hard stop was also not telemetered. To facilitate alignment in the event knowledge of the mirror position was corrupted, each mechanism had a "reference position". This reference was a known position and, similar to the soft stops, was sensed using an optical disk encoder and therefore independent of commanding a known number of steps enabled.

In general, except for the "soft stop" function, the MAE did not know the current mechanism position. As a consequence, the ground software needed to maintain a

record of the current expected actuator position and drive state of each of the twelve mechanisms. This record was updated each time one of the mechanisms was commanded.

To achieve initial alignment and focus, heavy usage of the MPAs was expected at the beginning of the mission, with only minor mirror adjustments expected later to compensate for structural changes from outgassing. Given this expectation for infrequent adjustments of the mirror positions, no position encoders were placed on the actuators and an on-board mirror motion manager, which could track mirror position through motion commands, was not developed. Post-launch, the four mirror channels (SiC1, SiC2, LiF1, and LiF2) were found to wander with respect to one another. The design savings and the lack of direct mirror tracking proved to be very costly in the operations phase where the frequent need for mirror adjustments required a significant modeling, planning, tracking, and analysis effort.

6.2 □ FPA Motion Control

The FPA electronics were functionally separated into two sides, one for each Rowland circle spectrograph. Each side contained one LiF and one SiC FPA mechanism. The complete subsystem consisted of four mechanisms, one electronics box, and the connecting harnesses. The FPA actuators provide motion of the slit plate along two axes: tangential to the Rowland circle (X) and along the radius of the Rowland circle (Z). These FPA axes are rotated by 30.5 degrees with respect to the IPCS axes, such that the FPA X axis is rotated towards the IPCS Z axis.

6.2.1 FPA X Axis

A High-Output Paraffin (HOP) actuator controlled via a closed loop system drove the X-axis. Operationally, all motion commands to the X-axis mechanisms were issued to the IDS FPA driver task. This task verified that the commanded position was within specified software limits, and then generated the appropriate FPA hardware command for the requested motion. The data number issued by the driver was stored in a command register that was used by a digital to analog converter to provide a reference signal for the control loop. The controller managed the temperature of the paraffin to maintain the FPA at the commanded position. The X-axis actuators were designed to allow a minimum of 10,000 individual motions and/or 1000 full displacements. The commandable range of motion was 400 microns. The FPA X axis actuators were adjusted routinely for purposes of channel alignment and for FP-split procedures.

6.2.2 FPA Z Axis

The Z-axis was driven by a stepper motor and lead-screw, commandable in increments of 38 motor steps. Each of these units resulted in a motion slightly less than 10 μ m. Limit sensors were used to prevent motion beyond the design limit of $\pm 280 \mu$ m. The practical operational limit, however, was $\pm 250 \mu$ m. The design requirement for each stepper motor was 80 in-flight motions. The history of in-flight FPA motions is given in Table 6.2-1. The first focus run was only partially-executed, but the second spanned the full range of -240 μ m to +240 μ m in steps of 40 μ m each.

The final FPA Z positions were set on 24 March 2000, except that the LiF2 Z position was adjusted on 29 June 2005 to improve the focus of FES-B, and then back again at the end of the mission for the final series of airglow observations.

OBS_ID	DATEOBS	TIMEOBS	LiF1	LiF2	SiC1	SiC2
Launch	1999-06-24		60	20	0	0
I8150109005	1999-11-23	17:55:05	Focus run			
P1020504001	1999-11-24	18:08:09	60	65	-100	-75
I8160101	1999-11-26	19:11:34	Focus run			
I2070801001	1999-11-27	06:49:49	64	66	-100	-77
P1010502012	1999-12-12	14:09:50	64	210	-238	-225
S5130301001	2000-03-24	13:53:37	-35	145	-100	60
M1051402002	2005-06-29	11:40:36	-35	-250	-100	60
S1001701001	2007-08-15	14:26:06	-35	145	-100	60

Table 6.2-1 History of FPA Z-axis motions. The first three columns give the observation ID, date, and start time for the observation immediately following a change in FPA Z position.

6.3 □ Detector Design and Pre-launch Characterization

6.3.1 Hardware and Software Description

The FUSE instrument included two Double Delay Line (DDL) detectors which collected incoming photons and measured their positions. Three FUV detectors were built at the Space Sciences Laboratory at the University of California, Berkeley. Unit FL01 remained on the ground as a spare and was used for ground testing, while units FL02 and FL03 were used in the instrument as Detector 1 (side 1 of the instrument, collecting photon events as part of the SiC1 and LiF1 channels) and Detector 2 (SiC2 and LiF2), respectively. The three detectors had identical physical characteristics, and were designed to be as similar as possible. Differences between them are due primarily to differences in the microchannel plates and the adjustments of the electronics to account for those variations. The differences in wavelength coverage between side 1 and side 2 of the instrument were determined by the mounting locations on the Rowland circle.

Each detector consisted of two segments. Mechanically, each detector was a single unit; electrically each segment was unique with most of its own electronics. Keeping the segments separated permitted each to be individually optimized. In addition, it ensured that a problem with one segment did not prevent its companion from being operated normally. Because of this design, one detector segment could be operated normally while the high voltage on the adjacent segment was turned off.

Light coming from one of the FUSE gratings to the detector first passed through a 95% transmission, +15 volt ion repeller grid, then through a 95% transmission 'QE

Grid' designed to improve the quantum efficiency of the system, before reaching the KBr-coated microchannel plates (MCPs). The photons striking the photocathode were converted to photoelectrons via the photoelectric effect, multiplied as they passed through the stack of three (Z-stack) MCPs, then proximity-focused onto the DDL anode. The DDL electronics determined the location of each charge cloud by measuring the time it took for the charge to propagate along the anode (for the X, or dispersion direction) or by charge division (for Y, or cross-dispersion). The top-level detector specifications are summarized in **Table 6.3-1**.

Table 6.3-1 Detector Specifications

Specification	Description
MCP pore size (pore diameter / center-to-center spacing)	10 μm / 12.5 μm (top & bottom plates) 12.5 μm / 15 μm (middle plates)
MCP pore bias angle	13°
MCP Configuration	Z-stack
MCP size	95 mm x 20 mm, 80:1 L/D
MCP resistance	< 30 M Ω
Anode Type	Double Delay Line
Photocathode	KBr
Ion Repeller Grid	95% transmission, 1247 x 1247 μm spacing, flat
QE enhancement Grid	95% transmission, 1042 x 1009 μm spacing, curved to match MCPs
QE in FUSE bandpass	14 – 30%
Active Area	85 x 10 mm x 2 segments ~7 mm gap between segments
Curvature of front surface of MCPs	826 mm radius
Number of Pixels	16,384 x 1024 per segment
Pixel size	6 μm x 10–17 μm , depending on segment
Detector resolution	~20 μm x ~80 μm
Lifetime Specification	> 10 ⁷ events per 10 ³ μm^2

Each detector subsystem was composed of three interconnected, modular assemblies. These were the Vacuum Assembly, Electronics Assembly, and Stim Lamp Assembly. The Vacuum Assembly was mounted in the spectrograph cavity and contained the detector imaging elements (grids, MCPs, anode, etc.) in a stainless steel vacuum housing, along with a high voltage filter module, charge amplifiers, timing amplifiers, a motorized door and mechanism, and ion pumps to maintain a high vacuum inside the vacuum box before launch. The Electronics Assembly, mounted to the instrument electronics baseplate in the electronics cavity, included the low- and high-voltage power supplies, Time-to-Digital-Converters (TDCs), Charge-to-Digital-Converter (CDCs), and a Data Processing Unit (DPU), along with an interface to the instrument computer – the Instrument Data System (IDS). The Stim Lamp Assembly consisted of a mercury vapor lamp which was mounted to the spectrograph structure inside the spectrograph cavity and was powered and controlled via the detector electronics. Details on each of these assemblies are given in the sections below.

Each detector subsystem included thirteen thermistors (**Table 6.3-2**) to monitor the temperature of the detector hardware. Although the temperatures of the anode and some parts of the electronics were known to affect the data, the thermistors information was only used as a general diagnostic, and detector stim pulses, described below, were used to account for temperature effects in the data.

Table 6.3-2 Detector 1 Thermistors

Telemetry Mnemonic	Location
I_DET1AMPATEMP	Segment A Charge Amplifier
I_DET1AMPBTEMP	Segment B Charge Amplifier
I_DET1DOORTEMP	Detector Door
I_DET1DPUTEMP	Data Processing Unit
I_DET1ELTEMP	Detector Electronics Assembly
I_DET1HVFLTRTEMP	High Voltage Filter
I_DET1HVMODLTEMP	High Voltage Module
I_DET1LAMPTEMP	Stim Lamp
I_DET1PCTEMP	Power Convertor
I_DET1PLTEMP	Detector Backplate
I_DET1TDCATEMP	Segment A TDC
I_DET1TDCBTEMP	Segment B TDC
I_DET1TEMP	

More details on the design of the FUSE detectors can be found in Siegmund et al. 1997 and Sahnou et al. 2000.

6.3.1.1 Vacuum Assembly

Each Vacuum Assembly consisted of a stainless steel vessel which contained the grids, MCPs, and anodes used for collecting the photons, along with two 4 liter per second ion pumps; also included as part of this section and mounted outside of the vacuum box was much of the electronics used for calculating the locations of the photons. Since the MCPs and the photocathode had to be operated and stored in a vacuum environment, a recloseable door was included in the design. During ground testing in vacuum the doors were opened to allow FUV light to reach the MCPs. When ground testing was complete, the doors were closed and the vacuum maintained with the ion pumps. A pumping port allowed the vacuum box to be evacuated with a ground vacuum pump, and then an attached valve could be closed once the pressure was low enough for the ion pump to maintain the pressure. The doors were opened in orbit on July 16 and 17, 1999, after the spectrograph cavity had partially outgassed, and they were never closed again. Two sapphire windows (one for each segment) on each door allowed visible light to reach a portion of the MCPs when the doors were closed. This permitted some ground testing of the detector while it was at a safe pressure ($< 10^{-6}$ Torr) despite the fact that the instrument was at normal atmospheric pressure.

Inside each vacuum box were two electrically independent segments mounted as a single mechanical and optical unit. Since the MCPs were part of the optical system,

the MCP stackups were mounted to and precision aligned to the detector backplate. The backplate had an optical cube which was used to align the detector during spectrograph integration and test. The preflight specification was that the front surface of the MCPs be held to within 25 μm of the 826 mm Rowland circle in order to ensure the highest resolution. During detector installation, shims were inserted to align the MCPs on each detector to the Rowland circle by using an optical cube on each backplate. The MCP positions had been previously determined with respect to the cubes to within $\sim 37 \mu\text{m}$. During the alignment of Detector 1, a 6.3 arcsecond tilt was inadvertently introduced, but the instrument resolution was not limited by this tilt.

Each stackup contained a Z-stack of three 95 mm \times 20 mm MCPs which acted as the photon-sensitive surfaces, although a front aperture mask limited the active area of each segment to 85 \times 10 mm, with a ~ 7 mm gap between them. The top and bottom MCP in each stack had 10 μm pores on 12.5 μm centers, while the middle plates had 12.5 μm pores on 15 μm centers; these were different in order to help minimize the moiré pattern which often occurs when identical MCPs are stacked (Tremisn et al., 1999).

The top plates were coated with an opaque KBr photocathode in order to improve the sensitivity to FUV radiation. Photons impinging on the front surface of one of the MCPs, which were held at a high potential, created photoelectrons which were accelerated down the pores due to a high potential maintained across the plates. Each time an electron struck the walls of one of these pores, multiple secondary electrons were generated, so that a single photon incident on the top plate resulted in a cloud of $\sim 10^7$ electrons which was several millimeters in diameter exiting the back side of the third plate. These electrons were accelerated across a 7 mm gap to a helical double delay line anode with a period of 600 μm and an active area of 94 \times 20 mm, where they were collected. The anodes were constructed on a flexible RT/Duroid substrate, and were curved to match the MCPs. The anode-MCP separation was 7 mm, and voltage difference was 550 volts.

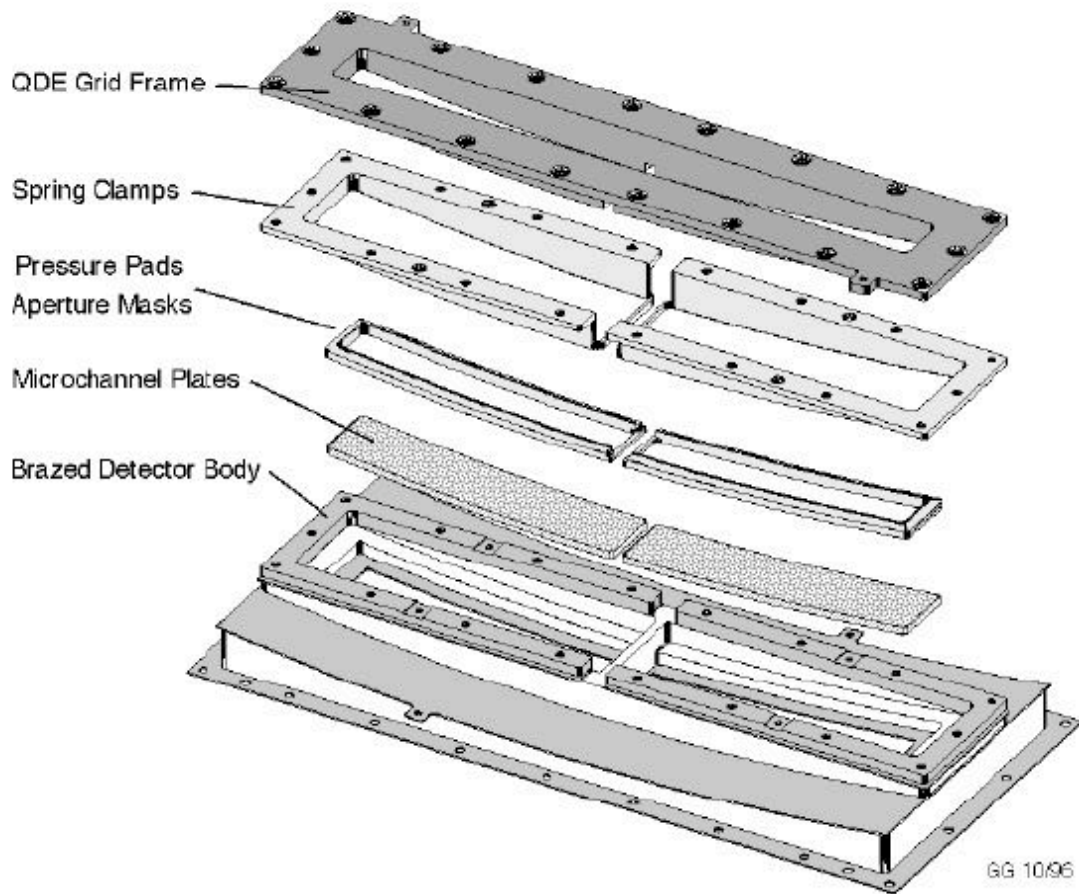


Figure 4.4.1: Detector Body Assembly

Figure 6-5 Expanded view of the detector stack mounting in the FUSE detector. The QE grid is held by the frame at the top, and the curved MCPs are mounted to a cylindrical surface to match the Rowland circle.

In front of the MCPs were two 95% transmissive electroformed nickel mesh grids to improve the performance of the detector. The front, flat grid, which was mounted on the vacuum box aperture, sat approximately 35 mm in front of the MCPs and was held at +15 volts; it was designed to exclude ions from the vacuum cavity. This ion (or plasma) grid was powered whenever the detector electronics were powered; it was not controllable in flight, but housekeeping telemetry was available to show the status of the grid voltage. In addition, a Quantum Efficiency (QE) grid, which was curved to match the curvature of the MCPs, was placed 6 mm above the front surface of the MCPs in order to improve the QE of the system by forcing photoelectrons generated by the MCP web back down the pores. The QE grid was held at 1200 volts above the front MCP. It was the source of the optical anomaly known as the ‘worm’ (see section 4.3.4).

The detector body assembly was bolted to a stainless steel backplate which provided the mechanical and thermal interface to the rest of the instrument. A mu-metal magnetic shield, which surrounded the body assembly and shielded it from external magnetic fields, was also mounted to the backplate. This entire assembly was enclosed inside the vacuum box.

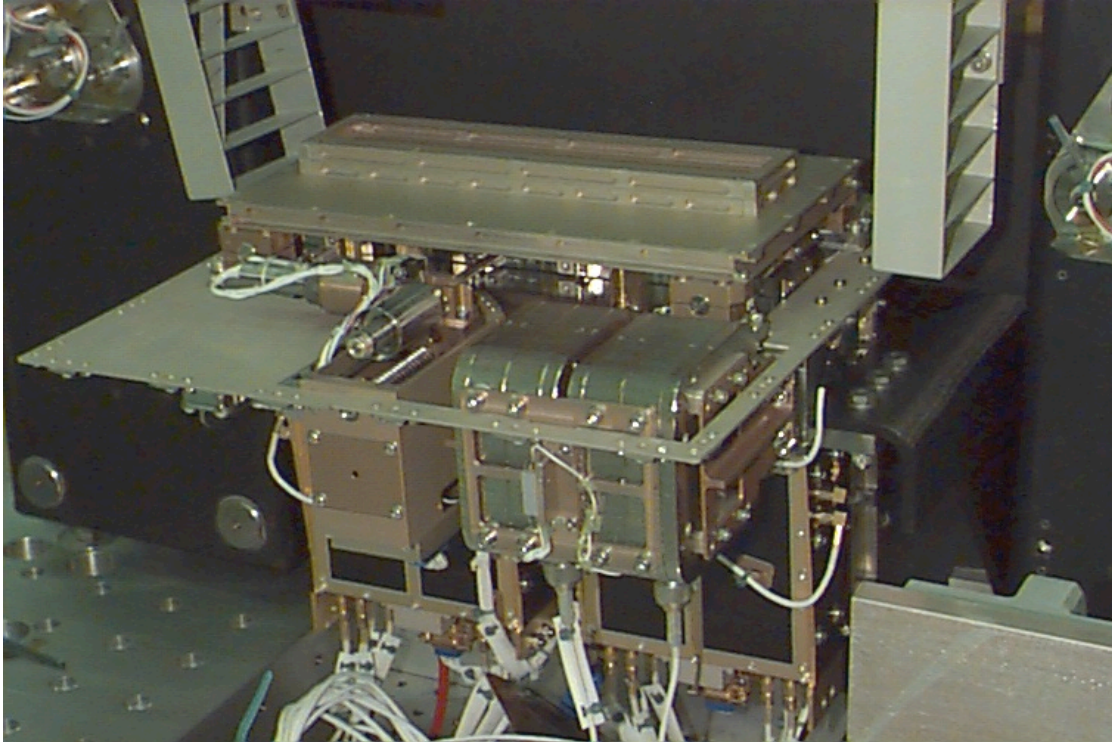


Figure 6-6 A FUSE detector Vacuum Assembly mounted to the detector mounting bracket in the spectrograph cavity. The door assembly is at the top, with the light baffle protruding. Two ion pumps are visible at the front right, and the high voltage filter module, charge amplifiers, and timing amplifiers are visible behind them. The ladder-like structures at the top on either side of the detector are spectrograph baffles.

Also mounted to the backplate, but outside of the vacuum box, were two high voltage filter modules which provided the MCP, QE grid, and rear-field voltages. The backplate also supported the amplifiers, which amplified the charge collected by the anode before passing them on to the Detector Electronics Assembly. The Vacuum Assembly was thermally connected to the electronics baseplate via copper straps, which also provided chassis grounding. Figure 6-6 shows a photograph of a Vacuum Assembly mounted in the FUSE spectrograph.

6.3.1.2 Electronics Assembly

There was one Electronics Assembly for each detector; each consisted of nine interconnected electronics boxes (Figure 6-7). The major functional components of each were:

1. The power supplies, which were responsible for providing power (high voltage to the high voltage filter modules and ion pumps and low voltage power for other components) to the detectors.
2. A Delay Spool, used to delay the signal from one side of the anode in order to ensure that the START pulse always preceded the STOP pulse.
3. Two 14 bit Time-to-Digital Converters (TDC) modules, which measured and digitized the signals from the vacuum assembly electronics into digital signals in order to measure the X (dispersion direction) coordinates of an incident photon.
4. Two Charge-to-Digital Converters (CDC) modules to digitize the charge from the upper and lower delay line for use in calculating the Y (cross-dispersion) position of an incident photon.
5. A Data Processing Unit (DPU), which processed the digital signals from the TDCs and CDCs, provided command and housekeeping functions, and provided an interface to the IDS computer and other parts of the instrument.



Figure 6-7 Electronics Assembly and Stim Lamp Assembly of the spare detector.

Functional block diagrams of the system are shown in **Figure 6-8** and **Figure 6-9**. The following sections describe some of these components in more detail.

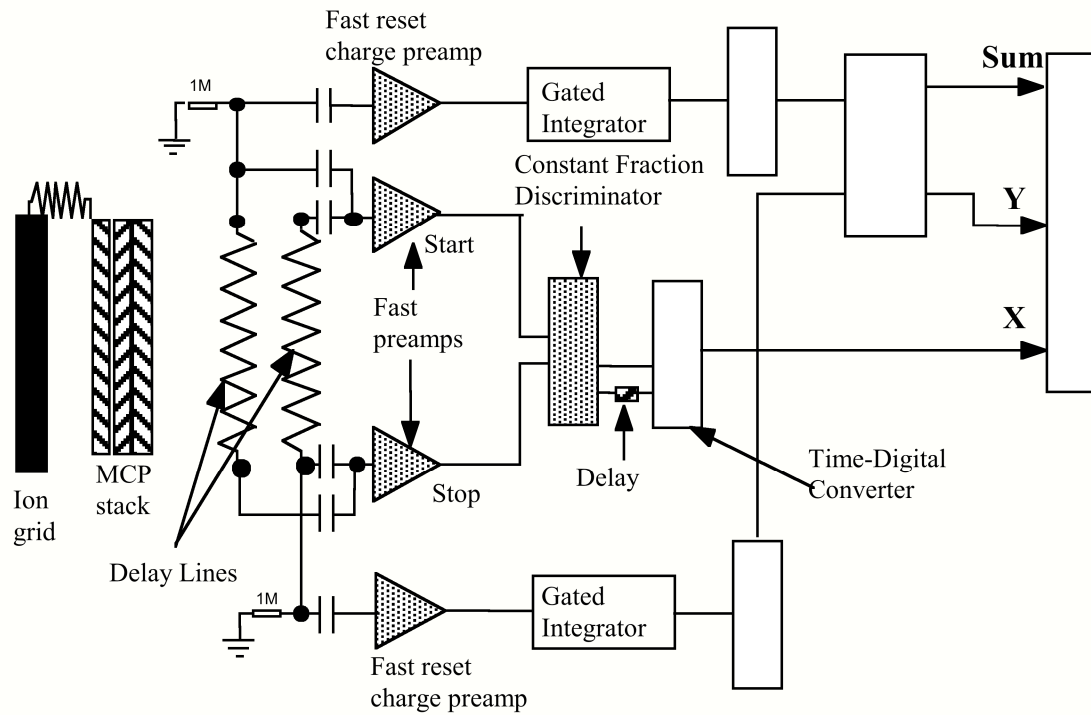


Figure 6-8 Block diagram of the encoding electronics for the FUSE detectors.

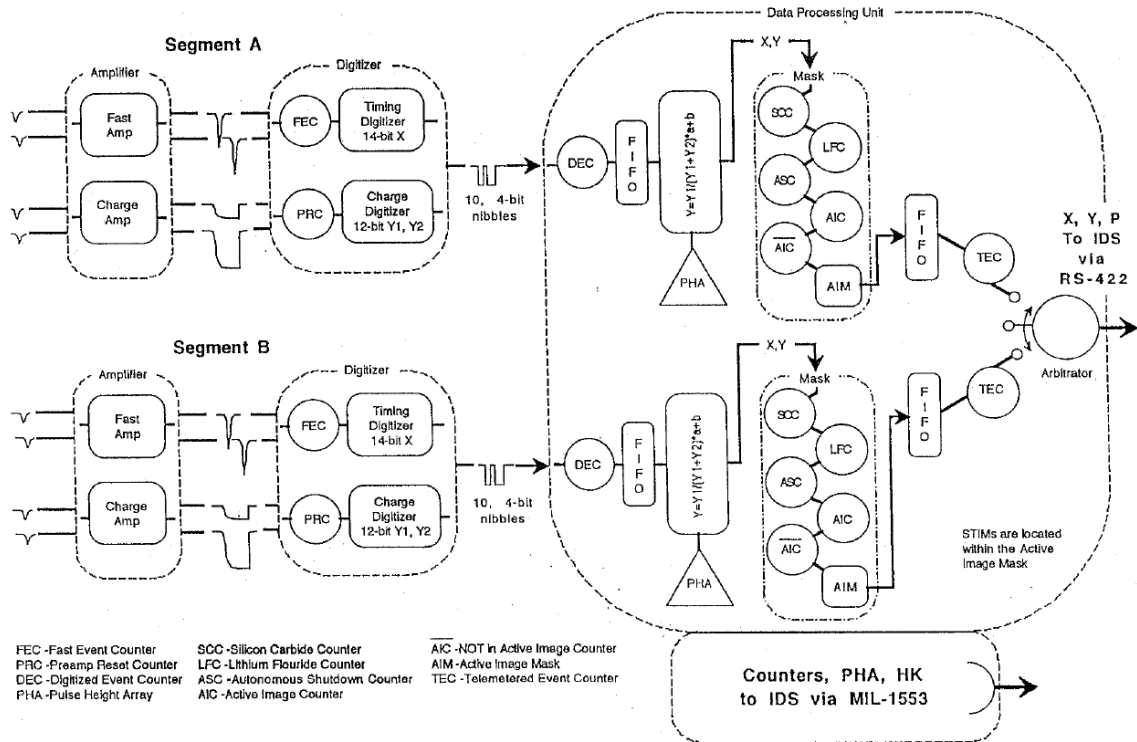


Figure 6-9 Functional Block Diagram of the Detector Electronics Assembly (hardware and software).

6.3.1.2.1 Digitizers

The timing digitizers determined the X (dispersion direction) position of the charge cloud to $\sim 20 \mu\text{m}$ by measuring the difference in time it took the charge pulse to propagate to the two ends of the anode, and then digitized the results to 14 bits (16384 pixels). The scale was adjusted so that the pixel size was very close to $6.0 \mu\text{m}$, although detector distortions meant that it varied with position. Deviations were generally only a few percent, except at the ends of each segment, where they could be much larger.

In the Y (cross-dispersion) direction, separate Y1 and Y2 signals from the upper and lower half of each DDL anode were digitized to 12 bits by the charge digitizers. The digitized X, Y1, and Y2 values were then passed to the detector DPU for further processing.

6.3.1.2.1.1 Stim Pulses and Thermal Stability

Since both anode and electronics temperatures were known to affect the measured location of photon events in the dispersion direction, it was necessary to provide a thermal correction to the data in the CalFUSE pipeline. Rather than relying on the measured temperatures, however, the positions of two stimulation ('stim') pulses on each segment were used for this correction. These pulses were generated by injecting

charge into the amplifiers so that pseudo-events are created near the left and right ends of each segment, beyond the active area of the MCPs. Since the stim pulses passed through the same electronics as incoming photons, this method provided a more accurate method of measuring the thermal effects on the data than relying on the temperatures. The stim pulses were normally commanded on for 59 seconds at the beginning and end of every exposure, although for snapshot exposures they were left on throughout the exposure. Stim rates varied slightly from segment to segment, but were approximately 45 counts per second per stim, giving a total rate of about 90 per second per segment.

Prelaunch ground testing using the spare detector showed that the stim pulses moved as a function of temperature. In particular, the temperatures of the anode (best tracked via the backplate thermistor) and the electronics (tracked with the TDC temperature) were both shown to affect the stretch (the separation between the two stims) and shift (position of the mean stim position) of the detector format, with the anode temperature dominating the former, and the electronics temperature dominating the latter. On orbit stim pulse data show strong correlations between backplate temperature and stretch, and between the stretch of two segments on the same detector, which is consistent with the ground measurements. The inflight shift measurements, however, showed very different behavior between the segments (Figure 6-10).

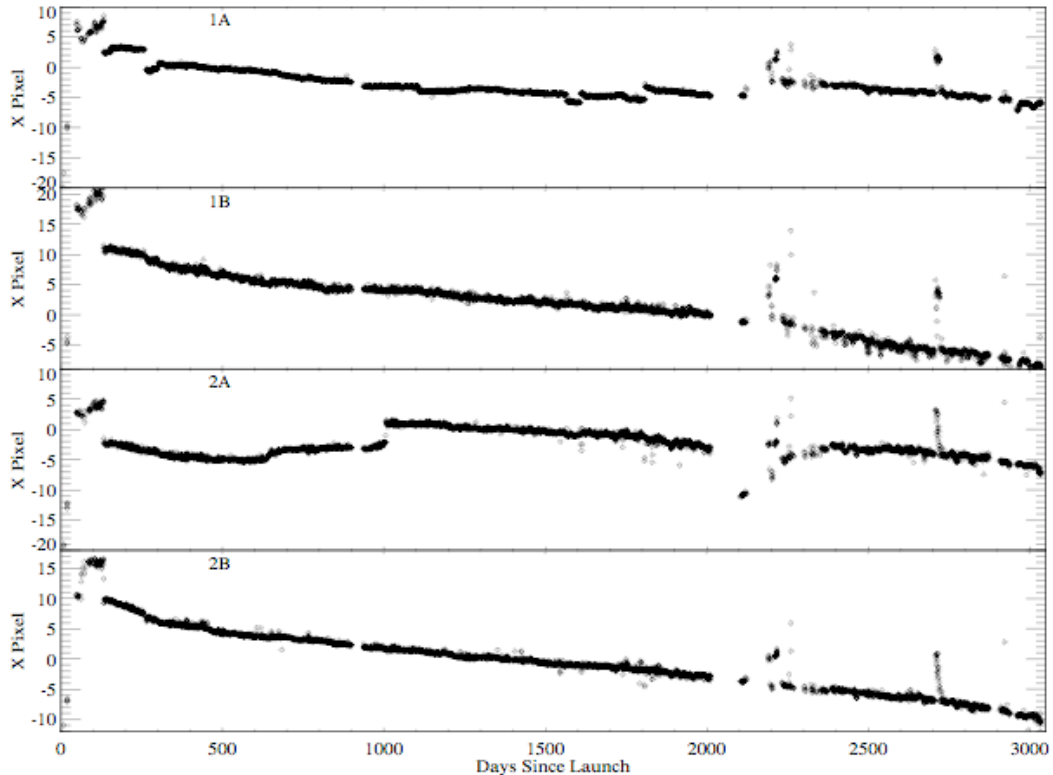


Figure 6-10 Detector X shift, as measured by the change in position of the stim pulses, for all four segments during the mission. Long term trends appear to dominate short term temperature effects, particularly on segments 1B and 2B.

The positions of the stims in an exposure are measured by CalFUSE, and a linear shift and stretch is applied to the raw data in the dispersion direction in order to move the stims to their nominal position. In the cross-dispersion direction only a shift is applied, since their separation is too small to allow reliable stretch information.

Because the stim pulses are artificially generated, their shape does not exactly match the properties of events from the MCPs. In fact, the shapes of the stim pulses change as a function of count rate, with a sharp, single-peaked image at low count rates turning into a double-peaked distribution at high count rates. For normal FUSE count rates, the second peak was small and thus did not cause CalFUSE difficulty in measuring the position.

The correction for thermal effects based on stim pulse positions assumes that the corrections are linear over the detector, and that the thermal environment is changing slowly. Large temperature changes, such as those due to bringing the detector high voltage from SAA level to full, could result in rapid changes of the scale during an exposure, and those effects are much harder to correct for. In addition, this method assumes that the stims accurately track the overall detector format. While this is believed to be true in general, numerous unexplained changes in stim position that

could not be correlated with any known external effects were seen (Figure 6-10). These may result in uncorrected errors in the calculated wavelength scale. Some exposures are missing one or both stim pulses. In those cases, CalFUSE must assume positions based on a record of typical positions from other exposures.

6.3.1.2.2 Data Processing Unit

6.3.1.2.2.1 Overview

The detector Data Processing Unit (DPU) was responsible for the electronic processing of the collected photon events output by the digitizer. DPU memory contained two 16 KB regions from which code could be executed; these were known as the upper core (UC) and lower core (LC) memory regions. At boot up, a control program was loaded into memory from an onboard EPROM. This was a basic version of the DPU code (version 16200) which had been programmed into the PROMs before spectrograph Integration and Test in 1997. Other versions of DPU code (Section 6.3.1.2.2.7) could then be loaded (from the ground or IDS memory) into UC memory, and execution switched there.

The main functions of the detector Data Processing Unit (DPU) were:

1. Accepting commands from the IDS on the MIL-STD-1553 Instrument Data Bus and passing them on to the detectors.
2. Collecting the photon event data (X, Y1, and Y2) from the digitizers and calculating the Y coordinate (Section 6.3.1.2.2.2)
3. Applying masks to the data (Section 6.3.1.2.2.3) and counting events.
4. Packaging the science data and sending it on to the IDS via the RS-422 Science Data Bus.
5. Protecting the detector in case of count rates that were too high (Section 6.3.1.2.2.3).
6. Accumulating 7 bit pulse height histograms (Section 6.3.1.2.2.4).
7. Monitoring current draw from the high voltage and auxiliary power supplies, and reporting diagnostics if necessary (version 16500 of the code and above - Section 6.3.1.2.2.5)
8. Collecting housekeeping telemetry from the detector.
9. Monitoring the detector behavior, and issuing a diagnostic code if an unexpected event occurred (Section 6.3.1.2.2.6).
10. Formatting housekeeping status, counters, and pulse height information and passing it to the IDS via the Instrument Data Bus.
11. Continuously calculating checksums of specified regions of detector memory, and issuing diagnostic codes when the checksum changed.

6.3.1.2.2.2 Calculation of Y Position

After the output from the digitizers was passed to the DPU, the Y coordinate was calculated by taking the ratio of charge between the two halves of the DDL, as $Y = Y1/(Y1+Y2)$, where Y1 and Y2 are the charge on the upper and lower half of the

delay line. This result was digitized to 10 bits (1024 pixels), although the accuracy was only $\sim 80 \mu\text{m}$. Y pixel sizes varied from ~ 9 to $\sim 17 \mu\text{m}$ in the raw data, depending on detector and segment. The pulse height, or total charge collected, was also digitized at this point as part of the y calculation. The result was digitized to 7 bits and used to construct a pulse height histogram (Section 6.3.1.2.2.4).

6.3.1.2.2.3 Masks and counters

For each segment there were four programmable masks (shown in the block diagram in Figure 6-9) which were used to monitor the count rate in a specific region of the detector. Each mask had an associated counter which counted the number of events in each of the regions defined by the masks. The masks and counters were the Active Image Mask and Active Image Counter (AIC), the SiC and LiF masks and counters, and the Autonomous Shutdown Mask and Autonomous Shutdown Counter (ASC). The latter was also known as the SAA counter, since it was designed to measure background counts in the South Atlantic Anomaly. Each of the counters recorded the number of events that fell in a particular mask region on each segment. DPU commands were used to enable or disable regions of the segment for each counter and mask in 16×16 pixel regions. A complete set of aperture-specific masks for all four segments was loaded near the beginning of each observation script via the `set_det_mask_f` flight script. This script cleared all previous masks, then loaded an Active Image Mask that covered the entire segment, an Autonomous Shutdown Mask that fell on an unilluminated portion of the segment, and SiC and LiF masks that were placed to collect essentially all the events from the aperture specified for that observation.

The Active Image mask was used to define the region of a segment to pass to the IDS, thus acting as a spatial filter. It could have been used to exclude a region around a hot spot, for instance, so that the Science Data Bus would not be overwhelmed by these events. However, these masks were left enabled everywhere on all four segments throughout the mission. Thus, the Active Image Counter recorded the total number of events passed from the detector to the IDS on the Science Data Bus. Each event which passed through all the thresholding was output as a 32 bit word containing the detector ID (1 bit - MSB), segment ID (1), x (14), y (10), pulse height (5), and a format bit (1) to identify this as a photon event. These words were passed on to the IDS for further processing via the Science Data Bus.

The SiC and LiF masks were used to define the regions of the detector to use for target peak up, so they were different for each aperture and each segment. The objective was to determine the count rate from the object in the slit, while minimizing the count rate from the other apertures and the detector background. These masks included the entire spectral range covered on each segment, so they included any airglow in the aperture.

The Autonomous Shutdown Mask was used to monitor a region on the detector which was not illuminated by any of the apertures, so it provided a way to monitor the detector background. The DPU code used the count rate for bright object protection; if the count rate over a specified time for a particular segment exceeded a predefined threshold, the high voltage on that detector segment was lowered to SAA level. This protection was designed to minimize the chance of scrubbing the detector due to an extremely high count rate at nominal gain. As originally envisioned, this was designed in to the system primarily to protect against passing through the SAA without lowering the high voltage (as a result this counter was also known as the ‘SAA counter’). In practice, most of the shutdowns were due to event bursts, which complicated the way thresholds had to be set (Section 4.4.3.3).

The SiC, LiF, and Autonomous Shutdown masks were changed six times during the first two years of the mission (Table 6.3-3) in order to better align them with the position of the spectra and make them match the SIA tables (Section 6.3.3).

Table 6.3-3 Summary of detector mask changes during the mission

Approximate Date	Purpose
At Launch	Prelaunch values
8/20/1999	Adjusted SiC1 and LiF1 based on first view of side 1 spectra
11/5/1999	Adjusted SiC2, LiF2 and ASC2 based on first view of side 2 spectra
4/1/2000	Clear ASC mask before setting to avoid adding default mask to new ASC
4/19/2000	Change ASC mask on segment 2A
11/18/2000	Reinitialize ASC mask to avoid SEUs
10/17/2001	Change size of ASC2 mask to avoid contamination from MDRS
11/19/2001	Match masks to SIA tables
4/18/2003	Special AICs for bright objects

An additional counter, the Fast Event Counter (FEC – also known as the Front End Counter) measured the total number of events over the entire segment at the output of the fast amplifiers. The number of counts lost before the FEC, e.g. due to the MCPs themselves, is very small at typical FUSE count rates, and was therefore ignored. The IDS code monitored the FEC rate for each segment and shut off the high voltage for that segment whenever the rate exceeded 45,000 counts per second for three seconds. These values were hard coded, but IDS scripts were written to poke the relevant memory locations in order to change them if desired. They were changed temporarily several times during the mission when bright objects were observed.

The Digitized Events Counter, or DEC, counted the number of events that were processed by the digitizer and reached the DPU FIFO (again, over the entire segment). This was typically less than the number of counts in the FEC, since there were electronics dead time effects which caused events to be discarded in the digitizer. The DEC and FEC were used in the calculation of the dead time of the instrument (Section 6.9).

A summary of the masks and counters, along with their functions is given in Table 6.3-4.

Table 6.3-4 Detector masks and counters

Mask / Counter Name	Mnemonic	Operates On	Bit in Mask Word	Description
Fast Event Counter or Front End Counter	FEC	Full segment	N/A	Total counts reaching the detector
Digitized Event Counter	DEC	Full segment	N/A	Events above threshold
Preamp Reset Counter	PRC	Full segment	N/A	
Active Image Counter	AIC	Modifiable	1 (LSB)	Counts sent to the IDS
Silicon Carbide	SiC	Modifiable	2	Peakup in SiC channel
Lithium Fluoride	LIF	Modifiable	3	Peakup in LiF channel
Autonomous Shutdown Counter	ASC or SAA	Modifiable	4 (MSB)	Detector background

All counters were stored as 24-bit values (0 – 16,777,215) and were updated once per second. They counted continuously from the time the detector was turned on, so they would regularly roll over. They were typically sent to the ground via housekeeping telemetry once every sixteen seconds, although that rate changed in certain telemetry modes.

The FEC, AIC, SiC, LiF, and ASC counter values are saved for each exposure in the housekeeping (hskpf.fit) files, and the first four of these are used to populate arrays in the Intermediate Data File created by CalFUSE. The FEC, DEC, SiC, LiF, and ASC counter values at the beginning and end of each exposure are also recorded in the engineering snapshot and then copied into the header of the science data files. CalFUSE uses the counter information for calculating dead time (Section 6.9) and Y blooming (Section 4.4.7.1) effects. It should be noted that because the SiC and LiF counters change with aperture, the count rates for observations taken in different apertures are not directly comparable.

6.3.1.2.2.4 Pulse Height Histograms

As described previously, a 5-bit pulse height for each photon event is transmitted to the IDS along with the position information. For TTAG exposures, all of this information was sent to the ground, but for HIST exposures this pulse height information is discarded along with the timing information. However, for both TTAGs and HISTs data, the detector DPU also accumulated a 7-bit pulse height histogram over each detector segment and sent it (in pieces) to the IDS. The IDS accumulated these pulse height distributions for all four segments and downlinked a complete set of PHDs every 128 seconds. Although these full-segment PHDs could not be used to determine gain as a function of position, they were useful diagnostics which could be used to monitor the gain of the detector during high count rate observations, such as the stim lamp exposures or other HIST observations. The higher resolution was also potentially useful for setting the onboard charge thresholds, but they were never adjusted (except for testing) in flight.

6.3.1.2.2.5 Current Protection

An important function of the DPU code was to monitor the current draw of the microchannel plates (HVIA and HVIB for segments A and B), and the auxiliary current power supply (AUXI). The AUX power supply was used to power the ion pumps, the detector door, and the stim lamps.

More details are given in the discussion of High Voltage Transients in Section 6.3.5.

6.3.1.2.2.6 Detector Diagnostic Codes

An important job of the DPU code was to continually monitor the detector hardware and software to look for out-of-limit conditions. When a problem was identified, a diagnostic code was issued and other protective action was taken if warranted (Table 6.3-5). Since the two detectors were independent, they each issued their own diagnostic codes.

Table 6.3-5 Selected DPU Diagnostic Codes

Diagnostic (hex)	Description	Effects on operations
16	AUXI threshold exceeded* (mini-crackle)	None
18	CRC changed in lower RAM	Associated CRC change triggers IDS process to reload DPU code
19	CRC changed in upper RAM	Associated CRC change triggers IDS process to reload DPU code
1A	CRC changed in ROM	None
1B	Watchdog reset as part of power up	None
20	CRC changed in segment A mask	None
21	CRC changed in segment B mask	None
22	Counts in ASC counter exceed threshold in one of the segments (SAA shutdown)	Drop HV on affected segment to SAA level.
27	HVIA threshold exceeded (mini-crackle)	None
28	HVIB threshold exceeded (mini-crackle)	None
2A	HVIA threshold exceeded for longer than persistence time* (crackle)	HV shut down on both segments.
2B	HVIB threshold exceeded for longer than persistence time* (crackle)	HV shut down on both segments.
2E	AUXI threshold exceeded for longer than persistence time* (crackle)	HV shut down on both segments.

* Not included in DPU code version 16200

The diagnostic codes in the table above can be divided into three types:

1. Power on (1B) – When a detector is powered on, a diagnostic 1B was issued.
2. CRC changes (18, 19, 1A, 20, 21) – A background process in the DPU code continually checked the detector code (stored in both RAM and ROM) and masks for changes. Although some changes were expected (when uploading

new masks at the beginning of an observation, for example), many unexpected changes due to bit flips were seen during the mission (see Section 6.3.4).

3. High count rates (22) – When the number of counts in the ASC for a segment exceeded a defined threshold, the detector HV on that segment was dropped to SAA level. This behavior was designed primarily to protect the detector from passing through the SAA at full voltage levels, and it did serve that purpose several times during the mission (Section 4.4.8).
4. High voltage problems (16, 27, 28, 2A, 2B, 2E) – See Section 6.3.5.

6.3.1.2.2.7 DPU Code Versions

Six different versions of DPU code were used during the mission. The properties of each are summarized in Table 6.3-6. Version 16200 was resident in the detector DPU PROM, and was loaded into lower core memory when a detector was turned on. It was used during detector ground characterization, spectrograph integration and test, and part of instrument and satellite integration and test. This version had no protection for high voltage transients (crackles).

Version 16500 was provided by UC Berkeley in early 1999 to add protection and diagnostics after the first detector crackle was seen during instrument testing at Goddard Space Flight Center. This version also decreased the range of upper core code memory checked by the CRC checking task. This decreased the susceptibility to upper core SEUs by about 25%, since only 10,544 bytes (instead of 14,336) were being checked.

UC Berkeley provided Version 16600 for improved crackle protection after initial on-orbit experience. It added downlinking of the UC CRC (in addition to the LC CRC which had been in previous versions) so that automated code loading could be implemented. It also extended the CRC change made in the previous version to the lower core code region.

After an increase in crackles in 2001, Berkeley provided version 16603, which was functionally identical to 16600 except for an increase in the persistence from 20 msec to 60 msec.

Late in the mission, several additional versions were built at JHU with increased persistence values. Only two of those modified versions, 16710 and 16720, were ever used during normal operations.

Start Date	Code Version	Threshold ¹ (digital units)		Persistence (msec) ²			Notes
		HVI	AUXI	HVIA	HVIB	AUXI	
1999:181 ³	16200	128	128	N/A	N/A	N/A	Version in DPU ROM
1999:191 ⁴	16500	128	128	20	20	255	Added crackle protection
1999:334	16600	128	128	20	20	255	Downloaded UC CRC
2000:323	16600	128/182	128	20	20	255	Change to flight script
2001:326	16603	128/182	128	60	60	255	Increased persistence
2006:290	16603	182	128	60	60	255	Change to ramp up script
2006:333	16710	182	128	128	60	255	Used for detector 2 only
2007:025	16720	182	128	128	128	255	Increased persistence

Table 6.3-6 DPU code versions and crackle-detection thresholds used during the mission. Different values were used during stim lamp exposures.

6.3.1.3 Stim Lamp Assembly

The detector Stim Lamp Assemblies (one for each detector) included the mercury vapor stimulation (or “stim”) lamps, a mounting bracket, and a pinhole aperture to coarsely control the amount and direction of light reaching the detectors. They were mounted to a structural bracket in the spectrograph cavity, approximately 1.25 meters from the detectors. Their location allowed direct, quasi-uniform illumination of each detector, with count rates of ~2,000 to ~12,000 counts per second, depending on segment. The stim lamps were not designed to provide a true flat field of the detectors, but rather were included to provide general diagnostics of detector health. Before launch, the lamps were used to provide detector aliveness tests while the instrument was at atmospheric pressure by illuminating the MCPs through the sapphire windows in the vacuum doors. On orbit, they were used regularly throughout the mission as a means of monitoring detector performance, especially gain sag (Section 4.4.2).

The stim lamps were powered through the detector auxiliary power supply, which also powered the ion pumps.

¹ The threshold was set via ground command, but the values listed were rarely changed. They were set to higher values during HV ramp ups and stim lamp operations.

² Persistence values are only approximately milliseconds.

³ Date first used on orbit. Version 16200 was resident in detector ROM and was used for much of the pre-launch testing

⁴ Date first used on orbit. Version 16500 was delivered during satellite integration and test and was used for ground testing starting in late 1998.

6.3.2 Normal Detector Operations

6.3.2.1 High Voltage Ramp-up

Ramping up the high voltage was a complex process with many built in safeguards to ensure that the detector remained safe. The ramp-up scripts:

- enabled the IDS rule which monitored the AUX current for out-of-bounds conditions
- set the HV levels to zero
- set the SAA levels to their proper values
- set the SAA integration and reduce times
- set the HV current threshold to accommodate possible turn on transients
- armed the detector
- turned the QE grid on
- powered on the high voltage
- reset the HV current threshold for more protection.

Only after all of these steps were taken would the HV be ramped above its turn on (2500 volt) level. The ground scripts used for ramp-up referenced a file which contained the proper voltages. Separate scripts used for raising the high voltage for testing purposes did not permit increases of more than 10 digital units at a time to guard against accidentally increasing the high voltage to an unsafe level.

6.3.2.2 High Voltage Management: Occultation Manager

The detector occultation manager was implemented during the mission in order to minimize the amount of gain sag at the location of airglow lines. At the beginning of the mission, the high voltage was normally left at FULL except when passing through the SAA. This meant it was always ready for a peak-up or an observation, but it also meant that any photons falling on the detector removed charge from the MCPs, even though they weren't necessarily being collected by the IDS. Once the differential gain sag problem became obvious, development began on an occultation manager, which lowered the MCP high voltage to SAA levels whenever it wasn't needed. This decreased the amount of unnecessary charge depletion by removing several sources of non-productive exposure:

- (1) Airglow lines illuminated the detectors during occultations and other times between exposures, causing significant localized charge depletion.
- (2) It was not uncommon for a slew to a new target and the acquisition of that target to occur well before an exposure began. This could be due to an intervening SAA or occultation, for instance. The target could remain in the aperture at full high voltage for many minutes before the exposure began.

Before the implementation of the occultation manager, this time contributed to the detector exposure and gain sag, even though no data was collected.

- (3) Similarly, after an exposure was completed, the target sometimes remained in the aperture until it was time to slew to the next target. Before the occultation manager, this would also add detector exposure without the benefit of collecting any additional data.

The occultation manager was used starting on 20 November 2001, and used for the rest of the mission. It was only turned off during times when the high voltage was being ramped up, and during other special tests.

6.3.3 SIA tables

As described previously, the FUSE detectors were photon-counting detectors, and the DPU produced a location and pulse height for each detected event. These positions were passed via the Science Data Bus to the IDS, which could either send that information on to the spacecraft (after adding timing information) for eventual downlink to the ground (TTAG mode), or add it to a two-dimensional image (HIST mode), discarding the pulse height information in the process. Due to memory limitations, an image of all four 16384×1024 segments couldn't be stored in IDS memory. Instead, only the regions around the primary spectra were saved in memory, and they were typically binned by 8 in the cross-dispersion direction. The primary exceptions to this procedure were the M999 stim lamp exposures, which were binned 2×2 , and for which the entire detector area was saved.

For each HIST observation, a Spectral Image Allocation (SIA) table was used to define the detector regions which were saved to memory. The SIA tables varied with the aperture chosen, and they also changed during the mission as a better understanding of the location of the spectra was gained. SIA tables were actually part of the IDS, but because they define how the detector data is saved during histogram exposures, they are described here.

SIA tables consisted of an 8×64 array for each segment, with each array element referencing a 2048×16 pixel region on the detector. Each array element could be set to 1 to save the data from the associated detector region in IDS memory, or 0 to discard it. In most cases, the observation scripts for histogram exposures called the `init_bulk_memory_f` script, which loaded the standard set of SIA tables for all apertures. A special set of SIA tables for histogram stim lamp exposures were uploaded from the ground when needed. The standard SIA tables were changed several times during the first few years of the mission (Table 6.3-7 through Table 6.3-12). These changes were made primarily to adjust the positions to ensure that all data from the aperture was being collected. Note that the masks (**Table 6.3-4**) were eventually set to be the same as the SIA tables, but they did not match early in the mission.

The SIA tables were downloaded to the ground with the science data, and they are stored in the primary data unit in the raw FITS files. Although they are not used by CalFUSE, they can be examined to verify that the expected mask was used and was not corrupted. The typical SIA table consists of up to 16 rectangular regions turned on, which include, for each segment, the detector regions where the SiC and LiF spectra fall, along with the area around each stim pulse. In many cases, one or more of the stim pulse regions overlap with the spectral regions. The tables below describe the regions of each detector segment covered by the SIA tables during the mission.

It is important to note that since the SIA tables operate on the raw data coming from the detector, they are not in the geometrically-corrected FARF, but in a distorted frame which is not corrected for geometric distortions or thermal shifts and stretches. Thus, the SIA table regions were oversized to avoid losing data.

Table 6.3-7 SiC HIRS SIA Tables used during the mission

Approximate Start Date	All	1A	1B	2A	2B	Table Names
	X Range	Y Range	Y Range	Y Range	Y Range	
11/20/1999	0 - 16383	160 - 319	128 - 287	288 - 399	400 - 495	siahirs1x8b
5/17/2000	0 - 16383	160 - 319	112 - 271	288 - 399	400 - 495	siahirs1x8c, siahirs1x8d

Table 6.3-8 SiC MDRS SIA Tables used during the mission

Approximate Start Date	All	1A	1B	2A	2B	Table Names
	X Range	Y Range	Y Range	Y Range	Y Range	
11/12/1999	0 - 16383	288 - 447	240 - 399	208 - 319	224 - 335	siamdrs1x8b
1/13/2000	0 - 16383	288 - 447	240 - 399	208 - 319	352 - 463	siamdrs1x8c siamdrs1x8d

Table 6.3-9 SiC LWRS SIA Tables used during the mission

Approximate Start Date	All	1A	1B	2A	2B	Table Names
	X Range	Y Range	Y Range	Y Range	Y Range	
10/11/1999	0 - 16383	16 - 175	0 - 175	384 - 495	480 - 591	sialwrs1x8b
3/4/2000	0 - 16383	16 - 175	0 - 175	352 - 463	448 - 559	sialwrs1x8c, sialwrs1x8d, sialwrs1x8e

Table 6.3-10 LiF HIRS SIA Tables used during the mission

Approximate Start Date	All	1A	1B	2A	2B	Table Names
	X Range	Y Range	Y Range	Y Range	Y Range	
11/20/1999	0 - 16383	624 - 783	608 - 767	544 - 655	592 - 703	siahirs1x8b
5/17/2000	0 - 16383	640 - 799	608 - 767	560 - 671	592 - 703	siahirs1x8c
3/27/2001	0 - 16383	640 - 799	592 - 767	560 - 671	592 - 703	siahirs1x8d

Table 6.3-11 LiF MDRS SIA Tables used during the mission

Approximate Start Date	All	1A	1B	2A	2B	Table Names
	X Range	Y Range	Y Range	Y Range	Y Range	
11/12/1999	0 - 16383	768 - 927	736 - 895	464 - 575	544 - 655	siamdrs1x8b siamdrs1x8c
6/20/2001	0 - 16383	752 - 927	720 - 895	464 - 575	544 - 655	siamdrs1x8d

Table 6.3-12 LiF LWRS SIA Tables used during the mission

Approximate Start Date	All	1A	1B	2A	2B	Table Names
	X Range	Y Range	Y Range	Y Range	Y Range	
10/11/1999	0 - 16383	480 - 639	464 - 623	624 - 735	656 - 767	sialwrs1x8b
3/4/2000	0 - 16383	480 - 639	464 - 623	624 - 735	672 - 783	sialwrs1x8c
5/18/2000	0 - 16383	496 - 655	480 - 639	624 - 735	672 - 783	sialwrs1x8d
5/1/2001	0 - 16383	496 - 655	464 - 639	624 - 751	656 - 799	sialwrs1x8e

6.3.4 Single Event Upsets

The electronics for the two FUSE detectors were turned on six days after launch, on June 30, 1999. On July 2, the Detector DPU code reported a change in the checksum value calculated by its Cyclic Redundancy Check (CRC) routine. Since this CRC calculation was done over a range of internal detector memory that contained the executing DPU code, this meant that the code had been corrupted. The following day, a similar error was reported on Detector 2, but neither had any apparent effect on the detector performance. The third reported CRC error, however, caused a loss of some Detector 1 telemetry. Only by rebooting the detector was the telemetry restored. These errors continued to be reported at a rate of one every few days throughout the mission. Their cause was later determined to be single event upsets (SEUs) in the DPU memory, due to radiation from the South Atlantic Anomaly (SAA). This susceptibility to SEUs was due to the choice of RAM in the DPU; although the memory chip chosen had a high threshold to total radiation dose and was immune to latchup, it had a relatively low resistance to Single Event Effects (SEEs).

Since the regions of memory being corrupted contained the DPU code that was controlling the detectors, this was potentially a very serious problem. Although the detector software was robust and it was believed to be unlikely that a single bit flip could cause any permanent damage to the detector, as a precautionary measure rules were developed to minimize the danger. An intensive investigation was conducted to formulate a plan for responding before the high voltage was first turned on. In order to minimize the risk to the detector, the decision was made to only operate the high voltage when a code image was loaded into both Lower Core (LC) and Upper Core (UC) memory. If an SEU occurred in the active memory region, a command was issued to jump to the alternate core on the next ground station pass, and an uncorrupted version of the code reloaded from the ground. If the error was in the inactive memory core, it was simply reloaded to repair it. If both cores were found to be bad during a ground station pass, the detector was rebooted, which shut down the high voltage on that detector. Since recovery from a detector reboot required close to

24 hours because the ramp-up steps were commanded from the ground, this was a major cause of inefficiency early in the mission. In addition, the IDS flight script `det_hv_f` was modified to reload several important detector parameters (SAA count rate limits, SAA integration times, SAA HV levels, SAA reduce time, HV current limit, and AUX current limit) after every SAA passage.

This procedure was performed manually until 8 January 2000, when version 16600 of the DPU code was loaded onboard, along with modified IDS scripts that autonomously detected and repaired the code. Although the code was initially loaded from IDS memory, starting in April 2000 IDS EEPROM memory was used to free up memory for IDS scripts.

Before the autonomous code repair was implemented, 122 SEUs had been detected on the two detectors and repaired manually. After these changes, the autonomous correction code permitted the IDS to identify an SEU and correct it autonomously within three minutes in most cases.

There were 1285 SEUs detected on the two detectors during the mission. These were divided as shown in Table 6.3-13. The fact that they were roughly evenly distributed between Upper Core and Lower Core memory, and Detector 1 and 2, shows that the susceptibility was due to the choice of parts rather than a single bad chip (note that UC and LC for a particular detector were located on the same memory chip). No obvious correlations of the SEU rate with time were seen, aside from changes in the rate due to modifying the size of the memory area checked.

Detector	Lower Core	Upper Core
1	335	271
2	299	343

Table 6.3-13 SEUs by detector and memory core.

Although most of the SEUs had no noticeable effect on the operation of the detectors, the consequences could be more severe when certain parts of the code were affected. In some cases, a detector watchdog reset occurred, causing the detector to reboot. Other times unusual behavior was seen, such as a loss or corruption of detector telemetry. Those cases usually required rebooting the detector from the ground to recover.

As expected, nearly all of the SEUs occurred while the detector was in or near the SAA. Figure 6-11 shows the location of FUSE in its orbit when each SEU occurred. The figure shows that they were concentrated near the center of the SAA, and that the spatial distribution was similar for the two detectors. Only fifteen of the 1238 SEUs for which the location could be identified did not fall within the SAA contour shown.

The CRC calculation took up to 40 seconds to identify a bit flip, depending on where it is in memory. In addition, CRC values and diagnostics were reported in telemetry

only once every sixteen seconds. As a result, the times reported are likely to be somewhat later than the actual time of the SEU, and the locations marked on the figure will be slightly misplaced from their actual position.

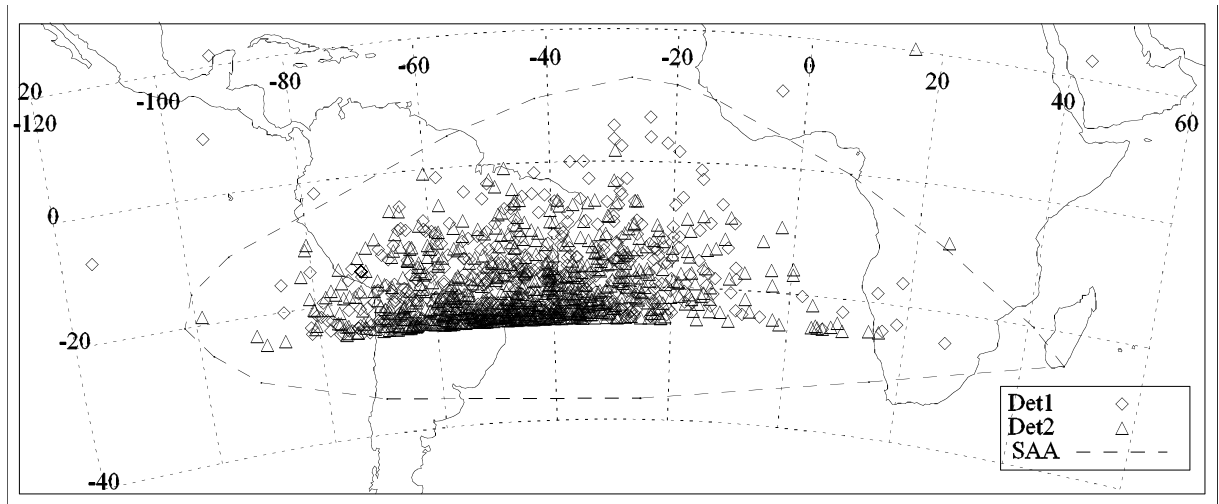


Figure 6-11 Positions of SEUs during the mission. The dashed line shows the SAA region used by Mission Planning after 17 September 2003. No events occur below -25° due to the orbit of the satellite.

In addition to the DPU code, detector masks (Section 6.3.1.2.2.3) were stored in the same memory chips, and thus were also susceptible to corruption. The CRC check done by the DPU code only checked mask memory when a mask was changed, however, so it was not possible to tell when this occurred. As a result, there were instances early in the mission where a mask bit was switched off due to an SEU, causing a loss of events in that region of the detector. Once this effect was identified, the observation scripts were modified to reload the masks before every observation. This greatly decreased the likelihood of this problem.

6.3.5 High Voltage Transients (Crackles)

During satellite-level testing, the detector high voltage power supply current periodically had excursions that were large enough to potentially cause damage to the detectors. To minimize the likelihood of a detector failure on orbit due to one of these high voltage transients, or ‘crackles’, UC Berkeley modified the DPU software to monitor the high voltage power supply currents on segments A and B (HVIA and HVIB), and the Auxiliary Power supply current (AUXI), at a sample rate of approximately 1 millisecond. After these modifications, whenever these currents were greater than or equal to a threshold (a ‘mini-crackle’), a diagnostic was issued by the detector DPU. If this threshold was exceeded for a particular length of time (the persistence), the high voltage for both segments of the affected detector would be turned off and an additional diagnostic issued.

In addition, a portion of DPU memory was set aside for use as a circular buffer containing the last 1024 samples (approximately 1 second) for each of these three currents, along with three histograms that stored their distribution.

The thresholds could be set via ground command, but because the maximum current of most crackles was so high, changing the threshold had a limited effect. The persistence, however, could only be modified by changing the DPU code. Each change required modifying the code followed by extensive testing. Section 6.3.1.2.2.7 describes the DPU code versions used during the mission, along with the thresholds and persistence values for each.

Figure 6-12 shows the three currents during a typical crackle event, as saved onboard in the circular buffer. Although the details of each crackle event were different, the basic features were similar in most cases:

- (1) One of the currents (in this case HVIA, the high voltage current on segment A), showed some oscillatory behavior and then went off scale.
- (2) The AUX current followed a similar shape as the segment current, but had a much lower value. Since it did not reach its maximum, it often showed the oscillation more clearly.
- (3) The current draw of the other detector segment (HVIB) was also affected.
- (4) When the (HVIA) current eventually exceeded the threshold (182 in this case) for the persistence time (60 msec), the high voltage shut down, and the currents all dropped to zero.
- (5) One of the currents (in this case HVIA, the high voltage current on segment A), showed some oscillatory behavior and then went off scale.
- (6) The AUX current followed a similar shape as the segment current, but had a much lower value. Since it did not reach its maximum, it often showed the oscillation more clearly.
- (7) The current draw of the other detector segment (HVIB) was also affected.
- (8) When the (HVIA) current eventually exceeded the threshold (182 in this case) for the persistence time (60 msec), the high voltage shut down, and the currents all dropped to zero.

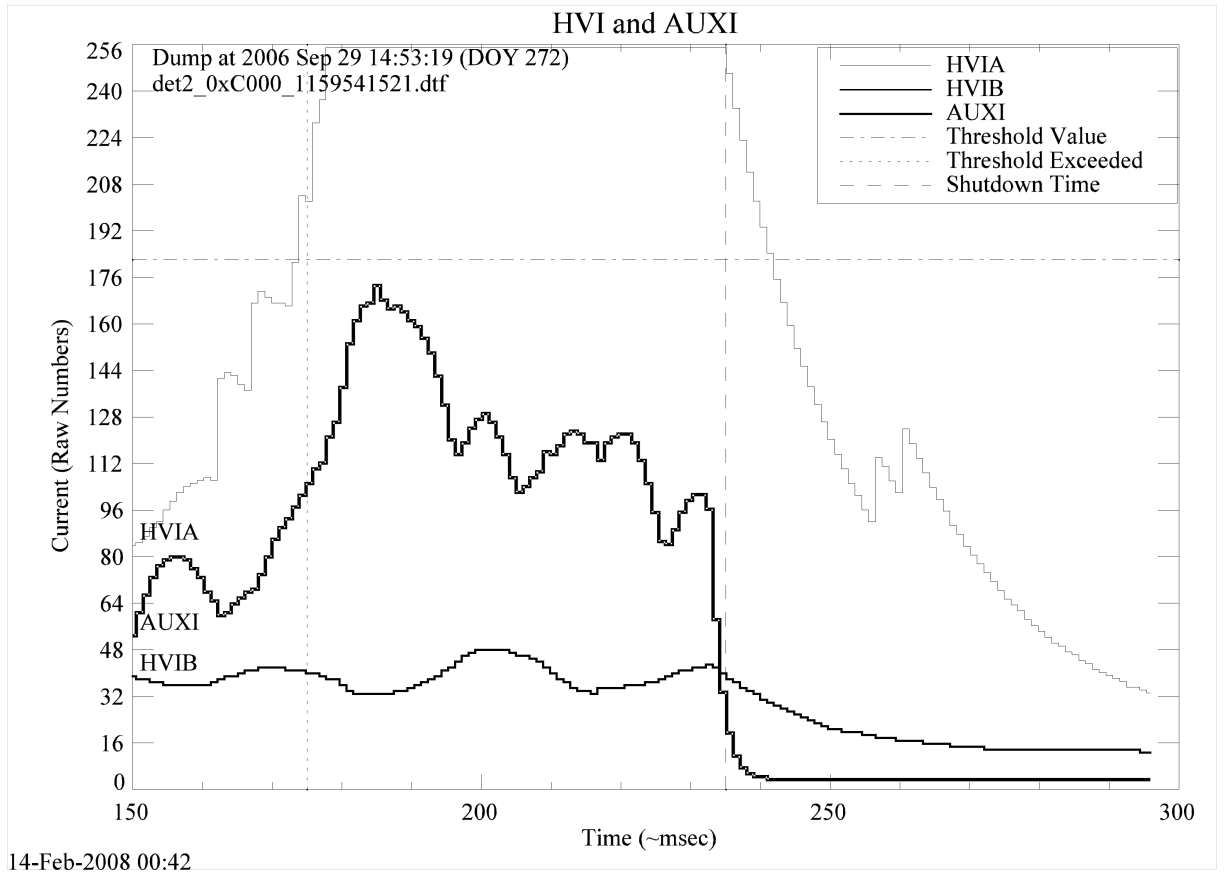


Figure 6-12 HVIA, HVIB, and AUXI during a crackle.

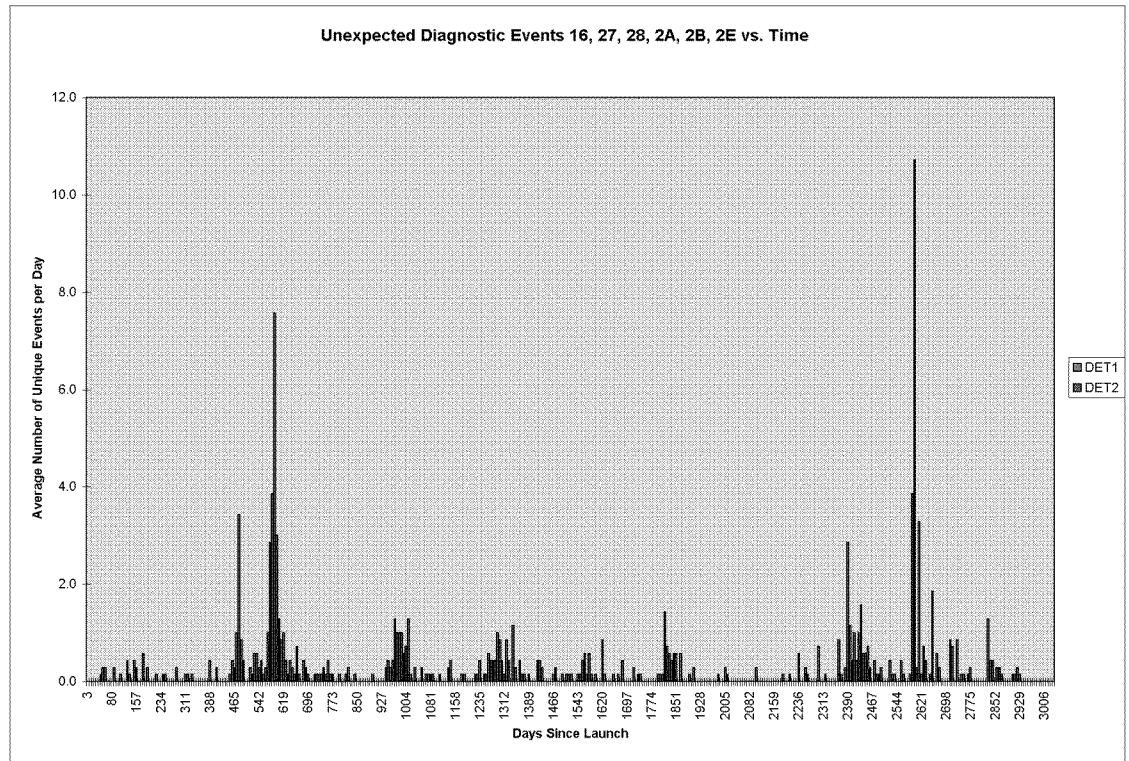


Figure 6-13 Number of crackles and mini-crackles vs. time.

Table 6.3-14 summarizes the numbers and types of crackles and mini-crackles for each detector segment during the mission, while Figure 6-13 shows their distribution as a function of time. Recall that mini-crackles had no effect on operations, while crackles shut down the high voltage on both segments of the affected detector, which required a high voltage ramp-up from the ground. Since the thresholds and persistence values changed during the mission, the crackle rates at different times cannot be compared directly, but it is clear that the incidence of crackles is episodic, for reasons that were never understood. It is also thought that they were more likely to occur soon after a high voltage ramp-up.

Table 6.3-14 Number of mini-crackles and crackles during the mission. The values in parentheses are the diagnostic value (in hex) issued by the detector.

Detector	Mini-Crackles			Crackles		
	HVIA (27)	HVIB (28)	AUXI (16)	HVIA (2A)	HVIB (2B)	AUXI (2E)
1	695	67	114	6	18	0
2	456	0	239	75	0	8

Crackle shutdowns were the most common reason that the high voltage on one of the detectors was not at FULL as planned during an exposure. Since the time to return the high voltage to its nominal value after a shutdown could be a day or longer, this was a

major source of inefficiency. Plans to automate the high voltage ramp-up process were developed, but had not been implemented by the time the mission ended.

Similar current protection scheme is used on the GALEX and COS detectors, but the DPU code for those detectors provided more flexibility on setting thresholds and persistence values.

6.4 □ Fine Error Sensor Cameras

6.4.1 FES CCD Detector

The CCD detector was a modified version of a SITe SIA003A. This was a 1024 × 1024 pixel thinned backside-illuminated CCD die mounted on a 2-stage thermo-electric cooler (TEC) and sealed in a kovar package with a fused silica window. The CCD quantum efficiency, full-well depth, charge-transfer efficiency, dark current, and readout noise were all in accord with pre-flight measurements. Basic characteristics of the CCD are given in Table 2.7-2.

Half of the CCD die was masked, so that the CCD could be operated in frame transfer mode. After a given exposure duration, the image would be transferred rapidly to the region under the mask and then read out slowly so that the readout noise would not affect the accuracy of the centroid calculation.

CCD thermal control was achieved through the use of an external radiator in conjunction with a thermo-electric cooler (TEC). The CCD package was coupled to the external radiator by means of a heat strap fabricated from flexible copper braid that was fused at either end into a copper block. In general, the spacecraft attitude was maintained so that the radiator of the active FES was shaded from the sun. During in-orbit checkout the TEC setpoint was chosen to be -32C for FES-A and -30C for FES-B. Lower setpoints could be maintained at some attitudes, but the reduction in dark current did not justify the operational inconvenience of tailoring the setpoint for each attitude. With the advent of two-wheel and one-wheel operations later in the mission, which necessitated a much wider range of spacecraft roll angles, on-board scripts were developed that would autonomously adjust the TEC setpoint in response to the changing thermal environment. The resulting higher dark current and slightly-degraded FES performance was accepted, as the pointing performance was then limited by the torquer bars and not the FES.

6.4.2 Performance and Anomalies

6.4.2.1 FES-A Failure

The first in a series of intermittent spontaneous FES-A reboots occurred on day 105 (April 15) of 2005. When the reboots occurred, FES-A was left in Boot mode, and could not be commanded to application mode without first cycling the power. In addition, the FES would frequently not recover unless it was left powered off for

several minutes to an orbit. This led to the suspicion that some component in the controller had an intermittent problem with heat-sinking. We attempted to mitigate this problem by lowering the temperature of the FES-A surroundings and by having the IDS flight scripts autonomously handle the power cycling and rebooting sequence. We operated in this mode for several months, *but ultimately decided to switch to FES-B on July 12, 2005*. FES-A was not used for guiding during the rest of the FUSE mission.

The cause of this problem was not determined. FES-A had been subjected to survival temperatures (-5C), along with the rest of the FUSE instrument, between Dec 28 2004, when the Roll RWA failed, and March 22, 2005, when version T31 of the ACS software was loaded. The reboot problems began a few weeks later. It was suspected that this prolonged cold soak had precipitated the problem.

6.4.2.2 FES-B Focusing

Following the initial focusing of the LiF2 channel for optimal spectrograph performance in IOC, the PSF of star images in FES-B was found to be 2–3 times larger than desired (the FWHM was 4–6 pixels instead of 2 pixels), indicative of defocusing of FES-B. This caused the light from any given star to be spread over many more pixels than would be the case if FES-B were properly focused, reducing the contrast between the signal and the background.

Although FES had no internal focus adjustment mechanisms, the focus could be adjusted by moving the LiF2 FPA and/or the LiF2 primary mirror along the Z-axis (focus direction). If the FPA was moved, the only impact to FUV data in that channel was to reduce the throughput of the MDRS and HIRS apertures. If the LiF2 primary mirror could also be moved, the spectral resolution of the LiF2 FUV data will be degraded. FES-B was used successfully with these large star images during periods when the FES-A was being annealed. When FES-B was made the permanent guiding camera, however, the likelihood of guiding problems with faint stars was too large. FES-B was refocused by moving the LiF2 FPA by 400 microns (See section 6.2). The resulting image quality was comparable to that of FES-A.

6.5 □ IDS: Instrument Data System

6.5.1 IDS–ACS Interface

The IDS was responsible for managing FES operations, for attitude determinations based on FES data, and for initiating slews. In essence, the IDS and FES were an integral part of an extended attitude control system architecture. Communications between the ACS and IDS were handled by Fine Pointing Data (FPD) packets (IDS to ACS) and ACS status messages (ACS to IDS) transferred across the SDB. Measured quaternions, covariances, and configuration flags were sent to the ACS once per

second in FPDs for fine pointing management. In return, the ACS provided status messages back to the IDS.

The spacecraft was responsible for the health and safety of the satellite. Therefore the ACS was free to reject individual FPDs or ignore the IDS altogether. The IDS did not command the ACS, but changed the status of FPD flags to in effect request ACS activities. The ACS monitored state changes in the FPDs and responded accordingly.

6.5.2 Observation Sequencing and Fine Guiding

Slewing and target acquisition was controlled by scripts executing in the IDS. The scripts controlled sequencing of commands, while complex functions such as processing of FES images or attitude determination were performed by the embedded guidance task software in the IDS. Except for centroid computations performed by the FES when in tracking mode, all fine attitude calculations were performed by the IDS.

The main steps in a basic target acquisition sequence were as follows:

- 1) The IDS sends a new attitude to the ACS, initiating a slew, and then waits for the slew to complete.
- 2) The IDS commands the FES to obtain & deliver a full FOV image
- 3) The IDS processes the image and determines locations of up to 30 stars.
- 4) The IDS commands the FES to centroid 3 to 6 of the brightest stars at 1 Hz, computes quaternions, and transmits them to the ACS. These quaternions are flagged as “unknown”, because the stars have not yet been identified. These data were used to maintain a precise fixed spacecraft attitude while the absolute attitude was determined from the FES image. (see Section 8 for a discussion of quaternions).
- 5) The IDS compares the objects in the image to the star catalog uplinked for this observation and determines the absolute attitude.
- 6) The IDS sends the absolute quaternion to the ACS, which initiates a slew to remove the residual attitude error.
- 7) After the slew, the IDS commands the FES to centroid pre-selected stars surrounding the target, at a rate of 1Hz or 0.5 Hz. As each set of centroid data is received by the IDS, it computes quaternions from reported star positions, and sends them to the ACS for input to the attitude-determination filter.
- 8) At the end of the target visibility period, the IDS commands the FES to stop tracking stars, and the IDS stops generating FPDs. The ACS maintains coarse tracking using gyros and TAMs.
- 9) For multi-orbit observations, return to step 2 above when the target is next unocculted by the Earth, and the satellite is not passing through the SAA.

More complex acquisition procedures were needed for some observations. The main variations are described briefly here.

Offset acquisitions. In cases where the star field in the vicinity of the target was too sparse for the star-ID process to work, or if there were a very bright source in the FES field of view, the first five steps of the acquisition sequence above would be performed at an offset field. After the field was identified, the correction slew request would include the offset needed to move directly to the desired target position.

Peak-ups. Observations using the MDRS or HIRS apertures would include a pickup procedure following step 7 in the basic acquisition sequence. Peakups are described in Section 4.2.2.

FES-assisted acquisitions. In these acquisitions, the target would be left at the reference point position, away from the apertures, and the FES would be commanded to measure its position as well as that of the guide stars. The IDS would then compute the actual position of the target and then command a short slew to place the target in the proper spectrograph aperture. This mode was initially envisioned for objects such as comets that might have poorly-known coordinates, but in practice it was often used for routine observations.

6.5.3 IDS Thermal Control

6.5.3.1 Thermal Design

The IDS was responsible for the operation of the instrument thermal control system used in normal operations. Temperature data from instrument thermistors were collected from the IPSDU, averaged, and then used to control 32 heater zone switches in the IPSDU. Overall management was specified by a user-defined thermal control table. The table identified which thermistors were associated with each thermal zone and the upper and lower temperature thresholds for the zones. Up to 4 thermistors were monitored for a zone and, when the average temperature fell outside the zone thresholds, the heater was turned off or on. By executing one full cycle of the algorithm every 16 seconds, the IDS guaranteed that the temperature of each thermal zone was maintained to ± 0.25 C of the desired temperature. Space for two tables was provided to facilitate the loading of a new table while under thermal control of another.

6.5.3.2 Thermal Performance

The deadbands in the thermal control tables were set at ± 0.25 C. The control system was able to maintain temperatures within this deadband, with the exception of the equipment panels which were controlled to within 1C, which was adequate for the electronics modules mounted on these panels.

Under nominal three-wheel operations instrument temperatures were well-controlled about a daily mean temperature that exhibited no long term trends. In particular, the mirror bench temperatures on the shaded (+X or LiF) side of the instrument exhibited no change in daily mean temperature over the mission. During the subsequent two-wheel phase with roll-offsets the temperatures were also, in general, well-controlled. However, for some of the heater zones in the lower sections of the instrument a

gradual increase in the daily mean temperature was evident - including the SiC1 mirror bench.

The behavior of the zones in the upper half of the instrument was slightly different. This includes the spectrograph structure, the GMA shrouds, and the gratings. Each of these zones maintained constant or nearly constant temperatures until the pitch wheel failure in December 2001. Following restoration of 3-axis stabilization, the mean temperature in each of these zones was slightly ($<0.1\text{C}$) higher. The temperatures of these zones exhibited a few slight mean temperature changes/offsets later in the mission and the SiC grating temperatures increased gradually by 0.05C over the last few years of the mission.

The LiF grating temperatures were well-controlled. The combination of controlling the grating pie-pans in conjunction with their thermal mass was successful in providing a stable environment for the optics. Under normal operating conditions the grating temperatures were controlled to within 1C . However, the grating temperatures, in particular for the SiC temperatures, varied with solar beta angle.

The zones within the instrument were controlled very well throughout the mission. The slight changes that were seen were presumably due to minor degradation of the multi-layer insulation with exposure to solar UV radiation and atomic oxygen. The distinct step in temperatures seen at the time of the roll wheel failure in particular may be the result of such exposure, as this was the first time in the mission that exterior surfaces of the instrument not covered by silver teflon blankets were exposed to the Sun for an extended period.

The temperatures of the telescope baffles were not controlled, as there were no functional or survival requirements to heat the baffles. The baffle mounting to the structure was designed to decouple mechanical stresses from differential thermal contraction of the baffles with respect to the structure. However, the significant variations in telescope alignment found on orbit that correlated with the Solar beta angle and orbit pole angle, and with orbit phase, suggests that this decoupling was not adequate. The temperatures of the door closure and unlatch HOPs, located near the top of the baffles, are seen to vary on orbital timescales by $4\text{-}5\text{ C}$ on the LiF side and by $6\text{-}8\text{ C}$ on the SiC side. These temperatures vary with spacecraft attitude as well: typical variations early in the mission were $3\text{-}5\text{ C}$ on the LiF side, and $12\text{-}15\text{ C}$ on the SiC side. Typical temperatures at the tops of the baffles were -40 C and below on the LiF side, and -20 to -40 C on the SiC side.

6.6 □ Instrument On-orbit Performance

6.6.1 Telescope Focus

6.6.1.1 Post-launch Focus Assessment Details

The FUSE instrument was focused pre-flight with the provision for in-flight focus adjustments for the mirrors and FPAs. On-orbit focus adjustments were expected due

to (1) the unavailability of a laboratory FUV source with a light beam collimated to roughly one arcsecond accuracy and (2) the anticipated focus changes associated with gravity release and changes in the positions of the optical elements resulting from moisture desorption from the optical bench structure.

The on-orbit instrument focus procedure was essentially a two-step process. First, the telescope was focused by adjusting the mirror to FPA distance for each channel. Then each spectrograph was focused by adjusting the distance from the telescope mirror to the spectrograph grating for each of the four instrument channels. The FPAs were then re-adjusted to maintain the previously determined telescope focus.

The telescope focus was determined through a series of knife-edge tests performed by scanning a target across the edge of the FPA slit. The knife-edge test was repeated for a set of FPA positions to determine the location along the optical axis where the light cut-off was sharpest. Then the FPA for each channel was moved to place the aperture at the best telescope focus as indicated by this test. The FPA motions executed to attain the telescope focus for each channel are presented in Table 6.6-1.

FPA	FPA Motion Z-axis (microns)
LiF1	no change
SiC1	-99
LiF2	+48
SiC2	-81

Table 6.6-1 Initial in-flight telescope focus adjustments made November 23, 1999. Adjustments in the focus (Z) direction are limited to 10 micron increments of the FPAs. Small residual errors account for the slight departures from integral 10 micron changes in the adjustment values above. The true uncertainty in the magnitude of the computed focus adjustment was at least 30 microns.

Two programs were executed to determine the spectrograph focus. The first of these programs, I817, was executed during the December 7 – December 9th, 1999 time interval. Multiple stellar spectra of HD208440 were acquired through the LWRS aperture for each of 5 mirror positions stepped in 150 micron increments along the optical axis.

Data from program I817 and the earlier knife-edge tests enabled a robust determination of the best grating to mirror distance (the spectrograph focus) for the LiF1 and LiF2 channels. However, the signal-to-noise of the I817 data was relatively low for the SiC channels resulting in a less robust determination of the best spectrograph focus position for the SiC1 and SiC2 channel mirrors.

On December 12, 1999 the mirrors and FPAs were adjusted to the best spectrograph focus for each channel based on the data obtained December 7th-9th. LiF2, SiC1, and SiC2 previously had their FPAs adjusted to achieve the best telescope focus (mirror to FPA distance) as determined from the knife edge testing. For these channels, both the FPA Z position and the mirror focal distances were adjusted to focus the spectrograph and maintain the best mirror-to-FPA distance (i.e. the telescope focus) determined by the knife edge scans. For LiF1, the adjustment of the mirror location for spectrograph focus matched the required adjustment for mirror to FPA focus; hence the mirror only was moved. The FPA and mirror position adjustments made on December 12th 1999 are presented in Table 6.6-2 for each channel.

Channel	Initial FPA Z Position (microns)	FPA Z Motions Executed (microns)	FPA Z Position Dec 12, 1999 (microns)	Initial Z Mirror Position (microns)	Z Mirror Motions Executed (microns)	Z Mirror Position Dec 12, 1999 (microns)
LiF1	64	0	63	293	-200	93
SiC1	-100	-140	-238	-149	-150	-299
LiF2	62	150	212	25	150	175
SiC2	-77	-150	-225	82	-150	-68

Table 6.6-2 Spectrograph focus adjustments executed on December 12th, 1999 as a result of the I817 post-launch programs.

Given the low signal-to-noise of the spectrograph focus measurements conducted as part of program I817, a second spectrograph focus test was executed two months later as part of program I819. The target, WD0439+466: the central star of a planetary nebula, was observed in the LWRS slit. The spectrum exhibited many narrow molecular hydrogen lines, which were nearly ideal for focusing. Quality data combined with careful analysis resulted in a much better measure of the spectrograph focus. On March 16, 2000, the spectrographs were brought to their best focus position by moving the telescope mirrors along the optical (Z) axis. The magnitude and direction of these motions are provided in Table 6.6-3. These motions were generally in the opposite direction from the first spectrograph focus adjustment, but since the data were of significantly better quality, they were considered far more reliable. Corresponding adjustments were made to the FPA Z positions on March 24th 2000 to maintain the mirror-to-FPA separation for LiF2, SiC1, and SiC2; the LiF1 FPA Z position was adjusted by -100 microns (see Table 6.2-1 for the history of FPA Z motions). These focus positions remained the default throughout the remainder of the mission.

Mirror	Z Mirror Motion (microns) Executed December 12, 1999	Z Mirror Motion (microns) Executed March 16, 2000	Net Mirror Focus Adjustment (microns)
LiF1	-200	No change	-200
SiC1	-150	+125	-25
LiF2	+150	-60	+90
SiC2	-150	+250	+100

Table 6.6-3 Spectrograph focus adjustments executed as a result of the I817 and I819 post-launch programs. The spectrograph focus adjustments implemented March 16th, 2000, were used for nominal operations for the remainder of the FUSE mission.

6.7 □ Telescope Alignment Performance

During the IOC shortly after launch, it was realized that the telescope mirrors underwent periodic motions that shifted the target's image at the telescope focal plane and thus its spectrum in both *X* and *Y* on the detector. A source in either of the SiC channels could move as much as 6 arcseconds in a 2 kilosecond time interval. This motion had two effects on the data: first, flux was lost if the source drifted (partially or completely) out of the aperture; second, the was spectrum shifted on the detector, degrading spectral resolution for observations using the LWRS (30 arcsecond) aperture.

6.7.1 Initial Alignment

The procedure for the initial post-launch channel alignment was to perform a spiral search while guiding on the target using FES-A with LiF1 and the LWRS aperture. The FUV count rate was monitored while using the mirror actuators to locate the target position in the three non-guide channels. This method required use of a moderately bright FUV point source in a fairly isolated star field to provide sufficient counts and prevent confusion from nearby field stars. Overall, this method worked well and was used to initially align channels to a 15-arcsecond precision.

The data were analyzed to determine the mirror rotations required to remove the measured alignment errors at that attitude for each of the three non-guiding channels relative to the LiF1 channel. As further alignments and observations were attempted, it was found that all of the channels were moving with respect to each other, with misalignments as great as 40 arcsec.

Finer co-alignment was then performed by stepping the roughly co-aligned images across the edge of the LWRS slits. This method allowed for co-alignment to approximately 2 arcseconds. Early attempts to use this method were hampered by the

fact that the measurement and adjustment were not closed loop. Scans were made and mirrors adjusted, but no confirmation of the image position was made. FUSE would then slew to another target, which often resulted in co-alignment being lost due to changing the thermal environment of the instrument. Early in the mission the source of the misalignment was unknown and the lack of a closed loop mirror adjustment initially masked the thermal misalignment problem.

6.7.2 Mirror Motion Anomaly

The FUSE “Image Motion” was defined as the variation of the alignment of the SiC1, LiF2, and SiC2 channels with respect to the reference LiF1 channel used for guiding. Although these motions were generally quantified as being associated with the non-guiding channels, they were caused by the motions of LiF1 in combination with the other channels. The observed image motion was attributed to the thermal changes induced in the instrument by changes in boresight beta angle and orbital pole angle. The boresight beta angle is the supplement of the angle between the satellite-sun line and the instrument line of sight and the orbital pole angle is the angle between the orbit pole and the instrument line of sight.

To mitigate loss of data due to channel misalignment while retaining observing efficiency, the LWRS aperture became the primary observing aperture for most programs. For MDRS and HIRS observations, two peakups per orbit were executed to maintain channel alignment during an observation and obtain full spectral coverage while using these apertures.

6.7.3 On-orbit Mirror Motion Mitigation Strategy

A two-part strategy was developed to maintain alignment of the four mirror channels. This strategy included both a predictive component based on empirical modeling of changes in mirror position as a function of boresight attitude and a periodic re-baselining of the alignment.

6.7.3.1 Mirror Alignment: Baseline Maintenance

The re-baselining component of the alignment maintenance was achieved by performing xy-scans on a stellar target and performing near real-time analysis to determine the direction and amplitude of the corrective mirror motions required to attain alignment at that particular attitude. The alignment baseline was valid for a range of beta and orbital pole angles in the vicinity of the target. Alignment within a particular attitude range could be maintained for approximately two weeks, assuming that targets were scheduled within the allowed beta/pole zone. Approximately every two weeks, xy-alignment scans were performed, the data analyzed, mirror motions calculated and executed to remove the accumulated thermal and temporal drifts and maintain the mirror co-alignment at the current attitude. For targets within a beta/pole range with a different thermal environment over an orbital period, xy-alignment scans were required to establish the mirror co-alignment baseline at that attitude. It was also necessary to establish an alignment baseline for every hemisphere crossing of the satellite.

6.7.3.2 Mirror Alignment: Predictive Modeling

Given the sensitivity of the thermally induced mirror motions to the boresight attitude, maintaining channel alignment by performing xy-scans for each target would have been prohibitively inefficient. As a result, a model was generated that predicted the motion to be executed for each mirror to maintain channel alignment for each target observed. This predictive model was part of the planning and scheduling process. The mirror motion scripts were uploaded to the satellite and executed as part of the command sequence for each observation.

This predictive model for the corrective mirror motions was derived from the analysis of xy-scans taken at multiple attitudes in combination with the analysis of peak-up data using the 4-arcsecond wide MDRS and the 1.25 arcsecond wide HIRS aperture. The xy-scan data provided the magnitude and sign of the target mis-alignment in both the x and y direction. The peak-up data provided sign and amplitude information in the x-direction, but no y information was available. In addition to the dependence of the mirror mis-alignment motion on spacecraft attitude, temporal dependencies were also found but not completely nulled by the predictive model.

6.7.3.3 Channel Alignment Operations

Empirically, it was determined that the secular drift of the predictive model relative to observed target position in the different channels required obtaining xy-scans every two weeks to re-establish the model baseline. Extreme attitude changes, such as hemisphere crossings which were driven by the sun angle and typically resulted in large beta changes, were not well-modeled and required xy-scans at the target attitude to determine the appropriate mirror motions for channel alignment. In addition, mirror motions were a strong function of attitude for targets at large beta angles

Executing the scans, analyzing the data, and uplinking the corrective mirror motions impacted observatory efficiency. Since the channel misalignment resulted from thermal changes in the instrument environment local to the mirrors, it was imperative that the mirrors were in thermal equilibrium prior to executing the xy-scans. Thermalization periods of 6 -12 hours were required depending upon both the beta angle and the magnitude of change in the beta angle between targets. Analysis of scans taken with extreme attitude changes exhibited an exponential dependence of the target (i.e. mirror) position as a function of time, consistent with the thermal non-equilibrium hypothesis. Achieving full positional equilibrium could require 11 hours; however, the target was usually within the 30 arcsecond wide LWRS aperture and monotonically approaching equilibrium within 6-8 hours. As a result, to improve efficiency, observations were typically initiated before completion of the full thermalization period. For time-tag observations the data are processed by the CalFUSE pipeline as photon lists. Signal-to-noise permitting, this facilitates the comparison of data in temporal bins to remove secular drifts from the data.

The image motions for the two SiC channels were primarily in the X (dispersion) direction, although small corrections in Y were also occasionally required. For the LiF2 channel, the motion was exclusively in Y (perpendicular to dispersion), and significantly larger than the Y motion in the SiC channels. Y motions required corrective mirror adjustments. In the X (dispersion) direction the FPA was used to accommodate small changes in the predicted position of the target because FPA adjustments were simple to implement and resulted in no loss of observatory time. Due to the limited travel range of the FPAs, larger X motions corrections required mirror motions to achieve co-alignment.

Analysis of the xy-scan data and comparison of signal levels obtained in each of the channels during routine observations enabled the formulation of a set of rules to maintain alignment between alignment re-baselining observations.

These predictive model and alignment rules were incorporated into a planning spreadsheet that was executed prior to completing the detailed scheduling of targets. The primary alignment considerations were to restrict the changes in beta and pole angle to within 30 degrees of the previous target. In addition, large attitude changes required extending the observation time on a target to include the thermalization time for that attitude and delta attitude to ensure obtaining full spectral coverage, if needed. Hemisphere crossings and observations at high beta angle required long thermalization times and dedicated alignment activities. Long-term temporal dependencies were not well-modeled necessitating the need for re-baselining alignment scans approximately every two weeks.

Alignment activities were required at both low and high beta angles. Motions of the LiF2 mirror at high beta angle (>90 degrees) were not well modeled and the consequently observations requiring LiF2 data were not executed at high beta angles without a dedicated alignment activity. Due to the paucity of data at high beta angles, we were not able to improve the predictive model in this regime. Pole angle was a less important consideration than beta angle for maintaining alignment. Observations at a single beta angle for a large range of pole angles supported this conclusion.

Later in the mission, planning constraints necessitated by operational changes arising from failures of the FUSE reaction wheels and associated with spacecraft safety took precedence over alignment constraints. This periodically resulted in either increased re-baselining activities to achieve mirror co-alignment, which was operationally inefficient, or acceptance of limited spectral coverage as a result of mis-aligned channels. To ensure that observations were acquired with the necessary spectral coverage, Guest Investigators were required to specify the channels essential for their science program. This information was propagated through the MP database and factored into the scheduling and detailed sequencing of observations.

6.7.3.4 Orbital Motion

Image motion was also found to have several time dependencies. A very repeatable orbital motion was found, and was well mapped for CVZ targets (Figure 6-14). This source of this motion was attributed to the thermal cycle of the orbit. For some

targets, a 24-hour period motion of as much as 8 arcsec full amplitude was observed. This motion appeared to be roughly sinusoidal in shape. There were also apparent long-term time dependences for some of the motions, but a paucity of continuous data inhibited characterizing this temporal dependence.

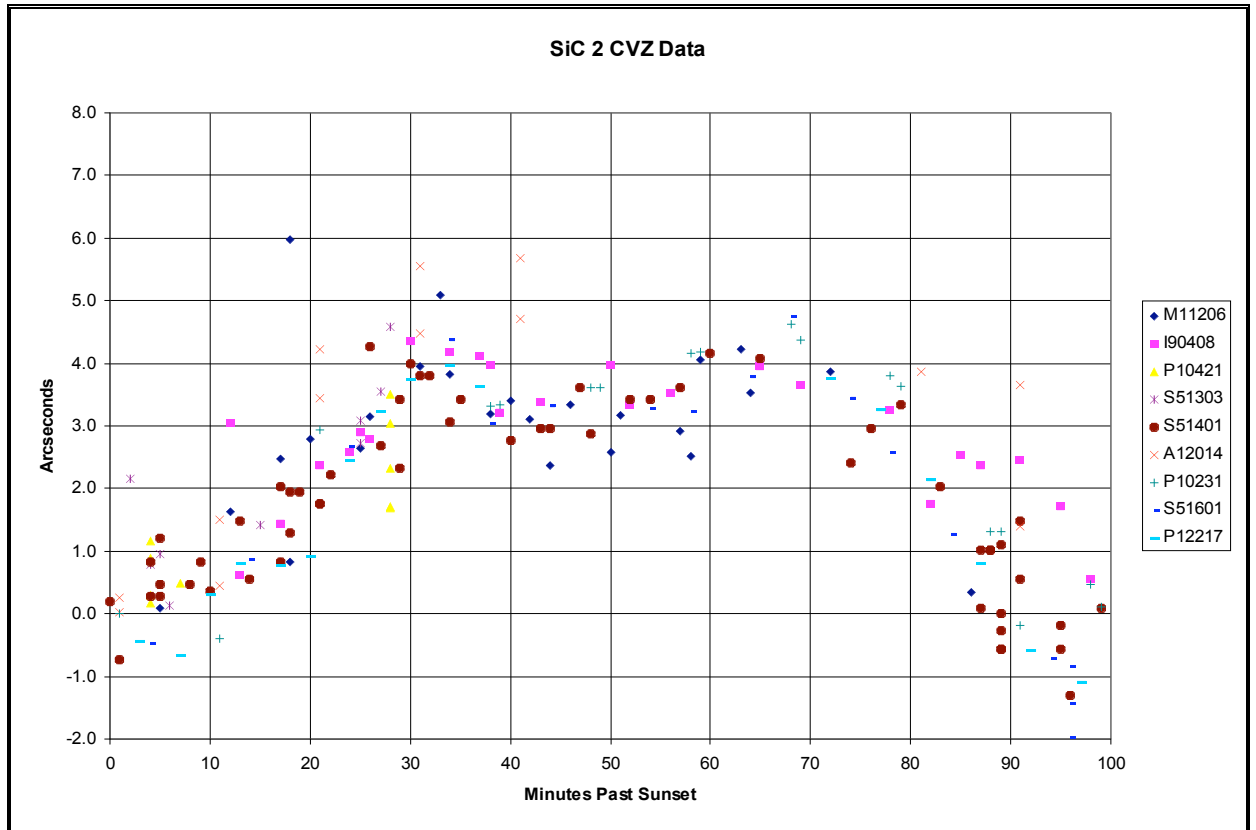


Figure 6-14: Orbital Dependency of Image Motion for Selected Targets

6.7.3.5 Impact and Evolution of Image Motion Corrections

Image motion impacted FUSE science data in several ways. (1) Channels were misaligned for targets at beta and pole angles near the edge of the range of nominal operations. To mitigate this, the predictor set was continually expanded and improved. As a result, channel loss decreased over time. (2) Re-alignment activities reduced the time available for science data collection. Thus, realignment activities were streamlined to use significantly less time than required early in the mission. (3) Motions of the spectral image could result in the loss of spectral resolution, especially for long exposures at high and low beta angles. Consequently, short histogram exposures (<500 s) were used for bright targets. Time-tag data is corrected for this motion in data processing using an empirically derived correction. A more detailed discussion is presented in the the CalFUSE pipeline paper (Dixon, et. al 2007). The bright limit for time-tag data was increased to allow more targets to use this mode. (4) Tracking orbital motion for medium and high resolution aperture observations required additional FPA motions, and impacted efficiency.

6.7.3.6 Target Peak-up Strategy for MDRS and HIRS Observations

To maintain co-alignment of the channels at the arcsecond level required for the MDRS and HIRS apertures, an on-board peak-up procedure was employed. This procedure slewed the telescope in small steps to move the images across the narrow aperture. The FUV count rate at each point was used to calculate the position of the image centroid for each channel. Next, FUSE was slewed to the peak position for the guiding channel. Then, each of the other three FPAs were moved to the calculated location for each of their peak count rates. In performing this operation, it was quickly determined that the images moved over an orbit while pointing at a single target. Consequently, procedures were developed and implemented to perform peakups twice per orbit to maintain alignment when using the narrow apertures. The inclusion of mid-orbit peakups resulted in reduced observing efficiency, but enabled full spectral coverage using the MDRS and HIRS apertures.

6.7.4 Channel Alignment: Observations and Analysis

As discussed in Section 4.2.3.1, the real-time channel alignment process was time consuming. Large overheads were incurred as a result of the time required to thermalize at the target attitude, execute the scans, wait for ground station passes to downlink the data, perform the scan analysis, generate the mirror motion scripts, and then uplink the corrective mirror motions at the next available pass opportunity. This need for ground station communications for data downlink was both a time and a scheduling constraint. To eliminate overheads and streamline this process as much as possible, on-board detector counter data was acquired instead of science exposures. Figure 6-15 depicts xy-scan counter data used to analyze an observation. The first peak in the counts/second (occurring at between 400-100 seconds) is the y-scan; the second peak is the x-scan. The four channels are each graphed using a different color. From inspection of the graph, all channels are aligned in the y-direction. However for the x-scans, the SiC data (blue peaks) are offset from the LiF1 guide channel data indicating a misalignment of the SiC1 and SiC2 mirrors.

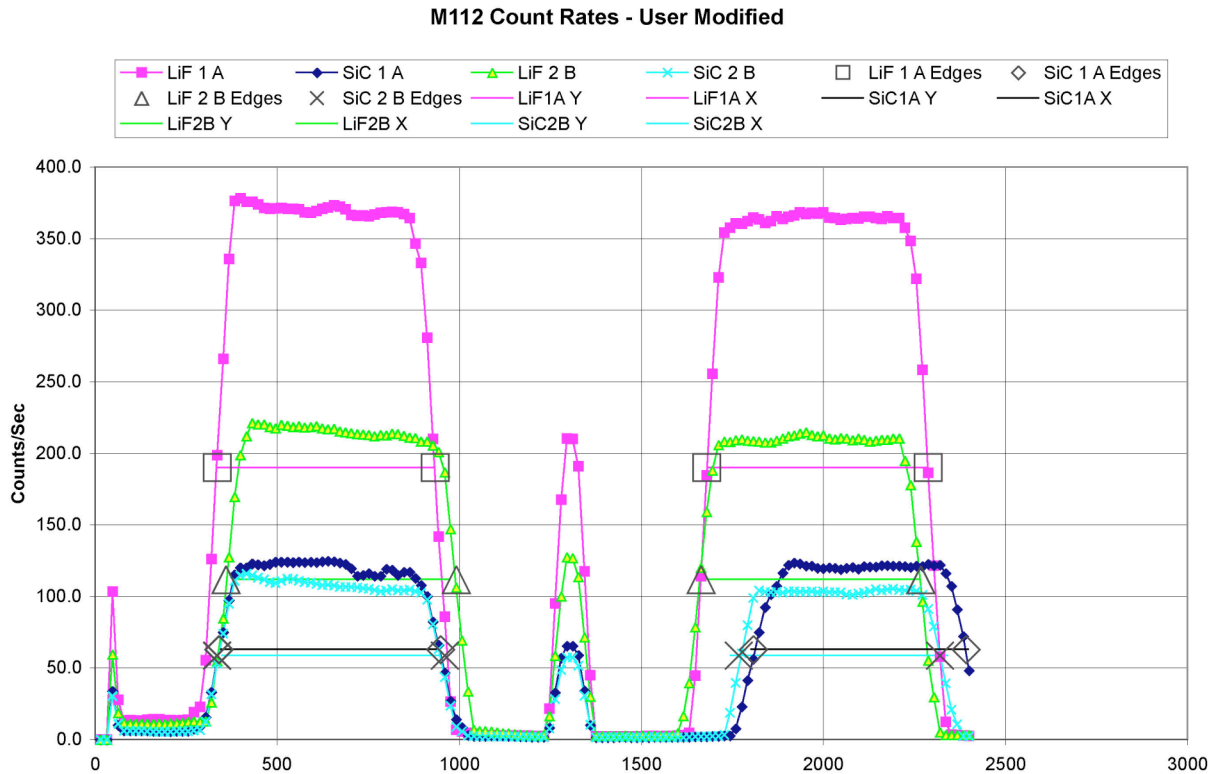


Figure 6-15: xy alignment scans as depicted using the Alignment Tool Graphical Analysis. These data are discussed in Section 6.7.4.

With the loss of reaction wheels, the pointing jitter increased. Now, one of the primary observation scheduling constraints was the availability of torque authority, and, in one-wheel mode, using target sequencing to manage the spacecraft momentum. Minimizing the changes in beta angle and pole angle between subsequent observations became a secondary consideration. This change in planning strategy resulted in larger predictive mirror motions and larger deviations of the mirror position from the predicted position. As a result of the larger alignment errors and the increased difficulty in executing maneuvers in one-wheel mode, the alignment scan pattern was changed both in its spatial coverage and from a step and dwell pattern to a series of continuous scans. This in turn necessitated a new alignment assessment tool, the Channel Alignment Tool (ChAT) shown in Figure 6-16. In addition to the xy-scan pattern, diagonal scans were also executed to increase the diagnostic capability in one-wheel mode where the amplitude of pointing excursions was much larger than previously experienced when pointing was controlled using three reaction wheels. The erratic scan trajectories in Figure 6-17 and Figure 6-18 exemplify the difficulty of fine-pointing with only a single wheel.

The graphical interface provided by ChAT for interaction with the alignment scan data greatly facilitated analysis of the scans. Regions of pointing excursions and high background were now easily identified and excised from the alignment analysis.

Results:

MJD 54162.7529 - 54162.8860 (2007-03-03)

M7170602001 to M7170602002

Channel	Axis	Width	Center	Shift	Mirror	Motions
LiF1A	X	29.71	-1.34	-2.93	LiF1A	Ry = -3
LiF1A	Y	33.36	-0.45	-7.79	LiF1A	Rx = 8
SiC1	X	30.00	-0.25	-1.85	SiC1	Ry = -2
SiC1	Y	34.84	-7.80	-15.15	SiC1	Rx = 15
LiF2	X	30.13	1.60	0.00	LiF2	Ry = 0
LiF2	Y	31.61	7.34	0.00	LiF2	Rx = 0
SiC2	X	30.07	-1.45	-3.05	SiC2	Ry = -3
SiC2	Y	33.61	-1.21	-8.55	SiC2	Rx = 9

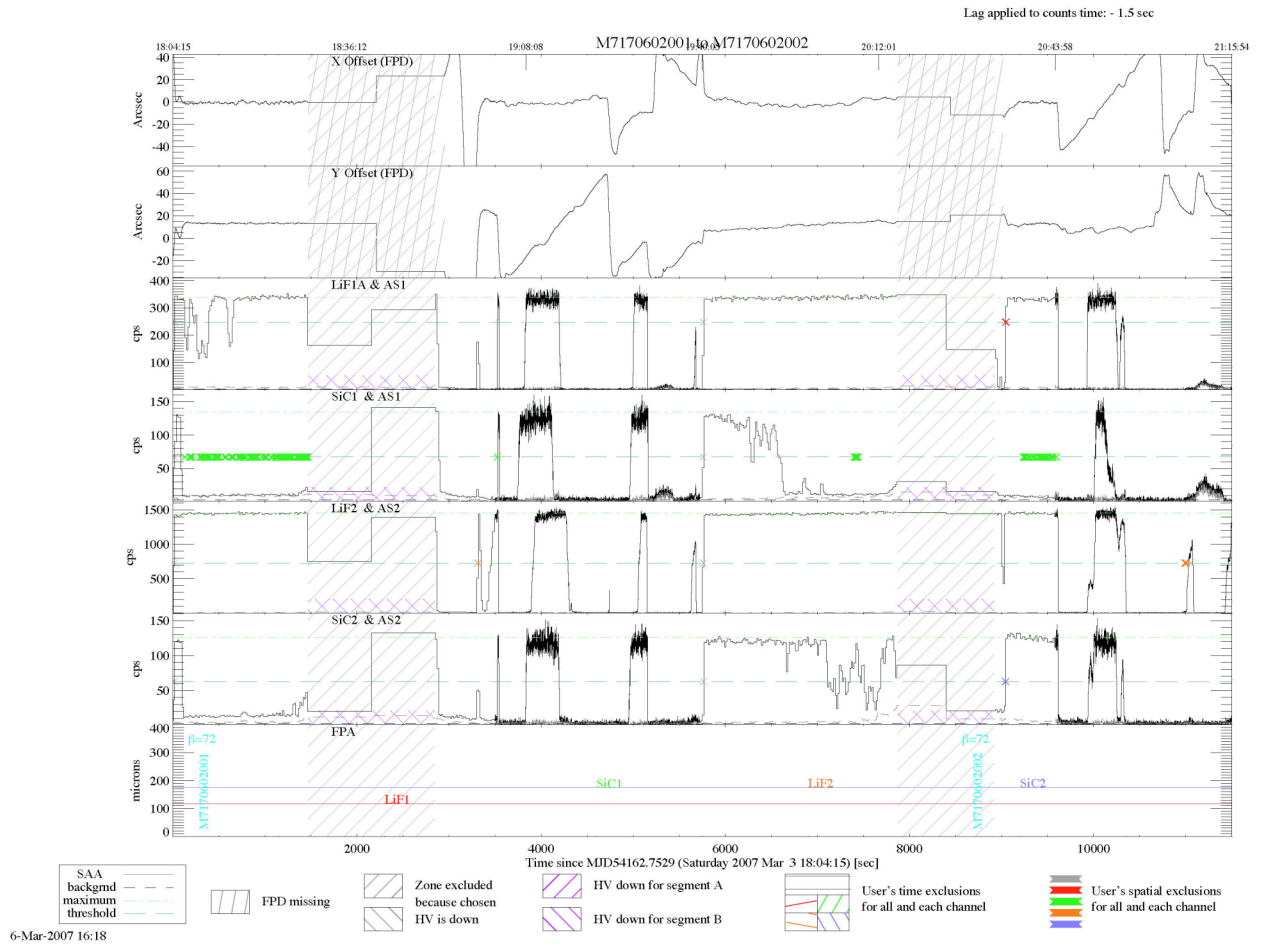


Figure 6-16: Example of Channel Alignment Tool (ChAT) Results

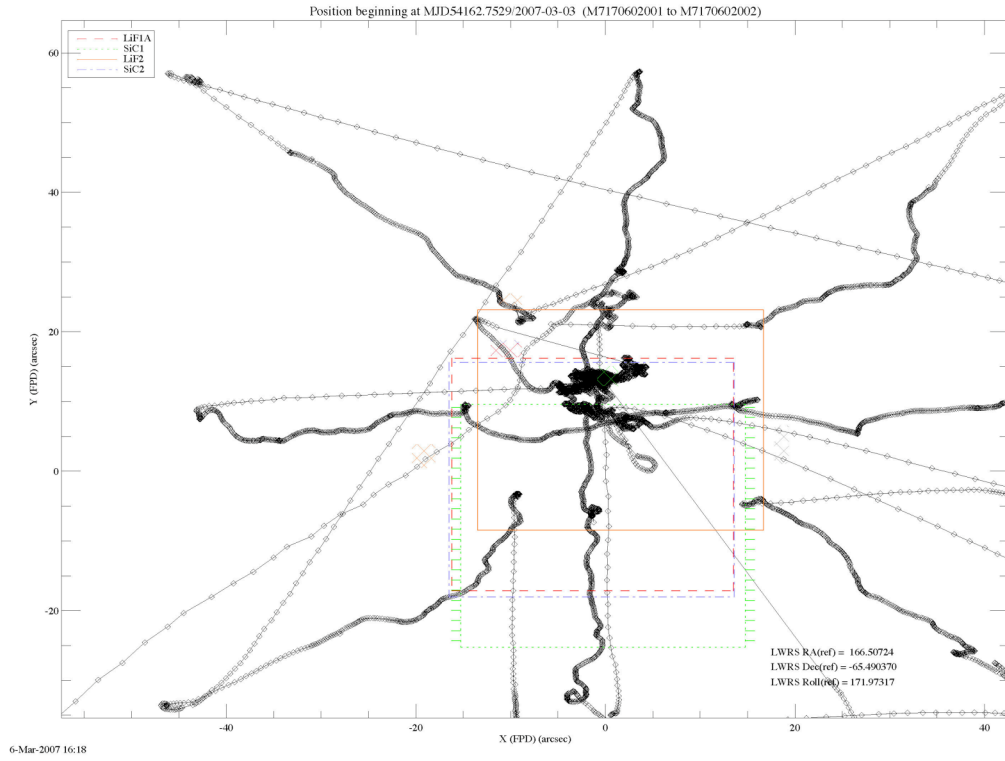


Figure 6-17: (Revised) One Wheel Mode Alignment Scan Pattern

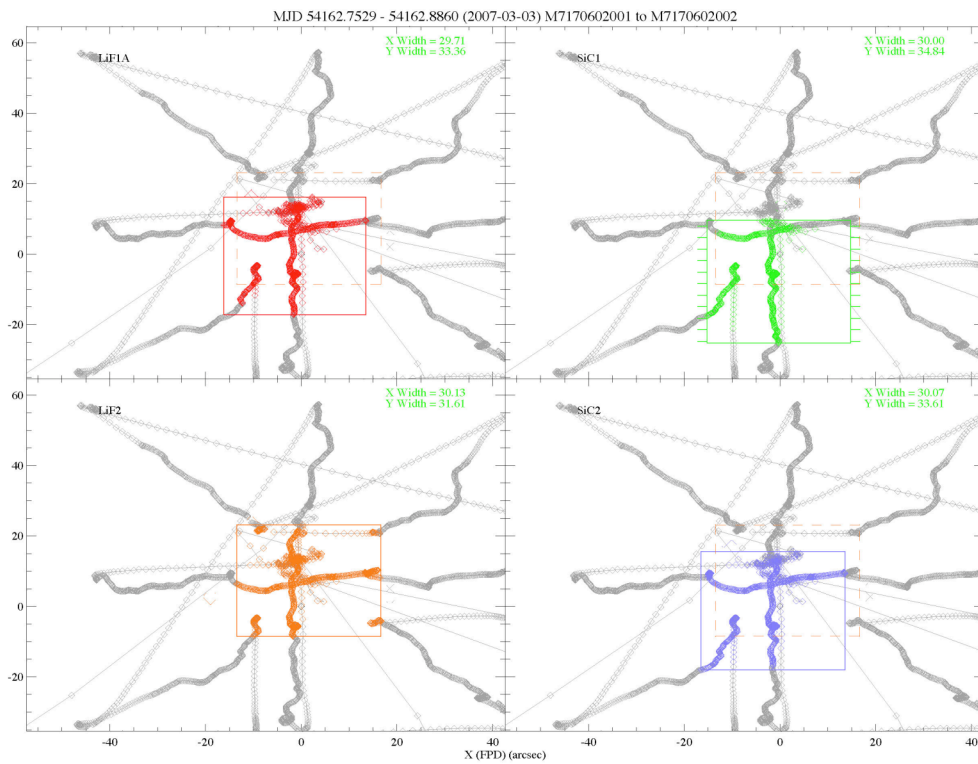


Figure 6-18: One Wheel Mode Alignment Scan Pattern Results

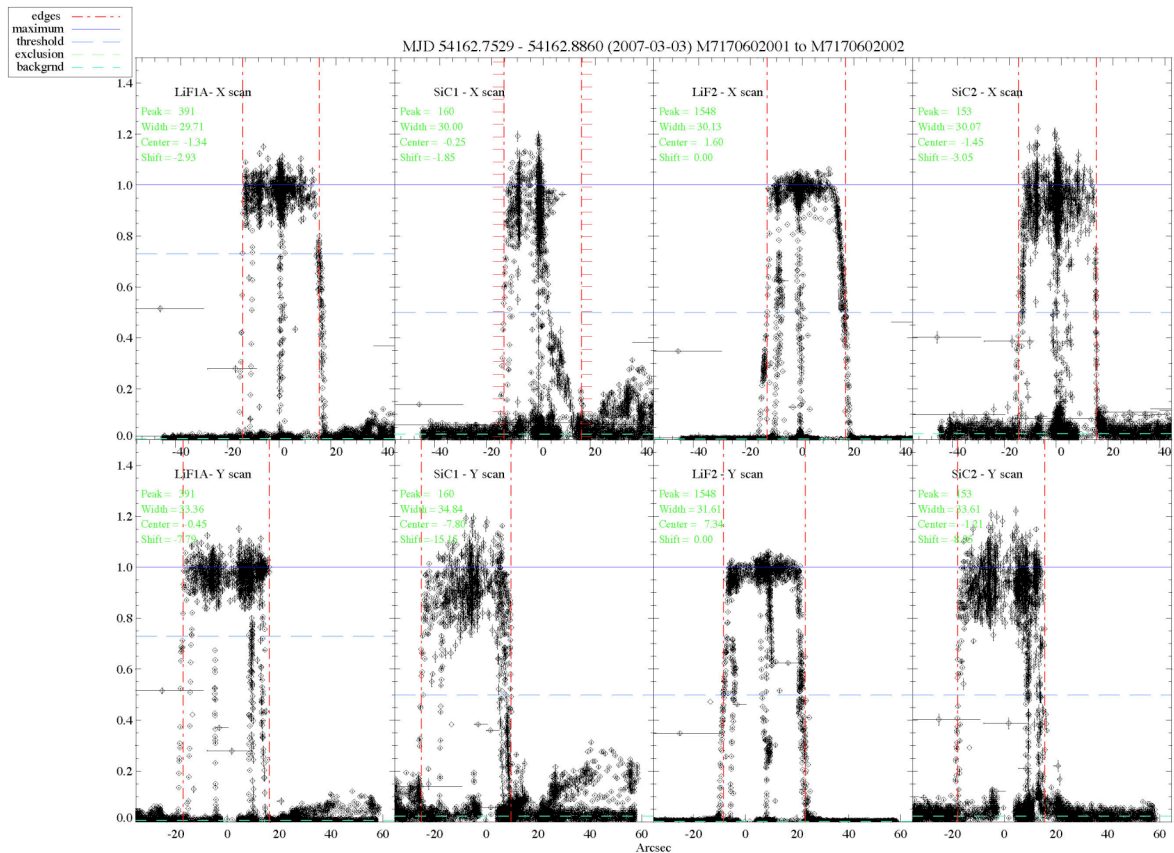


Figure 6-19: Additional ChAT Sample Results

Confirmation of the successful execution of the commanded mirror motions was inferred by one of four methods: examination of the command sequence to verify that it had completed properly, execution of another set of X- and Y-scans, analysis of a follow-on peak-up activity, and/or analysis of the count rate of the next sufficiently bright target at a comparable attitude. Depending upon the availability of ground station contacts, addition scans or peak-ups could require several hours or more to perform the scans and downlink the data. Consequently, a confirmation of mirror motion execution was rarely performed. In practice, confirmation of the count rate from the next bright target was the primary method used to confirm that the mirrors had been moved to their desired positions.

Examination of the telemetry over the eight year lifetime of the mission never revealed an instance where the mirror motion command only partially executed. With one exception, the infrequent instances where the mirror motion did not appear to execute could be traced to a manual tracking error somewhere in the alignment maintenance process. Consequently, steps were taken to automate the procedure as much as possible.

For the first five years of the mission, LiF1 was the guide star channel and the LiF1 mirror actuators were not moved. In 2005 due to anomalies with FES-A (see Section

3.2.3.1) LiF2 became the guide star channel. The restriction on moving the LiF1 mirror was then lifted, and LiF1, SiC1 and SiC2 mirrors were moved to align with LiF2.

6.7.5 Mirror Motion Accuracy

There was no explicit test of the accuracy of the mirror motions and the mirror motions were not telemetered. It could be inferred from multiple realignments that the inaccuracies of the motions are small compared to both the requirements and measured orbital motions. Peakup test data showed motion accuracy about R_y for the SiC 1, LiF 2, and SiC 2 mirrors of better than 2 arcsec for small (< 6 arcsec) motions. Moderate size motions (< 30 arcsec) have been shown to have accuracies of better than 4 arcsec. This had significant positive impact on operations after the loss of the reaction wheels, when prioritized scheduling as a function of spacecraft momentum management was needed. This required additional mirror motions for a greater number of observations and hence, greater flexibility in the mirror motion scripts.

6.7.5.1 Mirror Motion Tracking and Actuator Performance

Due to the thermally-induced relative motions of the four telescope mirrors (LiF1, LiF2, SiC1, and SiC2) with respect to one another (Sections 4.1.1, 6.6.1.1, and 6.7.2 - 6.7.4) the total number of mirror motions executed was much higher than the ~ 900 motions per actuator that was predicted before launch.

The actuators were designed for 1.0×10^6 motions, far more than could reasonably be done in even a very long extended mission. As a result, although the number of actuator motions for each mirror were tracked, there was no cause for concern in their usage for channel alignment. Furthermore, any loss of a single actuator on any number of mirrors is a soft failure that will cause a minimal loss of data.

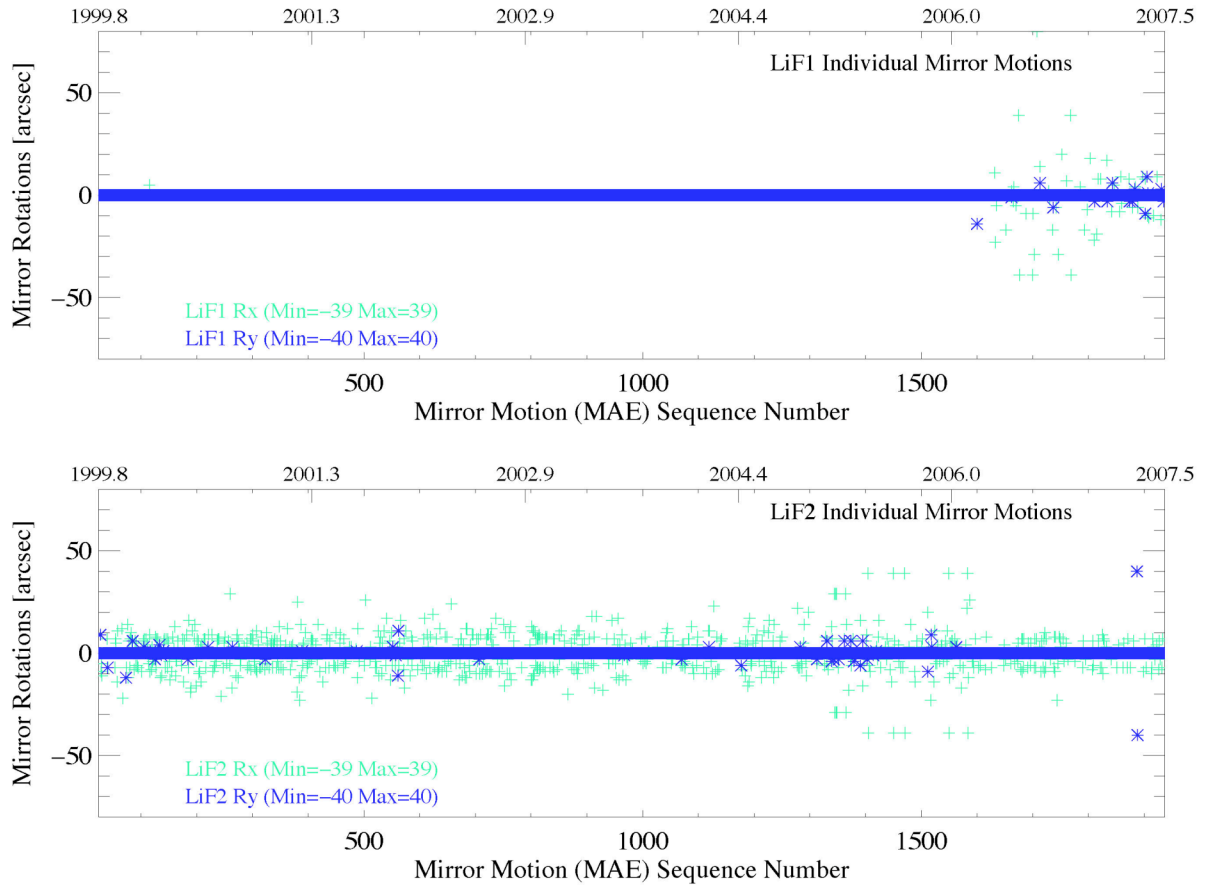


Figure 6-20: Time series of individual mirror motions executed to maintain co-alignment of the LiF channels.

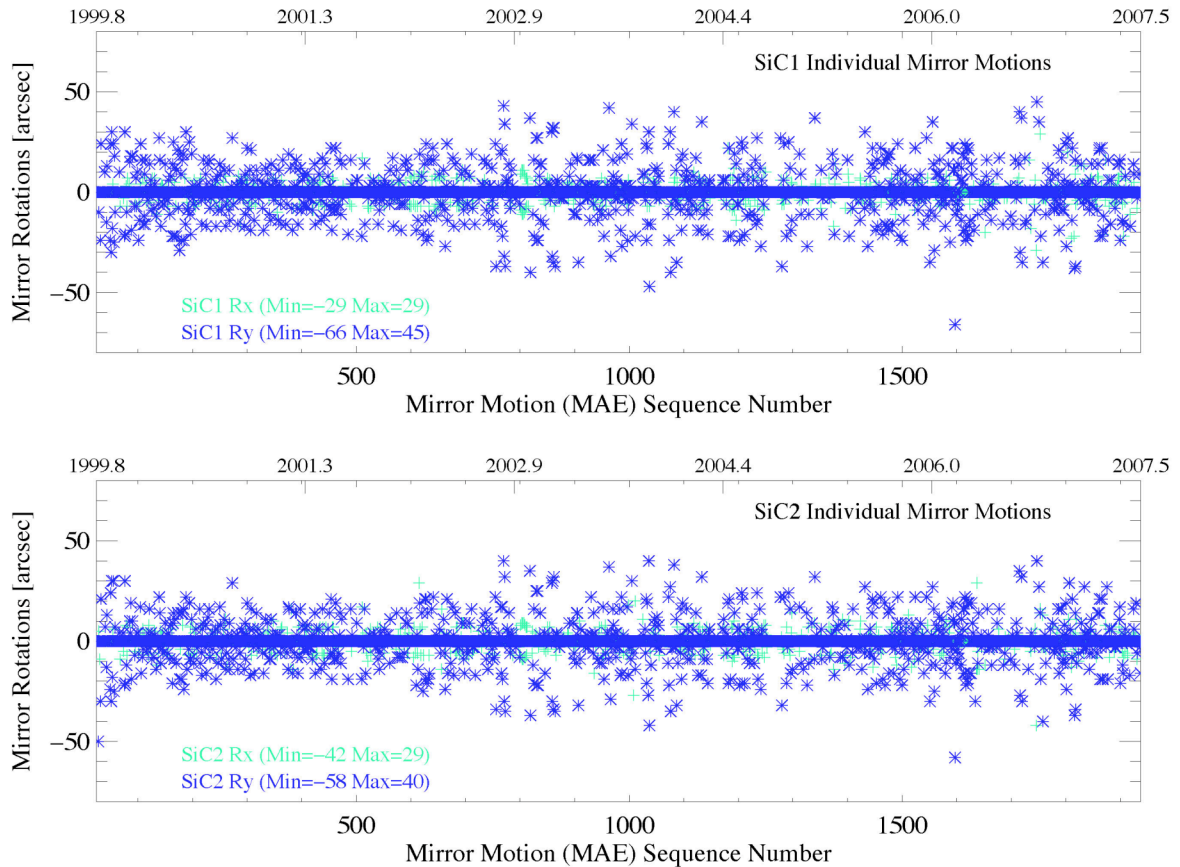


Figure 6-21: Time series of individual mirror motions executed to maintain co-alignment of the SiC channels.

The mirror actuators were not run over their entire range of motion in flight. However, the defocus tests, which were performed to assess the feasibility of executing bright target observing programs, did move the actuators to within 20% of their full range of travel for the LiF2, SiC1, and SiC2 mirrors. The LiF1 mirror was not defocused, since as the guide channel at that time, the risk was not justified. No adverse effects were noticed and the mirrors returned to their nominal in-focus positions as commanded.

The secular drifts of the actuator position associated with mirror co-alignment over the lifetime of the mission is shown in Figure 6-22 and Figure 6-23. The position of the actuators for each mirror, the overall repeatability of the system, and the ability of the model to keep the mirror motions within a well defined range is illustrated. The use of LiF2, rather than LiF1, as the guide channel in early 2006 is evident from the plots. In April 2006, the predictive model became less robust as is indicated in the frequent use of larger actuator motions to obtain co-alignment.

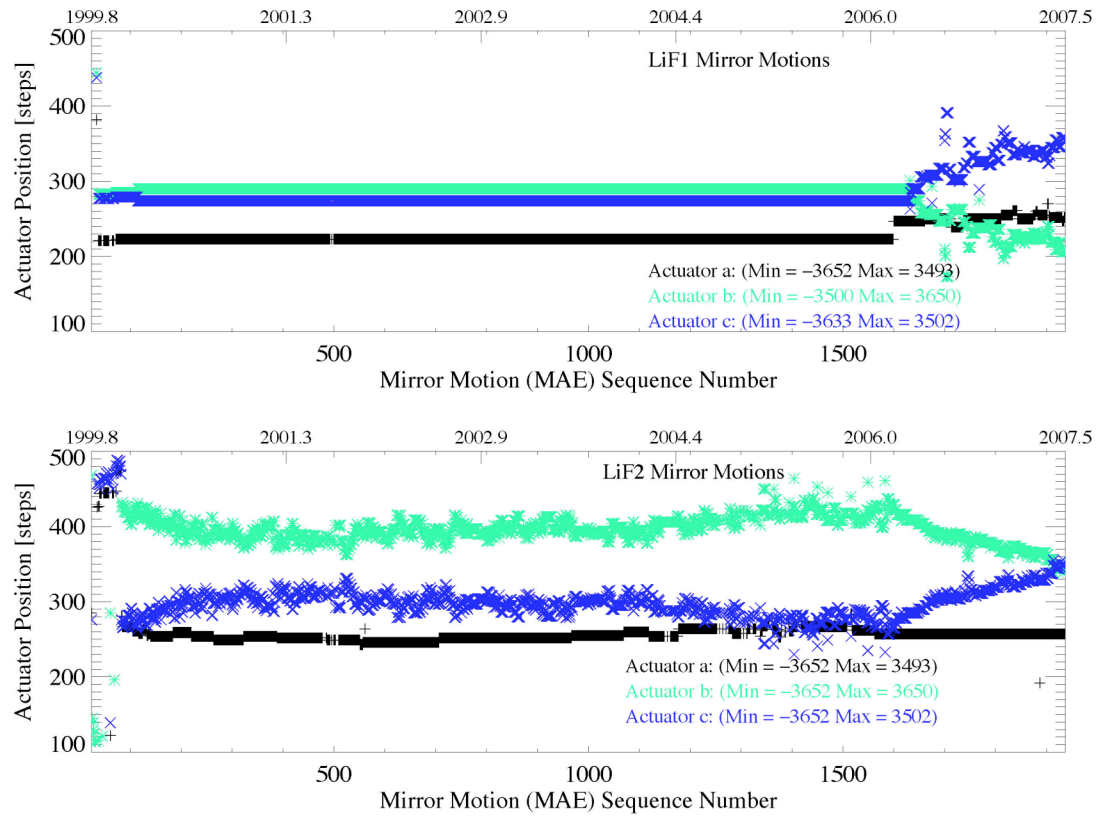


Figure 6-22: The range of motion for each of the LiF1 (top) and LiF2 (bottom) mirrors illustrating that although to co-alignment position for each actuator exhibits a secular drift with time, this change is small and well within the range of travel for each of the actuators.

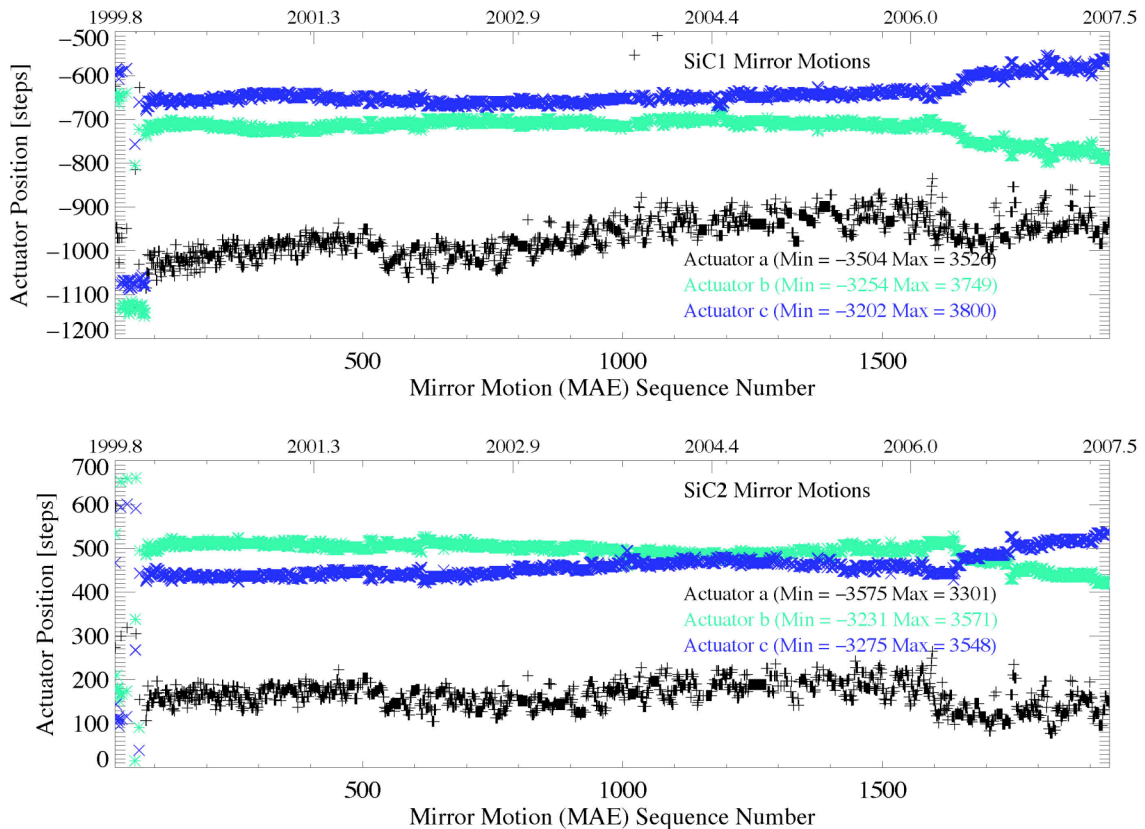


Figure 6-23: The range of motion for each of the SiC1 and SiC2 mirror actuators.

6.7.6 Spectral Motion Anomaly: Thermal & Mechanical Analysis

During IOC an investigation team was assembled to determine the cause of the observed spectral motion. The functional form of the motion with orbital phase was suggestive of differential thermal heating of the instrument. A full FUSE thermal math model was correlated to the thermal balance test data obtained during thermal vacuum test at GSFC (November 1998, January 1999) and input into a structural Finite Element Model (FEM). This model was then used to infer temperature induced image motions. Results of the analysis showed that, as expected, the temperature of SiC side of the instrument and spectrograph increased as beta angle increased. These results were in agreement with flight data depicting the SiC mirror bench and spectrograph heater duty cycles decreasing by 11% and 7% respectively as the instrument's exposure to the sun increased. LiF mirror bench duty cycles were only minimally affected by sun angle changes. SiC baffle temperatures at the upper attachment flexure changed as much as 28 degrees Celsius when the beta angle changed from 70 to 105 degrees. The corresponding change to the LiF side was only

about 1 degree Celsius. Quasi-steady-state temperature variations at these points, caused by orbital influences, were 1 degree Celsius.

Since the spectral motion was first discovered using airglow lines, the possible sources of the motion were isolated to the gratings, FPAs, and detectors. Because the SiC and LiF lines incident on a common detector behaved differently, the detector was exonerated as the cause of the observed motions. The grating bench was eliminated as the cause of the spectral motion because the amplitude and directionality of the spectral motions are larger in X than in Y and it was expected that any motions caused by the grating bench would be larger in Y than in X. Neither were the FPAs regarded as a significant contributor to the spectral motion since observations using the LWRS slit, which is much larger than the image of a typical astronomical source, show similar motions in the spectrum of a point source and in airglow lines that fill the slit.

The FUSE Grating Mount Assemblies (GMA) were also investigated for any potential contribution to the in-flight spectral motions. The existing thermal distortion analysis was reviewed for orbital variation for the GMAs. A overview of the design was also performed. The review of the GMAs was limited to the mount assembly since the FUSE on-orbit performance shows no evidence that the grating glass itself could be distorting. During the instrument design phase, a thermal model of the GMA was constructed and coupled to the satellite model to predict an on-orbit temperature map for the grating assembly components. That analysis predicted that for each individual piece part of the GMA, the orbital temperature change laterally in IPCS X and Y was negligible (< 0.02 Celsius). The orbital temperature change in the mount in the IPCS Z is ~ 0.2 degrees Celsius, and the worst case orbital temperature change between the inner and outer tube temperatures is 0.2 degrees Celsius. The FEM distortion analysis showed that translations of the center of the grating are within short-term stability requirements.

However, the model analysis was not regarded as conclusive given the large size of the mount and the relative flexibility of titanium, the primary material of construction. A test simulating the on-orbit environment was regarded as the best verification of the mount's thermal stability.

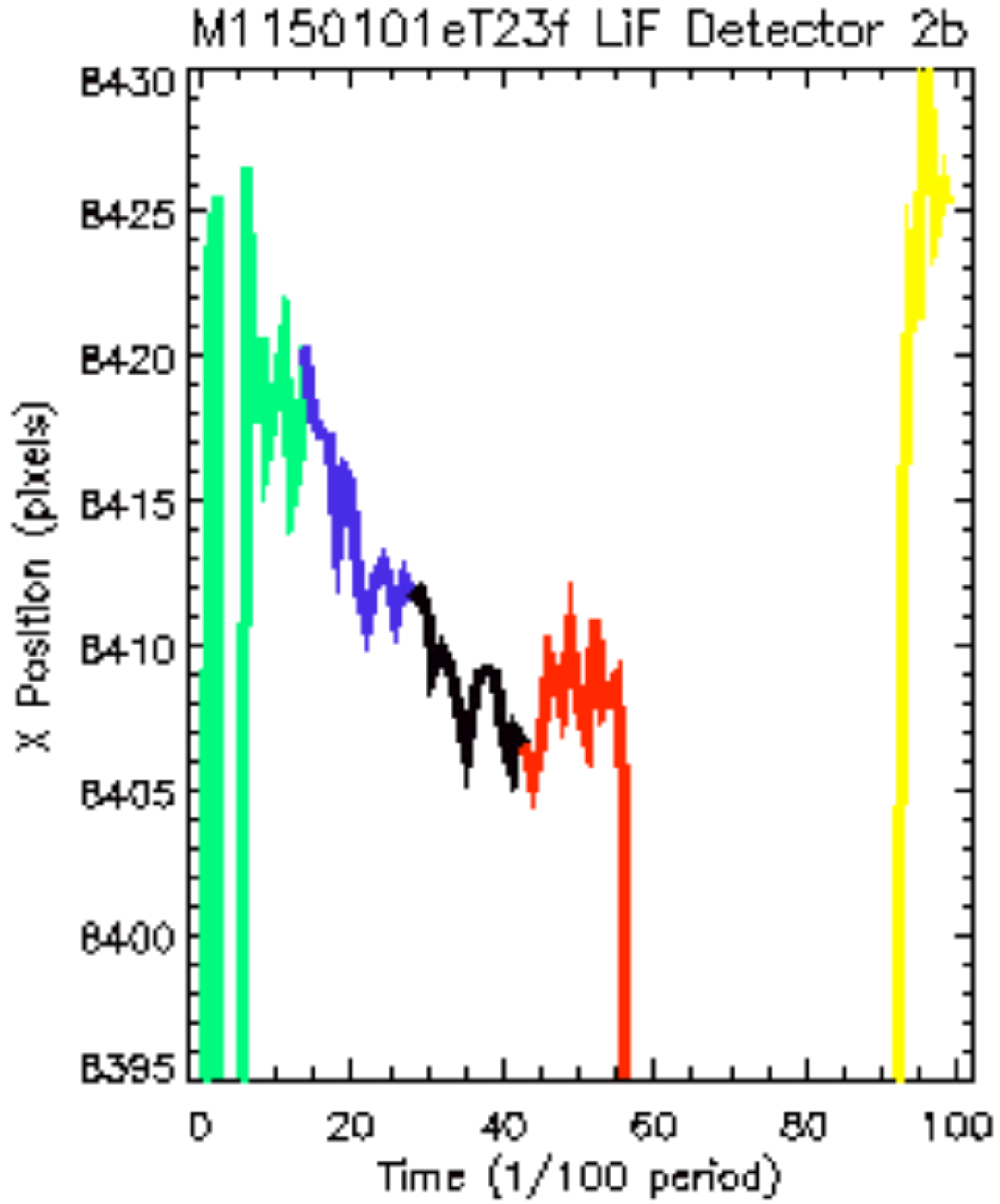
Consequently, pre-launch tests were conducted to determine if the gratings distorted with temperature. The gratings were heated using their shrouds while monitoring their spectral images for changes. The glass temperature was raised from 21 to 28 degrees Celsius while the shroud temperature peaked at ~ 40 degrees Celsius. A post-launch re-examination of this data found that the image moved 19 pixels on the detector (~ 114 microns) for this temperature change in the direction of IPCS +X for the SIC1 channel. Concurrent observations using the LiF1 channel, without heating its shroud, exhibit only a ~ 3 pixel motion. These results and the magnitudes of the motions are supported by a FEM/thermal analysis done for FUSE by the University of Arizona.

The resulting hypothesis was that the direct conductive path from the shroud to the grating mount hardware was heating the "wedge" non-uniformly, possibly leading to a grating rotation. While not conclusive, this test data illustrates the potential sensitivity of the grating mount assembly to temperature change.

Subsequently, an on-orbit test was conducted to test the hypothesis that the heaters may have been thermo-electrically coupled to the spectrograph GMA.

To evaluate this hypothesis, the two grating shrouds (LiF2 and SiC2) on the +y spectrograph axis were permitted to drift to a lower temperature while the other two grating shrouds (LiF1 and SiC1) were held at their nominal set point of 23 C. A temporary set point of 19 C was chosen for the heaters. This temperature was chosen to permit acquisition of Lyman beta airglow spectra for 2 orbits without the heaters cycling while keeping the gratings at or above the spectrograph temperature, a contamination related issue albeit not a severe concern after ~15 months in orbit.

Although the time required for the GMA shrouds to reach their test thermal set-point was significantly faster than expected, a few conclusions could be drawn. The motion of the spectrum in the dispersion direction was not alleviated by operating with the GMA shroud heaters off. Changing the temperature results in an offset in the zero point position of the spectrum on the detector in the dispersion direction. And, the functional form of the relative motion of the spectrum was the same at the lower grating temperature as it is at the nominal temperature. The spectral motion exhibited after the GMA shrouds were returned to their nominal temperature was the same as it was before the temperature was lowered.



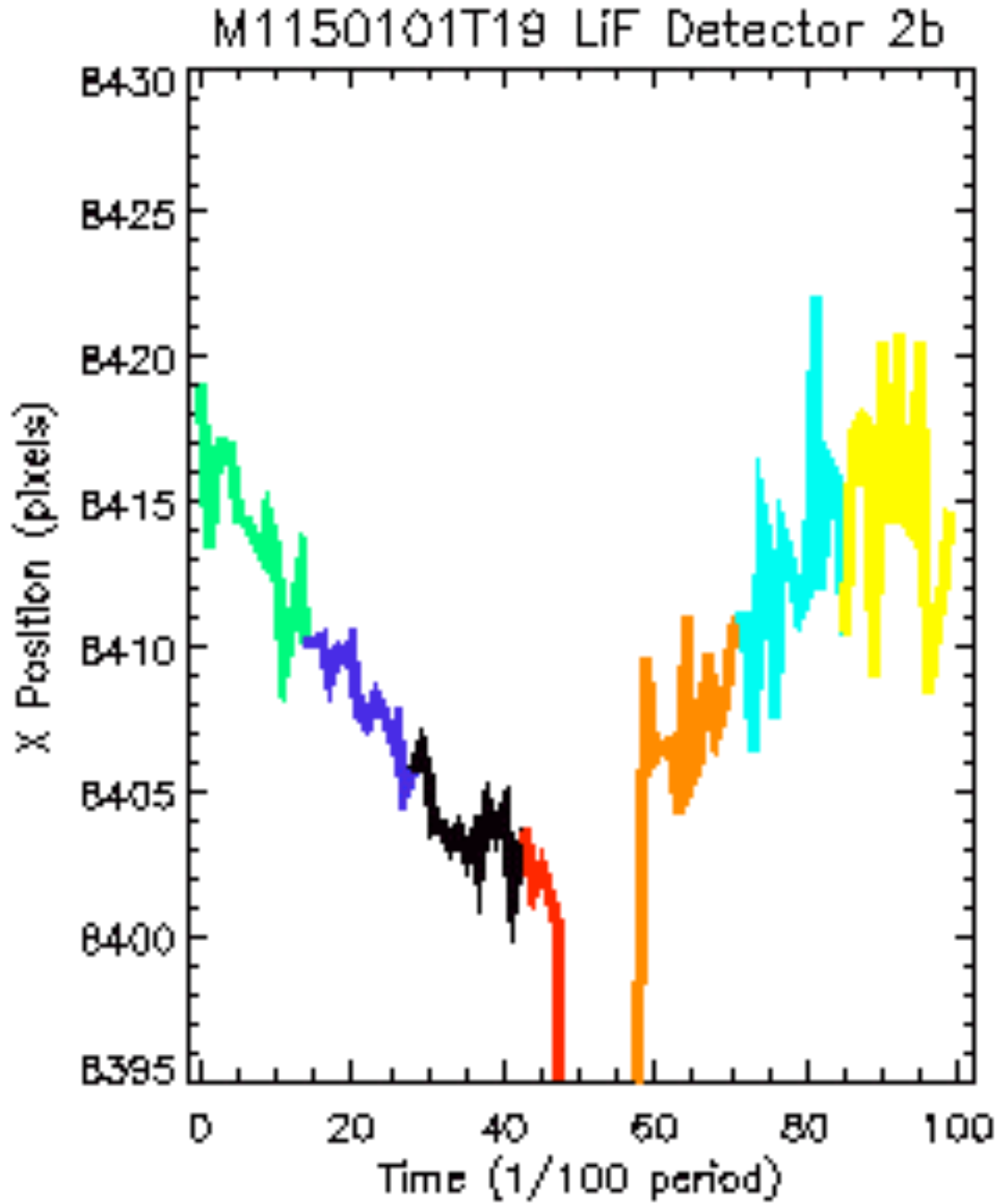


Figure 6-24: LiF2B data over an orbital period illustrating that the spectral motion observed with the GMA shroud at 19 C (top) is shifted/offset by ~5-6 pixels from the data acquired with the GMA shroud at the nominal 23 C (bottom).

6.8 □ Optical Design Specifications

FUSE/FUVS Optical Baseline Design Current Parameters

Each Rowland Circle has 1 SiC Barrel and 1 LiF Barrel
Both LiF Barrels will be on the "Dark" side of the spacecraft to ease FES baffling requirements.

Wavelength coverage:

SiC1 = 905.0-993.3/1002.7-1091.0Å
SiC2 = 917.6-1005.9/1015.3-1103.6Å
LiF1 = 994.9-1089.2/1099.2-1193.5Å
LiF2 = 981.5-1075.8/1085.7-1180.0Å

<u>SiC</u>	<u>LiF</u>
Alpha: 24.0°	Alpha: 25.0°
Beta: ($\lambda = 986\text{Å}$) 9.31660°	Beta: ($\lambda = 1107\text{Å}$) 9.76612°
Ruling Density: 5767 grooves/mm	Ruling Density: 5350 grooves/mm
γ : -75.921°	γ : -69.358°
δ : +72.5367°	δ : +58.0989°
Rc: -4288.25mm	Rc: -3979.61mm
Rd: +4321.09mm	Rd: +3641.07mm
df: +0.0810	df: +1.06545
Radius of Curvature: 1652 ±1 mm	Radius of Curvature: 1652 ±1 mm

df: Defocus offset of the detector from it's position on the Rowland circle along the diffracted central ray is included in diagrams. Positive motion moves the grating closer to the detector. No detector rotations are introduced.

Focal length (F) = 2245mm (mirror parabola vertex to slit in Z-direction)

Grating spherical radius = 1652mm

Telescope mirror parabolic profile: $Z = \frac{x^2}{4F}$

Mirror active area: SiC = 1331cm²
LiF = 1333cm²

Grating active area: SiC = 653cm²
LiF = 648cm²

Grating dimensions: 26.6cm (dispersion) x 27.5cm (imaging) x 6.3cm (thickness)
(allowing 3mm each side recording tolerance and 1mm each side alignment tolerance).

FUSE/FUVS OPTICAL DESIGN BASELINE
 ROWLAND CIRCLE PAIR 'A'

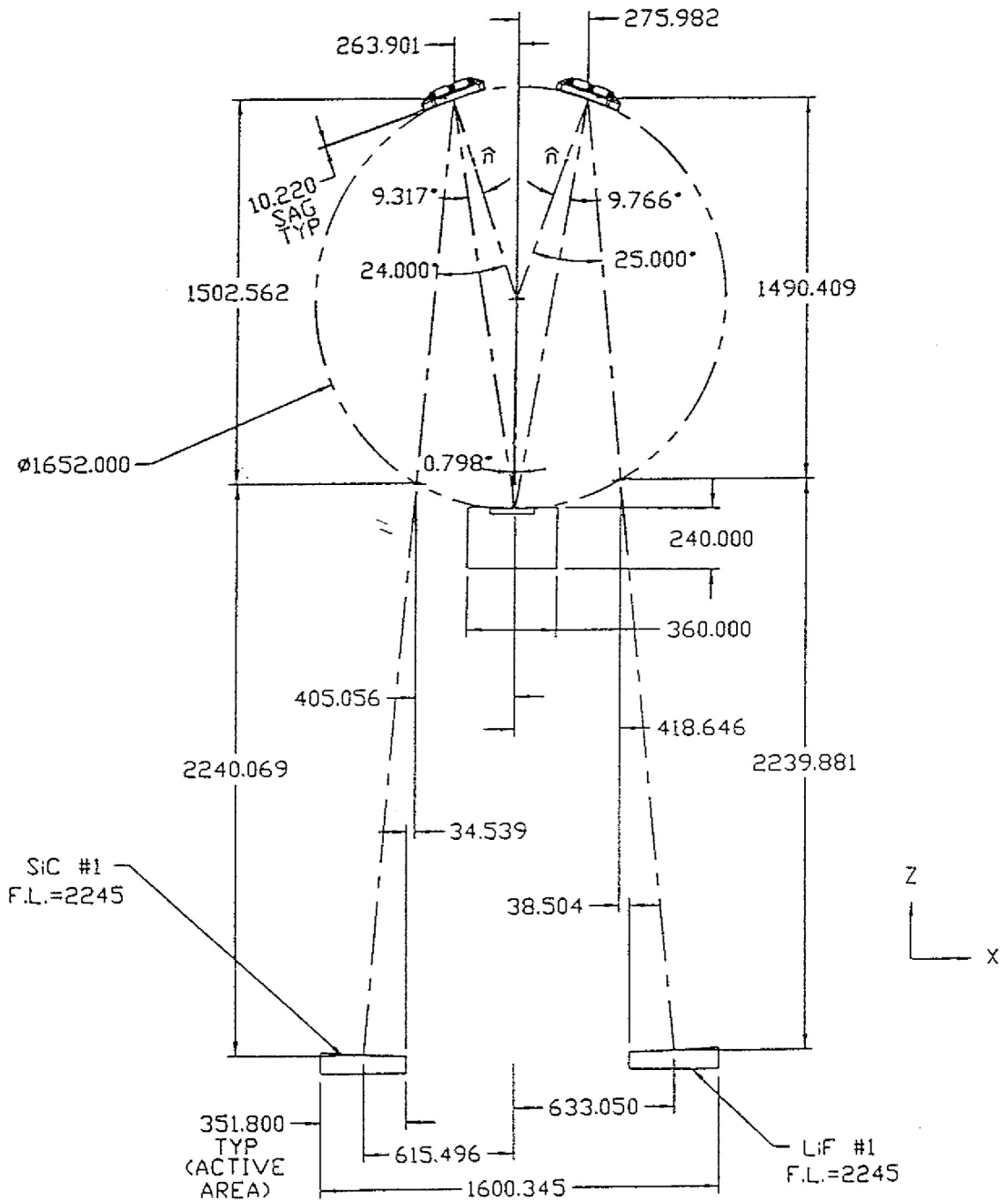


Figure 6-25 Optical element layout for LiF1, SiC1 channels.

FUSE/FUVS OPTICAL DESIGN BASELINE
ROWLAND CIRCLE PAIR 'B'

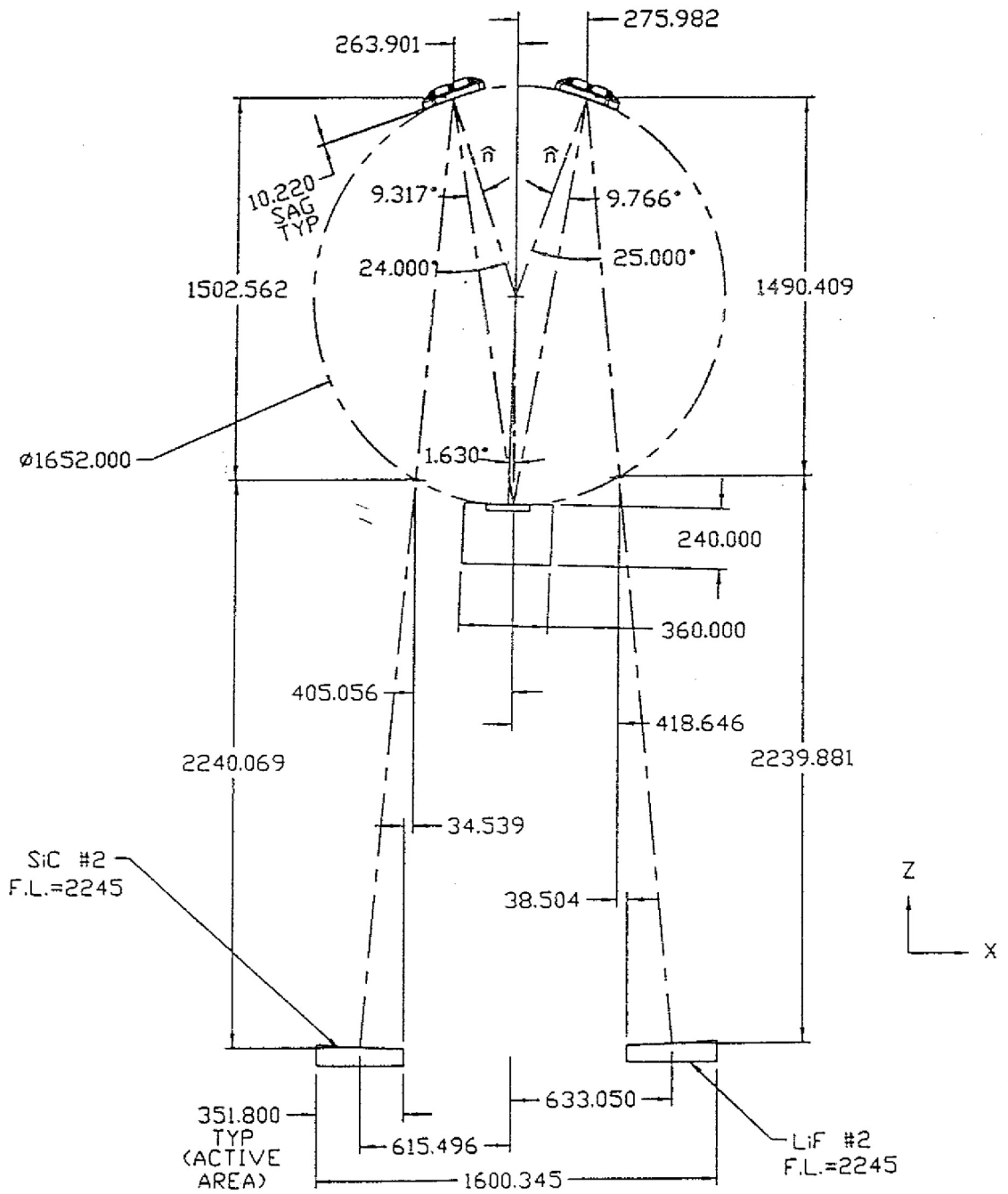


Figure 6-26 Optical element layout for LiF₂, SiC₂ channels.

FUSE/FUVS OPTICAL DESIGN BASELINE

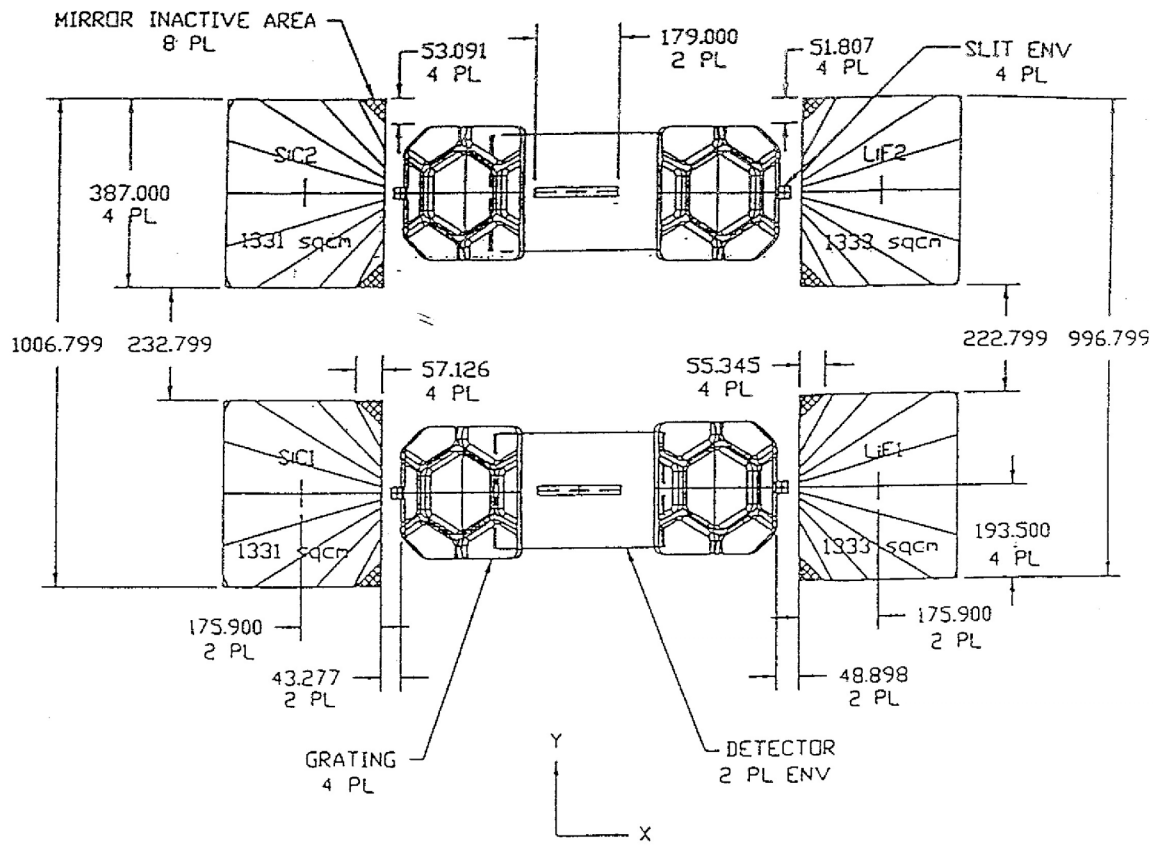


Figure 6-27 Optical element layout, top view.

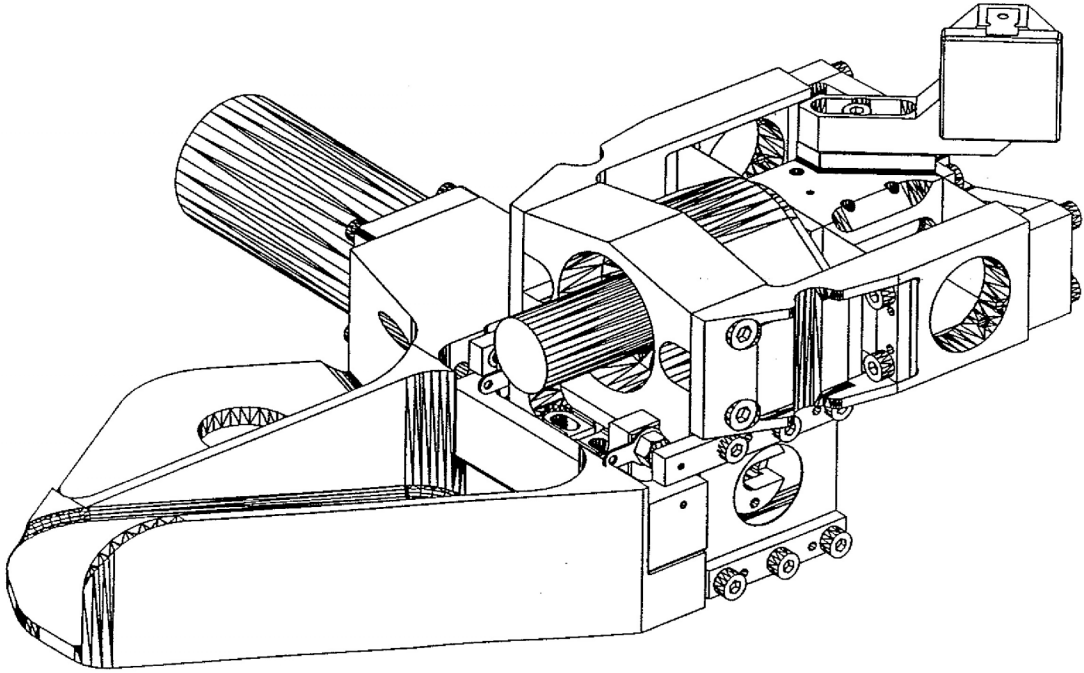


Figure 6-28 Line drawing of an FPA mechanism, showing the two-axis stage and aperture plate.

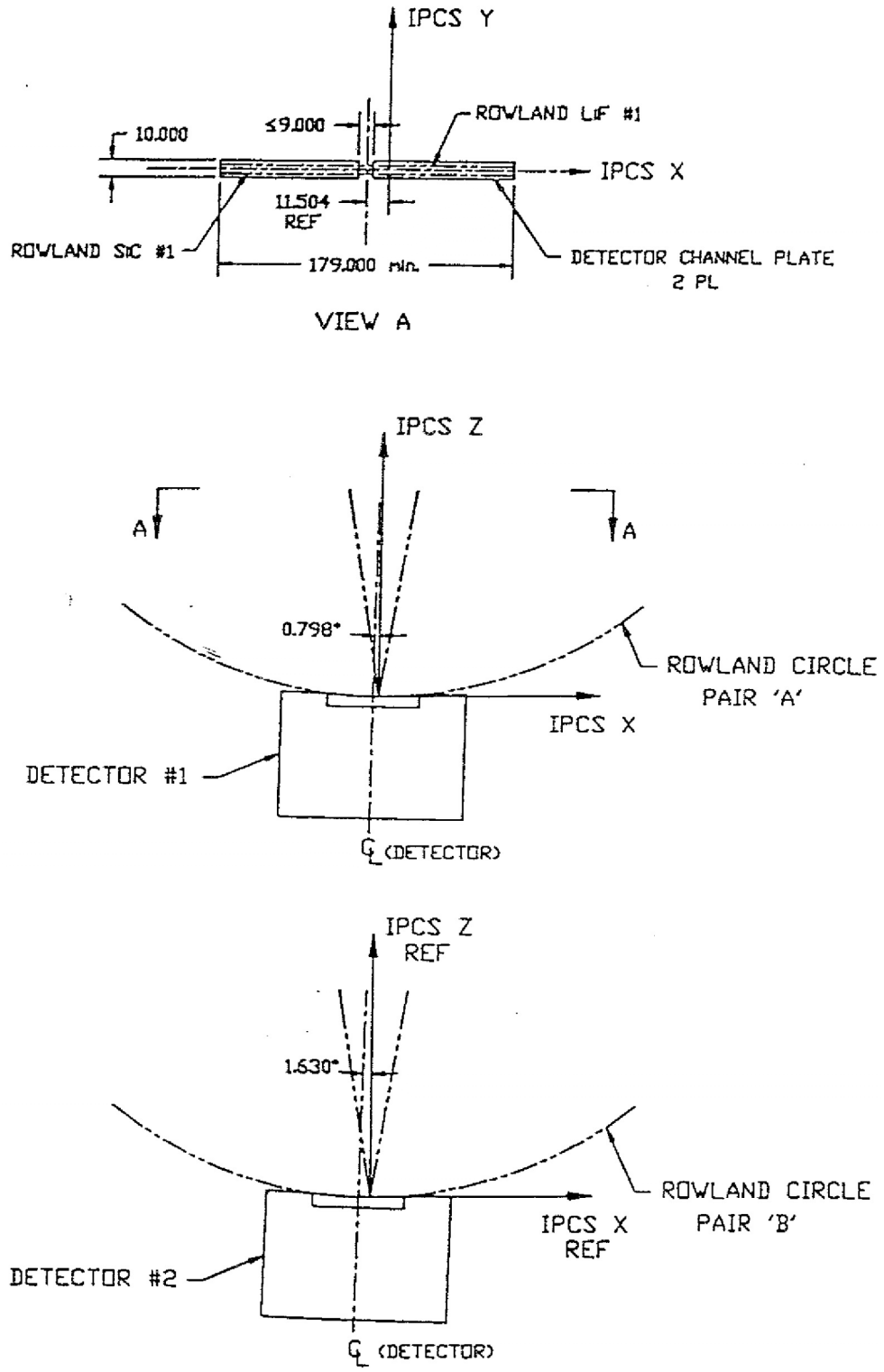


Figure 6-29 Details of optics layout at detector surfaces.

**FUSE/FUVS
OPTICAL COMPONENT LOCATIONS**

	IPCS		
	x	y	z
SiC #1			
Grating Optical Center	-263.901	-2.500	1608.624
Slit	-405.056	-2.500	106.063
Mirror Optical Center	-615.496	-2.500	-2134.006
Detector #1 Optical center	0.000	-2.500	0.000
SiC #2			
Grating Optical Center	-263.901	617.299	1608.624
Slit	-405.056	617.299	106.063
Mirror Optical Center	-615.496	617.299	-2134.006
Detector #2 Optical Center	0.000	617.299	0.000
LiF #1			
Grating Optical Center	275.982	2.500	1603.417
Slit	418.646	2.500	113.009
Mirror Optical Center	633.050	2.500	-2126.872
Detector #1 Optical Center	0.000	2.500	0.000
LiF #2			
Grating Optical Center	275.982	612.299	1603.417
Slit	418.646	612.299	113.009
Mirror Optical Center	633.050	612.299	-2126.872
Detector #2 Optical Center	0.000	612.299	0.000

Note:

Optical Center is defined as the intersection of the central ray with the optic surface.

	x	y	z
Detector #1 Geometric Center	-11.504	0.000	0.080
Detector #2 Geometric Center	-23.496	614.799	0.334

Figure 6-30 Positions of optical elements.

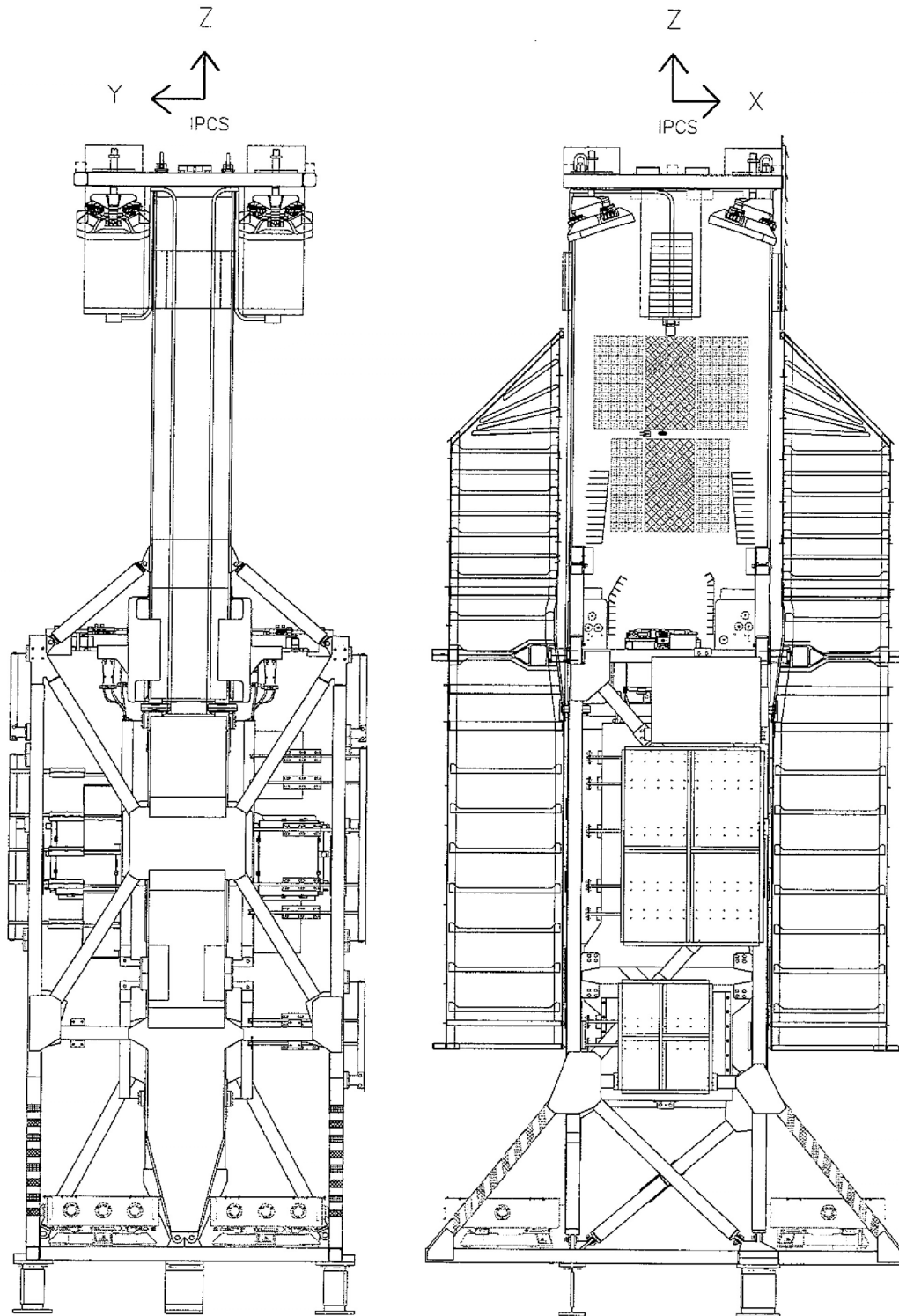
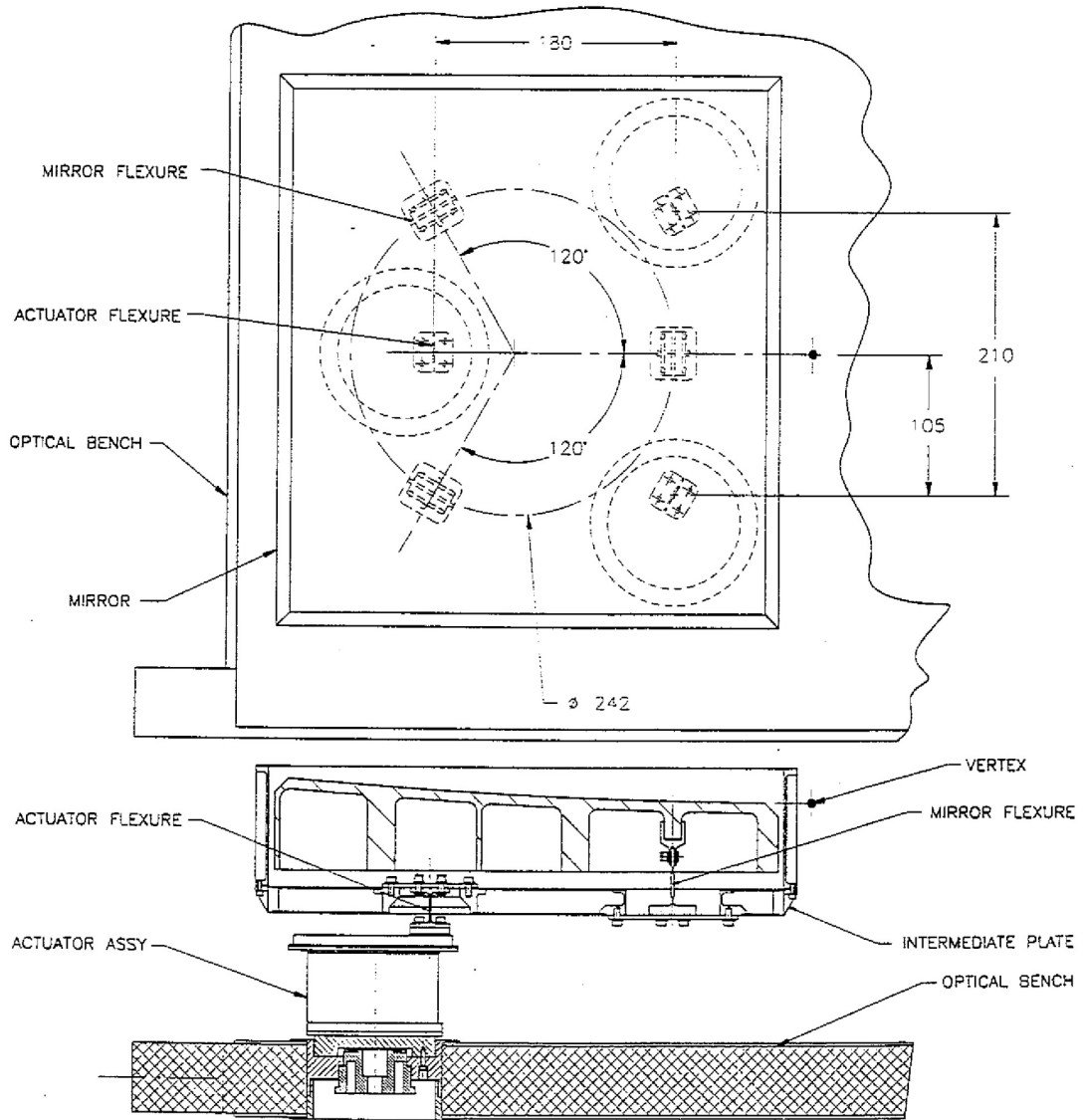


Figure 6-31 Side views of instrument, showing the structure, optics, baffles, electronics, and radiators. Left: Y-Z view, Right: X-Z view.



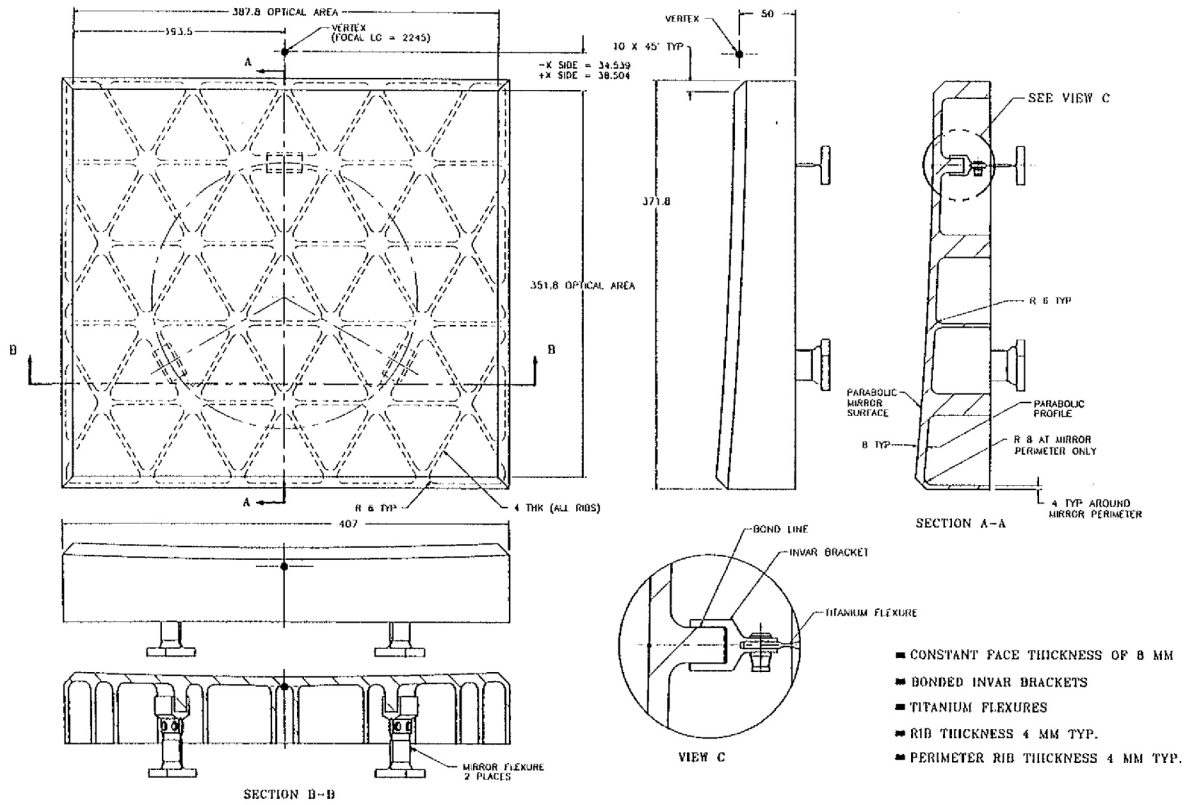


Figure 6-32 Section views of a primary mirror. Top: "pie-pan" enclosure, intermediate plate and bench are shown, with positions of the actuators. Bottom: mirror dimensions and vertex position are shown.

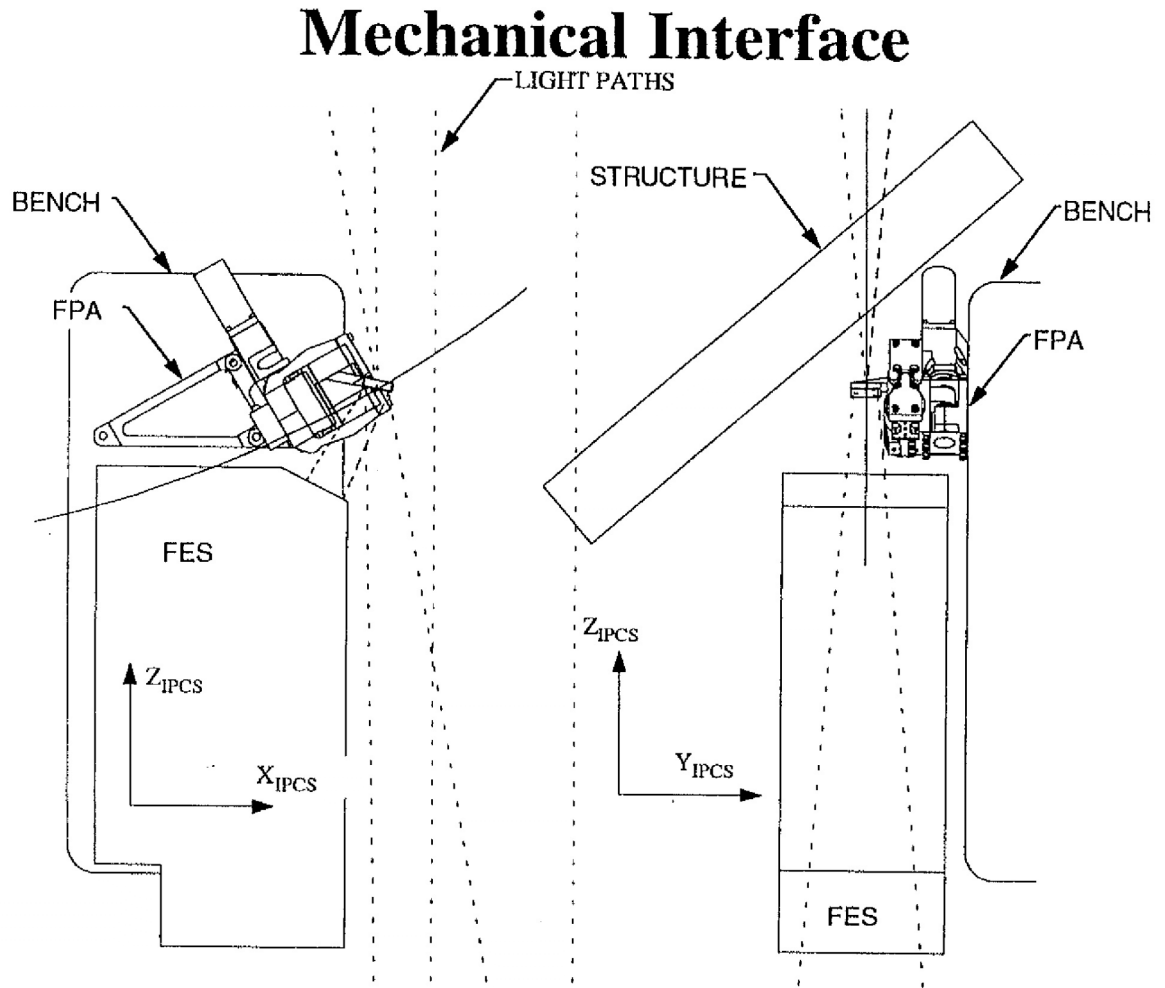


Figure 6-33 Close-up view of light paths at the FPA-FES interface.

GMA Section View

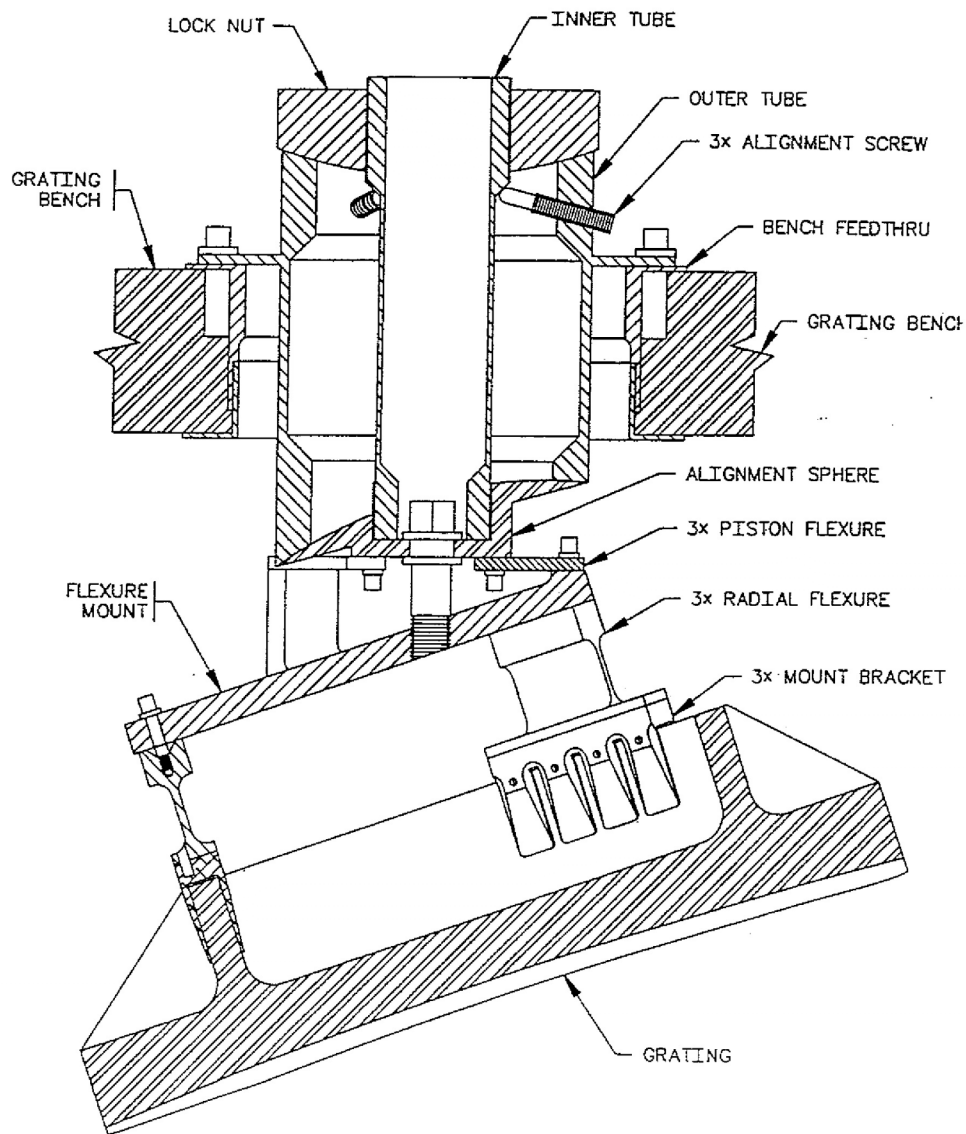


Figure 6-34 A section view of a grating mount assembly and grating are shown.

6.9 □ Dead Time

There were multiple effects which caused photons that reached one of the detectors to be lost before they could be properly recorded. We refer to these collectively as “dead time.” Corrections for these effects, which are a function of count rate, are made in the CalFUSE pipeline. Figure 6-35 and Figure 6-36 show the flow of data through the detector places in the data flow where dead time effects occur. Information on the treatment of dead time effects by CalFUSE can be found in Dixon et al. 2007.

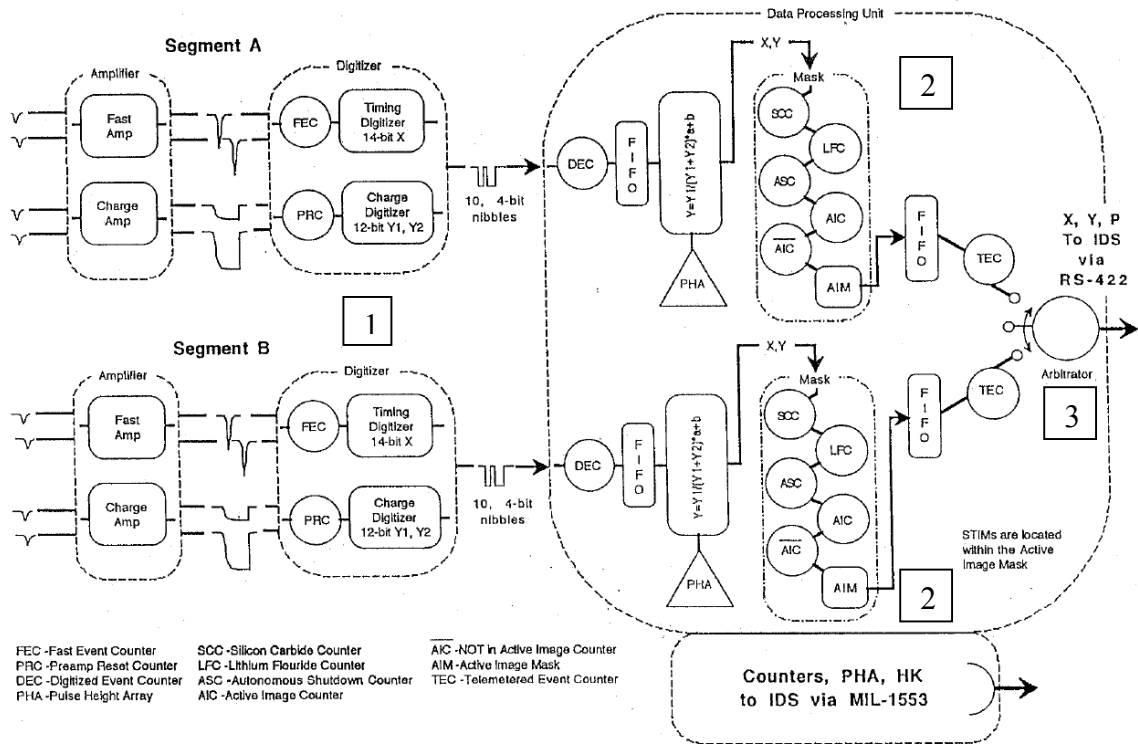


Figure 6-35 Functional block diagram showing the flow of events through the detector electronics (1 of 2). Counts incident on the detector can be lost (1) at the digitizer; (2) due to counts falling outside the Active Image Mask; and (3) in the Round Robin, which combines the data from two segments on one detector.

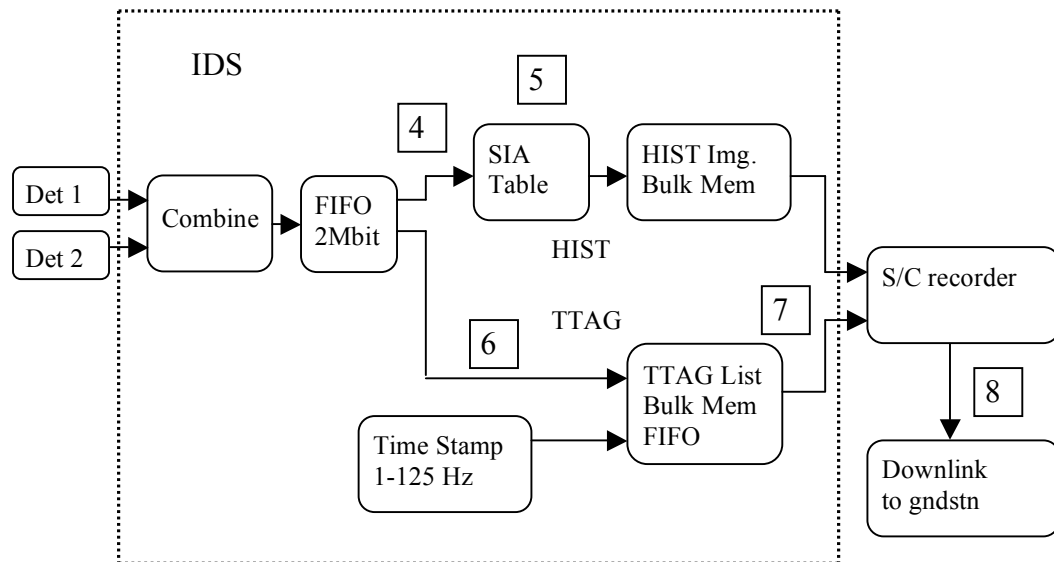


Figure 6-36 Functional block diagram showing the flow of events through the detector electronics (2 of 2). Counts can be lost (4) in the IDS if the count rate is above 32,000 cps (HIST only); (5) due to screening by the SIA table (HIST only); (6) in the IDS if the count rate is above 8,000 cps (TTAG); (7) if the FIFO fills (TTAG); or (8) between the spacecraft and the ground system.

The following effects, numbered to match the figures, are potential contributors to the dead time.

- 0 **MCP response time:** The first of these effects is the response time of the MCPs themselves. If the count rate is too high in a particular region of the plate, local gain sag may occur and subsequent photons may not generate enough charge to be detected by the electronics. The count rates for this to occur, however, are well above the count rates seen during the FUSE mission, so this has a negligible effect on the data.
- 1 **Detector Electronics Dead Time:** The inability of the detector front end electronics to process two events that arrive within a very short time interval leads to the electronics dead time. Analysis of the electronics design by UC Berkeley [memo reference] showed that this effect could be characterized by the following equation:

$$P_{\text{live}} = \exp(-R t_a) / (1 + R t_{\text{ism}} - X^{10} + X^6 + 4X^2 - 4X),$$

$$X = \exp(-R t_{\text{clk}}),$$

where $P_{\text{live}} = (1 - \text{Dead time})$; R is the input count rate, as given by the FEC; and t_a , t_{clk} , and t_{ism} are constants related to the design of the Input State Machine in the DPU ACTEL.

Analysis of science data for each segment was used to calculate the best-fit values of t_a , t_{clk} , and t_{ism} in the above equation so that they could be used by the pipeline. The correction applied could then be calculated for each segment of each exposure based on the measured FEC rate.

The parameter values in CalFUSE are given in Table 6.9-1, which were based on data obtained early in the mission. A reanalysis using all the data from the mission resulted in updated parameters, given in Table 6.9-2. The differences between the two fits are negligible for most FUSE observations, but can reach a few percent for targets at or above the bright limit. Live-time curves computed from these parameters are plotted in Figure 6-38 and Figure 6-39.

Segment	t_a	t_{ism}	t_{clk}
1A	2.76	11.68	1.50
1B	4.66	10.28	1.66
2A	5.23	8.37	1.27
2B	4.23	6.31	0.00

Table 6.9-1 Detector deadtime parameter values used by CalFUSE.

Segment	t_a	t_{ism}	t_{clk}
1A	5.53	9.94	2.25
1B	4.28	14.31	3.11
2A	4.85	8.89	1.08
2B	4.90	11.30	3.45

Table 6.9-2 Updated detector deadtime parameters

- 2 **Active Image Mask:** An Active Image Mask (Section 6.3.1.2.2.3) which excluded part of the detector would result in a loss of counts. Since these masks were left wide open for the entire mission, this had no effect.
- 3 **Round Robin:** The “Round Robin” combined the events from two segments on a single detector into a single data stream for passing to the IDS.
- 4 (HIST) **Data Bus Limit (IDS Dead Time):** A maximum of 32,000 counts per second could be passed on the data bus in HIST mode. If the sum of the Active Image Counter rates on all four segments exceeded this value, CalFUSE scaled the counts appropriately. Stim lamp exposures

were the most common causes of exceeding this limit.

- 5 (HIST) **SIA Table Screening:** Use of an SIA table limits event storage to specified regions of the detector.
- 6 (TTAG) **Data Bus Limit (IDS Dead Time):** In TTAG mode, the maximum throughput is 8,000 counts per second.
- 7 (TTAG) **FIFO Size and Drain Rate:** A 9 MB (default) region of memory acted as a FIFO to buffer the data stream on the way to the spacecraft recorder. Once this FIFO was full, it could be drained at only ~3500 counts per second. Thus long TTAG exposures at high count rates had regular data dropouts (Figure 6-37). As a result, TTAG exposures were typically limited to count rates of less than ~2500 counts per second.
- 8 **Transmission to the Ground:** Data could be lost between the spacecraft recorder and the building of the raw data files.

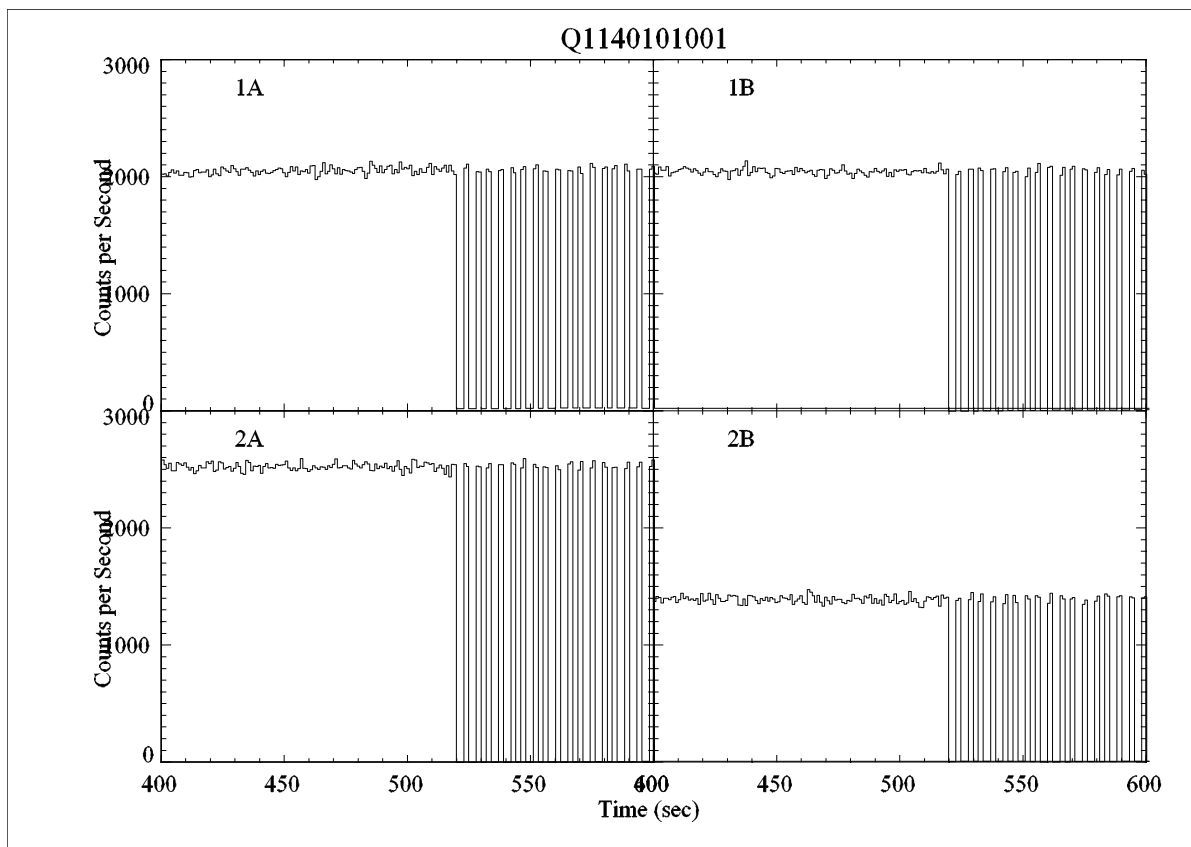


Figure 6-37 Apparent count rate as a function of time for exposure Q11401001, which was obtained in TTAG mode, despite having a count rate of more than 100,000 counts per second. For the first ~520 seconds the count rates on all four segments

were constant, with their sum limited to the 8,000 cps TTAG data bus limit. For the remainder of the exposure, regular data dropouts appeared as the FIFO filled.

All of these effects have been considered to be independent of time in CalFUSE. There were suggestions in the data that the electronics dead time may have changed during the mission, but the effect, if present at all, is small.

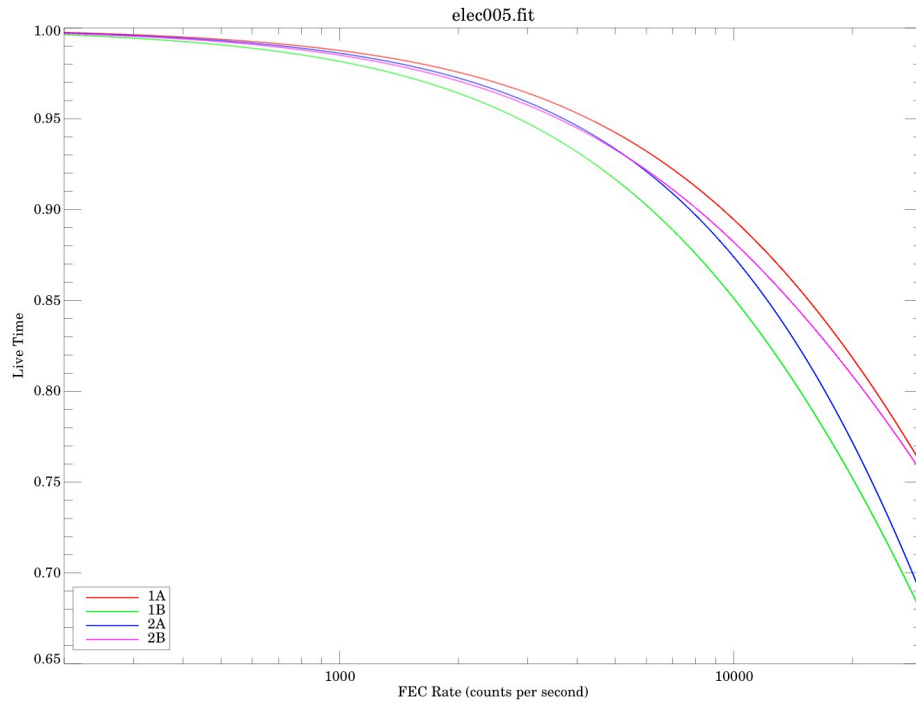


Figure 6-38 Detector live-time calibration used by CalFUSE.

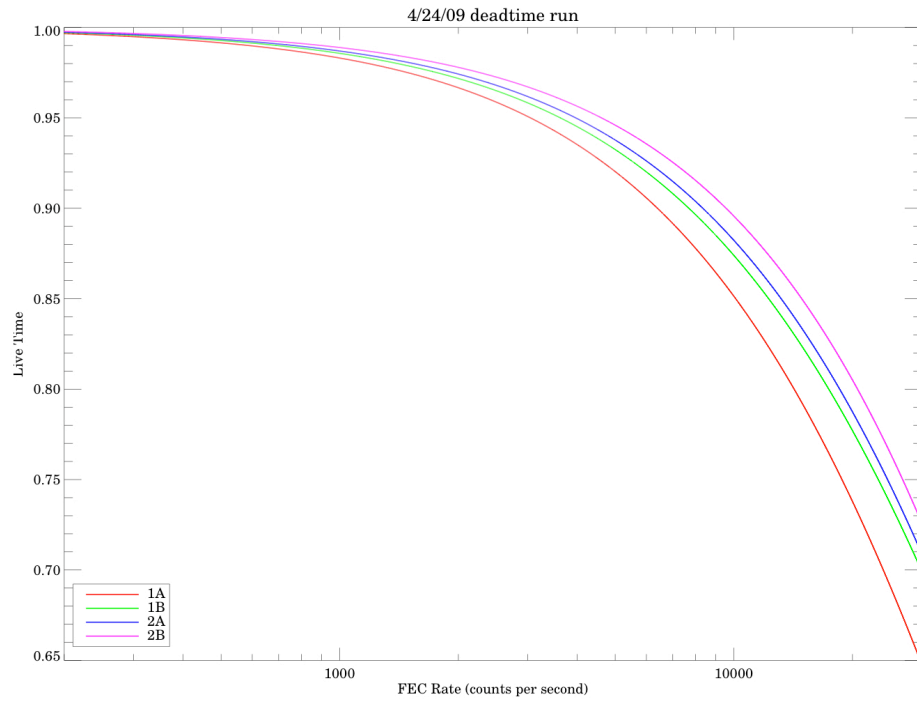


Figure 6-39 Updated live-time calibration curves.

7 Attitude Control System Technical Appendix

7.1 □ In-flight ACS Performance Summary

Over the first two and a half years of the FUSE mission, the satellite attitude control system design using the FES and IDS to provide fine guidance data to the ACS worked as intended. Many parameters were tuned-up during in-orbit checkout: FES to S/C alignment, FES optical distortion calibration, IDS image processing parameters, IDS Star-identification parameters, and FES timing and subarray sizes. Most parameters needed only one adjustment; the image processing parameters needed several iterations over the first year of the mission, however, as various (e.g. crowded, high/extended nebulosity, extremely bright star) star-fields were encountered. Specific star field tables were generated and loaded for particular observations that needed them. Pointing stability was typically a half-arcsecond or better, and slews and target acquisitions were efficient and reliable.

Over the subsequent years of the FUSE mission, however, the ACS subsystem experienced the lion's share of the mission-critical hardware anomalies. Four of the six gyro channels failed, and each of the four RWAs failed, ultimately resulting in the termination of the mission. The flight software in the FES, IDS, and ACS was rewritten to accommodate the loss of gyros. Subsequent to each wheel failure, the ACS software was further rewritten to compensate for the reduction in attitude control. The target acquisition scripts in the IDS were rewritten on a nearly continuous basis to improve the robustness of operations.

However, in other respects, performance of the ACS remained nominal throughout the mission.

The Tri-axial Magnetometers (TAMs) performance exceeded pre-launch expectations. They were calibrated to better than 0.2 degree, whereas the pre-launch expectation was 2 degrees.

The performance of the Coarse Sun Sensor (CSS) assemblies was similar to other Explorer Platform missions using similar assemblies. Apart from the additional signal from the Earth's albedo corrupting the CSS readings, there were no anomalies in the CSS subsystem during the mission.

Prior to the advent of one-wheel operations, the solar arrays were typically moved only during slews to new targets. Typically the slews were much smaller than 90 degrees with an average of three slews per day. After one wheel operations began, the Solar Array Drive (SAD) mechanisms were in use for much more time than envisioned pre-launch. Nevertheless, there were no anomalies of the SAD hardware during the mission.

The “gyroless” attitude determination software worked quite well, so the gyro failures had no direct impact on FUSE science data beyond increased overheads needed for target acquisitions. If anything, pointing stability improved because the angular rates determined from FES data had lower noise than those of the gyros.

The loss of reaction wheels, however, did have an impact on the quality of the science data. Pointing of the FUSE spacecraft was originally controlled with all four reaction wheels, which typically maintained a pointing stability of 0.2"-0.3". After the failure of the yaw and pitch reaction wheels, it became necessary to control the spacecraft orientation along the A axis (see Figure 3-1) with MTBs. Spacecraft drift increased along this axis: typical values were 1-2 arcsec, but drifts of many arcsec occurred occasionally. Without correction, such motions of a target within the LWRS aperture (the default aperture in this mode) could degrade the resolution of the spectra, so the CalFUSE pipeline was modified to correct the data for spacecraft motion during each exposure. For time-tag observations of point sources, individual photon events were repositioned based on fine pointing data (FPD) in the telemetry. For histogram observations, it was only possible to correct for the exposure time lost to large excursions of the target outside the aperture.

Following the failure of the roll-axis wheel, the frequency of large pointing drifts increased significantly. However, the transition between stable pointing and unstable pointing was rather abrupt. If the magnetic torque available exceeded the gravity gradient, then the pointing often remained stable to a few arcsec, though excursions of 5-10 arcsec were more common than before. If the gravity gradient exceeded the available magnetic torque, however, then the resulting excursion would move the source far out of the aperture. Thus, the main impact of one-wheel operations was on observing efficiency and limitations on target availability, rather than on spectral resolution.

7.2 □ Inertial Reference Unit Failures

The chronology of the major events associated with the IRUs over the course of the mission are listed in Table 7.2-1. Two of the low-intensity flags were set in IRU-A roughly six months after launch, and the third was set three months later. This rapid drop in laser intensity prompted initial thinking about how to operate with reduced or without gyros; with the failure of the first channel in May 2001, planning for gyroless operations began in earnest. The ACS switched autonomously to IRU-B when the first channel failed in IRU-A. The first version of “gyroless” attitude determination and control software was uplinked the week of April 16, 2003. When the first channel (Z) in IRU-B failed in July 2003, the software began using the new rate estimator logic in place of the failed gyro channel. In May 2004, noise in the IRU-B pitch axis began to increase. This was first noticed in August, and reached the point of significantly degrading performance in September. This gyro channel was manually removed from use on September 24, 2004. This failure mode differs from that of the other channels, in that the gyro continued to provide data. Data from this channel might have been usable with suitable filtering, but this possibility was never pursued. When the roll wheel failed in December 2004, IRU-A was powered back on so that there would be gyro data on all axes while trying to get one-wheel control to work.

The roll axis in IRU-B failed on April 17, 2005, which ended the use of IRU-B for guiding. It was occasionally powered on thereafter, for thermal or other ancillary reasons. The pitch and yaw channels in IRU-A continued to operate normally until the satellite was decommissioned in October 2007. The failures of the IRU-A Y and IRU-B Y,Z channels were similar in nature: the measured rate dropped abruptly to zero and remained exactly zero. There was no apparent change in performance prior to the failure. This behavior is consistent with cessation of lasing as a result of declining intensity.

DATE	EVENT
mm-dd-yyyy	
06-24-1999	Launch – IRU A ON
01-06-2000	IRU A Z low intensity
01-18-2000	IRU A X low intensity
04-19-2000	IRU A Y low intensity
05-30-2001	IRU A Y fails Switch to IRU B
08-31-2001	IRU B X low intensity
10-06-2001	IRU B Y low intensity
12-10-2002	IRU B Z low intensity
07-31-2003	IRU B Z Fails Begin 2-gyro ops
09-28-2004	IRU B X too noisy Begin 1-gyro ops
12-27-2004	Roll RWA Fails - Power ON IRU A&B
04-17-2005	IRU B Y axis fails
10-18-2007	Decommission FUSE

Table 7.2-1: IRU (gyro) Chronology of Events

7.3 □ Reaction Wheel Failures

FUSE had four reaction wheels to control the attitude and perform slews. Three of the wheels were mounted along the body axes, while the fourth (called “skew”) was mounted at 54.7° to each of the body axes. All of the wheels ultimately experienced failures, with the failure of the fourth wheel leading to the end of the mission. Each wheel suffered two failures: an initial failure after which the wheel could be restarted, and a final failure from which recovery was not possible. Table 7.3-1 summarizes the major wheel events, listed by wheel.

Wheel	Axis	Date	Description
1	Yaw (X)	2001:047:13:15	Stopped due to torque checks. Restarted on day 2001:054.
		2001:329:23:24	Final failure
2	Pitch (Y)	2000:217:10:04	Did not respond to torque commands. Restarted on day 2000:258
		2001:344:06:50	Final failure
3	Roll (Z)	2002:351:13:19	Stopped for 2 hours and then autonomously restarted
		2004:362:14:16	Final failure
4	Skew (S)	2007:128:16:27	Wheel stopped. Restarted on day 2007:134, stopped again, restarted on day 2007:144.
		2007:193:20:46	Final failure

Table 7.3-1: FUSE Reaction Wheel events.

7.3.1 Pitch & Yaw Reaction Wheel Failures: ~December 2001

In late 2001, the FUSE project was hit with a near-mission-ending failure of two out of the original four reaction wheel assemblies (RWAs). The yaw wheel failed on Nov. 25, 2001, but normal operations continued with three RWAs. Two weeks later, on Dec. 10, 2001, the pitch RWA also terminated operations. Each wheel had recovered from one previous stiction event. However, the Nov/Dec 2001 events were hard failures and these wheels never worked again. The initial attitude control system required three wheels to maintain three-axis stability for science operations.

After establishing a safe mode for the satellite, the team put its efforts into assessing and implementing a two-wheel control system, using the magnetic torquer bars (MTBs) to replace the missing axis. The gyroless software design was already well underway at this point, but several aspects of the software had to be redesigned to accommodate the interactions of the loss of controllability with the loss of continuous rate information. The safe-modes in particular had to be completely redesigned.

Seven weeks after the loss of the yaw and pitch reaction wheels in November-December 2001, a new ACS control mode was implemented in the flight software to control the satellite in all three axes, using a hybrid of the remaining reaction wheels and the MTBs, acting against the geomagnetic field to control the third axis. A new coordinate system was adopted (SAZ) where the Z-axis is roll, the S-axis is the projection of the skew wheel onto the XY plane, and the A-axis is orthogonal to both the S and Z axis (Figure 3-1). The S and Z axes were controlled by the remaining wheels (skew and roll) but the A-axis was totally controlled with magnetic torque generated by the MTBs.

7.3.2 Roll Reaction Wheel Failure: December 2004

On December 27, 2004, telemetry was received indicating that the Roll RWA had stopped. Recovery attempts were unsuccessful. As with the other wheels, this RWA also had one previous stiction event but had been recovered to service for an additional period before the failure. This left only the skew-mounted RWA operational, and once again the ability to perform science operations was threatened. During the first month after this failure, it was difficult to maintain the satellite in a safe configuration while software responses were designed and implemented.

The loss of the roll wheel necessitated another software overhaul, beginning with the need for a new safe pointing mode for the satellite. The control authority with a single wheel was so limited that the satellite would easily fall into regimes where the attitude could not be controlled and a slew to the orbit pole was not possible. The orbit pole itself was often only marginally stable, and the need to use the MTBs to control two axes often resulted in loading the remaining skew wheel with excess momentum even when the gravity gradient itself was small. A non-inertial safe mode was developed where the satellite would be nadir pointed. This mode was largely gravity-gradient-stabilized: once the satellite had settled into this mode, only small additional control torques were needed to maintain control. Settling into this mode was often difficult, and many refinements of the control gains were made before this process was well-behaved. Management of the solar arrays in this mode was likewise refined several times.

The response to this failure followed the general direction of the two-wheel mode, only now the MTBs needed to control two axes while the remaining (skew) reaction wheel controlled the S-axis. In most circumstances the MTBs could not simultaneously provide pointing control while performing momentum unloading; the one-wheel mode operations workaround demanded the use of proper target sequencing as the principal strategy for managing the wheel momentum – momentum build up at one target could be counterbalanced at a succeeding target by torque in the other direction.

In order to accurately predict the wheel momentum in an MPS and avoid wheel saturations or on-the-fly replanning of the timeline (“momentum interventions”), it became necessary to include dynamic simulation capabilities in the Mission Planning MP tools. The final baselined MP operational tool included the modeling of the on-board controller, the torque distribution algorithm, the unloading algorithm, the slew generation algorithm as well as simulation models for attitude dynamics and kinematics.

After uploading revised ACS software and subsequent modifications based upon on-orbit operations, the observatory was finally declared operational again in November 2005, ~10 months after the roll RWA failed. As a result of project expertise gained during the first two months of difficult operations, significant improvements were seen in observing success and efficiency and many fewer trips into various safe modes were made.

7.3.3 Skew Reaction Wheel Failure: May 2007 & Observatory Decommissioning

The skew RWA had an initial stoppage on May 8, 2007, but did not appear to fail hard. It was restarted temporarily on May 8, within a few days of the stoppage. After making modifications to the safe mode control scheme, the wheel was restarted and over a two week period the excess friction in the wheel decreased to a level similar to that before the anomaly. Operations picked up again on June 12, 2007.

FUSE was operated in a revised single wheel mode for one month before the final wheel failure on July 12, 2007. After one month of wheel restart attempts (including all four wheels), the operational science mission was terminated by NASA on August 17, 2007. After end-of-mission tests, the satellite was decommissioned on Oct. 17, 2007.

7.4 □ Gyroless Attitude Determination

7.4.1 Basic Considerations

In the original conceptual design for FUSE operations, the ACS held the spacecraft inertially-fixed by applying torques to the RWAs so as to keep the angular rates measured by the gyros at zero. The attitude was determined from the TAMs in the absence of FES data. The TAM data are noisy, and provide instantaneous information only for the two axes perpendicular to the B-field direction. Over a period of many minutes, however, the satellite moves far enough along the path of the orbit that the orientation of the B-field shifts enough for the Kalman filter to accumulate knowledge about all three axes. As the filtered attitude estimate was updated, the ACS applied control torques accordingly to maintain the commanded attitude. When performing science observations, the data from the FES is used to provide absolute attitude information with sub-arcsecond accuracy. The target acquisition sequence employed with this system is described in Section 6.5.2.

Almost every aspect of the original attitude determination and target acquisition operations flow was redesigned to work in the absence of gyroscopes. The critical design considerations for the new system were as follows:

- FES data would replace gyro data for rate estimation, when available.
- FES data were not available during slews or during Earth occultations, so the ACS had to maintain at least a coarse attitude without it. In particular, the ACS had to estimate angular rates based on: TAM data, a detailed model of the external torques and satellite dynamics, and integration of the equations of motion.
- Prior to acquisition of guide stars by the FES, attitude drift rates were in the range 10"/sec to 20"/sec (sometimes higher). This is far higher than the typical rate of ≈ 0.025 "/sec achieved with gyroscopes, and required that guide stars be located and tracking initiated within 2-3 seconds of an FES full FOV

exposure, rather than the 30-60 seconds needed for this process by the original system.

- Once guide stars were acquired in the FES, accurate rate estimation was possible and pointing performance would be similar to what was achieved with gyroscopes.
- Because TAM data permitted attitude determination accurate to better than 1° only for directions perpendicular to the B-field, the overall attitude estimate accuracy could be 2° or greater prior to acquisition of FES data.
- Once tracking on guide stars was achieved, the ACS had to be able to control to the IDS-supplied attitude estimate rather than its internal attitude estimate, until commanded otherwise by the IDS. This would permit the use of FES data to hold a fixed attitude and provide accurate rate information while enough TAM data were accumulated to estimate an accurate 3-axis attitude, which occurred within 2–3 minutes. This required a new control mode in the ACS: the original modes would always attempt to remove attitude errors, which in this case would cause the FES to lose track of the guide stars.
- Because the initial attitude uncertainty was as large as 2° , the star table loaded to the IDS had to be increased in size to cover a region roughly 2° in radius, or about 16 times as large as the area that was covered by the original star table.
- The attitude errors after an occultation or after a large slew were limited by the accuracy of the TAMs, and were often on the order of 2° . Removing this error had to be performed in a time short with respect to the typical target visibility of 2000 seconds per orbit. In order to accomplish this, two additional types of slews were developed: “dead-reckoning” slews and guided slews. The dead-reckoning slews were used for slew lengths of about 12 arcmin up to several degrees, and were performed without attitude input from the TAMs. These slews were used for initial attitude correction maneuvers. The guided slews were used for slew lengths below about 12 arcmin; they are much slower ($< 10''$ /sec) than normal slews in order to permit tracking of guide stars by the FES during the slew. The guided slews were used for the final approach to the target.
- Any gyro channels that continued to function would be used for rate measurement.

7.4.2 Flight Software Modifications

The ACS, IDS, and FES flight software all required major modifications, the highlights of which are summarized briefly here.

The FES had two major new functional requirements:

- Identify guide stars autonomously from a full field of view image, and begin centroiding of those stars within 2 to 3 seconds of the full FOV exposure.
- Autonomously reposition the subimages used for centroiding to follow the motion of the guide stars.

The major new functions added to the IDS software to support gyroless operations were:

- Accommodate the new FES auto-tracking mode.
- Perform star-field identification with a catalog that encompassed an area 2° in radius.
- Perform tracking during slews.
- Select guide stars autonomously from the star catalog, and be able to change stars during slews.

The major updates to the ACS software were:

- Modified Kalman filter to estimate rates from TAMs and a non-linear dynamical model of FUSE.
- New “1 Hz” control law – controls directly to ‘unknown’ FPD updates rather than to the ACS attitude estimate.
- Dead-reckon slews – propagate open-loop on the dynamical model.
- Correction slews – exit from 1 Hz controller and slew to remove attitude error.
- Multiple levels of attitude estimate convergence and attitude control computed:
 - ACS status message packet sent to IDS modified to contain state information on both estimate and control: coarse ($> 2^\circ$), medium ($< 2^\circ$), and Fine (< 12 arcmin).
- New command interface from IDS: spare bits in FPD now used to send commands:
 - Set slew rate high or low (large target slews, or slow guided slews);
 - Enable/Disable TAM inputs to Kalman filter;
 - Perform correction slew.

As experience was gained with on-orbit gyroless operations, and with the idiosyncracies of two and one-wheel control, the interface between the IDS and ACS was augmented further. The ACS status message was modified to contain information on the status of the Kalman filter, the estimated angular rates, and the control law in use. The FPD command codes were expanded to include setting 5 different slew rates, setting the slew algorithm, enabling/disabling momentum unloading, resetting the Kalman filter covariances, setting the momentum bias for the wheel(s), and selecting control law gains.

The combined failure of reaction wheels as well as gyros was particularly challenging, as uncertainties in the propagated rates occasionally resulted in rates that were too high for the FES to acquire stars. Overall, however, the system did work and provided acceptable observing efficiency. Once guide stars were acquired, the low measurement noise of the FES resulted in better pointing stability than with gyros, for axes controlled by reaction wheels. For axes controlled by MTBs, the low bandwidth of the controller limited performance.

The IDS flight scripts that controlled target acquisitions were completely redesigned for the gyroless system. The previous linear sequence of acquisition steps was

replaced with a state machine. Autonomous rules operating in the IDS would monitor both the desired acquisition state and the actual state, and would trigger activation of the appropriate script when necessary. This design allowed for steps to be repeated as necessary, and for the system to respond gracefully if tracking was lost at any point. The ability to reacquire guiding autonomously greatly expanded the regions of the sky accessible for observations, as it was no longer necessary to require that a given spacecraft attitude be perfectly stable 100% of the time.

The basic flow of a target acquisition with the gyroless software was as follows:

- 1) Complete large slew or exit occultation.
- 2) Wait for angular rates to settle below ~ 12 arcsec/sec.
- 3) Do a fast FES autotrack. ACS uses “1Hz” control law. ‘fast autotrack’ means bin the FES image 4x4 and use 0.4 sec image exposure time to obtain centroids as quickly as possible. Request only two guide stars, allowing the subarray size to be 20x20 pixels, increasing the likelihood that stars could be acquired while the attitude drift rates were high.
- 4) Wait for ACS to report that the attitude estimate has converged to $< 2^\circ$.
- 5) If pointing error $> 2^\circ$, command ACS to do a correction slew to remove the error; go back to step 2.
- 6) Once error is $< 2^\circ$, repeat FES autotrack to get an image usable for Star_ID: FES image is binned only 2x2 and full FOV exposure time is 1 sec.
- 7) Process image, identify stars in image, compute pointing error (dq).
- 8) If pointing error $> 12'$, do a dead-reckoning unknown-to-known slew, go back to step 2.
- 9) If pointing error $< 12'$, do a guided slew to target Q.
- 10) Change to guide stars selected by Mission Planning.
- 11) If doing a moving target, do rendezvous slew and begin moving target track.
- 12) Proceed with the observation.

If pointing control were lost during an exposure, this acquisition sequence would be triggered automatically. The impact on the science data would be a gap in the midst of a time-tag exposure, and a reduction in the effective exposure time for a histogram exposure. CalFUSE corrections for such instances are discussed in [the FUSE Data Handbook 2009](#).

Papers describing gyroless attitude determination and control with only one or two reaction wheels are listed in Sections 12.3 and 12.4.

8 Satellite to Target Coordinate Transformation

8.1 □ Basic Definitions

The attitude control system (ACS) for FUSE used a quaternion representation for telescope pointing. Although most astronomers are not familiar with quaternions, their advantages for spacecraft control are numerous. Once a target position is parameterized this way, rotational transformations are vastly simplified, particularly because trigonometric functions are not needed. The FUSE archival user does not need to know the details of this system, but will encounter quaternions yielding attitude information from the satellite in the housekeeping file for each exposure ([FUSE Data Handbook, Sec. 5.2](#)). This section explains how they can be used to determine telescope pointing during an exposure.

For each fixed target, an observer provided the J2000 right ascension (α) and declination (δ) of the object and selected a science aperture at which to place it (LWRS, MDRS, HIRS, or RFPT). A particular position angle on the sky for the apertures could be requested as well. For moving targets, Mission Planners would use Percy (reference) to generate a table of FUSE-centered (α , δ) vs. time. See Sections 2.4 and 2.7.2, and Figure 2-10 for a discussion of the FUSE field of view and aperture orientation definitions.

When scheduling an observation, the Mission Planning system calculated the nominal spacecraft roll angle to keep the $-X$ axis of FUSE facing the Sun, with a 2.5° offset to place the radiator of the guiding FES slightly in the shade. For the two-wheel and one-wheel phases of the mission, the roll angle would often be offset further to provide better attitude control with the magnetic torquer bars or to minimize wheel momentum accumulation. For moving targets, the roll angle was determined at the beginning of the exposure and remained fixed along the path.

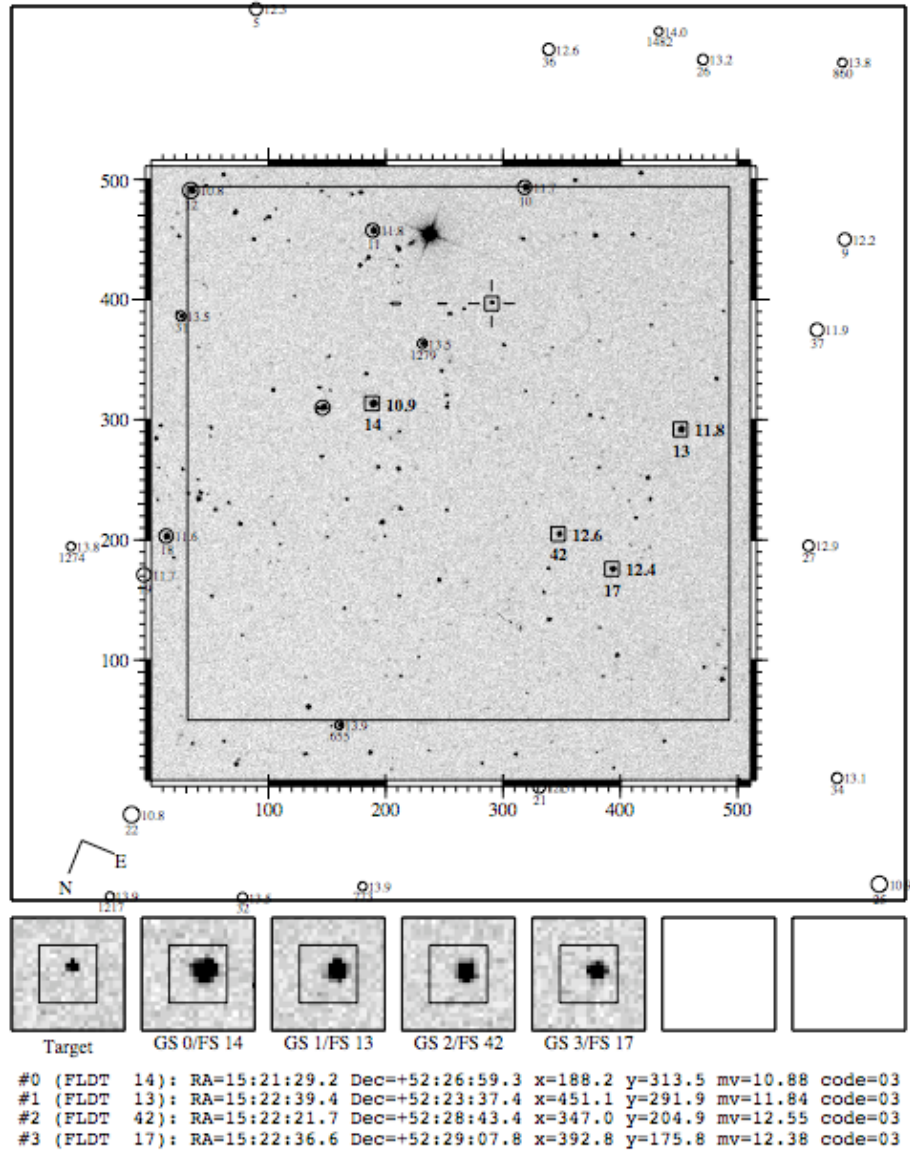
The planned pointing information is available in the primary header of the FITS files as RA_TARG, DEC_TARG and APER_PA, where the aperture position angle (APER_PA) and spacecraft roll angle are related by

$$\text{APER_PA} = 270^\circ - \text{Roll}.$$

A useful way of visualizing the resultant orientation on the sky is to look at the guide star plot in the MAST archive for the observation. A sample plot is shown below in Figure 8-1. For this observation, the roll angle was 157.86 degrees and the position angle was 112.14 degrees. The $+X_{\text{IPCS}}$ axis points down in these plots.

FUSE Guidestar Plot

Target name: PG1520+525 (F020:01:01) RA=15:21:46.9 Dec=+52:22:05.0
 Guidestar plot epoch: 2006:323:15:35:01 Beta=108.1
 Plot generated by calvani at 2006:317:14:40:04 Requested slit: LWRS
 from mps_2006_319_38985.001 Acq case: 15



Target field

Figure 8-1 This typical FUSE guide star plot shows the usable guide stars and aperture positions. The pixel coordinate scale is for FES-A. The orientation of North and East is shown in the lower left corner.

The target coordinates, roll angle, and aperture location were transformed in the SCC into a reference quaternion and aperture offset for uplink to the FUSE IDS. The quaternion product of these values define the location on the sky where the telescope reference point (RFPT, Figure 2-10) is placed so that the target would be centered in the aperture selected for the exposure. In the housekeeping file, this location is defined by the commanded quaternion values (AQECI2BDYCMD_[1,2,3], **FUSE Data Handbook, App. D**). These change with time when the spacecraft was slewing, e.g., positioning the target after an acquisition to the aperture or following a moving object, but otherwise remain constant during the exposure of a fixed target. The commanded quaternion is the position the attitude control system was trying to maintain at any time. In addition to the desired pointing, the housekeeping file contains two estimates of the actual pointing. One is the fine pointing data of measured quaternions calculated by the IDS from the guide stars (I_FPD_Q_ECI2BDY_[1,2,3]). The other is the ACS estimate using not only the guide stars, but also vehicle modeling and data from the gyroscopes, magnetometers, and coarse sun sensors (AATTECI2BDY_[1,2,3]). The ACS quaternions are not as accurate without guide star data, such as when tracking was lost. The commanded and measured quaternions were used by CalFUSE to create the jitter file for each exposure, yielding the difference between commanded and actual positions in the X and Y directions usually for every 1 or 2 seconds of time, depending on the guiding mode.

The following transformations can be used to convert from quaternions to (α , δ , Roll) of the reference point (RFPT). First note, to conserve space, the housekeeping files only contain three of the four components of the quaternions. In the FUSE convention, the fourth component is the pure rotational one and was forced to be positive by the ACS. Thus, since the quaternion is normalized to one, it can be calculated from the other three components:

$$q_4 = \sqrt{(1 - q_1^2 - q_2^2 - q_3^2)}$$

The IDS did not explicitly impose positivity of the fourth component, but because the reference quaternion was generated that way, the full FPD quaternion can be recovered as above for the ACS, except when the fourth component is nearly zero. In that case, if the signs of the other three components are opposite to that of the commanded quaternion, the fourth component needs to be made negative.

The conversion to celestial coordinates of the RFPT is

$$\alpha_{J2000} = \text{atan}(q_2q_3 - q_1q_4, q_1q_3 + q_2q_4)$$

$$\delta_{J2000} = \text{asin}(-q_1^2 - q_2^2 + q_3^2 + q_4^2)$$

$$\text{Roll} = \text{atan}(q_2q_3 + q_1q_4, -q_1q_3 + q_2q_4)$$

where we use a two-argument convention for atan such that $\text{atan}(y,x)$ is the arctangent of y/x .

8.2 □ Conversion of Raw FES Pixel Coordinates to Celestial Coordinates

The conversion of FES pixel coordinates to celestial coordinates is a multi-step process. The previous section described how to compute the location of the Reference Point (RFPT) on the sky and how to determine the orientation of the IPCS axes relative to North and East. This section provides a prescription for converting raw pixel coordinates to IPCS coordinates.

The first step is to remove the optical distortions in the FES cameras and to flip the FES CCD coordinate axes to match the IPCS coordinate axes. These corrections are applied via third-order polynomials:

$$\begin{aligned} x_c &= a_{00} + a_{10}x + a_{01}y + a_{20}x^2 + a_{11}xy + a_{02}y^2 + a_{30}x^3 + a_{21}x^2y + a_{12}xy^2 + a_{03}y^3 + \\ &\quad \text{fpa_shift_scale} * (\text{fpa_xpos} - \text{fpa_xrefpos}) \\ y_c &= b_{00} + b_{10}x + b_{01}y + b_{20}x^2 + b_{11}xy + b_{02}y^2 + b_{30}x^3 + b_{21}x^2y + b_{12}xy^2 + b_{03}y^3. \end{aligned}$$

Note that the formula for x_c includes a term to correct for the FPA position: the projected positions of the stars shift relative to the telescope boresight by an amount that depends on the FPA position. The FPA x position can be obtained from the FPALXPOS keyword in the FITS headers of FUSE data files; use one of the LiF1 files to obtain the LiF1 FPA position for FES-A images, and a LiF2 file to obtain the LiF2 FPA position for FES-B images. The value of `fpa_shift_scale` is -0.0127 pix/micron, and `fpa_xrefpos` is 117 microns for LiF1 and 175 microns for LiF2.

For the sake of completeness, polynomials for converting in the other direction are:

$$\begin{aligned} x &= c_{00} + c_{10}x_c' + c_{01}y_c + c_{20}x_c'^2 + c_{11}x_c'y_c + c_{02}y_c^2 + c_{30}x_c'^3 + c_{21}x_c'^2y_c + c_{12}x_c'y_c^2 + \\ &\quad c_{03}y_c^3 \\ y &= d_{00} + d_{10}x_c' + d_{01}y_c + d_{20}x_c'^2 + d_{11}x_c'y_c + d_{02}y_c^2 + d_{30}x_c'^3 + d_{21}x_c'^2y_c + d_{12}x_c'y_c^2 + \\ &\quad d_{03}y_c^3 \end{aligned}$$

where:

$$x_c' = x_c - \text{fpa_shift_scale} * (\text{fpa_xpos} - \text{fpa_xrefpos}).$$

The polynomial coefficients for FES-A and FES-B are given in Table 8.2-1 and Table 8.2-2, respectively.

The second step is to shift the origin from the corner of the FES to the Reference Point, and to convert from pixels to arcseconds:

$$\begin{aligned} X_{\text{IPCS}} &= (x_c - x_{\text{cRFPT}}) * 2.5505 \text{ arcsec/pixel}, \\ Y_{\text{IPCS}} &= (y_c - y_{\text{cRFPT}}) * 2.5505 \text{ arcsec/pixel}. \end{aligned}$$

The position of the Reference Point in corrected pixel coordinates is given in Table 8.2-3. Differences in the mean pixel scale between FES-A and FES-B are absorbed into the distortion coefficients. Note that the RFPT positions in Table 2.7-3 are given in raw FES coordinates, not corrected coordinates.

X Correction coefficients	Y Correction coefficients	X Distortion coefficients	Y Distortion coefficients
$a_{00} = 5.045641e+02$	$b_{00} = 5.048150e+02$	$c_{00} = 5.110495e+02$	$d_{00} = 5.112370e+02$
$a_{10} = 7.284088e-03$	$b_{10} = -9.744564e-01$	$c_{10} = 1.065623e-03$	$d_{10} = -9.973576e-01$
$a_{01} = -9.596945e-01$	$b_{01} = 1.688152e-02$	$c_{01} = -1.007200e+00$	$d_{01} = -5.505270e-03$
$a_{20} = -9.771181e-06$	$b_{20} = -2.338553e-05$	$c_{20} = 1.816278e-05$	$d_{20} = 5.992910e-07$
$a_{11} = -2.035237e-05$	$b_{11} = -6.424274e-05$	$c_{11} = -3.936880e-06$	$d_{11} = 2.357754e-05$
$a_{02} = -8.442830e-05$	$b_{02} = -1.812183e-05$	$c_{02} = 2.239781e-05$	$d_{02} = 5.003854e-06$
$a_{30} = -3.878807e-09$	$b_{30} = 2.880021e-08$	$c_{30} = -4.315068e-09$	$d_{30} = -5.786698e-08$
$a_{21} = 4.020260e-08$	$b_{21} = 2.085710e-09$	$c_{21} = -6.028321e-08$	$d_{21} = -2.144882e-09$
$a_{12} = 2.167710e-09$	$b_{12} = 5.577110e-08$	$c_{12} = -2.114705e-09$	$d_{12} = -4.187747e-08$
$a_{03} = 5.331478e-08$	$b_{03} = 4.392894e-09$	$c_{03} = -2.969829e-08$	$d_{03} = 3.984476e-09$

Table 8.2-1 Optical distortion coefficients for FES-A.

X Correction coefficients	Y Correction coefficients	X Distortion coefficients	Y Distortion coefficients
$a_{00} = 5.043866e+02$	$b_{00} = -3.322859e+00$	$c_{00} = -2.828305e+00$	$d_{00} = 5.090221e+02$
$a_{10} = 1.486478e-02$	$b_{10} = 1.019272e+00$	$c_{10} = 1.105978e-02$	$d_{10} = -9.911953e-01$
$a_{01} = -9.732869e-01$	$b_{01} = 2.834617e-02$	$c_{01} = 1.013356e+00$	$d_{01} = 2.141076e-02$
$a_{20} = -6.119336e-05$	$b_{20} = -4.949496e-05$	$c_{20} = -2.834457e-05$	$d_{20} = -3.637001e-05$
$a_{11} = 1.617153e-05$	$b_{11} = -5.698157e-05$	$c_{11} = -7.355215e-05$	$d_{11} = -7.469583e-06$
$a_{02} = -3.435449e-05$	$b_{02} = -4.949496e-05$	$c_{02} = -3.756898e-05$	$d_{02} = -7.815734e-05$
$a_{30} = 8.220668e-08$	$b_{30} = -2.633433e-08$	$c_{30} = 6.115820e-08$	$d_{30} = 2.006463e-09$
$a_{21} = -2.730496e-08$	$b_{21} = 1.694823e-07$	$c_{21} = 1.589610e-08$	$d_{21} = -8.888482e-09$
$a_{12} = -9.476450e-09$	$b_{12} = -1.291730e-08$	$c_{12} = 1.742133e-07$	$d_{12} = 2.916069e-08$
$a_{03} = 3.136447e-10$	$b_{03} = 5.579320e-08$	$c_{03} = 2.686495e-08$	$d_{03} = 8.575316e-08$

Table 8.2-2 Optical distortion coefficients for FES-B.

FES-A		FES-B	
X_{cRFPT}	Y_{cRFPT}	X_{cRFPT}	Y_{cRFPT}
136.02	266.36	107.73	257.20

Table 8.2-3 Reference Point positions in corrected pixel coordinates.

9 Airglow Appendix

Geocoronal emission, or airglow, was always present. Excitation mechanisms include resonant scattering of Solar emission lines, fluorescence, and electron impact. For species other than hydrogen, the gas is all local to the upper atmosphere. The scale heights vary with the Solar cycle, and the strengths of the emission lines vary accordingly. FUSE launched close to the maximum of the Solar cycle, and ended the mission during the minimum, so the airglow lines were stronger early in the mission than at the end. The distribution of hydrogen extends farther than the other species, and there is a non-negligible density of HI throughout inter-planetary space. The extended distribution of HI means that the telescope line of sight always encounters sunlit HI, and thus resonantly-scattered Ly β is present even during orbital night.

9.1 Upward-Looking Airglow

During normal science exposures, the line of sight was pointed away from the Earth, through the upper atmosphere. Emission was seen primarily from neutral atomic hydrogen, helium, nitrogen, and oxygen. During orbital night, emission was usually seen only from HI. Ordinarily, only Ly β was present, but other HI Lyman lines may be present when viewing at low Earth-limb angles. Emission from HeI 584 Å was also occasionally seen (in second order at 1168 Å) during orbital night. Emission lines present during orbital day are listed in Table 9.2-1. Emission from O I and H I shortward of 918 Å is also present, but is faint and the lines are often blended. See Morton (2003) for wavelengths of these features. The strongest lines of H I and O I are Ly β and 988.773 Å, respectively; line strengths decrease with wavelength shortward of these two lines. Emission to the low-lying excited states of the O I ground state also decreases with wavelength, and may not be seen for the multiplets shortward of 936.630 Å.

9.2 Downward-Looking Airglow

The emission spectrum seen when looking downwards towards the Earth is much richer than that seen looking up. Some spectra were obtained while pointed downwards, but the main impact of this emission for the FUSE project was excessive exposure of the detector at spots illuminated by this emission. These effects are described in Section 4.4.2.1, and changes to operations procedures to limit these effects are described in Section 6.3.2.2. The brightest lines are listed in Table 9.2-2; for additional information on downward-looking airglow, see Feldman et al. (2001).

Species	Wavelength (Å)
He I	584.334 (1168.668 in 2 nd order)
N I	1134.163, 1134.415, 1134.980
N II	1083.997, 1084.584, 1085.710
He I	537.030 (1074.06 in 2 nd order)
O I	1039.230, 1040.942, 1041.688
O I	1025.762, 1027.431, 1028.157
H I	1025.722
O I	988.773, 990.204, 990.801
O I	976.448, 977.959, 978.617
H I	972.537
O I	971.737, 973.234, 973.885
H I	949.743
O I	948.686, 950.112, 950.733
H I	937.803
O I	936.630, 938.020, 938.625
H I	930.748
O I	929.517, 930.886, 930.482
H I	926.226
O I	924.950, 926.306, 926.896
H I	923.150
O I	921.857, 923.204, 923.790
H I	920.963
O I	919.658, 920.998, 921.581
H I	919.351
H I	918.129
O I	918.044, 919.380, 919.961

Table 9.2-1 Airglow emission lines seen during orbital day when looking up.

Species	Wavelength (Å)
O I	1172.504, 1172.612, 1172.779
O I	1152.151
N I	1134.163, 1134.415, 1134.980
N II	1083.997, 1084.584, 1085.710
O I	1039.230, 1040.942, 1041.688
O I	1025.762, 1027.431, 1028.157
H I	1025.722
O I	988.773, 990.204, 990.801

Table 9.2-2 Strongest airglow emission lines seen looking down during orbital day.

10 FUSE Development and Operations Teams

The success of the FUSE mission was rooted in the expertise of the development and operations teams. The University of California Berkeley provided the MCP detectors. The spectrographs were built and integrated by the University of Colorado Boulder. The French Space Agency (Centre National d'Etudes Spatiale, or CNES) provided the diffraction gratings for the spectrograph and assistance for science operations throughout the mission. The Canadian Space Agency provided the two FES guide cameras for FUSE and science operations personnel. The telescope mirrors and grating blanks were manufactured by Tinsley Associates. Swales Aerospace was responsible for the instrument thermal design, the instrument structure, the baffles, and the baffle doors. The JHU Applied Physics Laboratory provided the mirror mounts and actuators, the Instrument Data System, the instrument power distribution unit, mission systems engineering, and managed the spacecraft procurement. The spacecraft bus was provided by Orbital Sciences Corp., and the Mission Operations Team were from Honeywell Technical Services Inc. The Space Telescope Science Institute provided portions of the FUSE mission planning and data pipeline software, and hosts the FUSE science data archive at MAST. Overall management of the mission development, mission planning, science data processing, and operations of the FUSE satellite were conducted at Johns Hopkins University. Project oversight and technical support was provided by Goddard Space Flight Center.

10.1 Team List

The following table lists the people who participated in the development and operation of the FUSE mission, beginning with Phase C/D in 1995. Many of the people on this list served in many capacities, and the space available for a description of their roles does not do them justice. We have attempted to make this list complete, but we know that there must be some whom we have overlooked, and many more who labored behind the scenes. We apologize for any omissions, and we thank everyone for their help in making FUSE a success.

Last Name	First Name	Institution	Role
Abate	Matt	OSC	Attitude Control S/W Testing
Abney	Faith	STSci	MAST Operations
Ajluni	Tom	SAI	ELV & Launch Site Interfaces
Ake	Tom	CSC	Operations Scientist
Alexander	Russ	CSA	CSA FUSE FES Project Manager
Allison	Gregg	CU	Spectrograph I&T S/W Support
Andersen	Harry	HTSI	Mission Operations Team
Anderson	Julia	HTSI	MOT Mission Planning Engineer
Anderson	Nancy	SAI	Procurement & Scheduling
Anderson	Sara	STSci	MAST Operations

Andersson	B-G	JHU	Guest Investigator Support Lead
Andre	Martial	IAP	Science Data Calibration
Andrews	John	CU	FUVS Project Manager
Androh	Aaron	JHU	Administrative & Logistics Support
Artis	David	JHU/APL	Instrument S/W Systems Engineer
Austin	Adam	HTSI	Mission Operations Team
Bachtell	Neal	JHU/APL	Mechanical Technician
Bailey	Leon	NSI	Contamination Technician
Bair	Tom	JHU	Mission Operations Team
Ballard	Ben	JHU/APL	IDS Software
Barkhouser	Robert	JHU	Mirror Subsystem Optical Engineer
Barrett	Paul	STScI	Science Data Calibration Software
Bell	Andrew	ComDev	FES Systems Engineer
Berman	Alice	JHU	Mission Planning Lead
Bertini	Alice	CU	FUSE Spectrograph I&T S/W
Bianchi	Luciana	STScI	E/PO Coordinator
Billings	Ron	JHU	Project Schedules
Blackman	Daniel	UCB	Detector Software
Blair	Bill	JHU	Observatory Operations Lead
Blevins	Bill	HTSI	Ground Station Support
Bogart	Dave	HEI	Safety
Boisvert	Chantal	JHU	Budget Analyst, Admin. Support
Bouloubasis	Matt	HTSI	Mission Operations Team
Bowers	Mike	ICS	SCC Development Team
Boyer	Robert	CSC	Science Operations Support
Bremmer	Hal	JHU	Deputy Project Manager for Resources
Brown	Marty	OSC	Satellite I&T Support
Brownsberger	Ken	CU	Spectrograph, Satellite I&T Support
Buchheit	Jim	SAI	Contamination Cover Design
Burchett	Diane	ComDev	FES Contamination Control Engineer
Burns	Rich	GSFC	Deputy Project Manager
Busse	Jon		Standing Review Committee
Calk	Howard	ICS	SCC Development Team
Calvani	Humberto	JHU	Mission Planner
Caplinger	Jim	CSC	IT support, Mission Planning
Cappelaere	Pat	ICS	SCC/GS/IDS Software Development
Cash	Webster	CU	Science Team
Cha	Alexandra	JHU	Science Data Calibration
Chayer	Pierre	CSA	FES & Science Operations
Christian	Damian	JHU	Science Operations Support
Civeit	Thomas	IAP/JHU	Mission Planning Software
Claffy	Rick	GSFC	Explorers Flight Assurance Manager
Class	Brian	OSC	Spacecraft ACS Lead Engineer
Coffelt	Ross	OSC	ACS S/W testing
Colley	Roger	CSA	FES Program Manager

Conard	Steve	JHU	Integration and Test Lead
Connelly	Doug	OSC	Satellite I&T Quality Assurance
Coopersmith	Jon	SAI	Contamination Control
Cowie	Lennox	U. Hawaii	Science Team
Crew	Keith	HTSI	Mission Operations Team
Cross	Aaron	OSC	ACS S/W testing
Crouse	Pat	GSFC	SSMO Project Manager
Dakermanji	George	JHU/APL	Power Systems
Davidson	Arthur	JHU	Science Team
Davis	Jim	ICS	C&T Database Support
Davis	Mark	HEI	Safety
Dequae	Philip	ComDev	FES Software
Diaz	Javier	UPRM	Ground Station Operations
Dickson	Charles	ICS	SCC Development Team
Dion	Shirley	HEI	Safety
Dixon	Van	JHU	Science Data Calibration S/W Lead
Dolbow	Annette	OSC	Satellite I&T
Donakowski	William	UCB	Detector Mechanical Engineer
Dorsey	George	OSC	ACS H/W, Satellite I&T
Dupree	Andrea	SAO	Science Team
Dupuis	Jean	JHU	Science Data Calibration
England	Martin	CSC	Mission Planning
Englar	Tom	JHU/APL	IDS Guidance Software
Ehrenreich	David	IAP	Science Data Calibration
Errigo	Therese	SAI	Lead Contamination Engineer
Evans	Jordan	SAI	Lead I&T Mechanical Engineer
Ewing	Randy	JHU	Deputy Project Manager - Resources
Farzinpay	Farzin	OSC	Attitude Control S/W testing
Feldman	Paul	JHU	Science Team
Fernandez-Sein	Rafael	UPRM	Ground Station Ops Director
Fisher	Landis	JHU/APL	IDS Guidance Software
Forness	Paul	HTSI	Mission Operations Team
Fragomeni	Tony	SAI	Standing Review Committee
Frank	Larry	JHU/APL	Mission Systems Engineer
Friedman	Scott	JHU	JHU Project Scientist
Fullerton	Alex	JHU	Science Data Calibration
Gaines	Geoff	UCB	FUV Detector I&T Support
Gardner	Lisa	STScI	FUSE OPUS/DADS S/W
Gardner	Michael	HTSI	Mission Operations Team
Garner	Calvin	HTSI	Mission Operations Team
Gawne	Bill	HTSI	Mission Operations Team
Glubke	Scott	GSFC	GSFC S/C Engineering Lead
Godard	Bernard	IAP	Science Data Calibration Software
Graham	Rob	OSC	ACS Software
Green	James	CU	Spectrograph PI

Green	Richard	KPNO	Science Team
Gregory	Brian	ICS	I&T SCL script developer
Gresser	Ruth	ICS	I&T SCL script developer
Gummin	Mark	MAG Sys.	Detector Scientist
Hammond	Norma	ComDev	FES Project Manager
Hammond	Randy	JHU	Satellite I&T Optical GSE
Hardy	Tim	DAO	FES I&T Support
Harmon	Rick	GSFC	ACS S/W Consulting
Harrison	Keith	HTSI	Ground Station Engineer
Hart	Helen	JHU	Science Operations Support
Hawkins	Rob	STScI	Mission Planning Software
Heatwole	Scott	GSFC/WFF	1-wheel Obs Planning Software
Hebenton	Darren	HTSI	Mission Operations Team
Hebrard	Guillaume	IAP	Science Operations
Heefner	Kris	HTSI	Mission Operations Team
Heffernan	Kevin	JHU/APL	Standing Review Committee
Heggestad	Brian	JHU/APL	IDS Software Lead Engineer
Heller	Chris	STScI	FUSE OPUS/DADS S/W
Hill	Mark	JHU/APL	IDS Software Engineer
Hitzman	Bill	HTSI	Ground Station Support
Holmes	Chuck	JHU	Ground System Lead
Horner	Tim	SAI	I&T Mechanical Engineer
Hsu	Jin-Chung	STScI	Science Data Calibration S/W Support
Hueber	John	OSC	S/C Flight S/W
Hurley	Chris	ICS	SCC Software
Hutchings	John	DAO	Canadian Project Scientist
Hynes	Shane	SAI	Standing Review Committee
Ing	Frank	ComDev	FES Software
Irvine	Ron	U. Toronto	FES Software
Jeffries	Alan	ICS	SCC Software Development
Jelinsky	Patrick	UCB	Detector Project Scientist
Jenkins	Edward	Princeton U.	Science Team
Jennings	Tom	HTSI	Mission Operations Team
Jeyasunder	David	OSC	Spacecraft Electrical Systems Engineer
Johnson	Joel	CU	Alignment & Integration Support
Johnson	Timothy	HTSI	Mission Operations Team
Johnson	Carl A.	STScI	Planning S/W coordination
Joyce	JB	JHU	Program Manager (Phase E)
Kain	Shari	JHU	Budget Analyst
Kaiser	Mary Beth	JHU	Science Operations
Kenny	Debbie	STScI	MAST Operations
Kennedy	Herb	STScI	MAST Operations
Kennedy	Michael	JHU/APL	Mirror System Engineer
King	Thomas	KSC	Launch Site Support Engineer
Kochte	Mark	CSC	Mission Planning

Kong	Augustine	ComDev	FES Thermal Engineer
Kriss	Jerry	JHU	Science Data Calibration Software
Krueger	Tim	HTSI	Test Conductor
Kruk	Jeffrey	JHU	Observatory Scientist
Kushner	Gary	CU	Alignment, I&T Support
La	Jim	GSFC	Project Mission Engineer
Lanzi	Jim	GSFC/WFF	1-wheel Obs Planning Software
LaCour	Sylvestre	IAP	Science Data S/W, Calibration
Laronde	Terry	ComDev	IDS Project Manager
Lavender	Eric	ComDev	FES Project Manager
Lecavelier	Alain	IAP	Science Operations
Lees	Jeffrey	CU	BOS, FPA Mechanical Design
Lemoine	Martin	IAP	Science Data Analysis Software
Lennard	Mike	CU	FPA Electrical Design
Leoutsakos	Ted	HTSI	Mission Operations Team
Lepak	Mark	HTSI	Mission Operations Team
Lepore	Al	SAI	Harness Support
Levay	Karen	STSci	Science Data Archive
Li	Hsin	OSC	S/C Systems Engineering
Lindler	Don	SSC	Science Data Analysis Software
Linsky	Jeffrey	CU	Science Team
Lloyd	Carmela	CU	QA Engineer/Inspector
Lloyd	Les	OSC	Harness Support
Loregio	Paul	ComDev	FES Alignment Support
Lowles	Rob	ComDev	FES Systems Engineer
Mahmot	Ron	GSFC	SSMO Project Manager
Makowski	Joseph	OSC	S/C ACS Project Manager
Malina	Roger	UCB	Science Team
Mangus	Dave	GSFC	ACS S/W Consultant
Mark	Daniel	SAI	Instrument Manager, I&T Manager
Marshall	Madeleine	ICS	Standing Review Committee
Martinez	Mel	JHU	SCC – Mission Planning S/W interface
Massa	Derck	Hughes/STX	Science Data Calibration
Mattheiss	Augie	JHU/APL	IDS Engineer
McCarthy	Dennis	JHU	Program Manager (Phase C/D)
McGlochin	Sherry	CU	CU FUSE Deputy Project Manager
McGuffey	Doug	SAI	Swales FUSE Project Manager
Meadows	Gary	SAI	Electrical Integration Engineer
Mehalick	Kim	SAI	Stray Light Analysis
Mengers	David	GSFC	FUSE Mission Manager
Miller	Mike	OSC	Satellite I&T Deputy Project Manager
Miller	Warren	STSci	FUSE OPUS/DADS S/W
Miller	William	OSC	ACS S/W Testing
Miner	Mike	ICS	SCC Software Development
Mirantes	Annette	OSC	S/C Flight Software

Mitchell	Bill	OSC	S/C Flight Software
Mitchell	Karen	HTSI	Mission Operations Team
Moore	Robert	JHU/APL	IDS Lead Engineer
Moos	Warren	JHU	Principal Investigator
Morbey	Chris	DAO	FES Optical Designer
Morrison	Daniel	JHU/APL	Standing Review Committee
Moyer	Earl	SAI	Instrument Electrical Systems
Mueller	Ted	JHU/APL	APL S/C Manager
Murino	Marce	CU	Spectrograph Contamination Control
Murowinski	Rick	DAO	FES CCD Detector Support
Murphy	Edward	JHU	Science Data Calibration S/W Lead
Murphy	Gerry	CU	BOS Design & Testing
Murphy	Patricia	JHU/APL	IDS Software
Murthy	Jayant	JHU	Science Data S/W, Calibration
Nelson	Ken	OSC	Spacecraft Mechanical Engineer
Newman	Miles	SAI	Instrument Thermal Engineer
Noah	Karl	OSC	S/C Electrical Systems
Oegerle	William	JHU	Observatory Operations Lead
Offut	Jay	ICS	IDS, SCC Software
Ohl	Raymond	JHU	Mirror characterization
Oliveira	Cristina	JHU	Mirror characterization
Ooghe-Tabanou	Benjamin	IAP	Science Data Calibration
Ormond	Susanna	JHU	Contract Compliance Officer
Orndorff	Joe	JHU	Electrical I&T Engineer
Osterman	Steve	CU	BOS, FUVS I&T Support
Packard	Ed	GSFC	General support
Paradis	Tom	Boeing	Launch Site Support
Pedraja	Jose	JHU	Electrical Systems Engineer
Perry	Mark	SAI	Instrument Manager
Peterson	Don	CSA	Fine Error Sensor Project Manager
Pitts	Patricia	JHU	Science Operations Support
Pontius	Jim	SAI	Instrument Structure Design
Posner	Allan	ICS	SCC Development Team
Powell	Albert	HEI	Safety
Prouty	Kenneth	ComDev	FES Software
Pulliam	Don	OSC	Spacecraft Project Manager
Ramadas	Krishnan	HTSI	Mission Operations Team
Randell	Jerrold	ComDev	FES Electronics Engineer
Ravotta	Marino	Kelly Temps	Logistics Support
Redman	Kevin	GSFC	I&T Optical Alignment
Rerko	Bob	OSC	Satellite I&T Support
Richardson	Cathy	SAI	Instrument Structure & Baffle Engineer
Ridgaway	Michael	HTSI	Mission Operations Team
Roberts	Bryce	JHU	Mission Planner, Planning S/W
Roberts	Vicki	NSI	Alignment Technician

Robinson	Richard	CSC	Science Data Calibration
Romelfanger	Mary	JHU	Software System Specialist
Rosado	Ricardo	UPRM	Ground Station Operations Support
Rose	Jim	STScI	FUSE OPUS Development
Roth	Kathy	JHU	Science Data Calibration
Roufberg	Lew	OSC	S/C Systems Engineering
Rovner	Dan	OSC	ACS Flight Software
Rowe	John	CSC	Science Operations Support
Rucci	Tom	KSC	Launch Site Support Manager
Ruth	Michael	OSC	ACS Flight Software
Sahnaw	David	JHU	Detector Scientist, Science Data Calib.
Sankrit	Ravi	JHU	Guest Investigator Support
Savage	Blair	U. Wisc	Science Team
Scherzinger	Bruce	JHU/APL	IDS Software
Sembach	Ken	JHU	Science Ops - Science Team Liaison
Seylar	George	JHU/APL	EMI/EMC Support
Sherbert	Lisa	STScI	FUSE OPUS/DADS S/W
Shiblee	George	Microtemps	I&T Electronics Support
Shipley	Ann	CU	Grating Mount Ass'y Mech. Engineer
Shippey	Ed	GSFC	General support
Shull	Michael	CU	Science Team
Siegmund	Oswald	UCB	Science Team, Detector PI
Silva	Chris	HTSI	Mission Operations Team Manager
Simmons	Jeff	HTSI	Mission Operations Team
Slowinski	Steve	STScI	FUSE OPUS/DADS S/W
Smee	Steve	JHU	Satellite I&T Optical GSE
Smith	Caine	HTSI	Mission Operations Team
Smith	Chuck	OSC	Spacecraft I&T Manager
Smith	Jann	ICS	SCC Software Support
Smith	Myron	STScI	MAST Interface Development
Snow	Theodore	CU	Science Team
Sodano	Bob	GSFC	Mission Director
Sonneborn	George	GSFC	GSFC Project Scientist
Sonnentrucker	Paule	JHU	Science Data Calibration
Sontag	Chris	STScI	FUSE OPUS/DADS S/W
Spangler	Tom	JHU	I&T Support
Stakem	Pat	ICS	SCC Software Support
Stock	Joe	UCB	Detector Development Support
Stott	Dave	JHU/APL	Instrument Electrical GSE Design
Suchkov	Anatoly	JHU	Mission Planning
Swade	Daryl	STScI	FUSE OPUS/DADS S/W
Swam	Mike	STScI	FUSE OPUS/DADS S/W
Thaler	Romani	JHU	Configuration Control
Thienel	Julie	GSFC	ACS S/W Consulting
Thompson	Randy	STScI	MAST Interface Development

Thorpe	Bill	ComDev	FES Project Manager
Tiebert	Sharon	JHU	Administrative Support
Tiernan	Liam	ComDev	FES Lead Mechanical Engineer
Tompkins	Steve	GSFC	System Engineer
Vaclavik	Steve	HTSI	Mission Ops Team, Systems Engineer
Van Gaasbeck	Jim	ICS	IDS Flight Software
Van Steenberg	Michael	GSFC	GSFC Deputy Project Scientist
Vernot	Robert	SAI	Instrument Electrical Sys. Engineer
Vidal-Madjar	Alfred	IAP	Science Team
Wasson	Dave	OSC	Spacecraft Thermal Engineer
Weaver	Hal	JHU	Science Operations Support
Webb	John	SAI	Standing Review Committee
Weber	Laura	KSC	General support
Weinberger	Pete	SAI	Baffle Design
Welch	Ray	Welch & Co.	Standing Review Committee
Welsh	Barry	UCB	Detector Project Manager
Westfall	Jim	CU	FPA Electronics Design
White	Michael	JHU/APL	IDS Software
Wilkinson	Erik	CU	Spectrograph Scientist
Witmer	Kurt	OSC	Satellite I&T Support
Woodard	David	ICS	SCC Software Development
Woodgate	Bruce	GSFC	Science Team
Yienger	Judy	SAI	Instrument Mechanical Engineer
York	Donald	U. Chicago	Science Team
Zhang	Jingyun	ComDev	FES Optical Design Engineer
Zsoldos	Jennifer	OSC	ACS S/W, Satellite I&T

Table 10.1-1 FUSE development and operations personnel.

11 Acronym List

ACS	Attitude Control System
ADU	Analog to Digital converter Unit (=1LSB)
AIC	Active Image Counter
APL	Applied Physics Laboratory
ASC	Autonomous Shutdown Counter
ASIC	Application-Specific Integrated Circuit
AUX	Auxiliary power supply (Detector)
AUXI	AUX power supply current
BOS	Bright Object Sensor
bps	Bits Per Second
CalFUSE	FUSE data reduction and calibration pipeline
CCSDS	Consultative Committee on Space Data Systems
CCD	Charge Coupled Device
C&DH	Command and Data Handling
CDC	Charge to Digital Converter
CEU	Central Electronics Unit
CNES	Centre National d'Etudes Spatiale
COTS	Commercial Off the Shelf
CPU	Central Processing Unit
CRC	Cyclic Redundant Checksum
CSA	Canadian Space Agency
CSS	Coarse Sun Sensor
CTE	Coefficient of Thermal Expansion
CU	University of Colorado at Boulder
CVZ	Continuous Viewing Zone
DADS	Data Archive and Distribution System
DAO	Dominion Astrophysical Observatory
DDL	Double Delay Line
DEC	Digitized Event Counter
DLT	Digital Linear Tape
DPU	Detector Processing Unit
DQ	Delta Quaternion
EEPROM	Electronically Erasable Programmable Read-Only Memory
EPV	Extended Precision Vector
FARF	Flight Alignment Reference Frame
FEC	Fast Event Counter
FES	Fine Error Sensor

FIFO	First In First Out
FITS	Flexible Image Transport System
FOV	Field of View
FPA	Focal Plane Assembly
FPAE	FPA Electronics
FPD	Fine Pointing Data (packet)
FUV	Far Ultraviolet
FUSE	Far Ultraviolet Spectroscopic Explorer
FUVS	Far UltraViolet Spectrograph
GMA	Grating Mount Assemblies
GSFC	Goddard Space Flight Center
HIRS	High Resolution Aperture
H/K	Housekeeping (telemetry)
HOP	High Output Paraffin
HTSI	Honeywell Technology Solutions Incorporated (formerly Allied Signal)
HV	High Voltage
HVIA	High Voltage current in detector segment A
HVIB	High Voltage current in detector segment B
H/W	Hardware
IAP	Institut d'Astrophysique de Paris
ICS	Interface and Control Systems, Inc.
IDS	Instrument Data System
IOC	In-Orbit Checkout
IPCS	Instrument Prime Coordinate System
IPSDU	Instrument Power Switching and Distribution Unit
IRU	Inertial Reference Unit
IT	Information Technology
I&T	Integration and Test
JHU	the Johns Hopkins University
kbps	kilobits per second
KSC	Kennedy Space Center
LC	Lower Core
L&IOC	Launch and In-Orbit Checkout
LiF	Lithium Flouride
LWRS	Low Resolution Aperture
MAE	Mirror Assembly Electronics
MAST	Multi-mission Archive at Space Telescope
Mbps	Megabits Per Second
MCP	Micro Channel Plate

MDRS	Medium Resolution Aperture
MOT	Mission Operations Team
MPA	Mirror Positioning Assembly
MPS	Mission Planning Schedule
MTB	Magnetic Torquer Bar
MTBE	Magnetic Torquer Bar Electronics
NASA	National Aeronautics and Space Administration
NEA	Noise Equivalent Angle
OPUS	Operational Pipeline Unified System
OSC	Orbital Sciences Corporation
OSI	Observation Specific Inertial
PHA	Pulse Height Amplitude
PI	Principal Investigator
PROM	Programmable Read-Only Memory
PSF	Point Spread Function
RAM	Random Access Memory
RFPT	Reference Point – position of OSI on FPA
ROM	Read Only Memory
RWA	Reaction Wheel Assembly
SAA	South Atlantic Anomaly
SAD	Solar Array Drive
SADE	Solar Array Drive Electronics
SAI	Swales Aerospace Inc.
SAMA	Small Angle Maneuver Activity
SCC	Satellite Control Center
SEU	Single Event Upset
S/C	Spacecraft
SIA	Spectral Image Allocation (tables)
SiC	Silicon Carbide
SSC	Sigma Space Corp.
SSMO	Space Science Mission Operations
STScI	Space Telescope Science Institute
S/W	Software
TAM	Three Axis Magnetometer
TDC	Time to Digital Converter
TEC	Thermo-Electric Cooler
TTAG	Time-Tagged - science data storage mode
UC	Upper Core or University of California

UCB University of California at Berkeley
UPRM University of Puerto Rico Mayaguez
UTC Universal Time Coordinated

WFF Wallops Flight Facility

12 References and Further Reading

This section provides a bibliography of papers describing various aspects of the FUSE instrument and in-orbit performance. The papers are sorted into rough categories, and are listed in inverse-chronological order within each category.

12.1 Pre-launch Instrument Design and Testing

12.1.1 Optics

“Performance of the Far Ultraviolet Spectroscopic Explorer Mirror Assemblies,” R.G. Ohl, R.H. Barkhouser, S.J. Conard, S.D. Friedman, J. Hampton, H.W. Moos, P. Nikulla, C.M. Oliveira, T.T. Saha, 2000a, Proc. SPIE 4139 137

“Imaging performance of telescope mirrors for far-ultraviolet astronomy,” R.G. Ohl, T.T. Saha, S.D. Friedman, R.H. Barkhouser, H.W. Moos, 2000b, Appl. Opt. 39 4513.

“Optical alignment of the Far Ultraviolet Spectroscopic Explorer,” S. J. Conard, K. W. Redman, R. H. Barkhouser, & J. A. Johnson, 1999, Proc. SPIE 3765 495.

“Aging studies of LiF coated optics for use in the far ultraviolet,” C. Oliveira, K. Retherford, S. J. Conard, R.H. Barkhouser, & S. D. Friedman, 1999, Proc. SPIE 3765 52

"Interferometric alignment and figure testing of large (0.5 m) off-axis parabolic mirrors in a challenging cleanroom environment," R. H. Barkhouser and R. G. Ohl, 1999, Proc SPIE, vol. 3782, page

"Assembly and Test-induced Distortions of the FUSE Mirrors - Lessons Learned," R. G. Ohl et al., 1998, Proc SPIE, vol. 3356, page 854.

"Integration, Alignment, and Initial Performance Results of the Far Ultraviolet Spectroscopic Explorer (FUSE) Spectrograph," E. Wilkinson et al., 1998 Proc SPIE, vol. 3356, page 18.

"Unique Method of Micropositioning as Implemented in the FUSE Focal Plane Assemblies," J. Lees, G. Allison, J. P. Andrews, J. C. Green, J. Westfall, 1997 Proc. SPIE, vol. 3132, pp. 135-145.

"Final Flight Grating Mount Design for the Far Ultraviolet Spectroscopic Explorer," A. Shipley, J. C. Green, J. P. Andrews, E. Wilkinson, and S.N. Osterman, 1997 Proc. SPIE, vol. 3132, pp. 98-109.

“Holographic gratings for the Far Ultraviolet Spectroscopic Explorer: development, imaging, and efficiency tests of two prototypes,” S. Chambord, R. Grange, J.

Flamand, M. Saisse, J-L Reynaud, 1996 Appl.Opt. 35 3653.

“Design of the Far Ultraviolet Spectroscopic Explorer Mirror Assemblies,” M. J. Kennedy, S. D. Friedman, R. H. Barkhouser, J. Hampton, & P. Nikulla, in Space Telescopes and Instruments IV, P. Y. Bely and J. B. Breckinridge, eds., Proc. SPIE 2807, 172–183 1996.

"Optical Performance Budget for the Far Ultraviolet Spectroscopic Explorer," D. J. Sahnou et al., 1996, Proc. SPIE, vol. 2863, page 27.

"Design and Predicted Performance of the Far Ultraviolet Spectroscopic Explorer (FUSE)," D. J. Sahnou et al., 1996, Proc. SPIE, vol. 2807, page 2.

“Tolerance analysis of the Far Ultraviolet Spectroscopic Explorer (FUSE): a statistical approach,” E. Wilkinson, J.C. Green, D.J. Sahnou, 1994 Proc. SPIE 2283 261

“Design of the Far Ultraviolet Spectroscopic Explorer Spectrograph,” J.C. Green, E. Wilkinson, S.D. Friedman, 1994 Proc. SPIE 2283 12

R. Grange, "Aberration-reduced Holographic Spherical Gratings for Rowland Circle Spectrographs," Appl. Opt., vol. 31, pp. 3744-3749, 1992.

12.1.2 Detectors

“Long term gain variation in the FUSE detectors,” D. J. Sahnou, 2004 Proc. SPIE 5488, pp. 731-737.

“On-orbit performance of the double delay line detectors for the Far Ultraviolet Spectroscopic Explorer,” D.J. Sahnou, M.A. Gummin, G.A. Gaines, A.W. Fullerton, M.E. Kaiser, O.H.W. Siegmund, 2000 Proc. SPIE 4139, pp.

A. S. Tremsin, O. H. W. Siegmund, M. A. Gummin, P. M. Jelinsky, J. M. Stock, ”Electronic and optical moiré interference with microchannel plates: artifacts and benefits,” Appl. Opt., vol. 38, pp. 2240-2249, 1999.

O. H. W. Siegmund, M. Gummin, J. Stock, G. Naletto, G. Gaines, R. Raffanti, J. Hull, R. Abiad, T. Rodriguez-Bell, T. Magoncelli, P. Jelinsky, W. Donakowski, and K. Kromer, "Performance of the double delay line microchannel plate detectors for the Far Ultraviolet Spectroscopic Explorer," SPIE. vol. 3114, pp. 283 - 294, 1997.

12.1.3 Instrument Data System

"Scripted Operations in the Far Ultraviolet Spectroscopic Explorer Flight Software," D. A. Artis, L.J. Frank, & B.K. Heggstad, 2000, Proc. 51st International Aeronautics Conference.

"The Far Ultraviolet Spectroscopic Explorer (FUSE) Instrument Data System," B. K. Heggestad, & R.C. Moore, 1999, 18th Digital Avionics Conference

12.2 In-Flight Instrument Performance

"The D/H Ratio Toward PG 0038+199," G.M. Williger, et al. 2005 ApJ 625 210.

"FUSE: Lessons Learned for Future FUV Missions," H.W. Moos, S.R. McCandliss, J.W. Kruk, 2004 Proc. SPIE 5488 1.

"The FUSE Detectors: On Orbit Use and Lessons Learned," D. J. Sahnou, 2002, Proc SPIE vol. 4854 610.

"Abundances of Deuterium, Nitrogen, and Oxygen toward HZ 43A: Results from the FUSE Mission," J.W. Kruk, et al. 2002 ApJS 140 19.

"Deuterium Abundance toward WD 1634-573: Results from the FUSE Mission," B.E. Wood et al. 2002 ApJS 140 91.

"Overview of the Far Ultraviolet Spectroscopic Explorer Mission," H.W. Moos et al. 2000, ApJ 538 L1

"On-Orbit Performance of the Far Ultraviolet Spectroscopic Explorer Satellite," D.J. Sahnou et al. 2000 ApJ 538 L7

"On-orbit performance of the double delay line detectors for the Far Ultraviolet Spectroscopic Explorer," D. J. Sahnou et al., 2000, Proc SPIE, vol. 4139, p. 149.

"The Far Ultraviolet Spectroscopic Explorer Optical System: Lessons Learned," S. J. Conard, R.H. Barkhouser, J.P. Evans, S.D. Friedman, J.W. Kruk, H.W. Moos, R.G. Ohl, D.J. Sahnou, 2000, Proc SPIE, vol. 4139, p. 186.

"Performance of the Far Ultraviolet Spectroscopic Explorer mirror assemblies," R.G. Ohl, R.H. Barkhouser, S.J. Conard, S.D. Friedman, J. Hampton, H.W. Moos, P. Nikulla, C.M. Oliveira, T.T. Saha, 2000 Proc. SPIE 4139 137.

"The Far Ultraviolet Spectroscopic Explorer: 1 year in orbit," D. J. Sahnou et al., 2000, Proc SPIE, vol. 4139, p. 131.

12.3 Target Acquisition and Guiding, Attitude Control System

"FUSE: Emergency Operations and One-Wheel Gyroless Fine-Pointing Control," B. F. Class, J.W. Kruk, M.J. White, T.B. Ake, D. Rovner, M. Abate, 2007 AAS G&C Conf.

"Operations with the New FUSE Observatory: Three-axis Control with One Reaction Wheel," D. J. Sahnou, J. W. Kruk, T.B. Ake, B-G Andersson, A.F. Berman, W.P. Blair, R. Boyer, J. Caplinger, H. Calvani, T. Civeit, W.V. Dixon, M.N. England, M.E. Kaiser, M. Kochte, H.W. Moos, B.A. Roberts, 2006 Proc. SPIE vol. 6266 1.

"Three-axis Attitude Control with Two Reaction Wheels and Magnetic Torquer Bars", B.A. Roberts, J.W. Kruk, T.B. Ake, T.S. Englar, B.F. Class, D.M. Rovner, 2004, AIAA GN&C 2004-5245.

"FUSE In-orbit Attitude Control with Two Reaction Wheels and No Gyroscopes," J. W. Kruk, B. F. Class, D. Rovner, J. Westphal, T. B. Ake, H. W. Moos, B. Roberts, and L. Fisher, 2002, SPIE, vol. 4854 274.

"FUSE Attitude Control: Target Recognition and Fine Guidance Performance," T.B. Ake, H.L. Fisher, J.W. Kruk, P.K. Murphy, & W.R. Oegerle, 2000, SPIE, 4139, 175.

"FUSE Fine Error Sensor Optical Performance," J. W. Kruk, P. Chayer, J. Hutchings, C. Morbey, R. Murowinski, 2000, Proc SPIE, vol. 4139, p. 163.

12.4 Mission Operations and Observation Scheduling

"FUSE Planning and Scheduling Under One Wheel Attitude Control", Berman, A.F., et al., 2006, Proc: Fifth International Workshop on Planning and Scheduling for Space.

"The Evolution of the FUSE Spike Long Range Planning System", Calvani, H.M., et al., 2004, Proc: Fourth International Workshop on Planning and Scheduling for Space.

"Operations with the FUSE Observatory," W. P. Blair, J. W. Kruk, H. W. Moos, and W. R. Oegerle, 2002, SPIE, vol. 4854 241.

12.5 Other

"High Resolution FUV Spectroscopy of the Terrestrial Day Airglow with the Far Ultraviolet Spectroscopic Explorer," P.D. Feldman, D.J. Sahnou, J.W. Kruk, E.M. Murphy, H.W. Moos, 2001 JGR 106 8119

"Atomic Data for Resonance Absorption Lines III. Wavelengths Longward of the Lyman limit for the Elements Hydrogen to Gallium," Morton, D.C. 2003 ApJS 149 203.

“Spectrophotometric Results from the Copernicus Satellite. I. Instrumentation and Performance,” Rogerson, J. B., Spitzer, L., Drake, J. F., Dressler, K., Jenkins, E. B., Morton, D. C. & York, D. G. 1973, ApJ, 181, L97